The Origin of Multiple DSC Melting Peaks of Fischer-Tropsch Hard Waxes

A thesis submitted to the University of Cape Town in fulfilment of the requirements for the degree of Doctor of Philosophy

Glenda Vanessa Webber

B.Sc. (Potchefstroom University, Vaal Triangle Campus)
Hons. B.Sc. (Potchefstroom University)
M.Sc. (University of Stellenbosch)

Department of Chemistry
University of Cape Town
Private Bag X3
Rondebosch 7701
South Africa

November 2009

ACKNOWLEDGEMENTS

Associate Professor Alan Hutton, my promoter, for accepting this project.

Prof. Sandy Asher, Asher and Day Consulting, Pittsburgh, for facilitating the low-frequency Raman work and for being available as a soundboard to aid the interpretation.

Colleagues at Sasol Wax R&D (SA) (Ena Murray, Esmeralda Muller, Dr. Madelyn Bekker, Herman Boikanyo), Sasol Technology R&D (Dr. Adam Baran) and Sasol Polymers (Dr. Nyambeni Luruli and Josephine Makawa-Mbewe) for analytical support.

Amanda Kelly, Sasol Wax R&D, for administrative assistance.

John Beigley, my colleague at Sasol Wax, for facilitating internal approvals and for his 20 years of friendship.

Sasol Wax, specifically Louis Fourie and Helmuth Schulze-Trautmann, both MDs, for supporting this work.

Kate Smuts, Lindiwe Dube and Savi Govender for their assistance with the sourcing of literature.

Freddy Teddy, my beloved old cat, and Odie, Jack Russell extraordinaire, for keeping me company during many hours of writing.

And most importantly Angus, Daniel, Luke and Joshua Webber, Daddy and Ria for your unconditional love and all that you mean to me.

1 The LORD reigns, let the earth be glad;
let the distant shores rejoice.

2 Clouds and thick darkness surround him;
righteousness and justice are the foundation of his throne.

3 Fire goes before him
and consumes his foes on every side.

4 His lightning lights up the world;
the earth sees and trembles.

5 The mountains melt like **wax** before the LORD,
before the Lord of all the earth.

6 The heavens proclaim his righteousness,
and all the peoples see his glory.

7 All who worship images are put to shame,
those who boast in idols—
worship him, all you gods!

8 Zion hears and rejoices
and the villages of Judah are glad
because of your judgments, O LORD.

9 For you, O LORD, are the Most High over all the earth;
you are exalted far above all gods.

10 Let those who love the LORD hate evil,
for he guards the lives of his faithful ones
and delivers them from the hand of the wicked.

11 Light is shed upon the righteous
and joy on the upright in heart.

12 Rejoice in the LORD, you who are righteous,
and praise his holy name.

Psalm 97, New International Version

Abstract

The Origin of Multiple DSC Melting Peaks of Fischer-Tropsch Hard Waxes

Glenda Vanessa Webber

November 2009

The differential scanning calorimetry (DSC) analyses of the Fischer-Trospch (FT) hard waxes display multiple melting peaks, the origin of which is unknown. The phenomenon is sometimes referred to in the literature, but no attempt has been made to explain its cause. There are a few known causes of melting bimodality in n-alkanes and their mixtures, petroleum waxes and polymers. These are: polymorphism, chain folding and bimodal molecular weight distributions. It is shown in this work that these specific causes cannot explain FT hard wax melting behaviour.

Low-frequency Raman analysis was used to elucidate the crystalline nature of these waxes from the frequencies of the longitudinal acoustic modes (LAMs), which may be related to an effective sample chain length. It has been documented that low-frequency Raman analysis has been used for the measurement of n-alkanes, polymers and PE wax. The wax measurements performed for this work showed the occurrence of multiple LAM peaks, which are indicative of multiple crystalline domain sizes having discrete thicknesses. The equivalent carbon chain lengths of these domains were derived from the LAM frequencies. The wax DSC melt peak temperatures were assumed to be representative of the melting of average distributions of material within the waxes. The DSC maxima were mathematically modelled to derive equivalent carbon chain lengths. It was found that there was a good correlation between the apparent chain lengths derived from Boltzmann-corrected low-frequency Raman and DSC measurements. These two derived chain lengths also correlated with the carbon number equivalents of the molecular weight data measured directly by gel permeation chromatography (GPC). The FT hard wax DSC melt peaks were therefore found to be due to the melting of multiple domains of different average chain lengths. The multiple domains arise as a result of a crystalline segregation of material in the wax molecular weight distribution (MWD).

The underlying cause for this crystalline segregation is a reduction in crystalline lattice strain that would arise from a too-high chain length mismatch as a result of a too-broad wax MWD. The chain length mismatch is minimised by the development of multiple domains, which each have a narrower effective MWD.

A qualitative empirical structural model for the FT hard waxes was developed by incorporating elements from this and other work to optimise the gaps in a previously proposed model. The improvements comprised indicating the multiple domain size nature of FT hard wax; incorporating the bridged lamellar structure; and demonstrating the manner in which branched material would be accommodated in the crystalline structure.

Table of Contents

List of Tables

List of Figures

List of Abbreviations

C_n^{min}	smaller chain length size in a binary mixture of n-alkanes
C_n^{max}	larger chain length size in a binary mixture of n-alkanes
CCD	charge-coupled device
DGF	Deutsche Gesellschaft für Fettwissenschaft
DSC	differential scanning calorimetry
EC	extended chain
ED	electron diffraction
EFC	electronic flow-control
FC	folded chain
FT	Fischer-Tropsch
FWHM	full width at half maximum
GPC	gel permeation chromatography
HDPE	high-density polyethylene
HTGC	high temperature gas chromatography
LAM	longitudinal acoustic mode
L_{LAM}	effective lamellar thickness derived from a specific LAM
M_n	number-average molecular weight
M_w	weight-average molecular weight
M_z	z-average molecular weight
MEK	methyl-ethyl ketone
MIBK	methyl-isobutyl ketone
MW	molecular weight
MWD	molecular weight distribution
n_{LAM}	carbon chain length equivalent derived from a specific LAM
P_d	polydispersity, M_w/M_n
PE	polyethylene
SAXS	small angle X-ray scattering
SPI	septum-equipped programmable injector
SEC	size exclusion chromatography
TREF	temperature rising elution fractionation
XRD	X-ray diffraction

CHAPTER 1

INTRODUCTION

Historically, the first wax known to and used by man was beeswax. Nowadays, a wide range of waxes from various origins is available commercially. These waxes are used extensively in formulations for varied applications, either as a low-level performance-enhancing additive or as the main active ingredient.

1.1 DEFINITION AND OVERVIEW OF WAX

The definition of wax is broad, in order to encompass the many types of waxes and their varied compositions. The composite definition given by the German Association for Fat Science (Deutsche Gesellschaft für Fettwissenschaft, DGF) has been adopted by the EU customs tariff. The DGF definition for wax is as follows: [1]

(1) Drop melting point >40°C
(2) Melt viscosity should not exceed 10,000 mPa.s at 10°C above the drop melting point
(3) Polishable under slight pressure with a strongly temperature dependent consistency and solubility
(4) Kneadable or hard to brittle, coarse to finely crystalline, transparent to opaque at 20°C, but not glassy or highly viscous or liquid
(5) Melting should occur without decomposition above 40°C
(6) The viscosity should exhibit a strongly negative temperature dependence above the melting point and the liquid should not be stringy
(7) Melting should occur between ca. 50°C and 90°C (in exceptional cases up to 200°C)
(8) Combustion should occur with a sooting flame after ignition
(9) Waxes may form pastes or gels and are poor conductors of heat and electricity (i.e. they are thermal and electrical insulators).

The most general classification of wax is according to origin. It is generally accepted that there are two classes of wax, viz. natural and synthetic. Figure 1.1 shows a schematic of the classification of the different types of waxes.

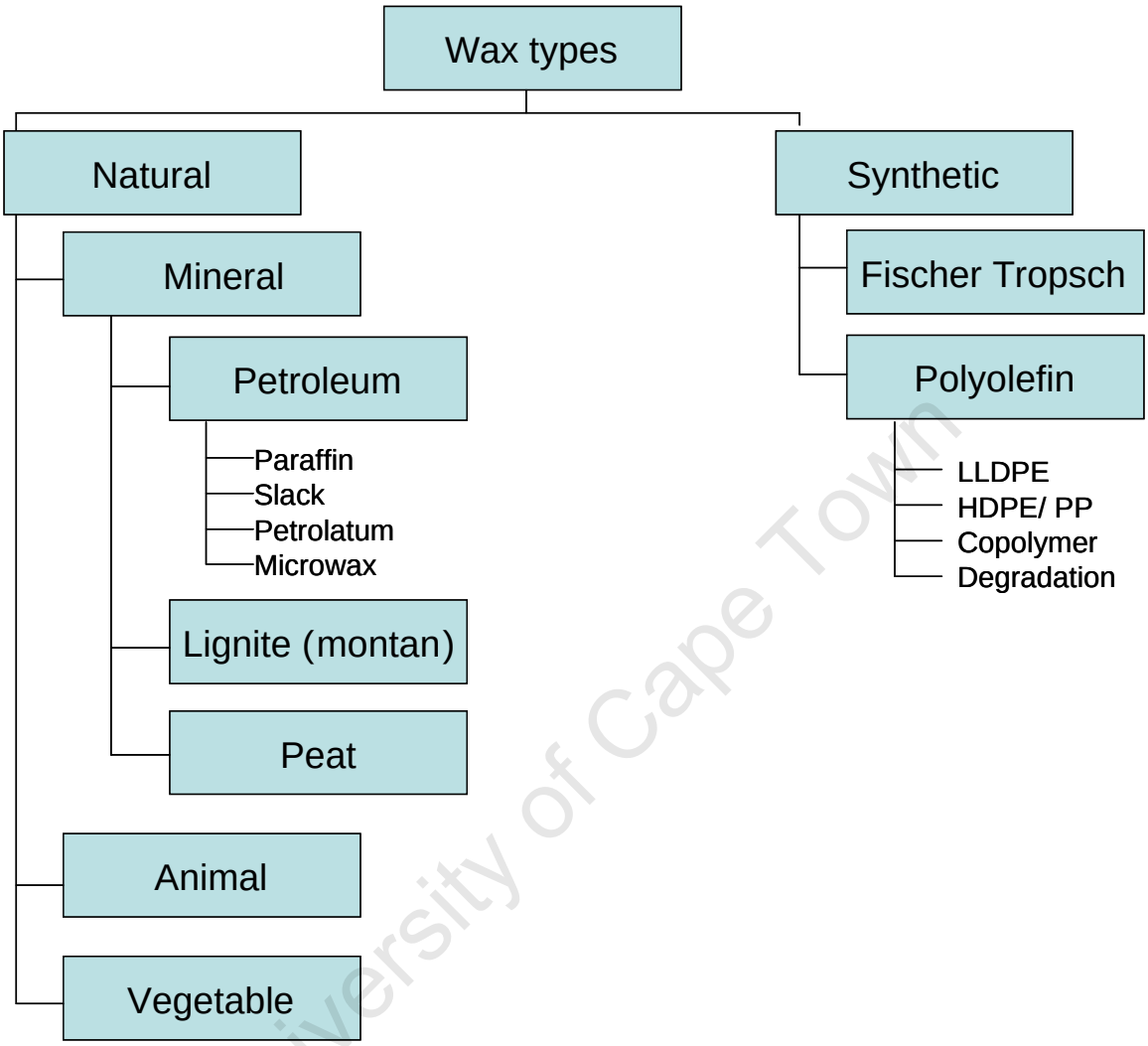

Figure 1.1: Classification of waxes according to origin

A wax is not composed of a single type of molecule but of a mixture of molecules. This mixture may vary widely in terms of molecular weight and molecular composition, depending on the origin of the wax.

1.1.1 Natural waxes [1]

The natural waxes are products of animal or plant metabolism and form as a result of the biochemical processes occurring in the organism. Animal and vegetable waxes are

complex mixtures of predominantly oxygen containing materials such as homologous esters of long-chain aliphatic alcohols and acids in the C_{16}-C_{36} range; bifunctional components, such as diols and oligoesters; free acids and alcohols; and homologous n-alkanes in the range ca. C_{15}-C_{37}. These waxes most often require further refinement to convert them into a commercially significant form. The carbon chain length distributions of the components in natural waxes are typical and distinctive for each wax type.

The most significant type of animal wax is beeswax. Beeswax is used by bees as the construction material for their honeycombs. This wax is produced in many regions of the world, but its availability is determined by weather conditions and the health of bee populations. Other insect waxes are shellac wax and Chinese insect wax, both derived from the secretions of specific beetles, and wool wax, from which lanolin is derived. The availability of the insect waxes is determined by the regional occurrence of the beetle. Wool wax is a sebaceous gland secretion that protects the epidermis and wool of the sheep from adverse weather and acidic perspiration.

The most well known and commercially significant vegetable waxes are carnauba and candelilla. Both are derived from vegetation which occurs regionally, the former in Brazil and the latter in the semi-deserts of the southern USA and Mexico. Carnauba is derived from the leaves of a specific species of palm tree, while candelilla is found on the leaves and stems of a specific shrub species. The availability of both types is highly regional and seasonal in nature. The annual yield of carnauba wax per palm tree is ca. 150g! The wax occurs in the outer cutinous layers of the leaves (carnauba) or leaves and stems (candelilla) and offers additional protection against the evaporation of water. Wax extraction is a highly labour-intensive process and the wax is purified and refined to produce various commercial grades. In recent years, a number of commercially significant vegetable waxes that are derived from the fruit of different species of palms in the Middle East and from soya crops have become available. The availability of these waxes is regionally wider spread, but the quality and properties may differ significantly in the class.

Animal and vegetable waxes are sometimes also referred to as recent natural waxes to distinguish them from natural waxes that have formed by fossilisation of organic material

during historical geological periods. This latter sub-class is more commonly referred to as mineral waxes.

Montan is a vegetable fossil wax which is present in the extractable, bituminous portion of lignite and peat. Bitumen contains a number of components, of which wax is one; if the wax composition of the bitumen is >60%, then it is referred to as montan wax. Deposits which yield this wax are highly localised in Germany, Russia and the Ukraine, California in the USA and China. The wax is extracted from the bitumen with solvent. Crude montan wax is a mixture of mainly homologous wax acids and wax esters, resins and asphaltenes. The crude wax requires refinement to lighten its very dark colour in order to make it commercially attractive.

The petroleum waxes are by-products from the processing of petroleum oils. The lower the required pour point of the oil, the greater the yield of petroleum wax extracted from the crude. The petroleum waxes are classified as macrocrystalline (paraffin wax) and microcrystalline (microwax). The former are obtained from light and middle lubricating oil cuts of vacuum distillation. The latter are extracted from vacuum distillation residues. There is also a class that is intermediate to these two types with respect to structure and composition (intermediate waxes).

The paraffin waxes are comprised of distributions of a homologous series of straight chain n-alkanes. The molecular weight of the specific paraffin wax fraction is determined by the boiling range of the lubricating oil distillate from which it originates. A significantly lower level of iso-alkanes of low branch density and monocyclic alkanes are also present. The molecular weights and composition of the n- and iso-alkanes in the intermediate waxes are comparatively higher than those of the paraffin waxes. Further processing of these waxes may be performed in order to reduce the oil component of the wax. This oil component is very short chain and highly branched material that is poorly entrapped in the crystal structure of the wax and may therefore result in undesirable wax application performance. The crude wax is referred to as slack wax, while the deoiled waxes are known as semi- and fully-refined paraffin waxes, depending on their level of refinement.

The microwaxes are comprised of a mixture of hydrocarbons in the form of n-alkanes, iso-alkanes, naphthenes, and alkyl- and naphthene-substituted aromatics. The composition is predominantly branched material and naphthenics. The highly branched nature inhibits crystallisation, resulting in a microcrystalline structure.

1.1.2 Synthetic waxes [(1)]

As the name implies, synthetic waxes are manufactured according to a commercial synthetic process. Polyolefin waxes are produced using polymerisation technology that is similar to that of their plastic counterparts. This class of wax includes high-density polyethylene (HDPE) and propylene (PP) wax, low-density polyethylene (LDPE) wax, co-polymeric waxes, degradation and polar polyethylene waxes.

The first two classes are manufactured by polymerisation of ethylene or propylene. The reactions are terminated prematurely in order to produce a wax rather than a plastic. HDPE and PP waxes are produced by the Ziegler-Natta low-pressure process using organometallic catalysts. This wax class displays the highest molecular weights (MW) of all wax types. The MW influences the overall properties of the wax. These waxes have a linear structure and are hard, brittle, tough and high melting. Their viscosities are relatively high for a wax.

LDPE wax is manufactured using a high-pressure process in the presence of radical initiators, such as organic peroxides. They are more branched than the HDPE waxes. Ethylene polymerisation by this method produces methyl branching. The MWs and viscosities of the LDPE waxes are higher than those of the HDPE waxes. They are also more flexible than the HDPE waxes.

Specific functionalities may be introduced into the polyethylene wax backbone by the introduction of other co-monomers during synthesis. This is done to decrease the hydrophobicity of the wax for emulsion applications. Examples of this type of wax are ethylene vinyl acetate and acrylic acid co-polymeric waxes. These waxes display properties that are determined by their branched structure, such as a reduction in hardness and melting point and an increase in flexibility and density.

The degradation polyethylene waxes are produced by cleaving the chains of plastic polymers at high temperature in the absence of air. This is an energy intensive process. The structure of these waxes is similar to that of the source material, with unsaturation being introduced by the mechanism of the cleavage reaction. A distinguishing characteristic of these waxes is that their carbon distribution displays both odd and even chain lengths, whereas the ethylene-based synthesised waxes display only even-numbered carbon chain lengths. Their overall properties are again determined by the MW and structure.

Fischer-Tropsch (FT) waxes bridge the property gap between the paraffin and polyethylene waxes. They are often referred to as polymethylene waxes but this does not qualify their nature as polymeric as they are not derived from a methylene monomer. There are currently only two producers in the world who produce FT wax for the intention of selling it as such, viz. Sasol Wax in South Africa and Shell MDS in Malaysia. FT wax is also produced at gas-to-liquid (GTL) facilities as an intermediate that is hydrocracked into diesel or fuel oils. FT wax was formerly produced in South Africa using either slurry bed or fixed bed technology with an iron catalyst from syngas (carbon monoxide and hydrogen) derived from the combustion of coal. Nowadays, both producers derive syngas from natural gas. The reactor waxes are processed by distillation, hydrogenation, oxidation and/ or blending in order to derive commercial FT wax products. These raw FT waxes contain a high percentage of n-alkanes with chain lengths in the range ca. C_{20}-C_{300}. Very low amounts of methyl branched, unsaturated and oxygenate material may be present, depending on the manner in which a cut has been processed.

1.1.3 Wax applications

The choice of wax depends on the performance properties required in the final application and is dictated by the wax properties. In certain instances, waxes from different classes may be used interchangeably in a specific application without affecting performance, but most often different waxes are combined for synergistic benefit. The applications for wax are more diverse than the traditional and obvious production of candles. Some of the more commercially attractive applications for waxes are:

- a component of hot melt adhesives to reduce the viscosity of the blend, thereby aiding processability, and to provide crystallinity to it for thermosetting

- an additive to inks in a micronised form to aid with the rub and scuff resistance and slip property of the ink film
- a component of emulsions for the waterproofing of paper, paperboard, fiber board and gypsum board
- a component of emulsions to reduce lint formation during the production of newsprint paper
- an emulsion component for temporary corrosion protection coatings
- a binder for equestrian race tracks
- the main component of polishes for leather, wood and ceramics
- a processing aid for the production of PVC and PE articles.

1.2 CHARACTERISATION OF WAXES

It has been shown that the different types of waxes may be distinguished on the basis of their melting profiles. [(2)] Differential Scanning Calorimetry (DSC) provides a characteristic melting profile or "fingerprint" for each wax, which may be used as a qualitative means to distinguish between the wax types. [(2)] DSC analysis measures the heat flow to or from a sample in a controlled atmosphere as a function of temperature or time. A sample will absorb or evolve heat during a phase transition. Thermal events in the sample appear as upward or downward deviations from the baseline. [(2)] The convention used in this work is to display the endothermic peak in the upward direction. The ASTM methods for the DSC analysis of polymers and petroleum waxes were adapted here in order to optimise the analysis time. [(3-6)] A full description of the analytical method used is given in Chapter 2.

An interesting phenomenon that is often observed in the melting profiles of waxes, n-alkanes and their mixtures is peak bimodality. There are many reasons for this behaviour that have been documented, and these are discussed below.

1.3 MELTING BIMODALITY AND CRYSTAL MODIFICATION

Melting bimodality in low-melting paraffin waxes is due to a crystal lattice transition. [(7-11)] This is illustrated in Figure 1.2 for two low-melting petroleum wax cuts. The DSC analysis of wax HNP3 displays a polymorphic transition at ca. 53°C, followed by a melting transition at ca. 66°C. On heating, the orthorhombic crystal form assumes the hexagonal (rotator) form a few degrees below the melting temperature. The DSC

analysis of the wax HNP9 displays only a melt transition at ca. 76°C. It is known that the type of polymorphism displayed by HNP3 only appears in waxes where the melting point is below 75°C. [7] Figure 1.2 and Table 1.1 illustrate this melting point dependence of polymorphism for these two waxes. HNP is a mark of Nippon Seiro Co. Ltd.

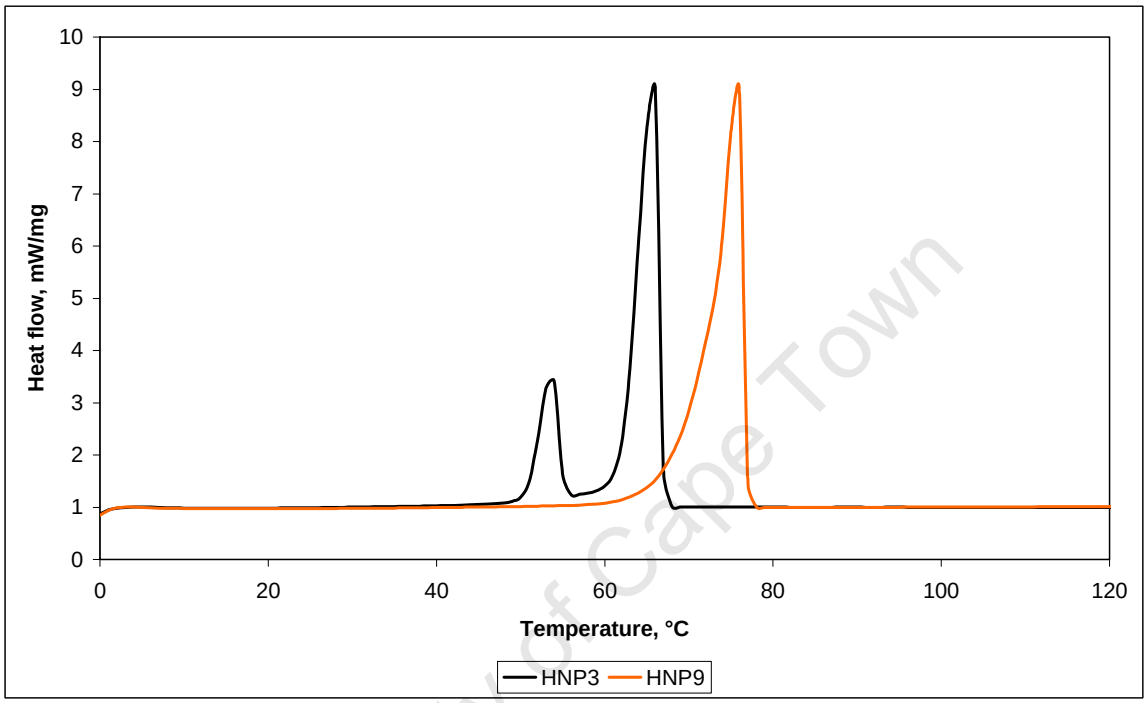

Figure 1.2: DSC analysis of two petroleum waxes showing polymorphism

Table 1.1: DSC melting data for two petroleum waxes

Wax	DSC melting maxima, °C
HNP3	53/66
HNP9	76

1.4 MELTING BIMODALITY AND CHAIN FOLDING

Chain folding is known to be another cause of DSC melting bimodality in some polyethylene (PE) waxes, crystalline polymeric materials and ultra-long n-alkanes. The polyethylene waxes display broad chain length distributions which span the range of oligomers and polymers. In these materials, the shorter chains crystallise in an extended chain conformation. [12] Crystallisation of chains in a folded conformation occurs when the chain lengths are $>C_{100}$ or $>C_{150}$, depending on the literature source. [12, 13] The

overall macro-crystal structure, or superstructure, therefore consists of mixed lamellae of both conformations. The degree of folding (number of folds) varies with crystallisation temperature and time (i.e. crystallisation rate). [12] Chain folding allows the very long chain material present in the wax to be optimally incorporated into the crystal structure, and is therefore of thermodynamic significance to the crystallisation process.

Bimodality due to chain folding is observed in the DSC analysis of polyethylene wax. A portion of the material in the lower molecular weight polyethylene waxes crystallises as folded chain (FC) crystals, with the rest crystallising as extended chain (EC) crystals. This results in a bimodal DSC melting peak. It is claimed that the first (lower temperature) and second (higher temperature) peaks may be attributed to the melting of EC and FC crystals, respectively. [12] The relative areas under the respective peaks are said to be representative of the amount of material present in each form. [12] This assignment of peaks contradicts that given for similar behaviour observed in long-chain n-alkanes. In these materials, the FC material melts at a lower temperature and is followed by the melting of EC material. [13] This occurs as the FC conformation is thermodynamically less stable than the EC crystallised material. [14] It is, however, also known that above a certain crystalline core thickness, the thermodynamic stability of the FC is greater than that of the EC, which possibly clarifies the seemingly contradictory interpretations. [14] This bimodality in pure, monosdisperse n-alkanes sometimes manifests as melting of the FC form, immediately followed by recrystallisation into the EC form, which then melts at a higher temperature. [13] The areas under the DSC endotherms would therefore not directly correspond to the proportions of the two crystal populations.

Figure 1.3 shows a DSC analysis for a polyethylene wax, Escomer H101, which displays a melting profile similar to that discussed in the literature. [12] Escomer is a registered trademark of Exxon Chemical Company. The assignment of DSC peaks to the melting of EC and FC material has been done according to this reference in order to illustrate this specific interpretation of the occurrence of FC material, as the reference describes the melting behaviour of a PE wax. [12] The relevance of this interpretation will be discussed further in Chapter 4.

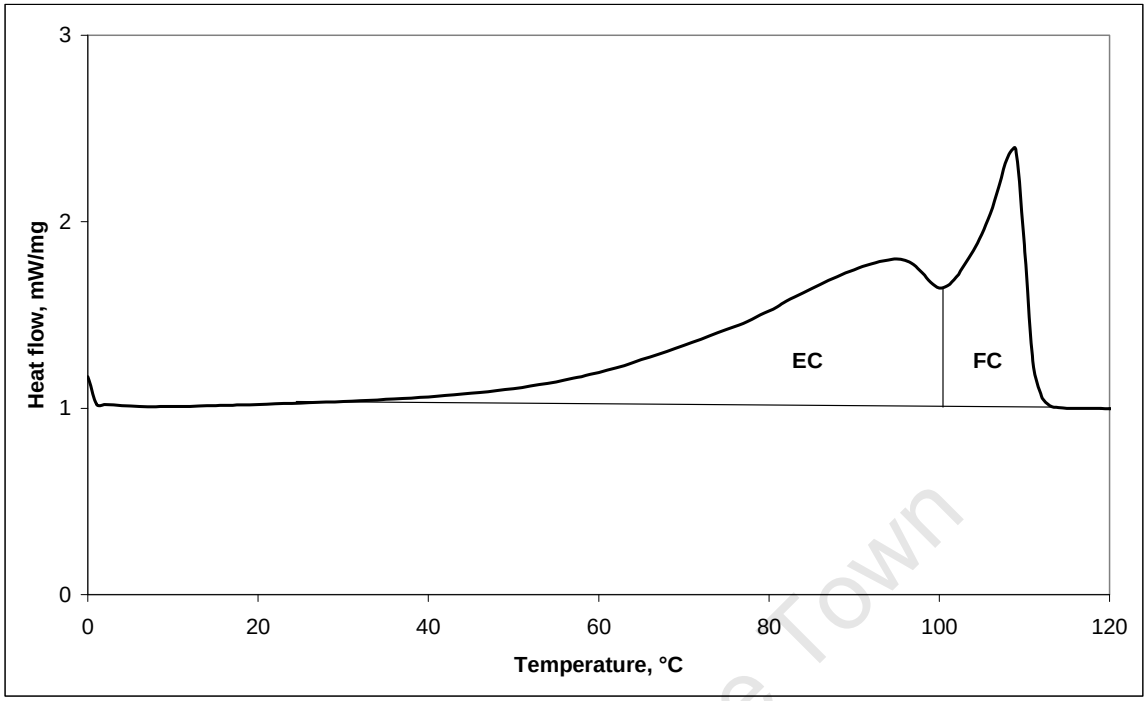

Figure 1.3: DSC analysis of a polyethylene wax showing the assignment of peaks to the melting of extended (EC) and folded (FC) chain crystals according to the literature [12]

1.5 MELTING BIMODALITY AND THE NATURE OF THE WAX MOLECULAR WEIGHT DISTRIBUTION

Another obvious cause of melting bimodality may be attributed to the wax having a bimodal molecular weight distribution (MWD). Figures 1.4 and 1.5 show the high temperature gas chromatography (HTGC) and DSC data for a low-melting Fischer-Tropsch wax. The HTGC data clearly show discontinuity in the carbon number distribution. This is mimicked by the DSC curve which also shows a bimodal melting profile. Note that this DSC curve also shows the orthorhombic-hexagonal transition at ca. 32°C, which is characteristic of low-molecular weight paraffinic materials.

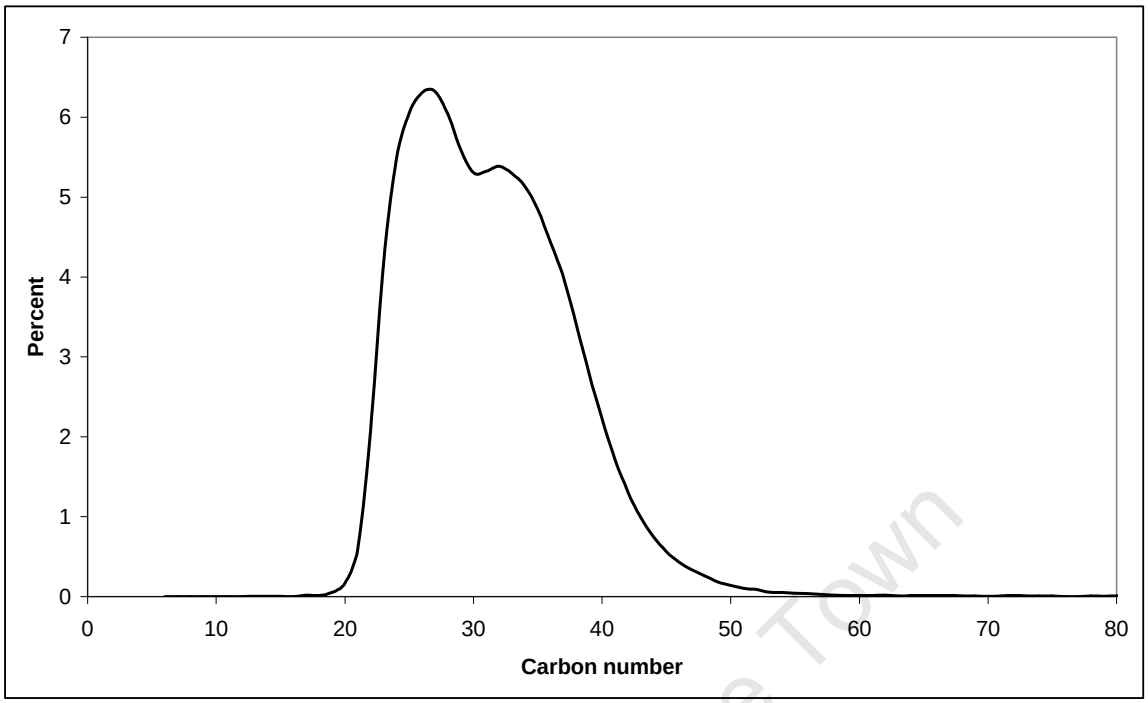

Figure 1.4: HTGC analysis of a low-melting Fischer-Tropsch wax

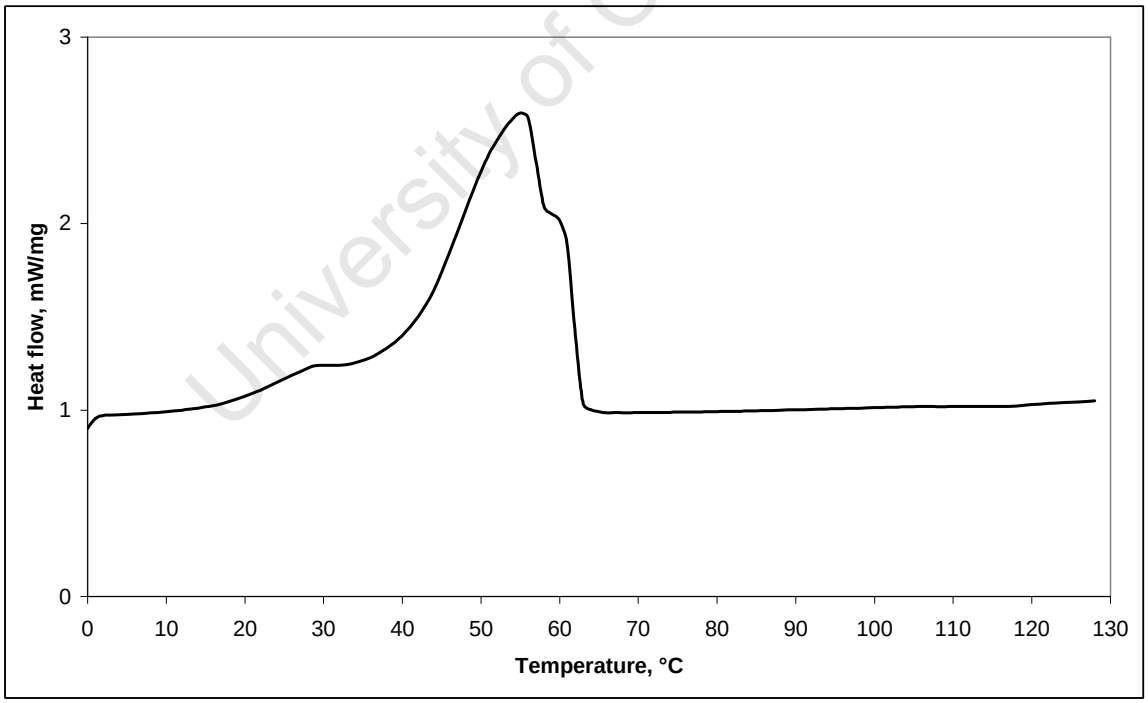

Figure 1.5: DSC analysis of a low-melting Fischer-Tropsch wax

1.6 MULTIPLE MELT PEAKS AND FISCHER-TROPSCH HARD WAXES

FT hard waxes, an economically significant class in terms of their unique combination of physical properties, also display multiple DSC melting peaks. Figure 1.6 shows a DSC comparison of two FT hard waxes, Sasolwax H1 and Sasolwax C105, with an intermediate melting FT wax, Sasolwax C80. The latter wax shows only one melting peak in its DSC analysis. It is included for comparison as it forms a homologous series with the two hard waxes. The MWs of the three waxes increase along the series Sasolwax C80, Sasolwax H1 and Sasolwax C105. The MW dependence of the FT wax multiple-melting phenomenon may therefore be interesting to consider.

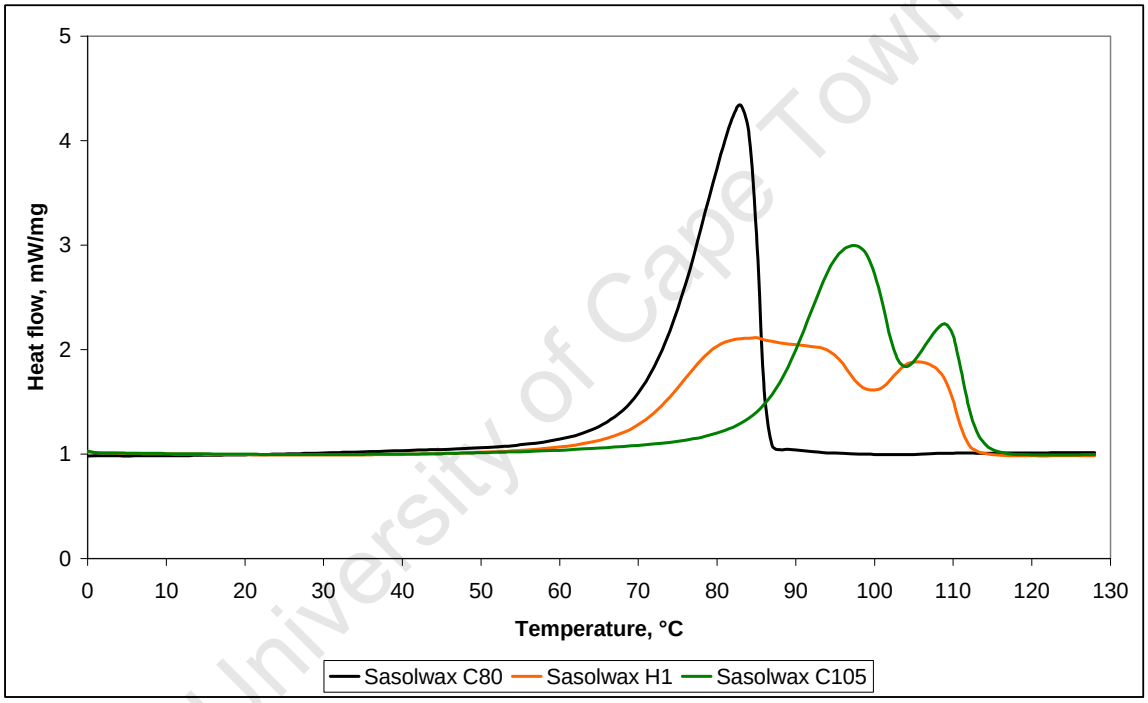

Figure 1.6: DSC melting profiles of the Sasol FT hard waxes H1 and C105, as well as Sasolwax C80, an intermediate melting FT wax

There is no literature which adequately explains the origin of the multiple DSC melt peaks apparent for this class of wax. [8, 15, 16] Visual inspection reveals no obvious link between the origin of these multiple-melting peaks and any of the theories discussed above. DSC as applied here is a qualitative tool and requires complementary information to allow an absolute interpretation.

The purpose of this work is to investigate the nature of the multiple melt peaks observed in the DSC melting profiles of the Sasol Fischer-Tropsch hard waxes.

This will involve the following:

(1) Determining whether the Sasol FT hard waxes meet the criteria documented for any of the above-mentioned types of melting bimodality.

(2) Using alternative analytical techniques to aid in the interpretation of the DSC data and to postulate a theory to explain the origin of the multiple-melting peaks of the Sasol FT hard waxes.

(3) Documenting the dependence of the nature of the multiple-melting peaks of the Sasol FT hard waxes on sample thermal history and composition.

(4) Developing a qualitative empirical model to account for the crystalline nature of FT hard wax.

CHAPTER 2

EXPERIMENTAL DETAILS, THE SOURCE OF THE WAX SAMPLES AND THE QUALITATIVE COMPOSITION OF FT HARD WAX

The analytical methods used in this work for the characterisation of the waxes were Differential Scanning Calorimetry (DSC); powder X-ray Diffraction (XRD); High Temperature Gas Chromatography (HTGC); Gel Permeation Chromatography (GPC); Temperature Rising Elution Fractionation (TREF) and low-frequency Raman spectroscopy. This chapter provides an overview of these techniques. The origin of the wax samples studied in this work is also given. Finally, the qualitative composition of FT waxes is defined as a basis for this work.

2.1 EXPERIMENTAL DETAILS

2.1.1 Differential Scanning Calorimetry (DSC)

DSC is a technique that may used to study the melting characteristics of a sample. DSC provides a characteristic melting profile or "fingerprint" for a wax, which may be used as a qualitative means to distinguish between the wax types. DSC analysis measures the heat flow to or from a sample in a controlled atmosphere as a function of temperature or time.

The DSC analyses were performed using a Perkin-Elmer Pyris 1 instrument. A conventional analysis was performed by melting the sample at 130°C, cooling at 20°C/min to 0°C and then recording the analysis between 0°C and 130°C at 10°C/min. The melting behaviour of waxes is known to be dependent on the thermal history of the sample. This thermal history is determined by the manner and rate at which a wax sample is crystallised. The temperature regime recommended for the conventional analysis of wax, and also prescribed by ASTM methods for wax analysis, involves melting the sample and then recrystallising it at a standard, reproducible rate in order to standardise its thermal history. [3, 4, 5, 6] This is particularly important for comparative work.

The cooling rate of 20°C/min used in the Sasol Wax R&D laboratory is historic and was optimised for sample throughput. Sasol Wax customers have in the last half century been accustomed to receiving test results performed using this method, and therefore some of this work has been based on this cooling rate. Some analyses are shown for various cooling rates from 5°C/min to quench cooled in order to illustrate the thermal history dependence of the wax melting profiles.

Where specified, the first melt analysis was obtained by loading the sample at 0°C and heating it at 10°C/min to 130°C. This enabled the melting profile of a sample to be measured which is representative of the original conditions under which the sample was crystallised. This also allowed a direct comparison of the DSC data of a sample with a specific thermal history with the low-frequency Raman data of the same sample with equivalent thermal history.

The sample size used was 2-3 mg and the analysis atmosphere was nitrogen. [2, 6] This sample size is considerably less than that recommended by the ASTM methods. A smaller sample size facilitates improved thermal-mass transfer, which allows a more accurate measurement of melting transition temperature.

The sample was measured into an aluminium sample pan, which was then fitted with an aluminium lid. The sample capsule was then mechanically sealed using a sample press. The capsule was loaded into the DSC sample furnace at the initial temperature of the analysis. An empty aluminium sample pan and lid was placed in the reference furnace to balance the thermal-mass contribution of the sample pan. The furnace assembly was cooled to -60°C using a two-stage intra-cooler accessory.

DSC temperature and enthalpy calibration was performed using indium and n-$C_{36}H_{74}$ standards. The n-alkane purity was >98%. The indium was obtained from Perkin-Elmer and the n-alkane from Sigma-Aldrich. A software correction was performed when required, based on the difference between the actual and expected values of the peak temperatures and fusion enthalpies. The convention is to use the onset of the melting peak for the calibration. The accuracy and practical significance of the melt onset determination deteriorate as the melting range of the sample increases. Many wax

samples display broad melting distributions and for this reason the maxima of the DSC melt peaks were considered for calibration of the instrument.

2.1.2 Powder X-ray Diffraction (XRD)

X-ray diffraction is a technique that may be used to probe the crystallographic structure of the material under investigation. A crystal comprises a regular three-dimensional arrangement of atoms in space. The lattice unit may be described by the dimensions of the cell axes and the angular relationships among the three axes. [17]

The crystalline morphology of wax samples was studied by recording their diffraction patterns. The tests were performed at room temperature and at temperatures around the transitions indicated by their DSC melt profiles. Two identical PANalytical X'Pert PRO Multi-Purpose Diffractometers (MPD) (XRD-1 for high temperature and XRD-2 for room temperature studies) were used to record the X-ray diffraction patterns. The instrumental parameters used are shown in Table 2.1.

The parameters used for the Anton Paar XRK-600 HT camera mounted on the XRD-1 diffractometer for HT XRD studies are as follows. A nitrogen atmosphere was used at atmospheric pressure and a flow rate of 50 ml/min. The analysis temperature was varied at a rate of 1°C/min using the steps shown in Table 2.2 below.

The wax samples were in the form of a powder or granules and were manually ground to a fine powder using an agate mortar and pestle. They were then loaded into a conventional sample holder for room temperature analysis or into a high temperature camera for high temperature analysis and exposed to X-rays.

The crystallographic data were determined using the PANalytical X'Pert HighScore Plus software by applying search-match algorithms using the International Center for Diffraction Data (ICDD) Powder Diffraction File (PDF) database. The crystallographic data may, however, be determined from the Bragg equation.

Table 2.1: XRD instrument parameters used for wax analysis

Instrument	XRD-1	XRD-2
Temperature	HT	RT
Sampling set-up	HT camera	Spinner stage
High voltage, kV	40	40
Tube current, mA	50	40
Divergence slit, °	1	1
Anti-scatter slit, °	2	2
Mask, mm	Fixed 10	Fixed 10
Detector	X'Celerator	X'Celerator
Soller slits, rad	0.04	0.04
Filter	Fe	Fe
Scan from	5° 2θ	5° 2θ
Scan to	105° 2θ	105° 2θ
Step size, °	0.0167	0.0167
Time per step, s	149.860 (or 24.765)	149.860
Scanning	Continuous	Continuous
Total time, hrs	2 (or 20 min)	2
X-ray tube	Co radiation LFF	Co radiation LFF
Source	Cobalt	Cobalt
Wavelength, Å	1.78897	1.78897

Table 2.2: Temperature steps used for HT XRD analysis

Sample:	***Sasolwax C80***	***Sasolwax H1***	***Sasolwax C105***
Temperature increments, °C	30; 50; 70; 80; 85; 91; 100	30; 50; 70; 77; 89; 96; 101; 109; 115; 125	30; 40; 60; 80; 90; 98; 103; 108; 114; 120; 130

Lattice spacings are derived from the Bragg relation nλ = 2d sinθ, where λ is the wavelength of the X-rays, d is the interplanar distance, θ is the angle of incidence, and n is an integer called the order of reflection. The measurement of the angles 2θ under which constructively interfering X-rays leave a crystal allow the lattice spacings to be derived from the Bragg relationship. [17] The wavelength of the X-ray source used for

these experiments was 1.78897 Å, which reduces the Bragg relationship to d = 1.78897/(2sinθ) for the first-order reflections. The d-values may therefore be calculated from the 2θ angle for each reflection. The lattice dimension parameters for an orthorhombic system may consequently be calculated using the equation $1/d^2 = h^2/a^2 + k^2/b^2 + l^2/c^2$, where *h*, *k* and *l* are the Miller indices for each reflection. The Miller indices are known and may be obtained in the literature. Table 2.3 shows the Miller indices for each reflection in an n-paraffin (reference 00-040-1995) sample. A series of equations may then be solved for the lattice parameters *a*, *b* and *c*. [17-19]

Table 2.3: The Miller indices for an n-paraffin (λ = 1. 78897 Å)

Reflection	d, Å	2θ, °	(*h k l*)
1	4.133	24.999	(1 1 0)
2	3.728	27.766	(2 0 0)
3	2.981	34.923	(2 1 0)
4	2.483	42.231	(0 2 0)
5	2.296	45.858	(0 1 1)

It is generally not required to calculate the lattice constants from XRD patterns as crystallographic data may be obtained from the literature, in various databases or derived using the XRD software.

2.1.3 High Temperature Gas Chromatography (HTGC)

HTGC is a boiling point separation technique that is used to measure and quantify the carbon number distribution of wax samples.

HTGC analysis was performed on a Varian CP-3800 GC. It was fitted with a temperature-controlled Varian septum-equipped programmable injector (SPI) for a capillary column. The injector was equipped with Electronic Flow Control (EFC). The detector type was flame-ionisation (FID) and the detector was also equipped with EFC. A Restek MXT-1 column was used (100% cross-linked dimethyl-polysiloxane, 15 m x 0.28 mm ID, 0.15 *μ*m film). The instrument was controlled with the Galaxie GC Workstation. The injector temperature was ramped between 40°C and 420°C at a rate of 70°C/min and then held at the final temperature for the duration of the analysis (49.57 min). An EFC flow rate of 3.5 ml/min was used for a time of 55 min. The column temperature was

held at 40°C for 5 min and then ramped at 10°C/min to 440°C where it was held isothermally for 10 min. The N_2 make-up, H_2 and air flows to the FID detector were 25 ml/min, 30 ml/min and 300 ml/min, respectively. [20] The full analysis parameters are shown in Table 2.4 below.

Table 2.4: HTGC analysis parameters for the analysis of wax samples [20]

Injector	
Initial temperature, °C	40
Initial holding time, min	0
Temperature ramp rate, °C/min	70
Final temperature, °C	420
Final holding time, min	49.57
Total time, min	55
EFC Flow Program	
Flow, ml/min	3.5
Holding time, min	55.0
Column	
Initial temperature, °C	40
Initial holding time, min	5
Temperature ramp rate, °C/min	10
Final temperature, °C	440
Final holding time, min	10
Total time, min	55
Detector (FID)	
N_2 make-up flow, ml/min	25
H_2 flow, ml/min	30
Air flow, ml/min	300
Detector temperature, °C	450

The analyses were performed using an internal calibration with an n-C_{36} standard. A stock solution was prepared by dissolving 0.1 g of the internal standard in 100 g of xylene. The concentration of this stock solution is calculated from $C_{std\ soln}$ (ppm) = (m_{C36}/ m_{xylene}) x 1,000,000, where m_{C36} and m_{xylene} are the masses of the internal standards and the xylene respectively. [20]

The sample was prepared by weighing 0.15-0.20 g wax into a flat-bottomed flask. A 1-2 g quantity of the n-C_{36} stock solution and an additional 50 ml of xylene were then

added to the wax. The sample mixture was heated carefully on a hot plate (set at ca. 75-80°C). Once the wax was dissolved, a small amount was transferred to a vial using a warmed pipette. A 0.5-1.0 µl volume of the sample was then manually injected onto the column using a heated syringe assembly. [20]

The carbon numbers were assigned to the peaks in the measured chromatogram by counting upwards and downwards from the n-C_{36} standard. The integration of each peak in the chromatogram was performed to determine their areas, which were then normalised with respect to the total area using the software. Optimal peak resolution is obtained using this method, but it is unfortunately still incomplete. The peak integration was done by using the horizontal baseline and "force-by-peak" integration options in the software. The peaks were then manually integrated by choosing the minimum point between unresolved peaks and applying the peak split function. The correct integration of peaks is illustrated in Figure 2.1. [20]

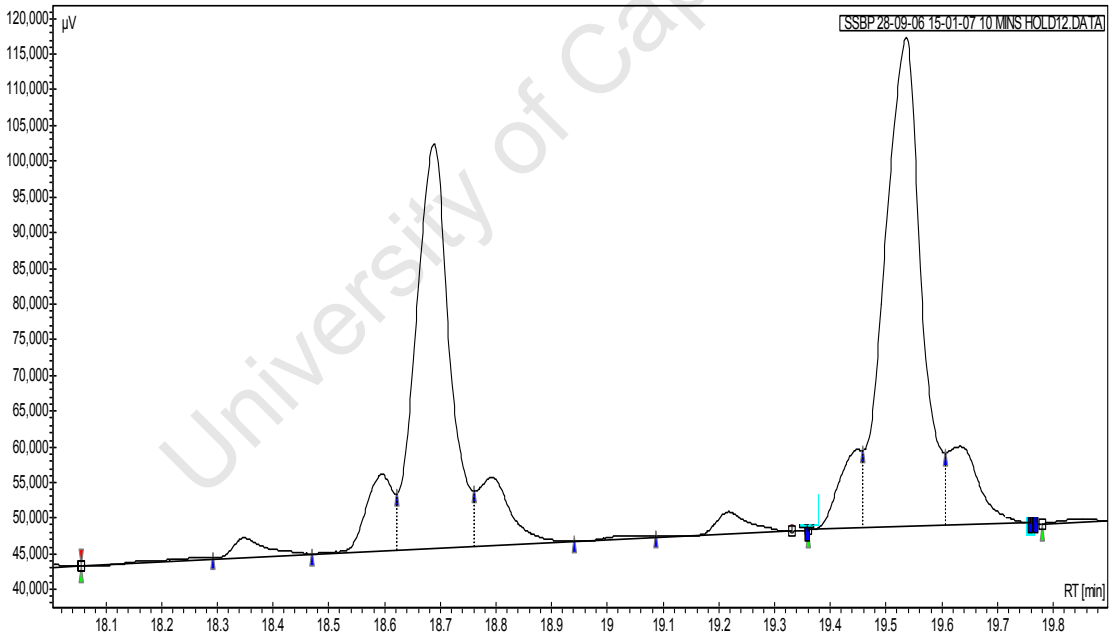

Figure 2.1: Correct integration of HTGC peaks [20]

The integration was performed by the Galaxie software with some user intervention, but the peak assignments were done manually and converted to a carbon number distribution using an Excel template. The calculation used for this purpose is:

C_c (%) = (area%$_c$ x $C_{int\ std}$)/ (area%$_{C36}$ – [{area%$_{C35}$ + area%$_{C37}$}/2]),

where C_c is the concentration of the carbon chain length of interest; area%$_c$ is the integrated peak area of the carbon chain length of interest; $C_{int\ std}$ is the percentage concentration of the internal standard; and area%$_{Cn}$ is the integrated peak area of the carbon chain length C_n.

The amount of n-C_{36} in the wax portion of the sample is calculated by averaging the areas of the n-C_{35} and n-C_{37} peaks. **(20)**

A typical raw-data chromatogram is shown in Figure 2.2 below. The main n-alkane peaks are those having the highest intensity and are clearly observed. There are also numerous lower intensity peaks that are apparent between these main peaks. Their assignments are indicated in Figure 2.2. (20)

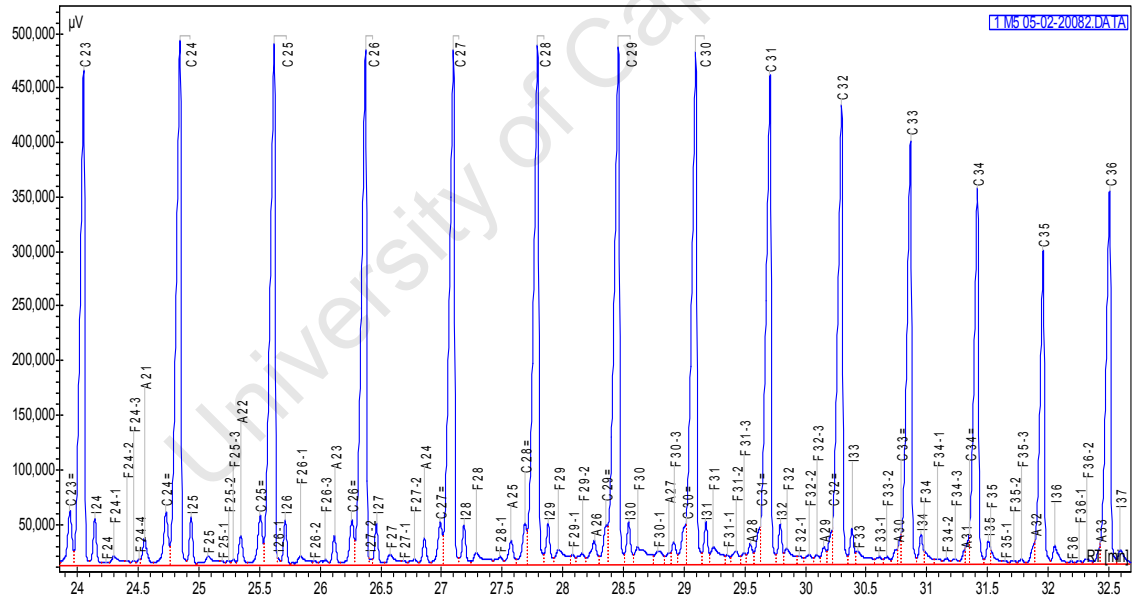

Peak assignment: C_n: n-alkane; C_n=: alpha-olefin with same carbon number as n-alkane; A: alcohol with carbon number C_{n-3}; I: iso-paraffin with carbon number C_{n+1}; F: other hydrocarbon components with carbon number C_{n+1}.

Figure 2.2: Raw-data chromatogram of a wax sample

2.1.4 Gel Permeation Chromatography (GPC)

GPC, or size exclusion chromatography (SEC), is a liquid chromatographic technique which separates molecules according to their molecular volume (size). This technique gives information on the molecular weight distribution of the sample. [21] The system is calibrated by relating the retention time of a series of compounds of known molecular weight and of chemical composition similar to that of the sample to be analysed, to molecular weight. [22]

GPC analysis was performed using a Varian PL-GPC system equipped with a differential refractive index (DRI) detector. Data acquisition was performed using Cirrus GPC/ Multi Detector software. The separation was performed on two PL gel 5 μm Mixed-D, 300 x 7.5 mm columns (molecular separation range 200–400,000 dalton). The mobile phase was HPLC grade o-xylene. The pump, injector and column compartments were programmed to 60°C, 100°C and 100°C, respectively. A flow rate of 1 ml/min and run time of 30 min were employed. Duplicate analyses of 200 μl volumes of a 0.05% w/w wax in o-xylene solution were performed. The calibration was performed using a 0.1% w/w solution of n-alkanes in xylene from C_{12} to C_{60} and polyethylene standards with chain lengths of C_{71} and C_{143}. These standards are available from Sigma Aldrich. The calibration curve is extrapolated over the range for which MW quantification is required. The linear fit correlation factor for the calibration curve was 0.9993. [2, 23]

It has been found that the concentration factor of a GPC time slice correlates with the mole percentage of the represented components in the sample. As the validation of this is not yet complete, the data presented here has not been corrected to mass percent from mole percent. [24]

2.1.5 Temperature Rising Elution Fractionation (TREF)

TREF is a preparative separation technique that allows materials, usually polymers, to be separated according to the crystallisabilities of the molecules in the sample. Sasolwax C105 was fractionated using a Holtrup Preparative Temperature Rising Elution Fractionation instrument equipped with two Julabo F32-HP chiller units. 5 g of wax was dissolved in 400 ml of xylene. 2 g of Irganox 1076 antioxidant was added to the mixture in order to prevent thermal degradation of the sample during fractionation. The mixture was warmed gently to boiling point and refluxed for 20 minutes. The sample was

transferred to the fractionation vessel, which was preheated at 120°C. After equilibrating, the sample was crystallised at 0.1°C/min (6°C/hr) to room temperature. Thereafter, the sample was fractionated stepwise by heating to the respective temperatures 40°C, 66°C, 79°C and 85°C and subsequently eluting the fractions using fresh solvent. The fractions were precipitated in 800 ml of chilled acetone. They were then washed with acetone and allowed to dry.

2.1.6 Low-frequency Raman Spectroscopy

Low-frequency Raman analysis may be used to determine the average size of the crystalline core thickness in a crystalline material. The crystalline core thickness may then be related to the chain length of the sample in order to obtain information on the manner in which the chains within the crystalline domains have crystallised. [25-27]

The lamellar sizes are calculated from the first order LAM modes of the sample using the equation $\nu_1 = (m/2L_{LAM})(E/\rho)^{1/2}$, where ν_1 is the vibrational frequency of the LAM mode; m is the order of the vibration; L_{LAM} is the length of the vibrating chain; E is the Young's modulus; and ρ is the density of the material. [25, 27-40] If the carbon number chain length equivalent of the crystalline core thickness size, n_{LAM}, is calculated using the first-order LAM from L_{LAM}, then the equation may be rewritten as $n_{LAM} = 2489.4/\nu_1$ on substitution of the parameters obtained from the literature. [13] The values of E and ρ used for PE samples are 2.9×10^{11} N/m^2 and 983.4 kg/m^3, respectively. [13, 37, 38]

The low-frequency Raman spectra were obtained on contract equipment through Asher and Day Consulting, Pittsburgh, USA using a Horiba T64000 Raman spectrometer between 10 cm^{-1} and 750 cm^{-1} employing the 488 nm Argon line. The instrument was operated in the subtractive mode using three (fixed) gratings in order to obtain superior low-frequency rejection of the exciting laser line. A charge-coupled device (CCD) detector was used for the measurements. The nominal spectral resolution was 2.4 cm^{-1} for an entrance slit of 100 µm. The data accumulation times were between 1 and 6 min. The sample geometry was microscope at 180° backscattering.

The instrument was tested by analysing a sample of dotriacontane ($C_{32}H_{48}$) to ensure that the expected LAM modes were detected.
The samples were supplied as pellets, flakes or a solid wax block. A flake, pellet or small piece of wax was placed on a microscope slide which was mounted in the instrument.

Multiple measurements were performed on each sample to ensure that the measurement was reproducible.

2.2 WAX SAMPLES

The wax samples used in this study were all commercial products obtained from various wax producers. Table 2.5 shows the origin and type (classification) of each of these waxes.

Table 2.5: Origin and classification of the waxes used in this work

Wax name	Wax producer	Wax type
HNP3	Nippon Seiro Co. Ltd.	Mineral – petroleum
HNP9	Nippon Seiro Co. Ltd.	Mineral – petroleum
Escomer H101	Exxon Chemical Company	Synthetic – copolymer
Sasolwax C80	Sasol Chemical Industries	Synthetic – FT
Sasolwax H1	Sasol Chemical Industries	Synthetic – FT (hard wax)
Sasolwax C105	Sasol Chemical Industries	Synthetic – FT (hard wax)
Sasolwax M5	Sasol Chemical Industries	Synthetic – FT
Waksol A	Sasol Chemical Industries	Synthetic – FT
Shell Sarawax SX-105	Shell MDS	Synthetic – FT (hard wax)
Polywax 1000	Baker Petrolite	Synthetic – HDPE wax
Polywax 2000	Baker Petrolite	Synthetic – HDPE wax
Polywax C4040	Baker Petrolite	Synthetic – HDPE wax

2.3 FT HARD WAX COMPOSITION

The unfunctionalised FT waxes consist of a mixture of a homologous series of predominantly n-alkanes. Different types of hydrocarbon molecules, such as iso-alkanes, alpha-olefins, alcohols and oxygenates may also be present in small amounts. These components originate during FT synthesis. The MW and MWD of a specific wax are determined by the conditions of its synthesis or the manner in which it is processed. HTGC analysis is the most suitable technique to determine the carbon number distribution of a wax. With recent developments in analytical technology, it is possible to characterise the carbon number distribution of the non-normal-alkane content of a wax sample. This can unfortunately be done only qualitatively due to limitations in the

technique. Although these improvements allow up to C_{120} to be measured, the technique cannot accurately quantify material above ca. C_{44} due to injector and detector discrimination towards the longer chain material in the sample. The result of a simple experiment to illustrate this discrimination is shown in Figure 2.3. The actual recovery from a series of injections of single n-alkane standards was measured and shows that above ca. C_{44} the sample recovery is less than 100%. [41]

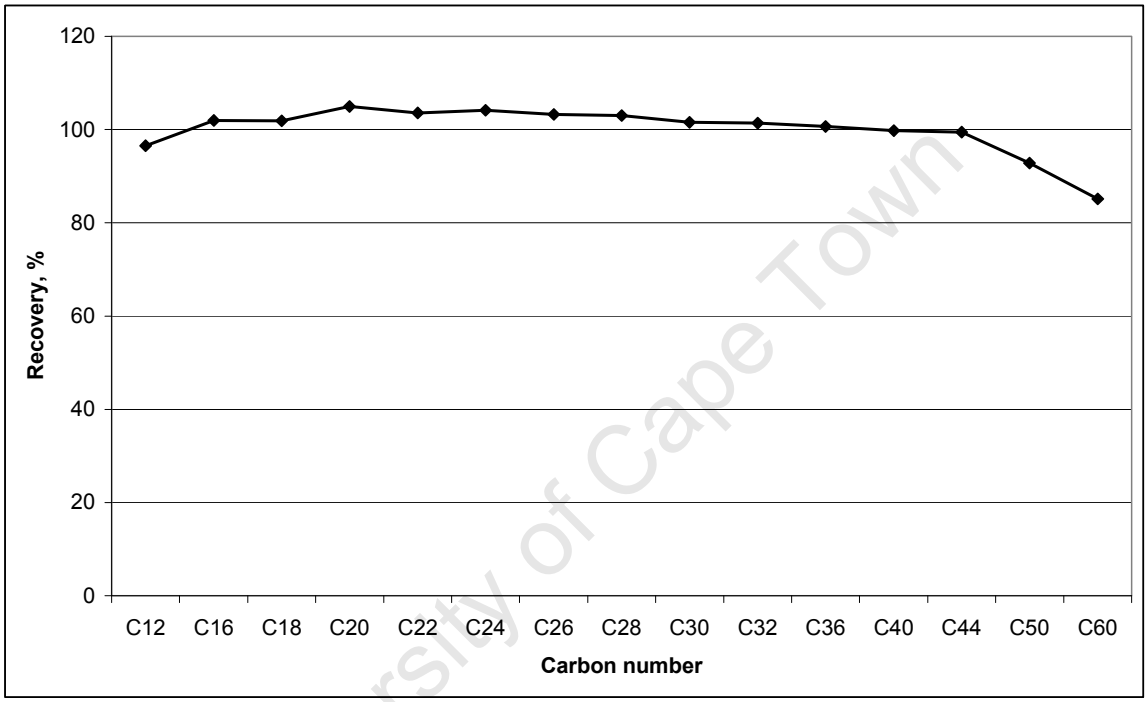

Figure 2.3: HTGC recovery of n-alkane standards up to C_{60} [42]

The slight over-recovery of the n-alkanes up to ca. C_{36} is within analytical error, but the under-recovery seen from ca. C_{44} is considered to be significant. HTGC can therefore not be used to identify the composition of FT hard wax quantitatively, but the information that it provides is certainly an interesting indication of wax composition on a qualitative basis, provided that it is used with caution. GPC analysis with a refractive index detector can provide only generalised, but certainly quantitatively more accurate, information concerning the wax MWD. [42] Table 2.6 shows a breakdown of the components in the Sasol waxes C80, H1 and C105 according to HTGC analysis. These data are normalised in order to allow a direct comparison. The recovery percentages are also shown in order to provide an indication of the amounts of each sample that were actually measured by the analyses.

Table 2.6: Composition of FT waxes according to their HTGC analyses

Component	Sasolwax C80	Sasolwax H1	Sasolwax C105
n-Alkanes, %	89.1	90.6	87.7
Alpha-olefins, %	0.0	0.1	0.2
Iso-alkanes, %	10.9	7.4	7.1
Alcohols, %	0.0	0.4	0.3
Other, %	0.0	1.5	4.8
Total recovery, %	78.3	74.9	60.2

Table 2.6 shows that the FT waxes contain predominantly n-alkanes and some iso-alkanes, with small amounts of unidentified (other) components. These other components may be aldehydes, acids, ketones or internal olefins. Figures 2.4 to 2.6 show the full HTGC analyses of the main components of these three waxes.

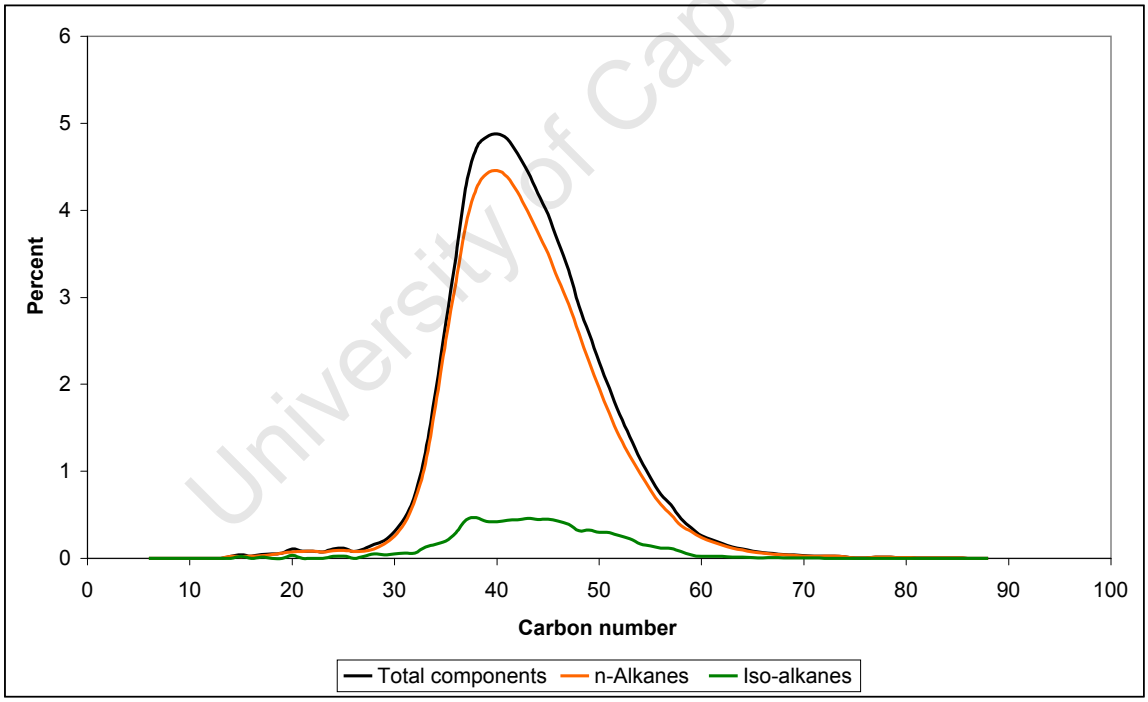

Figure 2.4: HTGC analysis of Sasolwax C80

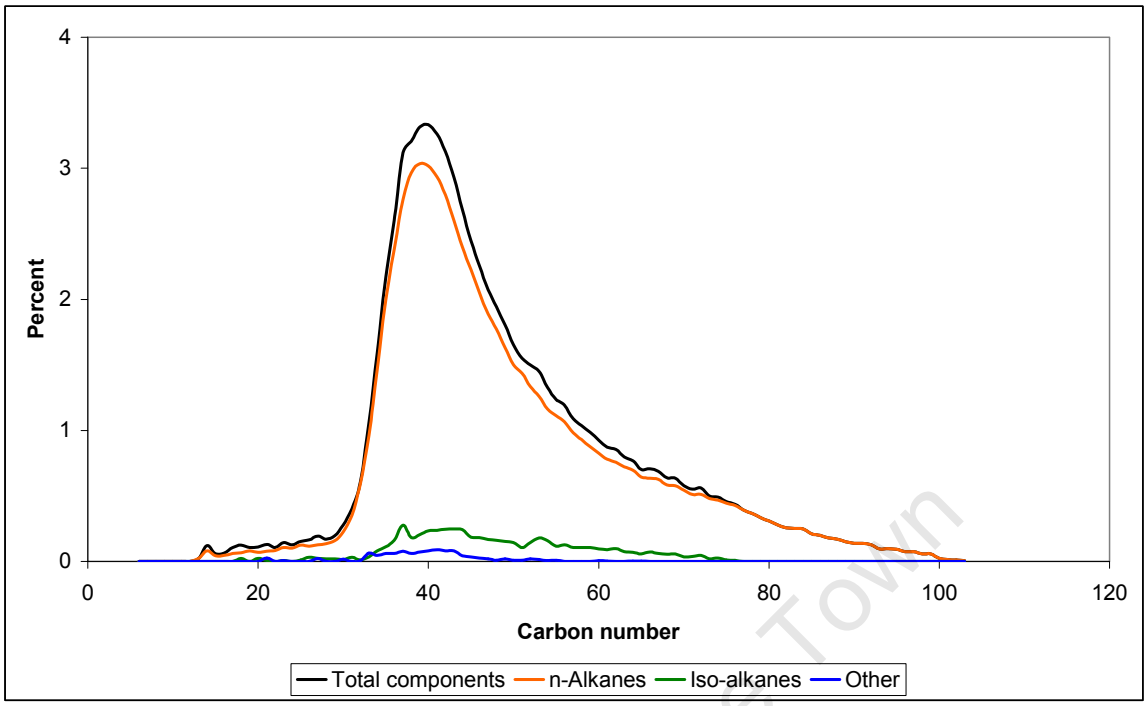

Figure 2.5: HTGC analysis of Sasolwax H1

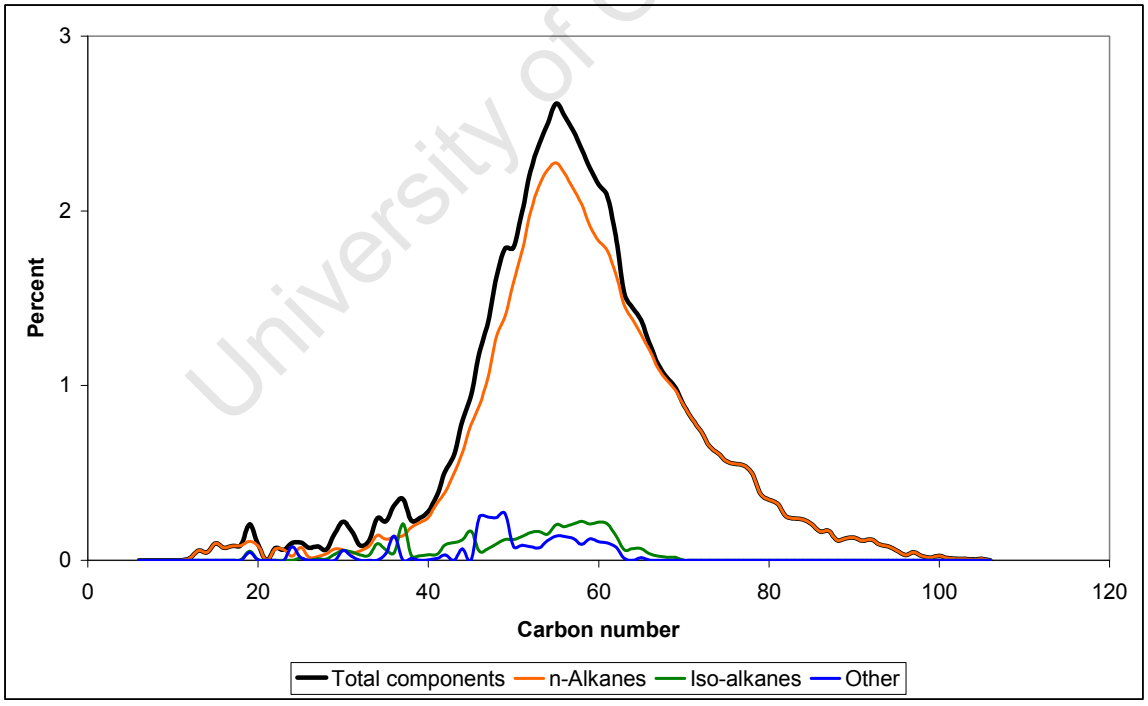

Figure 2.6: HTGC analysis of Sasolwax C105

Table 2.7 shows the MW parameters of the FT waxes from their GPC analyses with the corresponding derived carbon-number parameters.

Table 2.7: GPC parameters for the FT waxes

GPC parameter	Sasolwax C80	Sasolwax H1	Sasolwax C105
M_n, dalton	596	746	978
Carbon number from M_n	43	53	70
M_w, dalton	614	853	1078
Carbon number from M_w	44	61	77
M_z, dalton	632	1007	1213
Carbon number from M_z	45	72	87
P_d	1.03	1.14	1.10

The above data show that the HTGC recoveries of the waxes decrease with increasing wax MW. The polydispersity (P_d) data shown in Table 2.7 indicate that the MWD of Sasolwax H1 is the broadest of the three waxes, with that of Sasolwax C80 being the narrowest. P_d is a measure of the breadth of the MWD and is calculated from the ratio of M_w to M_n.

Figures 2.7 to 2.9 show the HTGC data compared with carbon number distributions derived from GPC analyses. This conversion is performed by converting log MW on the x-axis to a carbon number equivalent using a molecular weight unit of 14 dalton. The y-axis concentration factor is normalised with respect to the total MW. Data integrals are used to allow the concentration factors to be plotted as functions of whole carbon numbers and then smoothed using a moving average function. This method of processing the GPC data requires refinement, but is a sufficient illustration of the shortcomings of HTGC analysis of the higher MW FT waxes. [24] All three comparisons indicate that the GPC analyses analyse significantly more long-chain material than the corresponding HTGC analyses.

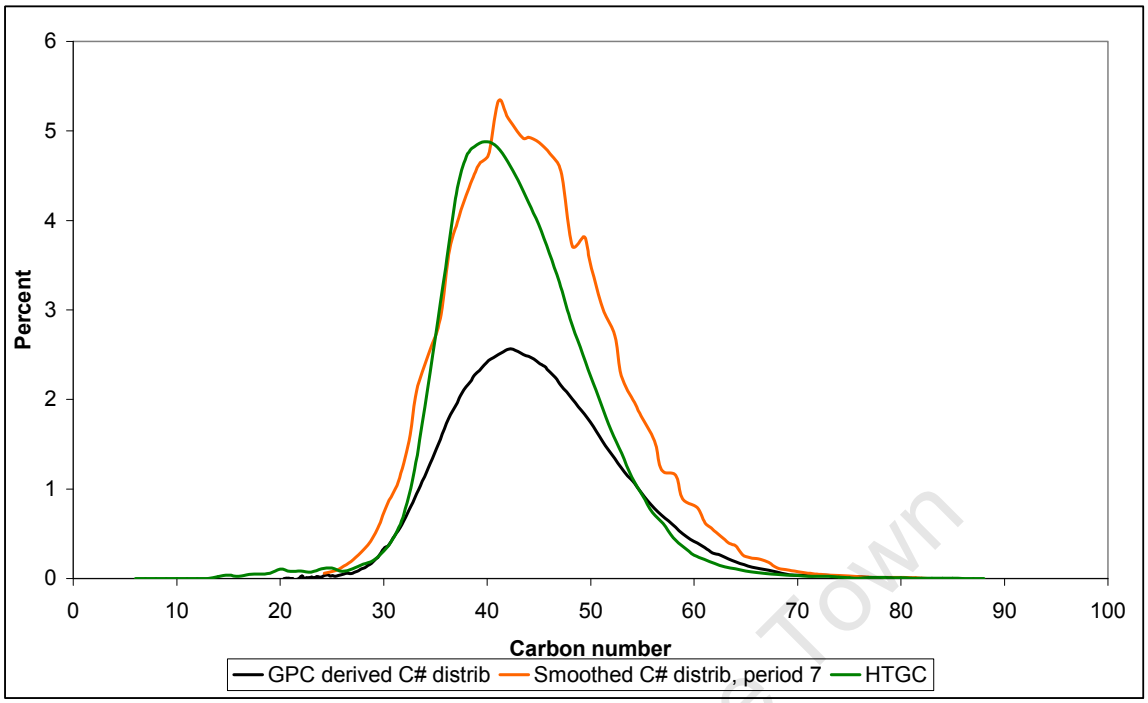

Figure 2.7: HTGC and carbon distribution derived from GPC analysis of Sasolwax C80

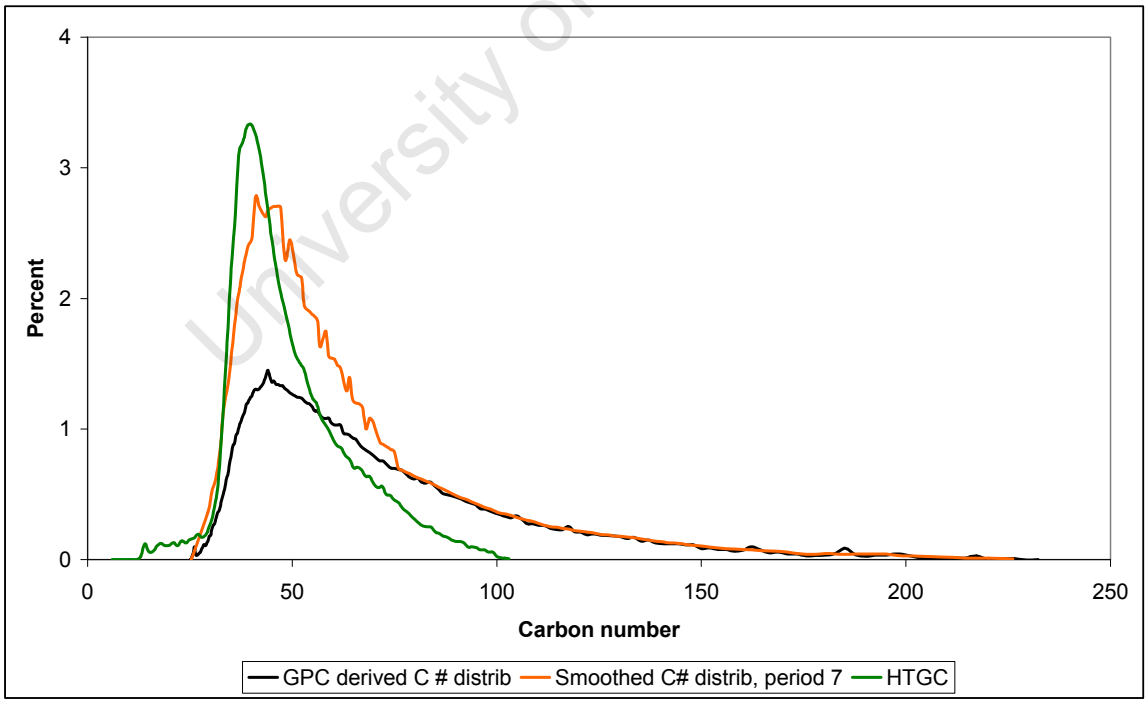

Figure 2.8: HTGC and carbon distribution derived from GPC analysis of Sasolwax H1

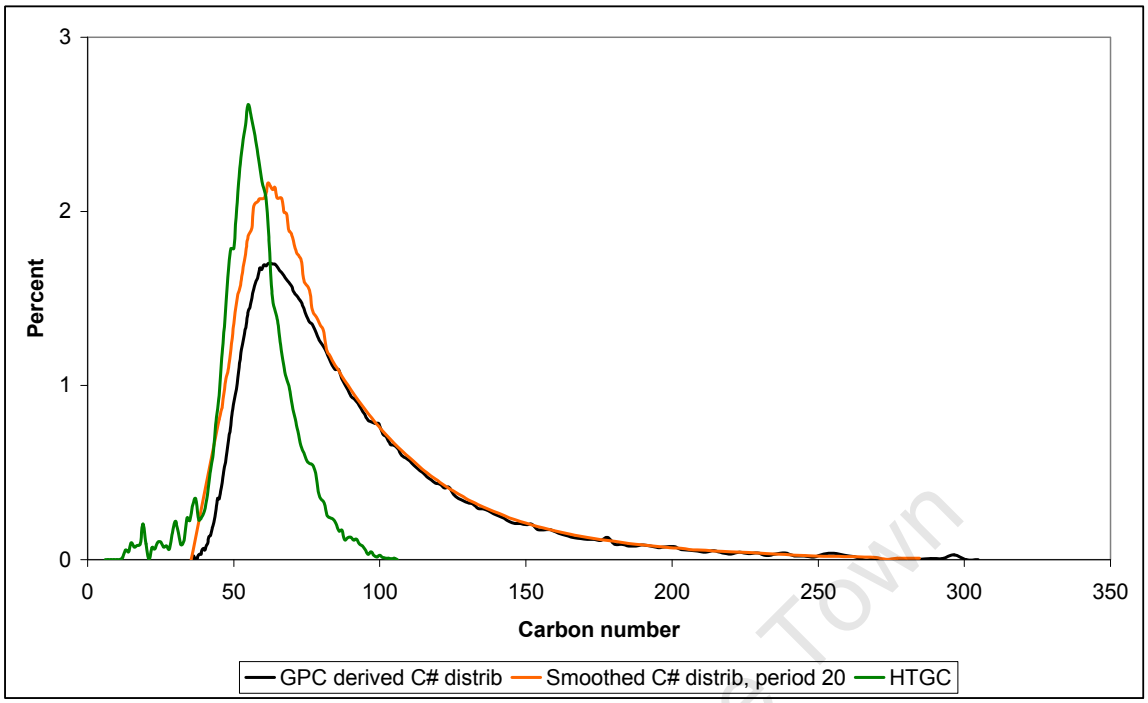

Figure 2.9: HTGC and carbon distribution derived from GPC analysis of Sasolwax C105

The comparison between the HTGC- and GPC-derived carbon distribution analyses clearly shows the inability of the former technique to quantify accurately the higher MW material in the waxes. The greatest degree of agreement between the two sets of analyses is seen for Sasolwax C80, which is the lowest MW wax. This comparison also illustrates that the HTGC analysis of the higher MW waxes, such as these FT waxes, should be interpreted with care.

This carbon distribution and MW information contextualise the composition of these waxes to provide a basis for the understanding of FT wax morphology.

CHAPTER 3

CRYSTAL MODIFICATION AND MULTIPLE MELT PEAKS IN FISCHER-TROPSCH HARD WAX

3.1 CRYSTAL MODIFICATION IN HYDROCARBON MATERIALS

Crystal modification or polymorphism is well documented and is referred to as being a reason for the melting bimodality observed in n-alkanes, mixtures of n-alkanes and low-melting paraffin waxes. [7, 9, 10, 11, 42-53]

n-Alkanes which melt below 75°C may crystallise in orthorhombic, monoclinic, hexagonal or triclinic crystal lattices. [45, 51-57] The n-alkanes with even carbon chain lengths (n) from 12 to 26 units crystallise in the triclinic form. The even n-alkanes with 28≤n≤36 display a monoclinic modification in the solid state. The triclinic and monoclinic phases are characterised by a tilted arrangement of chains with respect to the end-group planes. [58]

The even n-alkanes with n≥36 and the odd n-alkanes crystallise in the orthorhombic form. [45, 56, 58] The chain arrangement in the orthorhombic form is perpendicular to the end-group axis. The differences in the crystal modifications of the odd and even n-alkanes arise due to differences in the packing of the terminal methyl groups, with the packing efficiency of the latter type being greater than that of the former. [45] The introduction of even small amounts of homologous impurities into a specific n-alkane will cause the orthorhombic crystal habit to manifest, regardless of its chain length. [45, 56-58] The mutual tilting of a large number of long densely packed chains with homologous impurities is considered to be difficult from a kinetic perspective. [58]

Upon heating the n-alkanes may show solid-solid transitions to a different modification depending on the chain length and purity of the specific alkane. [45, 51-54] Polymorphism most commonly manifests as a hexagonal form which is stable just below the melting point in the odd n-alkanes from C_9 to C_{44} and in the even n-alkanes from C_{22} to C_{44}. [45, 51-58] Transitions between the orthorhombic and monoclinic phases are known to occur in very pure n-alkanes. The hexagonal form is also characterised by chains arranged perpendicularly to the end-group plane. A high degree of rotational freedom of the molecules around their chain axes is observed and it is therefore sometimes referred to as the rotator

phase. The solid-solid transition from the orthorhombic phase to the hexagonal phase is an order-disorder transition which is facilitated by the common perpendicular arrangement of chains in the two crystalline structures. Transitions between the triclinic or monoclinic phases and the hexagonal phases are more complex due to dissimilarities in the arrangement of the chains. [58]

The orthorhombic-hexagonal transition is apparent in the DSC melting curve of a sample as a secondary peak prior to the main melting peak. This n-alkane polymorphism is visually typical of that observed in the DSC analysis of low-melting waxes and is illustrated in Figure 3.1.

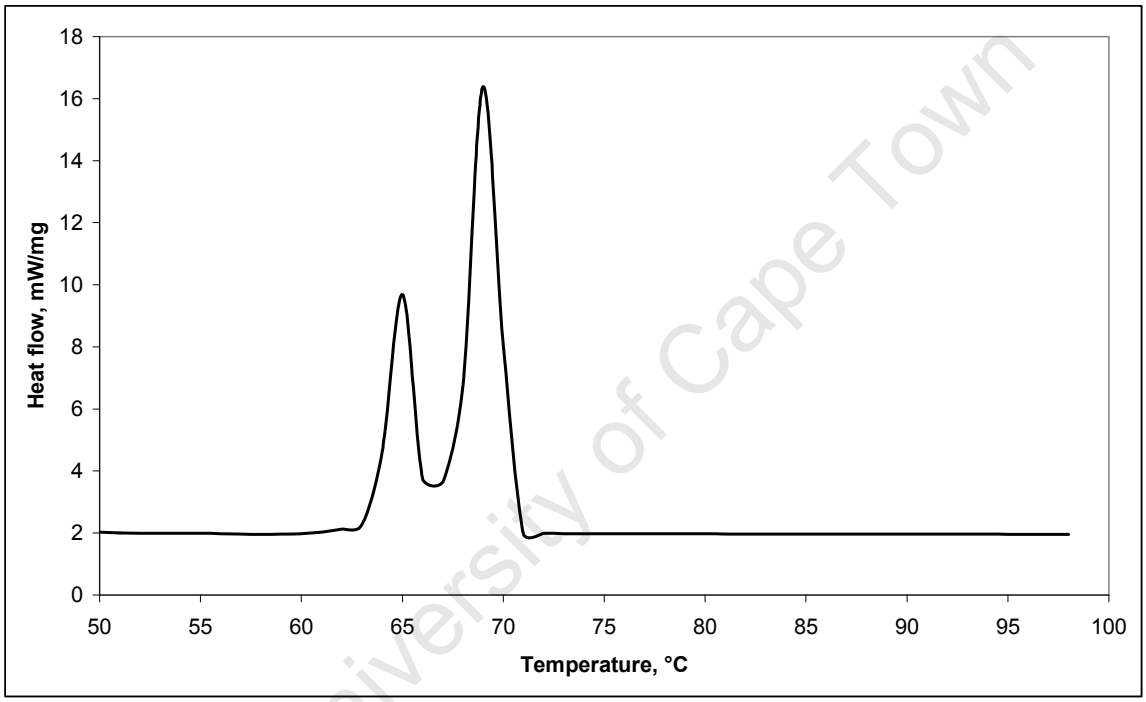

Figure 3.1: DSC analysis of n-C_{32} showing a polymorphic transition prior to melting

The same transition behaviour is observed in waxes and mixtures of n-alkanes, but they are known to crystallise in an orthorhombic lattice only. [42, 53, 59] Waxes melting above 75°C, or with a chain length >C_{39}, do not display polymorphism. [11, 47] The orthorhombic crystal form has also been identified in a FT wax with a melting point of ca. 72°C using electron diffraction (ED) analysis. [15, 60] Figure 3.2 is a schematic representation of the seven crystal systems in crystal lattice modifications. [61]

The polymorphic behaviour of low-melting paraffin or low-melting FT wax is influenced by the co-existence of mixtures of n-alkanes, which behave as a series of mutual impurities. When the average

carbon number of the mixture is $<C_{39}$, the solid wax crystallises in the orthorhombic form and undergoes a transition to the hexagonal form a few degrees below the melting point of the wax. Carbon chain mobility decreases as the molecular weight or average carbon number of a wax sample increases, resulting in the disappearance of polymorphism in n-alkanes and waxes having an average carbon number $>C_{39}$. [43, 47, 62]

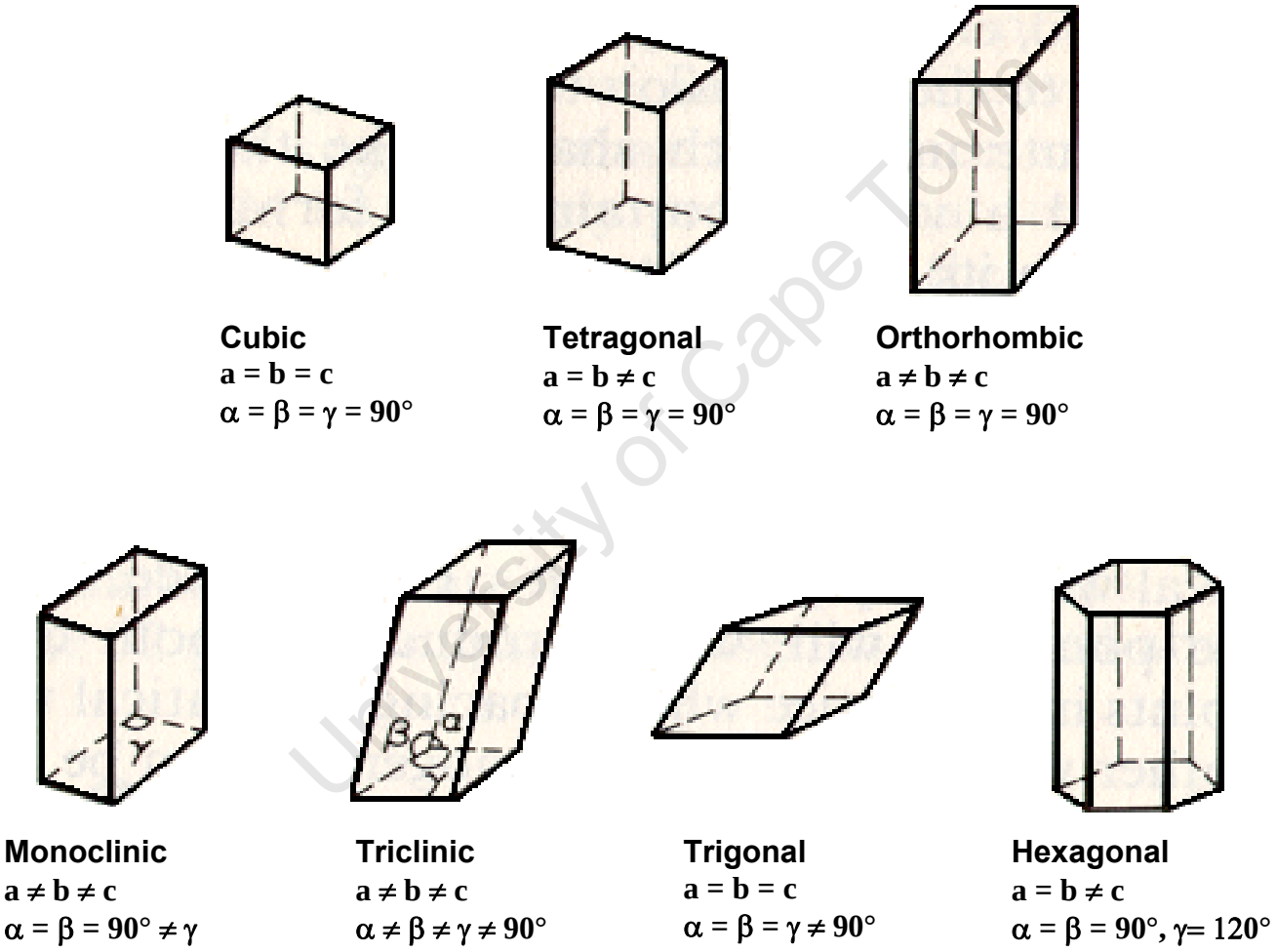

Figure 3.2: The seven crystal systems [61]

3.2 CRYSTAL MODIFICATION IN WAXES

The manifestation of crystal modification is illustrated for a series of FT wax cuts of increasing molecular weight in Table 3.1 and Figure 3.3 by way of GPC and DSC melt curve results. The carbon number related to a specific molecular weight parameter is derived by dividing the MW by 14 dalton, which is a molecular weight unit. The molecular weight parameters derived from GPC analysis are the number average MW (M_n) and weight average MW (M_w). These are calculated by using the equations $M_n = \Sigma(N_i.M_i) / \Sigma N_i$ and $M_w = \Sigma(N_i.M_i^2) / \Sigma(N_i.M_i)$, where N_i is the number of molecules with molecular weight M_i. M_n may be used to evaluate the MWD in terms of the lightest material that it contains. M_w gives an idea of the amount of heavier material that the MWD contains. M_z is a GPC parameter that is used to determine the heaviest material in the MWD and is calculated using the equation $M_z = \Sigma(N_i.M_i^3) / \Sigma(N_i.M_i^2)$. The ratio of M_w to M_n is the polydispersity (P_d) and allows the width of the MWD to be quantified. If $P_d = 1.000$, then the MWD is monosdisperse.

Table 3.1: Carbon number and DSC results of some FT waxes

Property	Waksol A	Sasolwax M5	Sasolwax C80
Molecular weight M_n, dalton	264	375	541
Average carbon number based on M_n	C_{19}	C_{27}	C_{39}
Molecular weight M_w, dalton	270	387	564
Average carbon number based on M_w	C_{19}	C_{28}	C_{44}
DSC melting range, °C	-18-33	10-60	22-87
DSC melting maximum, °C	30	55	82
DSC secondary maximum, °C *	-2	28	-

* due to polymorphism

Table 3.1 shows that the average carbon numbers of Waksol A and Sasolwax M5 are within the carbon number range for which a hexagonal-orthorhombic transition would be expected. These transitions are clearly apparent at ca. -2°C and 28°C, respectively, on the DSC analyses of Waksol A and Sasolwax M5. The DSC melting points of these two waxes are also below 75°C. The average carbon number and DSC melting point of Sasolwax C80 are both greater than the respective criteria that the literature claims will allow enough mobility for this transition to occur. [12-13] Its DSC analysis does not show a secondary transition characteristic of polymorphic behaviour. Sasolwax is a trademark of Sasol Chemical Industries.

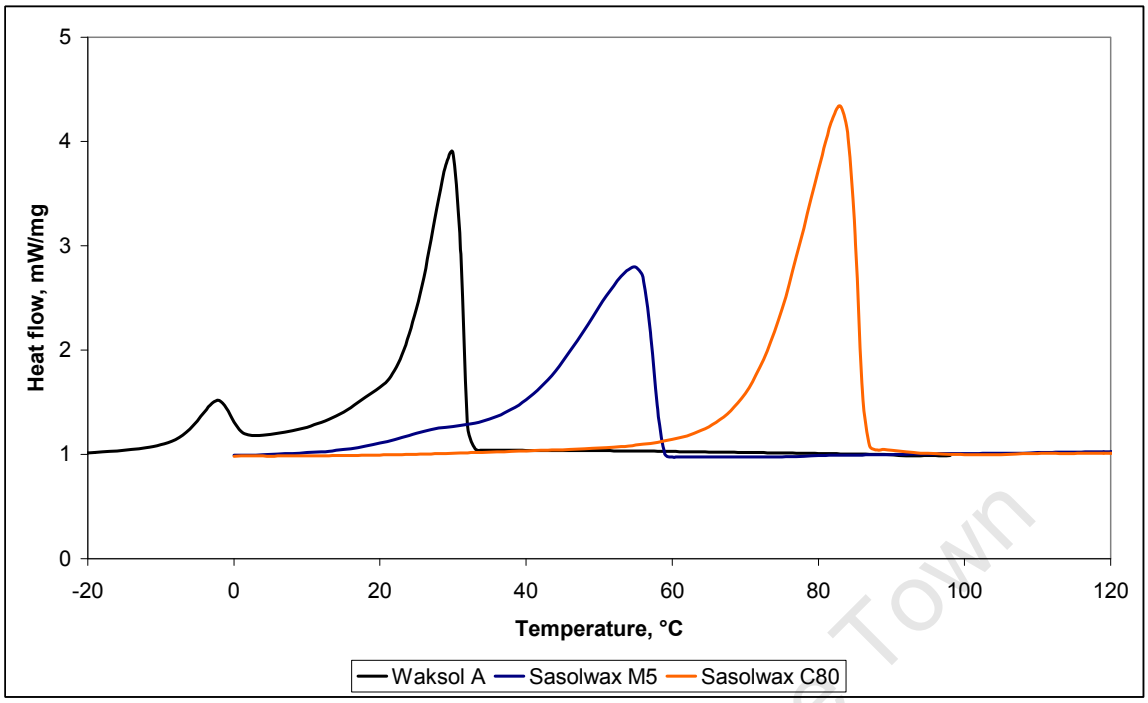

Figure 3.3: DSC analysis of some FT waxes displaying the relationship between polymorphism and wax melting range

The DSC data shown for the lower molecular weight waxes (Waksol A and Sasolwax M5) therefore qualitatively confirm that polymorphism will manifest when certain average carbon number or melting point criteria are met, as claimed in the literature. [11, 47]

As discussed in Chapter 1, the higher molecular weight FT wax samples (hard waxes) display multiple DSC melt peaks (see Figure 3.4). Visual evaluation of the DSC data indicates that the nature of these peaks is dissimilar to that of the lower melting waxes in terms of their shape, their peak temperatures and their relative intensities. Table 3.2 shows the molecular weight and DSC melting parameters of these two typical FT hard waxes.

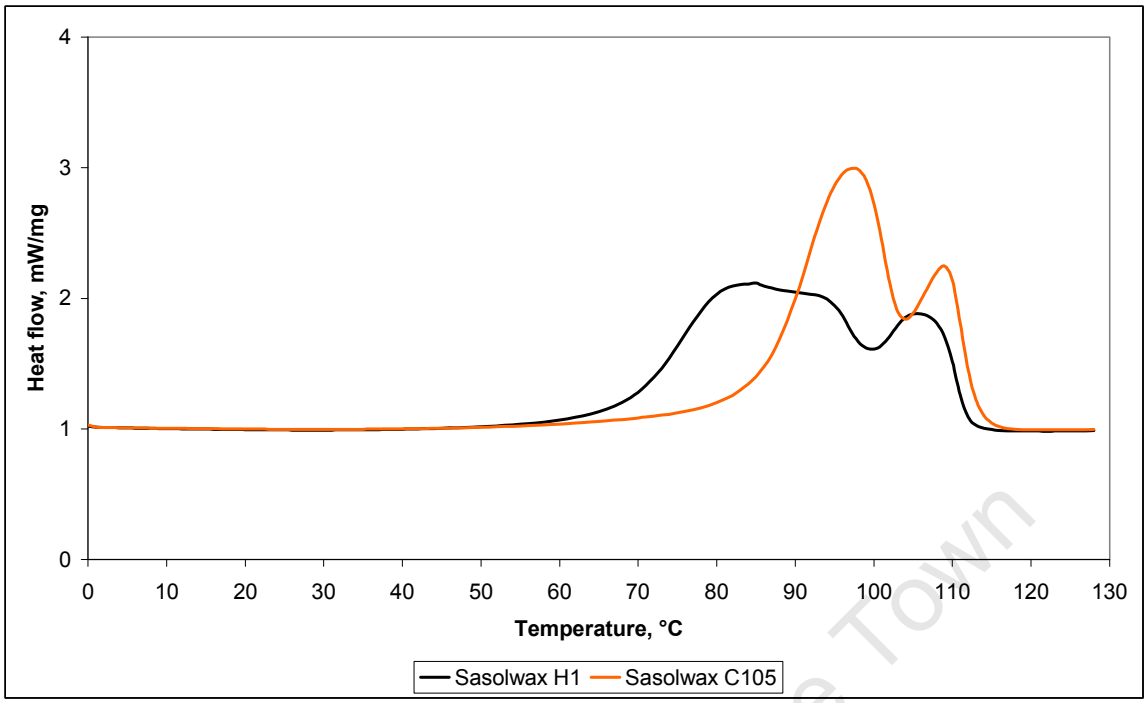

Figure 3.4: DSC analysis of two FT hard waxes

Table 3.2: Carbon number and DSC results of two FT hard waxes

Property	Sasolwax H1	Sasolwax C105
Molecular weight M_n, dalton	746	978
Average carbon number based on M_n	C_{53}	C_{70}
Molecular weight M_w, dalton	853	1078
Average carbon number based on M_w	C_{61}	C_{77}
DSC melting maxima, °C	84/105	98/110

It is apparent that the carbon number and DSC melting point data for both hard waxes are much higher than the respective C_{39} and 75°C cut-offs cited by the literature and it therefore does not appear as if the cause of the multiple melt peaks for these samples arises from polymorphism. [11, 47]

A direct measurement of the crystal form is, however, required to ascertain if polymorphism is present in these samples. This may be done using X-ray diffraction (XRD).

3.3 CRYSTAL MODIFICATION IN POLYMERS

Polymorphism may also occur in polymeric materials. The mechanism is thermodynamic and the occurrence of a specific crystal modification in a particular polymer may be dependent on temperature, pressure, stress or concentration of the crystallisation solvent. The transition from one crystal modification to another may also be governed by these factors. The transformation proceeds by either direct conversion of one modification to another or by the melting of the first modification, directly followed by recrystallisation into the second. [55] It is therefore useful to consider the polymorphic behaviour of polyethylene (PE) as it is a widely accepted model system for homologous lower molecular mass materials such as n-alkanes and waxes. [55, 63]

Linear PE is known to occur in orthorhombic, hexagonal and monoclinic polymorphs. [55, 64-65] A transition from the orthorhombic to the hexagonal form appears at and above ca. 3 kbar at 215°C. [56, 64-66] The conventional orthorhombic to liquid transition is observed at lower temperatures and pressures. [56] PE shows orthorhombic and monoclinic crystalline forms at normal pressure. The former form is the most stable and the latter has been reported in stressed samples. [65] The orthorhombic form is therefore the most predominantly observed crystal modification for polyethylene. [63, 65]

3.4 X-RAY DIFFRACTION ANALYSIS OF WAX CRYSTAL MODIFICATION

3.4.1 X-Ray diffraction theory

X-ray diffraction is a technique that may be used to probe the crystallographic structure of the material under investigation. A crystal lattice comprises a regular three-dimensional arrangement of atoms in space. The lattice unit may be described by the dimensions of the cell axes and the angular relationships among the three axes (see Figure 3.1). The elastic scattering of X-ray photons by atoms in the periodic lattice results in diffraction from which a pattern may be obtained for the material. Constructive interference results when the scattered monochromatic X-rays are in-phase. A plot of the angular positions and intensities of the resultant diffraction peaks is characteristic for the crystal modification. Lattice spacings are derived from the Bragg relation $n\lambda = 2d \sin\theta$, where λ is the wavelength of the X-rays; d is the distance between two lattice planes; θ is the angle of the incoming rays; and n is an integer called the order of reflection. The measurement of the angles 2θ under which constructively interfering X-rays leave a crystal allow the lattice spacings to be derived from the Bragg relationship. [17]

The most predominant crystal modification in longer chain n-alkanes is orthorhombic. For example, the space group notation for the orthorhombic crystal of linear polyethylene is *Pnam-D_{2h}* and the cell dimensions are *a* = 7.4069 Å, *b* = 4.9491 Å and *c* = 2.5511 Å. [66]

3.4.2 X-Ray diffraction of Fischer-Tropsch wax samples

XRD analyses of Sasol waxes C80, H1 and C105 were performed from room temperature to above the wax melting points in order to determine if polymorphic behaviour is present. The experimental parameters are discussed in Chapter 2. The waxes were analysed at the respective temperatures given in Table 2.2 in order to determine the temperature dependence of their crystal morphologies. The scans were performed at the characteristic DSC peak maximum and minimum temperatures and also at additional temperatures of the specific samples within the broader melting peaks.

3.4.2.1 Room temperature XRD

The room temperature phase composition of all three wax samples was identified as being orthorhombic in nature. The crystallographic phase compositions of the waxes are given in Table 3.3 and the XRD patterns are shown in Figure 3.5. The peak positions, intensities and full width at half maximum (FWHM) results for the (110) and (200) reflections are given in Table 3.4. Figure 3.5 and Table 3.4 show that the crystallographic data for all three wax samples are identical at room temperature.

Table 3.3: Crystallographic data for the phase composition of Sasol waxes C80, H1 and C105

Crystal system	Orthorhombic
Space group	P*nam*
a, Å	7.455
b, Å	4.966
c, Å	2.589
Alpha, °	90
Beta, °	90
Gamma, °	90

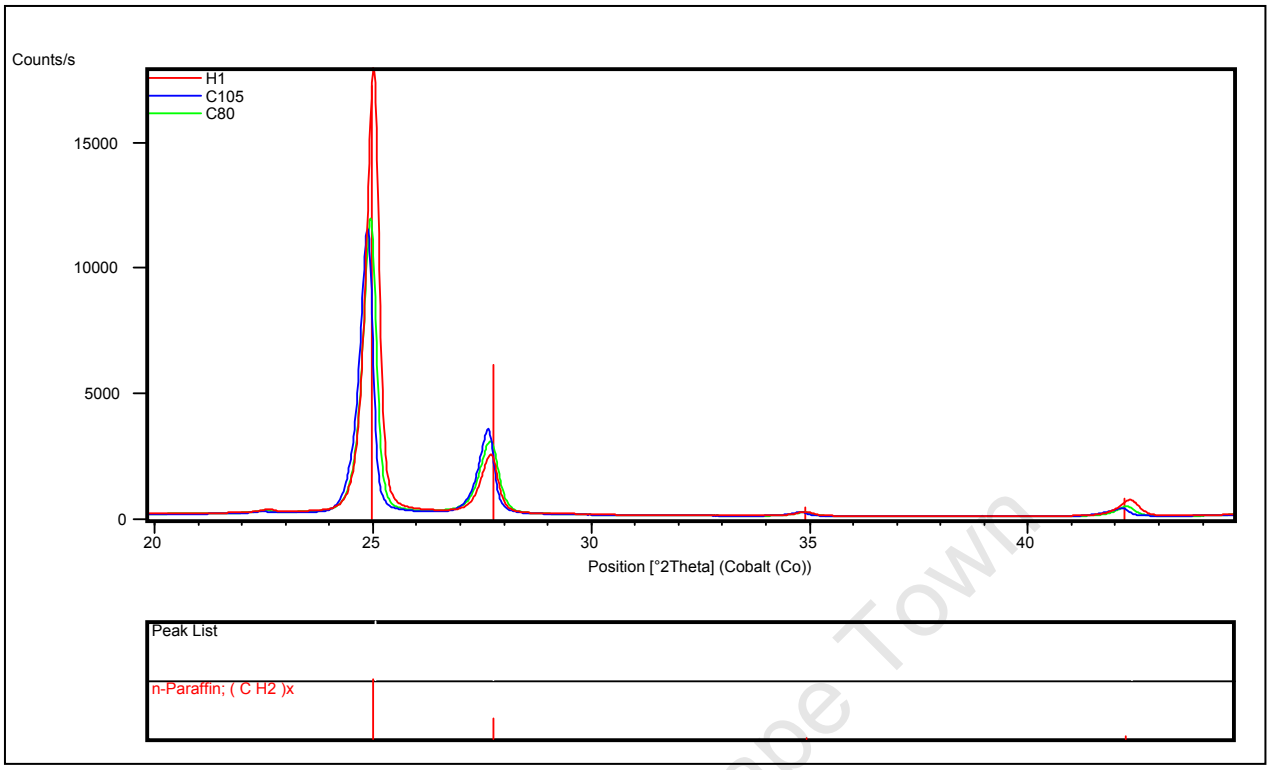

Figure 3.5: Room temperature XRD patterns for Sasol waxes C80, H1 and C105

Table 3.4: Peak positions and intensities for room temperature XRD patterns of the Sasol waxes

Wax	(110)			(200)		
	Peak position, 2θ, °	**Peak intensity, counts/s**	**Peak width (FWHM), °**	**Peak position, 2θ, °**	**Peak intensity, counts/s**	**Peak width (FWHM), °**
Sasolwax C80	24.95	1770294	0.36	27.69	430058	0.49
Sasolwax H1	25.02	2680691	0.34	27.69	346525	0.44
Sasolwax C105	24.88	1714509	0.35	27.63	504410	0.40

3.4.2.2 High temperature XRD

(i) Sasolwax C80

Figures 3.6 and 3.7 show the XRD patterns for Sasolwax C80 at temperatures up to and above the DSC melting peak at ca. 80°C, respectively. Table 3.5 shows the peak positions, intensities and FWHM results from these patterns.

Figure 3.6 shows how the peak intensities for the orthorhombic phase decrease with increasing temperature and that a peak shift occurs indicating a lowering of the sample crystalline content. This may be interpreted as a gradual change in the orthorhombic crystalline phase to an amorphous state due to gradual melting of the sample. The shifts in the reflections are not indicative of the occurrence of polymorphism or the existence of two polymorphic phases. Additional reflections would develop at the characteristic 2θ positions for the second polymorphic phase in either of these cases. The average carbon number of Sasolwax C80 is comparable to a carbon chain length of ca. n-C_{44}. The XRD pattern for n-$C_{44}H_{90}$ at 79°C is monoclinic with a space group $A2^2$. The peak positions are at ca. 21.4 deg 2θ (111); 22.3 deg 2θ (204); 22.8 deg 2θ (202); and 23.5 deg 2θ (200). [66a] This polymorphic form is, therefore, not seen on the Sasolwax C80 XRD patterns. The observed shift may be due to crystal lattice expansion as a result of heating, a change in the composition of the solid solution as melting progresses, or a lowering of the sample level as a result of melting. [19] Waxes display significant expansion on melting which lead to numerous problems in both lab and plant, and the first option may therefore be a plausible reason for the shift in the XRD reflections.

At ca. 80°C, which is the position of the Sasolwax C80 DSC melting peak, significant changes occur in the peak intensities. This is indicative of significant conversion of the amount of crystalline to amorphous material at this temperature. The splitting of the major phase reflections might again be caused by any of the reasons listed in the previous paragraph, or might be the result of surface changes that occur as a result of the partial melting of the sample. [19]

Figure 3.7 shows the XRD patterns for the sample above 80°C. The peak intensities of the orthorhombic phase continue to decrease as more of the sample melts. The appearance of the broad peak at ca. 22 deg 2θ is indicative of the appearance of an amorphous phase due to this melting. From ca. 85°C only the amorphous peak is apparent.

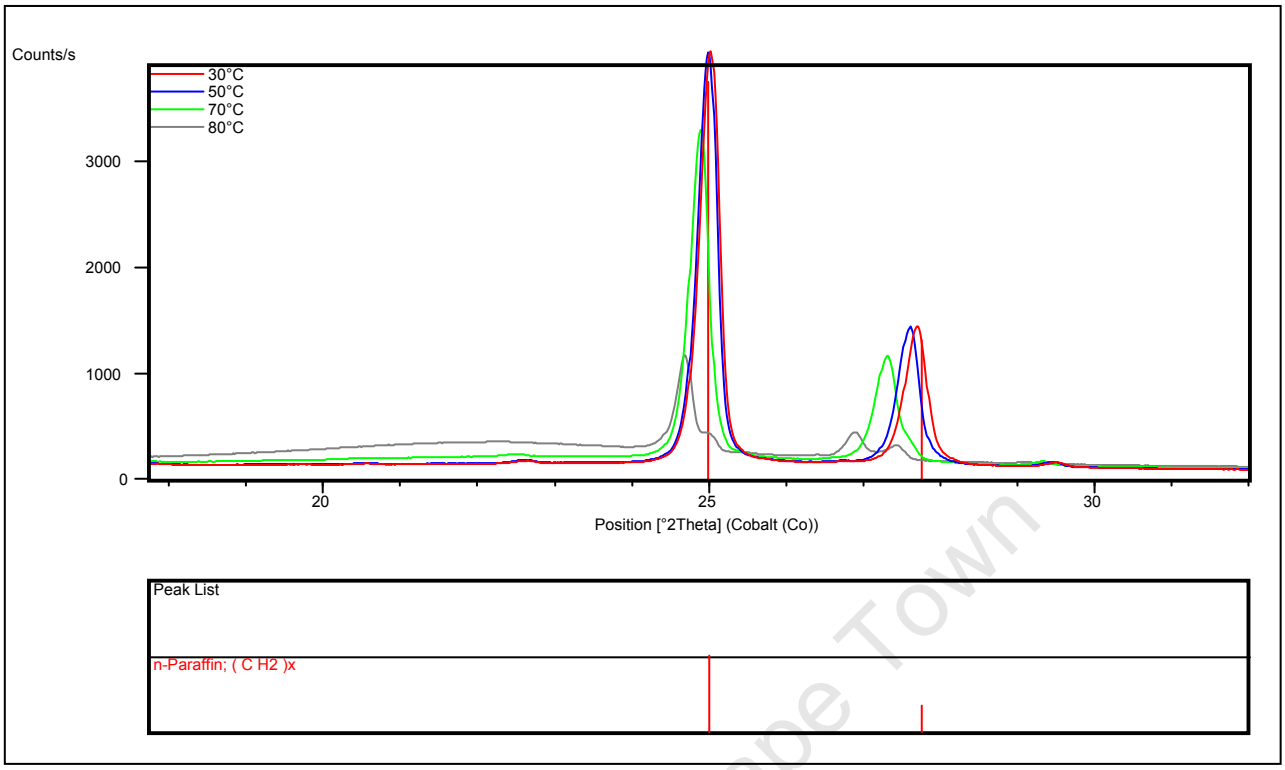

Figure 3.6: High temperature XRD patterns for Sasolwax C80 – up to 80°C

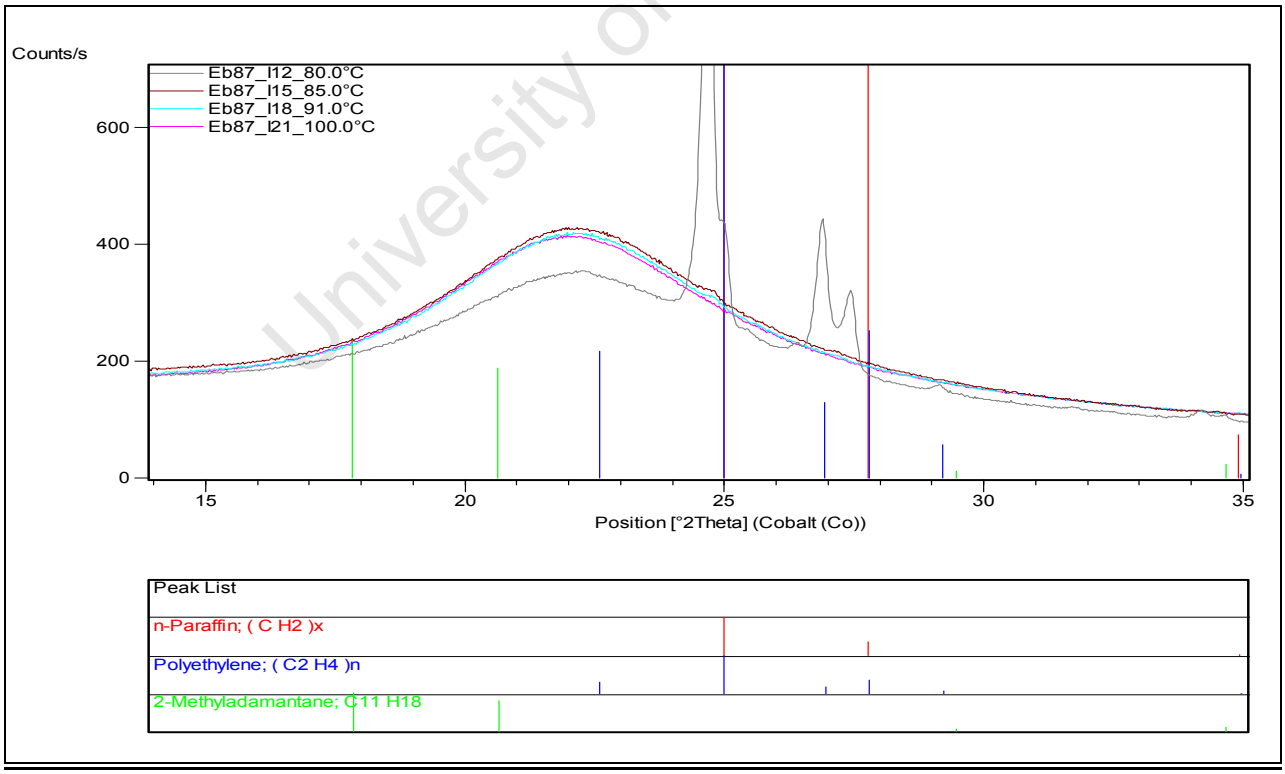

Figure 3.7: High temperature XRD patterns for Sasolwax C80 – above 80°C

Table 3.5: Peak positions and intensities for high temperature XRD patterns of Sasolwax C80

Temperature, °C	(110)			(200)		
	Peak position, 2θ, °	**Peak intensity, counts/s**	**Peak width (FWHM), °**	**Peak position, 2θ, °**	**Peak intensity, counts/s**	**Peak width (FWHM), °**
30	25.03	589504	0.29	27.70	196576	0.33
50	25.00	589070	0.29	27.61	194704	0.32
70	24.90	471741	0.28	27.31	151247	0.33
80	24.70 27.45	41076 15333	6.11 -	26.93 25.00	30119 26576	0.23 -
85	-	-	-	-	-	-
91	-	-	-	-	-	-
100	-	-	-	-	-	-

(ii) Sasolwax H1

Figures 3.8 and 3.9 show the XRD patterns for Sasolwax H1 up to and above 89°C, respectively. The peak positions, intensities and FWHM results from these patterns are given in Table 3.6. Similar behaviour to that of Sasolwax C80 was observed in that the major orthorhombic phase peak intensities decrease with an increase in temperature, indicating a gradual change of the crystalline phase to an amorphous state, due to gradual melting of the sample. The XRD pattern recorded at 77°C, which corresponds to the first DSC melting peak, shows that the peak intensities of the orthorhombic phase are relatively high. These intensities start to decrease significantly for each of the next recorded temperatures (from 89°C). No reflections are present at temperatures of 115°C and 125°C, which are above the melting point. This indicates the disappearance of the crystalline phase.

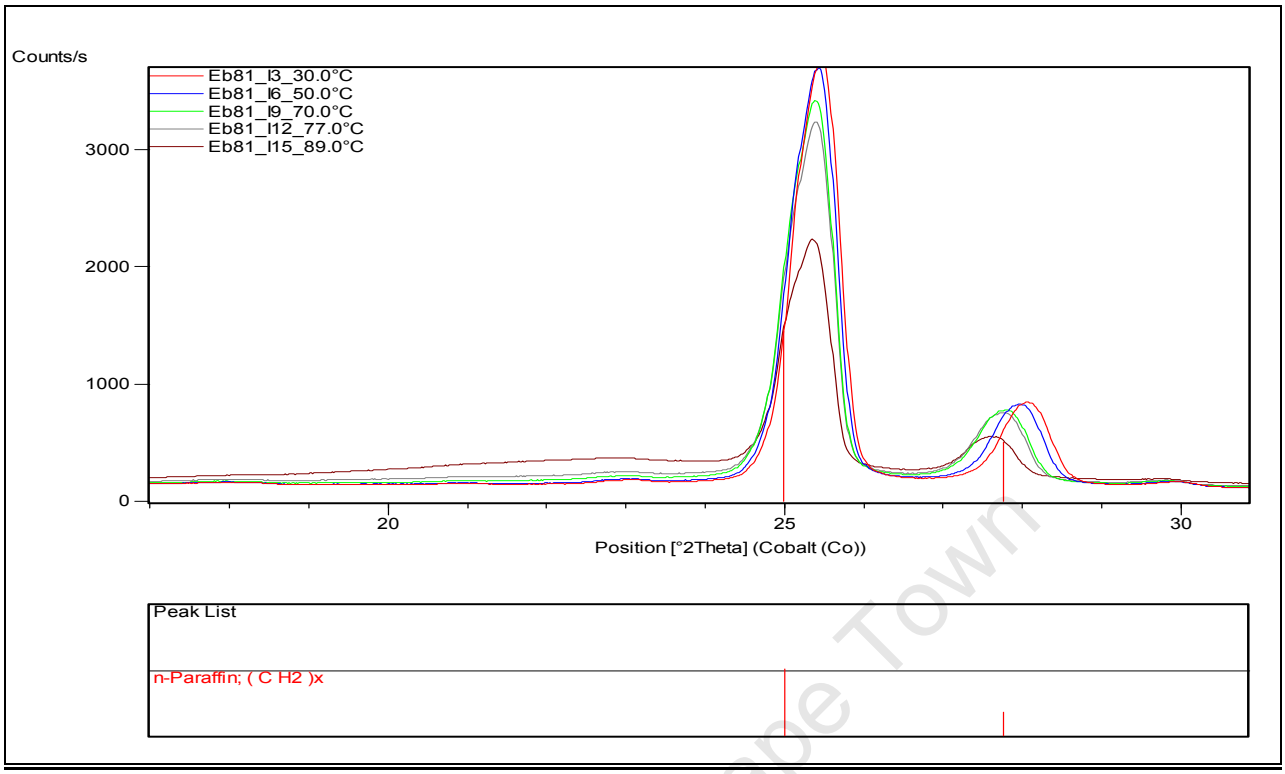

Figure 3.8: High temperature XRD patterns for Sasolwax H1 – up to 89°C

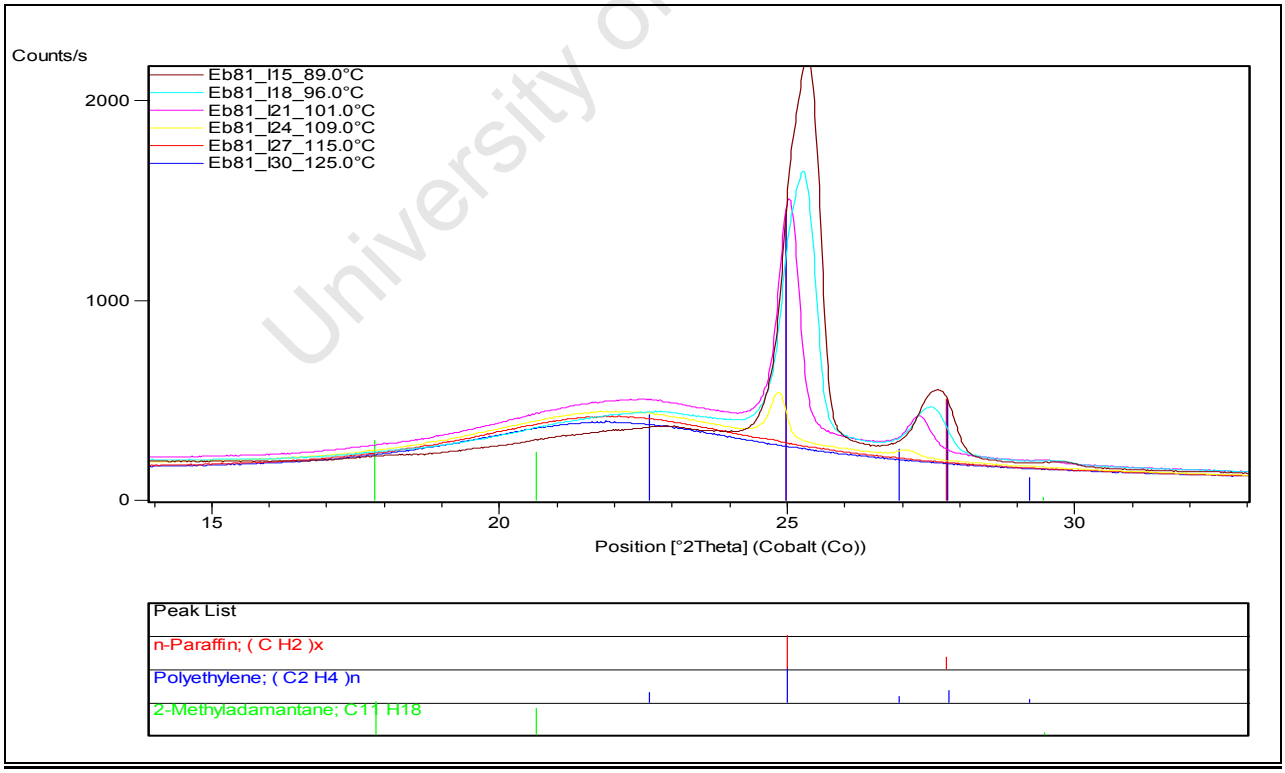

Figure 3.9: High temperature XRD patterns for Sasolwax H1 – above 89°C

Table 3.6: Peak positions and intensities for high temperature XRD patterns of Sasolwax H1

Temperature, °C	(110)			(200)		
	Peak position, 2θ, °	Peak intensity, counts/s	Peak width (FWHM), °	Peak position, 2θ, °	Peak intensity, counts/s	Peak width (FWHM), °
30	24.45	542909	0.66	28.06	102657	0.69
50	25.40	528023	0.67	27.96	99416	0.70
70	25.37	481833	0.68	27.78	88903	0.72
77	25.37	450290	0.69	27.75	83744	0.72
89	25.34	289312	0.67	27.62	47869	0.68
96	25.26	194592	0.61	27.51	32036	0.63
101	25.04	171179	0.41	27.31	23910	0.45
109	-	-	-	-	-	-
115	-	-	-	-	-	-
125	-	-	-	-	-	-

(iii) Sasolwax C105

The XRD patterns for Sasolwax C105 may be seen in Figures 3.10 and 3.11. The peak positions and intensities from the XRD patterns are given in Table 3.7. Again, similar behaviour is seen as with the other samples, indicating a gradual transition of the crystalline phase into an amorphous phase. At a temperature corresponding to the first DSC melting peak (ca. 98°C) there is a significant decrease in the peak intensities, with a complete disappearance of the crystalline phases at 120°C and 130°C, which are above the melting point.

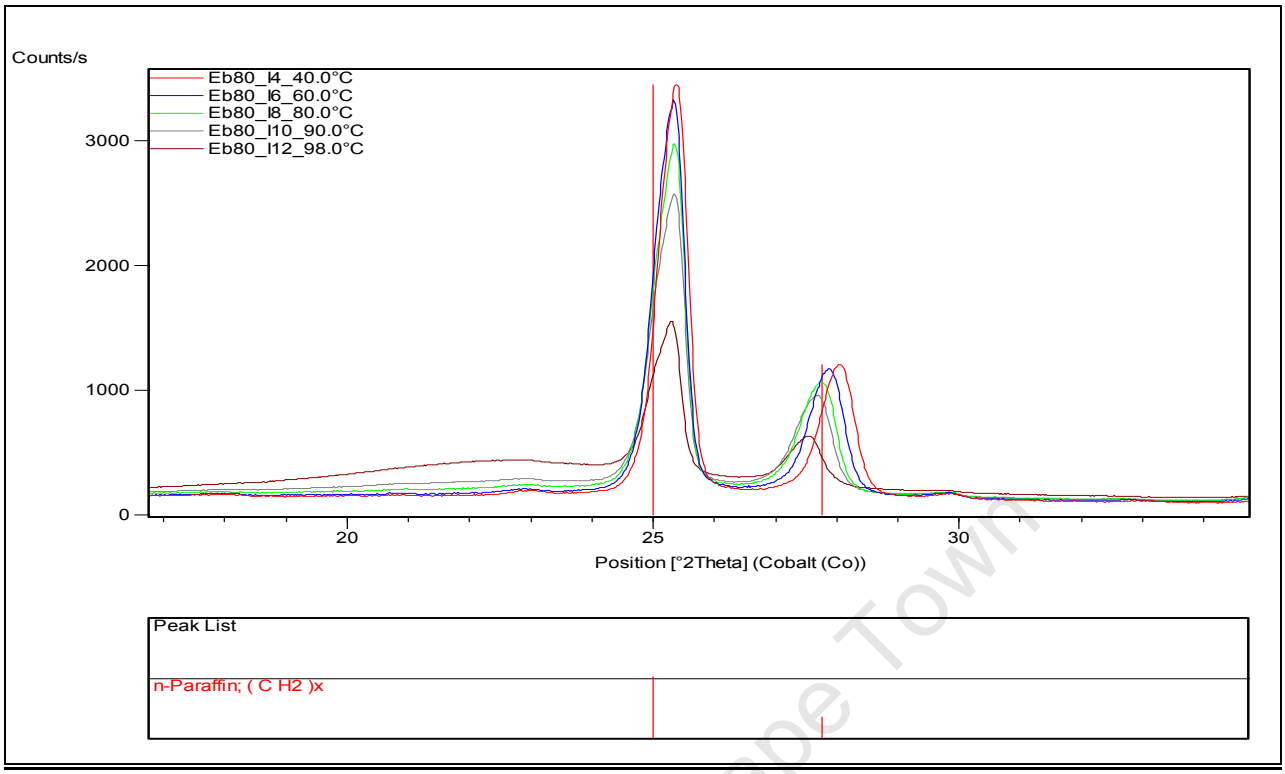

Figure 3.10: High temperature XRD patterns for Sasolwax C105 – up to 98°C

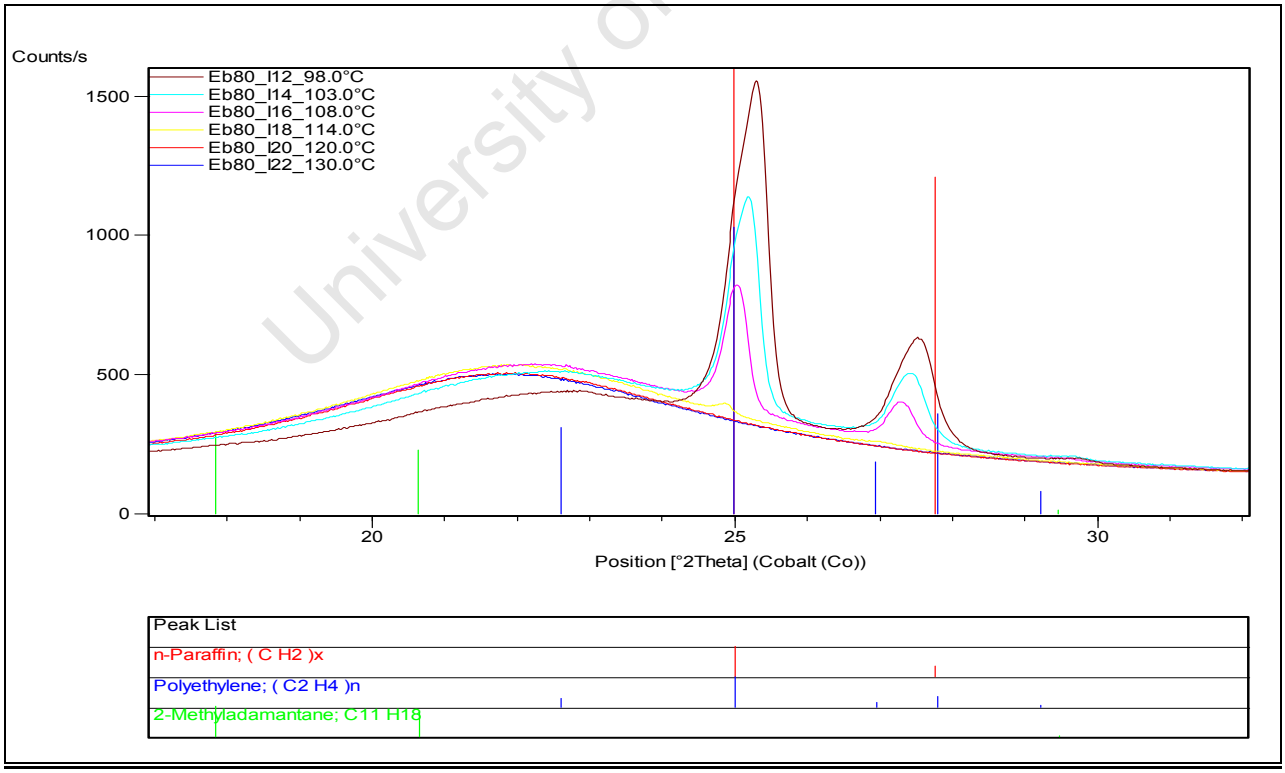

Figure 3.11: High temperature XRD patterns for Sasolwax C105 – above 98°C

Table 3.7: Peak positions and intensities for high temperature XRD patterns of Sasolwax C105

Temperature, °C	(110)			(200)		
	Peak assignment	Peak position, 2θ	Peak intensity, counts/s	Peak assignment	Peak position, 2θ	Peak intensity, counts/s
40	25.37	81709	0.55	28.04	25866	0.63
60	25.32	77495	0.57	27.87	24332	0.65
80	25.33	68060	0.59	27.74	21462	0.66
90	25.32	347191	0.61	27.67	112011	0.68
98	25.28	180835	0.56	27.53	56645	0.62
103	25.18	113591	0.47	27.43	34945	0.51
108	25.04	66337	0.38	27.31	20187	0.41
114	-	-	-	-	-	-
120	-	-	-	-	-	-
130	-	-	-	-	-	-

3.5 CONCLUSION

This XRD study shows that the crystalline phase composition is orthorhombic and is identical for all three FT wax samples. At temperatures corresponding to the first DSC melting peaks, a significant portion of the crystalline phase converts to the amorphous phase, most likely due to partial melting. Above the melting points, no crystallinity is observed.

The most significant finding is that none of the samples showed a phase transition from one crystal structure to another. This shows that the multiple melt peaks of the Fischer-Tropsch hard waxes are not due to crystal structure modification.

CHAPTER 4

MOLECULAR WEIGHT EFFECTS AND MULTIPLE MELT PEAKS IN FISCHER-TROPSCH HARD WAX

4.1 CHAIN FOLDING

4.1.1 Overview of chain folding in n-alkanes, waxes and polymers

The phenomenon of chain folding in polymers is well documented. Crystalline polymeric materials are known to crystallise in a lamellar structure with molecules generally arranged perpendicular to the crystal surface. [12, 25-26, 28, 31, 54, 59, 64-65, 67-73] The actual chain conformation may be either extended or folded (see Figure 4.1).

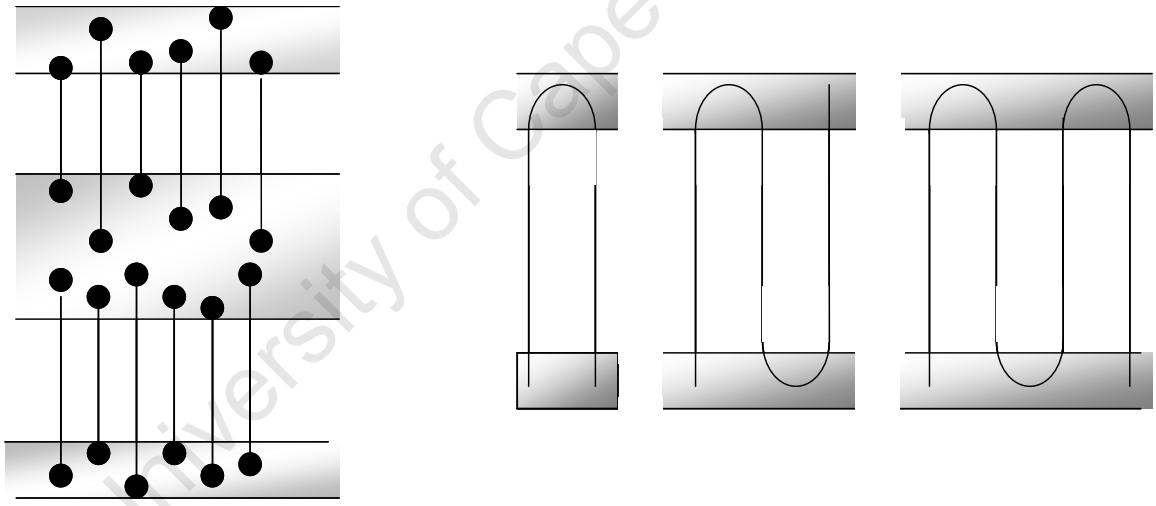

(a) **(b)**

Figure 4.1: The lamellar structure of polymeric materials. (a) Extended chain crystals. [12] (b) Folded chain crystals showing once, twice and three-times folded material. [13]

The lamellar thickness of extended chain crystals is related to the molecular weight distribution of the material. [12, 26, 45, 74] A chain-folded morphology has been inferred from the observation that the fold lengths are integral reciprocals of the total chain length of the polymer. [28, 45, 63-64, 67-70, 72, 75] The onset of chain folding in polyethylene polymer

occurs at C_{100}. [12, 45] The reason for chain folding is uncertain, but may be either thermodynamic or kinetic in origin. The thermodynamic theory relates to the stabilisation effect that folds and other defects would have on the crystal due to the influence that folding would have on molecular vibrations. The kinetic theory relates to the fact that the manifesting fold period is the most stable configuration for the prevailing crystallisation conditions. [67] The crystalline length or lamellar thickness determines the material melting point. [65, 70] The fold length in the FC conformation or the chain length in the EC conformation would therefore determine the melting point of a crystalline material. Polyethylene is often used as a structural model for paraffinic systems. [59, 65, 76] A consideration of its physical behaviour would therefore be helpful for understanding similar lower MW systems.

Extended (EC) and folded (FC) chains may co-exist in a heterogeneous structure when a polymer contains a broad molecular weight distribution of material that spans the fold onset carbon number. [12, 70] The resulting lamellae of different thicknesses pack together randomly to form clusters of finite sizes. The overall structure therefore displays eutectoid segregation of lamellar units that are incompatible due to crystal thickness differences. [12] The EC conformation is the most thermodynamically stable configuration. [40, 63-64, 70, 74]

PE with a MW of 3,000-4,000 dalton consists of both extended and once-folded material. Higher MW PE crystallises entirely in the folded conformation. [65] Chain folding has also been observed in ultra-long single n-alkanes having a carbon chain length greater than C_{150} and in PE wax. [12, 13] Other references claim that the onset of chain folding in n-alkanes is at chain lengths of C_{80}, C_{100} or C_{120}. [40, 45, 71]

The co-existence of extended and folded chain material may be identified qualitatively by DSC analysis of the material. The lower and higher temperature melt peaks have been assigned without qualification to the melting of the EC and FC material, respectively, for a high molecular weight polyethylene wax. [12] Long-chain single n-alkanes, however, display melting of the FC material before that of the EC portion. [13] The DSC melting curve shown in the literature is visually characteristic of many commercially available polyethylene waxes. [12] Figure 4.2 shows a DSC analysis for such a PE wax, viz. Polywax 2000. Polywax is a registered trademark of Baker Petrolite.

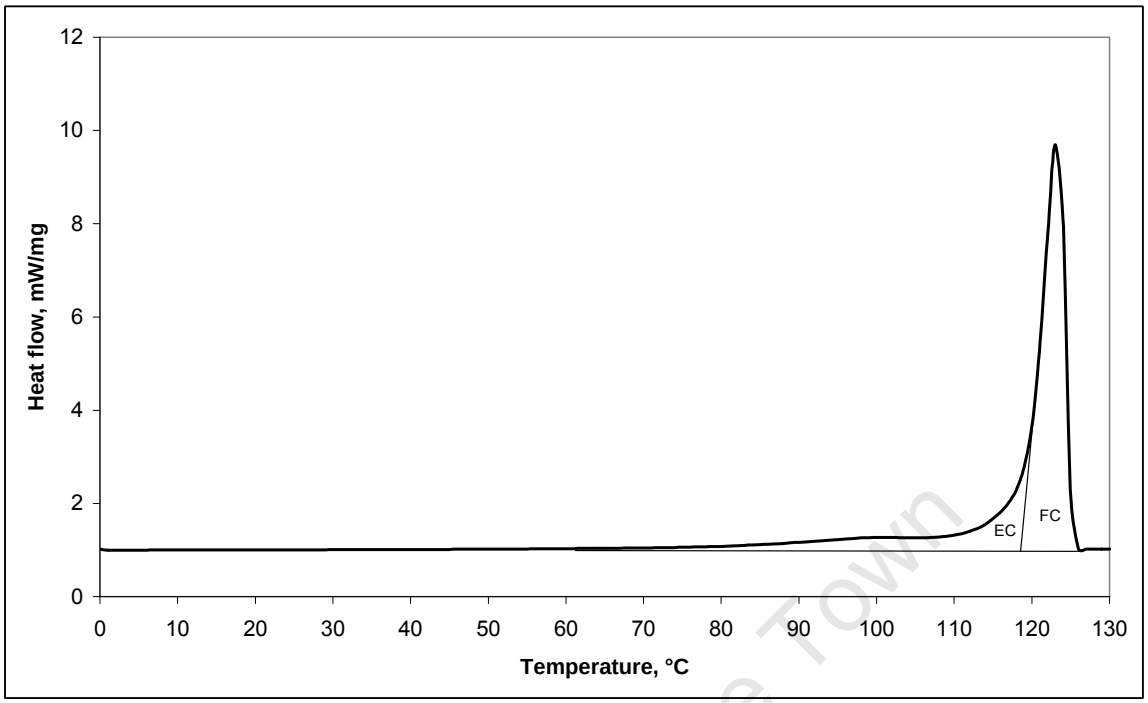

Figure 4.2: DSC analysis of Polywax 2000 showing how EC and FC material may be identified qualitatively according to the literature [12]

The area under the DSC melting peak that is assigned to the melting of FC material is said to represent the associated melting enthalpy and would correlate with the amount of this form present in the crystallised sample. [12]

4.1.2 Chain folding in polyethylene waxes

The phenomenon of chain folding and its dependence on carbon chain length may potentially be demonstrated using three commercially available high-density polyethylene (HDPE) waxes. Figure 4.3 compares their DSC analyses and Table 4.1 shows their molecular weight parameters determined by GPC analysis.

GPC, or size exclusion chromatography (SEC), is a liquid chromatographic technique which separates molecules according to their molecular volume (size). The technique is widely used to characterise high molecular weight synthetic polymers, which are usually composed of a distribution of chain lengths. This technique gives information on the molecular weight distribution of the sample. [21] The system is calibrated by relating the retention time of a series of compounds of known molecular weight and of chemical

composition similar to that of the sample to be analysed to the molecular weight. [22] Chapter 2 gives a description of how the GPC analyses were performed.

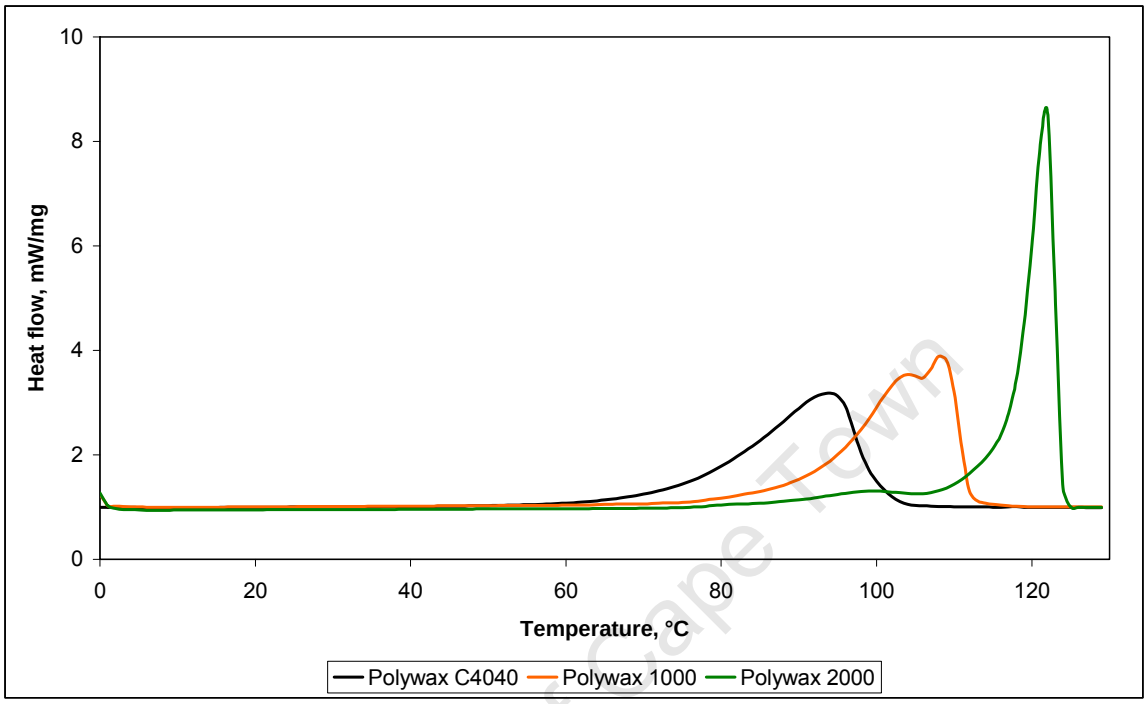

Figure 4.3: DSC analysis of three HDPE waxes

Table 4.1: MW parameters of three HDPE waxes

MW parameter	Polywax C4040	Polywax 1000	Polywax 2000
M_n, dalton	724	1033	2229
Carbon # from M_n	52	74	159
M_w, dalton	788	1184	2593
Carbon # from M_w	56	85	185
M_z, dalton	860	1371	3071
Carbon # from M_z	61	98	219

The carbon numbers were again derived from each of the MW parameters by dividing with 14 dalton, which is a molecular weight unit.

The DSC analysis of Polywax C4040 does not indicate any melting bimodality, which qualitatively indicates the absence of chain folding. The DSC analyses of Polywax 1000 and Polywax 2000 both indicate melt bimodality, which in qualitative terms could be

indicative of the presence of both EC and FC crystals. FC material appears to be predominant in the latter wax, according to the interpretation given in the literature for PE wax. [12] All three carbon number results for Polywax C4040 and Polywax 1000 are smaller than, and those for Polywax 2000 are greater than, the most cited chain length requirement for the onset of folding (C_{100}). The Polywax 1000 DSC melt bimodality therefore does not appear to be as a result of chain folding, while that of Polywax 2000 may well be. It should be noted that the positions of the higher temperature peaks of the three waxes increase with increasing MW. The existence of this trend is usually indicative of the melting of EC material, which could indicate that this particular assignment of the melting peaks for wax samples could be erroneous.

A quantitative evaluation of the material that would, according to the literature, chain fold, was performed on the basis of these two analyses. [12] This was done by comparing the area under the second DSC melt peak, said to represent the FC material, to the amount of material according to the GPC analysis greater than various carbon numbers cited as the onset of chain folding. The weight fractions were determined from the integral area percent corresponding to the molecular weight of the specific carbon number. The area percent was corrected for conversion to a linear scale by division by the local molecular weight. The result of this comparison is shown in Table 4.2.

Table 4.2: Attempt to quantify FC material in HDPE wax samples

MW parameter	Polywax C4040	Polywax 1000	Polywax 2000
% material due to 1st DSC melt peak	0*	67	11
% material due to 2nd DSC melt peak	0*	33	89
% material >C_{80} (GPC)	7	45	95
% material >C_{100} (GPC)	2	21	89
% material >C_{120} (GPC)	1	9	80
% material >C_{150} (GPC)	0	4	62

* single DSC melt peak

The GPC information – which absolutely quantifies the amount of material >C_{100}, the onset of chain folding – appears to show correlation with a quantitative analysis of the

DSC results for the sample Polywax 2000. The absence of DSC melting bimodality and a substantial amount of material $>C_{100}$ is sufficient quantitative evidence to conclude that Polywax C4040 would crystallise in an EC-only conformation. The presented data, however, provide insufficient evidence to conclusively assign the reason for the melting bimodality of Polywax 1000 to chain folding. This evidence appears to indicate that the Polywax 2000 crystallises in a predominantly chain-folded fashion. However, the DSC peak assignment for n-alkanes identifies the first and second melt peaks as representing the melting of FC and EC material respectively. [13] If the data in Table 4.2 are evaluated against this assignment, then the literature criteria for chain-folding do not apply to these samples. This will be discussed again later in this chapter.

4.1.3 Chain folding theory applied to the FT waxes

The above methodology was applied to the FT waxes in an attempt to provide some insight into whether chain folding could be the mechanism behind their melting behaviour. Figure 4.4 and Table 4.3 show the DSC analyses and GPC parameters of the Sasol waxes C80, H1 and C105.

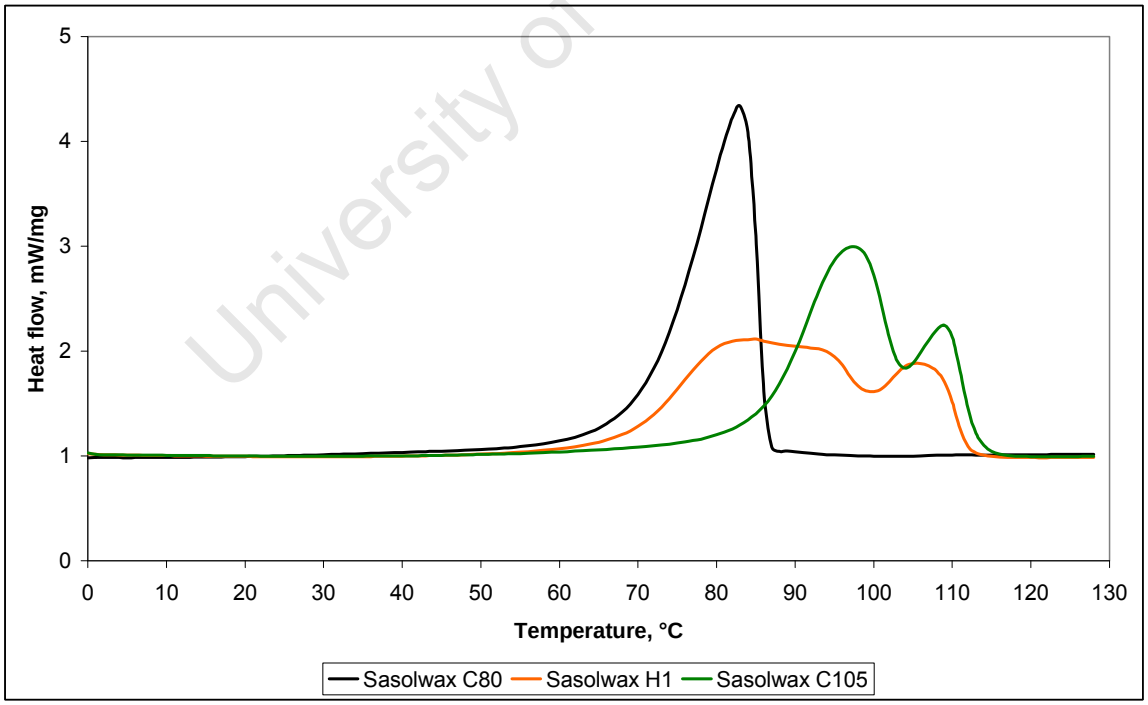

Figure 4.4: DSC analysis of FT hard waxes

Table 4.3: GPC and DSC parameters of the FT hard waxes

GPC/ DSC parameter	Sasolwax C80	Sasolwax H1	Sasolwax C105
M_n, dalton	596	746	978
Carbon # from M_n	43	53	70
M_w, dalton	614	853	1078
Carbon # from M_w	44	61	77
M_z, dalton	632	1007	1213
Carbon # from M_z	45	72	87
% material due to 1st DSC melt peak	0*	77	71
% material due to 2nd DSC melt peak	0*	23	29
% material >C_{80} (GPC)	0	17	36
% material >C_{100} (GPC)	0	8	19
% material >C_{120} (GPC)	0	4	9
% material >C_{150} (GPC)	0	1	4

* single DSC melt peak

The GPC-derived carbon number parameters of all three waxes are <C_{100}. Sasol waxes H1 and C105 do, however, contain a small percentage of material with chain length >C_{100}. The correlation between the DSC and GPC derived parameters for these two waxes is of the order of the Polywax 1000 results. The conclusion is, therefore, that there is also insufficient evidence to conclusively assign the cause of the melting bimodality phenomenon in these waxes to chain folding. It should also be noted that the DSC melting curves of the FT hard waxes do not appear to be visually similar to those of the PE waxes shown here and in the literature. [12]

A direct measurement of the lamellar thickness of these wax samples could help to establish whether chain-folded lamellae form during crystallisation.

4.1.4 Measurement of crystal lamellar thickness

Crystal lamellar thickness may be measured by a number of analytical techniques which include small-angle X-ray scattering (SAXS), low-frequency Raman spectroscopy to examine the longitudinal acoustic mode (LAM) and electron diffraction (ED) or electron

microscopy. [13, 25, 27 31, 65, 77] These techniques examine different properties of the material. [28]

SAXS measures the average repeat distance of stacks of uniformly sized lamellae. It may be used to determine the bulk assembly of crystalline materials in terms of the lamellar stacking. The measurement is made possible by the density difference between the crystalline lamellae and the disordered interlamellar region. The position of the small-angle peak indicates the average repeat distance of the stacks. SAXS cannot measure more than one lamellar periodicity if different lamellar sizes are mixed. The usefulness of SAXS is that it may determine the mode of lamellar stacking. [25-27, 65] SAXS is able to measure the long period of the material; this is the average size of the crystalline and amorphous regions. [65]

The frequency of the Raman-active first-order longitudinal acoustic mode (LAM) depends on the average chain length of the all-*trans* extended chains within lamellae. This is also referred to as the crystalline core thickness. [25-27, 31-33, 35, 37-39, 65, 73, 78-81] The LAMs are measured as peaks by low-frequency Raman analysis of the sample. The lamellar sizes are calculated from the first order LAM modes of the sample using the equation

$$\nu_m = (m/2L_{LAM})(E/\rho)^{1/2}$$

where ν_m is the vibrational frequency of the LAM mode; m is the order of the vibration; L_{LAM} is the length of the vibrating chain; E is the Young's modulus; and ρ is the density of the material. [25, 27-40, 72, 80-82] L_{LAM} would correlate with the fold length in chain-folded lamellae. [25, 27-40, 72, 80-82] The LAM mode is independent of the arrangement of lamellae in the stacks. It is possible to determine multiple lamellar spacings with low-frequency Raman analysis. [25-27] The technique has been applied to the measurement of multiple lamellar thicknesses in PE samples and in ultra-long single n-alkanes. [13, 25, 27-28, 31, 38] The presence of more than one lamellar thickness may be due to the co-existence of EC and FC material in samples with MWDs that are sufficiently broad to span the onset carbon number for chain folding, or where molecular segregation during crystallisation occurs. [12-13, 27] The measurement of multiple lamellar thicknesses is not possible with techniques such as SAXS or electron diffraction. Raman analysis has proven to be

superior to other techniques in terms of measuring lamellae and identifying their true origin. [25, 27]

Electron crystallography is an optical technique that allows the direct visual characterisation of atomic or molecular packing in crystalline materials. It makes the quantitative determination of crystal structure from electron scattering data possible and includes electron microscopy and electron diffraction. [44] Electron diffraction (ED) allows the useful combination of image and diffraction data to elucidate crystalline structure. Electrons are the radiation source and are scattered by matter more efficiently than X-rays or neutrons. Single crystals are preferred for electron diffraction experiments. Incorrect sample preparation may hinder the optimal extraction of data from this technique and data interpretation may be complex. [85] The technique may be used to determine the crystalline lamellar thickness in carbon number terms of a sample. [26, 42-43] The error on the determination of lamellar thickness with ED is greater than for low-angle X-ray diffraction. [42] ED is claimed not to be the preferred method for determining material crystal structures due to the limited data that may be obtained from the technique. [26] ED measures an *average* lamellar thickness in a localised region, which implies that it cannot measure multiple crystalline core thicknesses. [42] The multiple DSC peaks observed for a mineral wax could be explained by ED studies. [42]

Electron microscopy measures permeability variations induced in the sample by staining of the sample. Density differences in the various regions of the crystalline material cause the regions to stain differently. Etching may be also used to enhance the density difference. [65] Low permeability is associated with crystalline order and high original density. Regular lamellar stacking is again, as with Raman measurements, not a prerequisite for the observation of lamellar thickness, as this is done directly by visual inspection. Electron microscopy gives direct visual information about the stacking and arrangement of lamellae. The accuracy of the electron microscopy determination of the lamellar thickness may not be high due to distortion of the sample during preparation, difficulty in calibrating the microscope and a small sample size. Chain tilting may also be observed in the lamellar arrangement due to the influence that this would have on the density of the crystalline regions. [65] The crystalline segment length of material that crystallises with chain tilt may be calculated from the lamellar thickness and the chain tilt

angle. [39, 81, 85] Electron microscopy is primarily a qualitative tool that should be used in support of other analysis. [25, 27, 65]

Low-frequency Raman analysis therefore appears to be the most useful technique to qualify the manifestation of chain folding in the lattice structure of wax samples due to its ability to measure multiple crystalline core thicknesses of different sizes in the sample. [25, 27, 29] The LAM data for ultra-long n-alkanes has been correlated to their DSC data, showing that multiple LAM modes may be linked to corresponding DSC melting endotherms. [13] It should be noted that for these n-alkane samples, the first DSC melt peak was assigned to the FC and the second to the EC material. [13] In mono-modal materials this is due to the fact that the effective melting point is determined by the fold length, which would be smaller than the length of the EC material. [25] This is supported by the fact that the thermodynamic stability of FC material is also known to be less than that of EC material, which would imply that the FC portion would melt first, or would recrystallise into an EC conformation prior to melting. [40, 63-64, 70, 74]

As mentioned earlier, the lamellar crystalline core thicknesses may be calculated from the LAM modes of the sample using the equation $\nu_m = (m/2L_{LAM})(E/\rho)^{1/2}$. If the carbon number chain length equivalent of the crystalline core thickness, n_{LAM}, is calculated using the first-order LAM (L_{LAM}), then the equation may be rewritten as $n_{LAM} = 2489.4/\nu_1$ by substituting the parameters obtained from the literature. [13, 31] This technique was therefore chosen to further investigate the chain folding behaviour of the wax samples mentioned earlier in this chapter (Figures 4.3 and 4.4).

4.1.5 Low-frequency Raman analysis for measuring crystalline lamellar thickness and considerations for interpretation of the results

Raman spectroscopy measures inelastic light scattering of very weak intensity. It is able to measure three general types of molecular vibrations, viz., the internal modes, which are vibrations of atoms within molecules; the lattice modes, which are the vibrations of one polymer segment within its lattice environment; and acoustic modes, which are longitudinal vibrations within the molecules. The former two types of vibrations are known to occur above 80 cm^{-1} for PE. [73]

(i) Origin of LAM vibrations

Four specific kinds of vibrations are observed at low frequencies (< 600 cm^{-1}) in the polymethylene chain. These are the accordion-like vibrations (LAMs); in-plane bending vibrations; twisting vibrations; and out-of-plane bending vibrations. [35] The LAM movement involves an accordion-like extension of the chain by way of the in-phase expansion or contraction of the CCC bonds in materials such as n-alkanes and polyethylene. [86-87] The four types of low-frequency vibrations are illustrated schematically in Figure 4.5. [35]

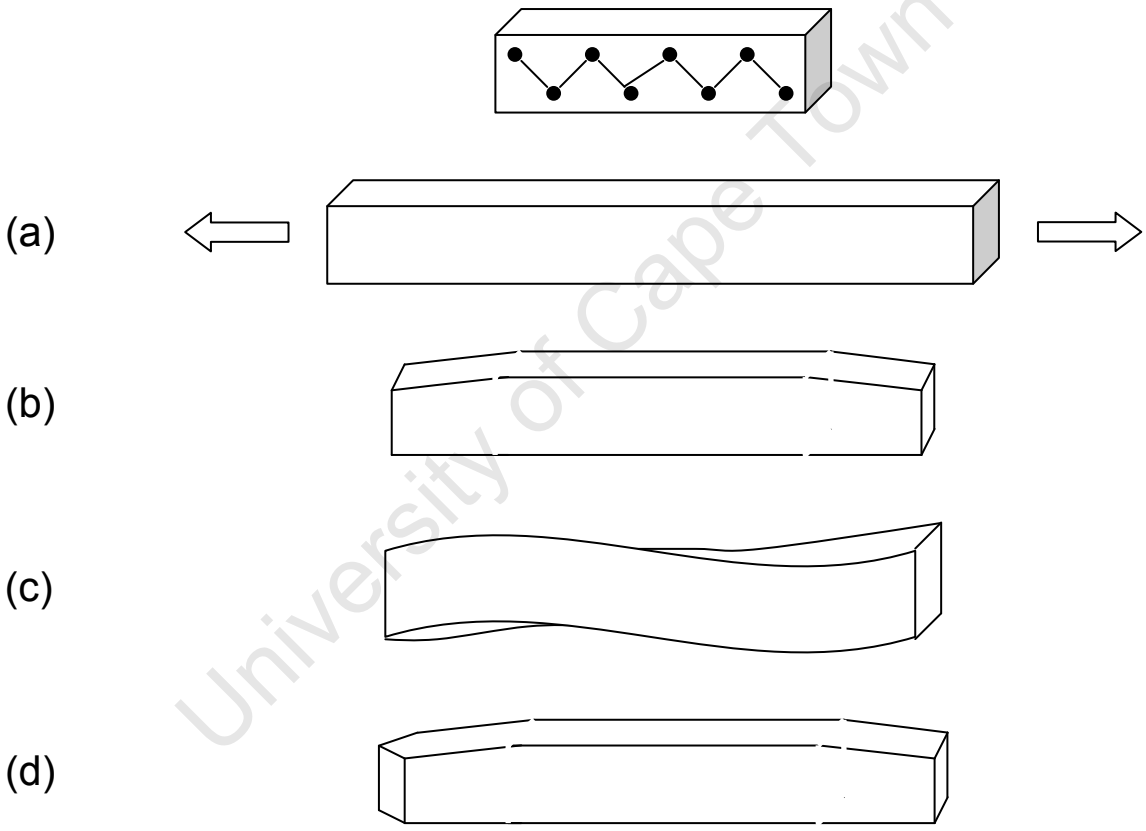

Figure 4.5: Low-frequency vibrations in the polymethylene chain. (a) accordion-like vibration; (b) in-plane bending vibration; (c) twisting vibration; (d) out-of-plane bending vibration. [35]

The positions, intensities and shapes of low-frequency Raman-active LAM bands of a crystalline material are determined by its morphology. [31, 34, 37-39, 56, 73, 79-81, 84, 88-91] For a

certain chain length, the frequency of the LAM vibration is higher than those of the other three types. [35] The lowest frequency molecular vibrations are therefore the LAMs. [86-87] Low-frequency Raman bands have been observed for short-chain n-alkanes, polyethylene and other polymers below 600 cm^{-1}. This is considered the low-frequency region in Raman measurements. [37, 86]

The accordion-like vibration in a chain displays maximum displacement of atoms at the surface of the crystal (chain ends) and a node of zero displacement in the center of the crystal. This motion will change the electronic polarisability of the crystal and will be Raman-active if the length of the crystal is less than or equal to the wavelength of the incident light. [30] LAM-1 is a symmetrical vibration around the center of the molecule. The skeletal backbone acts as a spring that vibrates longitudinally. [92]

Multiple orders of reflection arise from a single lamellar thickness. [73] LAM progressions are apparent in the low-frequency Raman vibrational spectra of all-*trans* n-alkanes. [34] Additional LAM bands occur at frequencies due to higher order modes of a single LAM vibration. [35] The frequencies of this progression of bands are chain length dependent according to the relationship $\nu_m = (m/2L_{LAM})(E/\rho)^{1/2}$ described before. Not all modes in this progression are Raman active. The even-numbered mode-values (m) give no change in polarisability and are therefore not Raman active. [37, 40, 84, 92] For this reason, only the odd numbered LAMs are Raman active. [36-37, 40, 73, 84, 87, 92] The higher-order LAM frequencies are therefore odd-number multiples of the LAM-1 frequency.

Figure 4.6 shows a schematic of the way in which the different orders of LAM vibrations arise. [37]

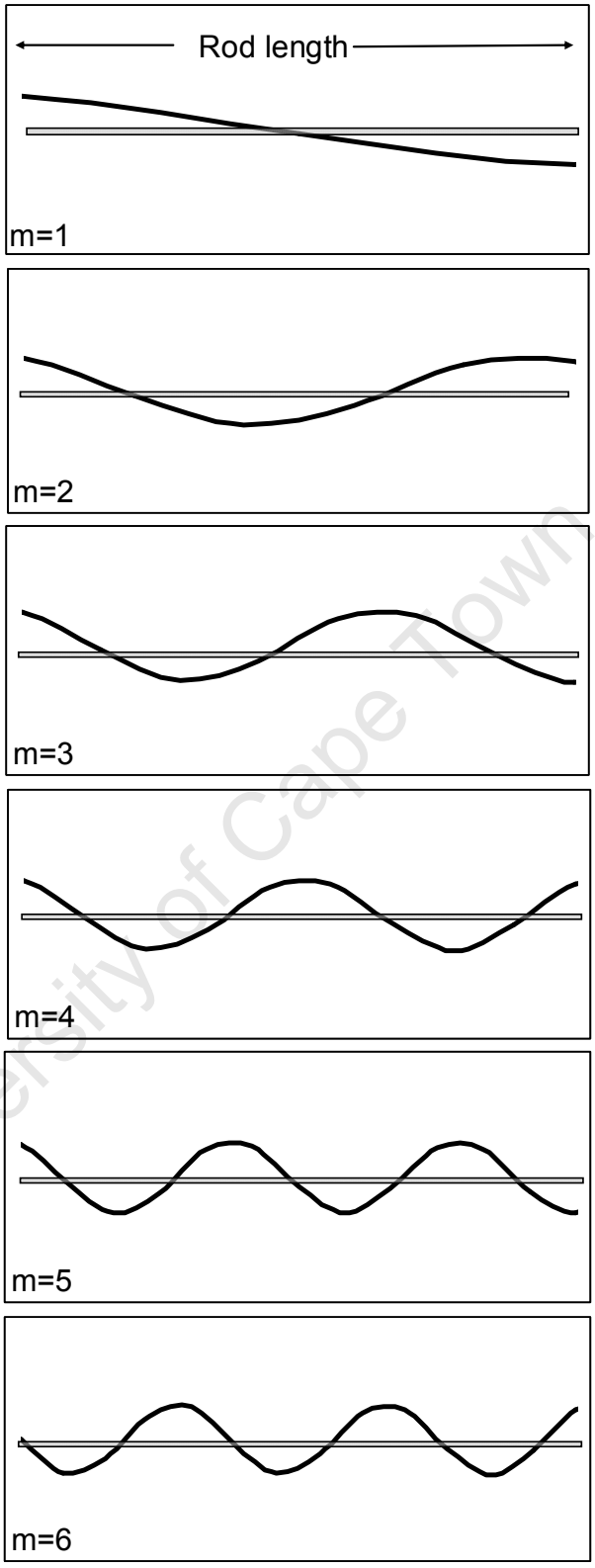

Figure 4.6: Vibrations arising for an elastic rod due to different orders of a single LAM [(37)]

The intensities of the LAM bands decrease with increasing order, which could result in their weakening to such an extent that the higher-order vibrations cannot be seen on the spectrum. [92] LAM-1 gives the strongest line of all bands in the progression. [36] The high intensity of the LAM-1 is due to the large change in polarisability of this mode. [37] LAM-3 could not be found in the spectra of a series of linear low MW PEs and in HDPE. [38] Weak LAM-3 vibrations could be detected for PE polymer and short-chain n-alkanes (up to C_{25}). [82, 86] The ability to observe several members of a LAM progression is considered remarkable for n-alkanes. [90]

The correlation between experimental and theoretical determinations of LAM frequencies is considered sufficient evidence to confirm their existence in the low-frequency Raman spectra of short chain n-alkanes. [37, 78, 90, 92] Agreement in the order of 0.5-2% between observed and calculated values of LAM-1 frequencies for n-alkanes has been obtained. [92]

(ii) The intensity of LAM vibrations

In general, LAM modes have low intensities. The intensities of the Raman-active bands decreases with increasing mode order. [72, 86] Not all LAM bands are Raman-active and not all active bands are observed due to their low intensities. [33, 82, 92] Despite the odd-numbered LAM modes being Raman-active, the intensities of the higher-order LAM peaks are so small that usually only the first few LAM modes may be observed. [73-74] The LAM-1 intensity is high due to the large bond polarisability potential. [38] The intensity of the LAM-1 band is also related to the number and length of the straight-chain segments in the lamellar layer. [32] Observed intensities are significantly affected by both the temperature and frequency of the experiment. [73] The bandwidth of LAM-3 is always broader than that of LAM-1, accounting for the lower intensity as peak broadening requires a reduction in peak height in order to conserve integrated intensity. [73]

The band intensity also has a relational dependence on the LAM Raman shift wavenumber. Therefore the intensity of the 3rd-order LAM is much lower than that of the LAM-1. Samples with MWs that are greater than those of short-chain n-alkanes have LAMs at much lower wavenumbers, which has a further effect of reducing the band intensity. [82]

(iii) The bandwidth of LAM vibrations

The width of the LAM band is rarely narrow for polymers. The width is usually a simple indication of a distribution of lamellar thicknesses due to the polymer MWD. [38, 73] The LAM bands of polymers consist of overlapping bands of a distribution of chain lengths. [73] When peak shapes are asymmetric, there is a strong probability of overlapping peaks. [38] The LAM bands of materials such as polymers, which consist of a range of homologous components, may result in overlapping LAM bands. The LAM bands of such systems will therefore be much broader than those of single-component straight-chain molecules due to the broad distribution of chain lengths that arise from the MWD. [88] The LAM is also characterised by the relative amount of each sequence length. [37] A chain-length difference of at least 4 is required for LAM bands to resolve. [88]

It was determined by studying n-alkanes that the LAM band for a single length distribution will have a finite width of 2.95 cm^{-1}. [38] Theoretically, a minimum bandwidth of 4 cm^{-1} is possible with consideration of peak broadening effects due to instrumental limitations. Band broadening of greater than 4 cm^{-1} is therefore considered significant. [73]

Tailing on a LAM-1 band may be due to conformational disorder in a sample. An intense broad band appears between 200 and 250 cm^{-1} when there is conformational disorder in a sample. If the spectrum does not display this band, then it may be assumed that the LAM-1 broadening is not due to disorder. [39]

(iv) Correction for Raman bandwidth, temperature and vibrational frequency

The frequency of the LAM-1 peak requires a Boltzmann correction unless the bandwidth is very narrow, which is usually the case. [34, 38-39, 73, 82, 90, 93] This Boltzmann correction is required in order to ensure that the correct frequencies and intensities for the higher order LAMs are considered. [38-39, 73] The Boltzmann correction is substantial when peaks are very broad, implying that the calculation of the all-*trans* lamellar length from the uncorrected data will therefore be too high. [38] These corrections may lead to significant changes in the LAM band frequency, and subsequently to the derived L_{LAM} or n_{LAM} values. [73]

The true peak position is perturbed by temperature and frequency factors. The frequency displacement is largest for the broad LAM-1 bands at the lowest frequencies. As the

breadth of the LAM-1 band increases, so does the magnitude of the frequency correction. It is therefore expected that large deviations of the corrected frequency from the measured frequency will be necessary when the band is asymmetric. [73]

The corrected frequency distribution is related to the measured Raman intensity by the relationship

$$f(L) \alpha [1- \exp(- \frac{hc\Delta\nu}{kT})] (\Delta\nu)^2 I_\nu^{obs}$$

where I_ν^{obs} is the Raman intensity at frequency ν. [40, 93] The value of kT/ hc is 207.233 cm^{-1}. [18] The Boltzmann correction factor is the term [1-exp(-hc$\Delta\nu$/kT)]. [34, 38-39, 73, 82, 90, 93]

(v) The effect of interference of the Rayleigh line

The scattered radiation due to very long crystalline chain segments may lie very close to the laser source wavenumber or Rayleigh line. [74] These peaks appear as bands on the wing of the Rayleigh line. [31-32, 38-39, 73, 81] They may also manifest as discontinuities on the edge of the Rayleigh line and have been interpreted as LAM bands for PE samples. [73, 93] Band profiles at low frequencies may be distorted by their proximity to the wing of the Rayleigh line. [81] If the LAM-1 is superimposed on the wing of the Rayleigh line, its frequency, shape and intensity will be perturbed. [31-32, 38-39, 74, 81]

(vi) Decoupling of vibrations

Trans-segments of a FC material will decouple at folds, resulting in LAM vibrations at frequencies that may be related to the fold-length segment. The stems on either side of the fold therefore vibrate independently. [37-38, 79, 81, 84] This is the reason why this measurement may be used to determine chain-folding in samples.

Decoupling may also occur at a conformational disorder site, such as a *gauche*- or kink-defect. Disordered chains have an effectively shorter length than ordered chains as the LAM measures the length of the all-*trans* portion of the chain. [88-89] This type of disorder effectively results in two shorter chain segments which are able to vibrate independently of each other. [38-39, 84] All-*trans* chains having an end-defect will not influence the LAM frequency. [89] The number of complicated defects that could result in a large disruption

in the LAM is small. [89] The frequency, rather than the intensity, of these bands is influenced by conformational disorder in the chains. [34]

The LAM vibrations of tie molecules which bridge the interlamellar gap in polymers are decoupled at the interlamellar gap. [94] Where appreciable bonding of end groups occurs across the interlamellar gap, chain-coupling will induce a LAM band at a lower frequency. [36]

(vii) The effect of branching on LAM frequency

Branching in the crystalline core does not affect the LAM frequency. Branching at the chain end will effectively decrease the length of the all-*trans* segment, therefore reducing the measured straight-chain length of the material. Randomly distributed branching will broaden the LAM peak. [38]

(viii) Multiple LAM-1 bands

Multiple bands have been observed for single long-chain n-alkanes. The n_{LAM} data derived from these bands showed a correlation with the occurrence of both EC and FC material in the crystalline morphology of the samples. It was possible to determine the fold periodicity of the samples from the Raman data. [13]

Two LAMs for PE crystals have been determined due to chains in different crystallographic sectors (200 and 110) being inclined at 34° and 29°, respectively. The frequency separation of the two components is not expected to be large and the LAMs may therefore be superimposed. The same is observed in $C_{94}H_{190}$, which may crystallise into either orthorhombic or monoclinic forms depending on the crystallisation conditions. The LAM frequencies would differ due to differences in the end-group packing of the two crystalline polymorphs. Due to the proximity of the two LAM bands, an asymmetrical broadening of the orthorhombic peak is seen. The bandwidth is taken as evidence of overlapping peaks. A Gaussian peak shape would be taken as evidence of a single-origin LAM. [81] An asymmetric distribution of crystal stem lengths could also account for an asymmetric LAM peak shape. [73]

(ix) Fluorescence

A main limitation of Raman spectroscopy is the occurrence of laser-induced fluorescence in the scattered light beam. This may be so intense that it obscures the Raman signal. The origin of this fluorescence in not always obvious. It may be due to the nature of the material being studied or due to the presence of sample impurities, such as additives. [38]

(x) Plasma lines

Sharp spectral bands may be observed in the low-frequency region of Raman spectra. These are plasma lines which scatter from the sample and appear as peaks on the spectrum. They may be removed by filtering with a small prism monochromator or plasma line dielectric filter. This becomes more difficult to do when the lines are close to the lasing line. Sample voids may also account for these intense lines and have been shown to reduce in intensity when a PE sample was annealed. [39]

(xi) Raman scattering

Excessive baseline sloping may sometimes be observed on a low-frequency Raman spectrum and is due to Raman scattering from the sample. If the scattered light is parallel to the sample's *c*-axis, then the spectrum displays the LAM modes superimposed on a broad Raman scattering background. This is not the case when the light is scattered perpendicularly to the *c*-axis. [39, 99] The correction for this Raman scattering is performed by subtracting the latter spectrum from the former and may only be done if both spectra are recorded. [39]

(xii) The origin of other vibrations in low-frequency Raman spectra

The bands observed in the low-frequency region of the Raman spectrum are not all due to LAM vibrations. [86] The intensity of bands in the 100-600 cm^{-1} region of the Raman spectrum originates from CC-stretching and CCC-bending vibrations. In the 600-1400 cm^{-1} region, the origin is almost entirely as a result of CC-stretching. [34] The number of bands that may potentially be observed in the low-frequency Raman region increases with increasing n-alkane chain-length. [86] The Raman spectra of the short-chain ($<C_{25}$) n-alkanes also display transverse acoustic modes (TAMs) which originate from out-of-plane molecular vibrations and methyl torsion vibrations. [86] TAMs occur at low-frequency and may overlap the LAM modes. [88] The TAM vibrations for short chain

n-alkanes occur in the frequency range 0-200 cm^{-1}. [34, 56, 86] The TAM vibrational frequency of certain bands is independent of molecular chain length, while those of other bands approach the Rayleigh line as the chain length of the n-alkane increases up to C_{36}. [56]

The methyl torsion vibrations are observed at ca. 250 cm^{-1}. They are not dependent on the molecular chain length. As the chains lengthen, the intensity of this torsion vibration decreases. They are therefore not detectable in low MW PE spectra. This type of vibration is a class of TAM. [86, 95] TAMs provide an explanation for the large number of bands observed in the region below 200 cm^{-1} for short-chain n-alkanes. [95]

A broad vibration at 100 cm^{-1} is due to a crystal lattice vibration characteristic of the orthorhombic crystal lattice. [29, 40, 82, 90] Due to its frequency, it is known to mask the LAM-3 vibration in some PE samples. [82]

A deviation from the all-*trans* conformation due to the presence of defects in the chain may lead to lower-intensity vibrations which do not originate from a LAM, but which may be difficult to distinguish from the LAMs in terms of the frequency at which it appears. The intensity and position of these vibrations may be predicted, but in a complex manner. They do not follow a pattern of decreasing intensity with increasing frequency. They would, however, be representative of a large degree of disorder which would be unlikely in a material capable of packing in the orthorhombic form. [89]

(xiii) Implication of structural defects for Raman spectra

The all-*trans* conformation is the most stable molecular arrangement for the n-alkanes. [33] The orthorhombic structure is comprised of chains in an all-*trans* conformation. [96-97] The conformation (*trans*- or *gauche*-) may be determined by Raman spectroscopy. [33] This measurement is sensitive to both conformational disorder and crystal structure. [88] The additional vibrations that manifest with the occurrence of the *gauche* conformation may be used to determine the level of conformational disorder. [33] The 1000-1200 cm^{-1} region in the Raman spectrum is sensitive to conformational changes.

A higher predominance of the *gauche* conformation is found in the interlamellar region, as this is the arrangement assumed by chain ends. [72, 88] There is no spectroscopic evidence (IR or Raman) that conformational defects are accommodated within the crystalline region (center of lamella) in pure short-chain n-alkanes. [90] The stem segment that protrudes past the lamellar boundary in binary n-alkane systems is by necessity three or four carbon numbers long. These stems will not keep the *trans*-structure, but will twist in the interlamellar region into *trans-gauche* (*tg-)* or *gauche-trans* (*gt-)* structures in order to accommodate the chain ends in the interlamellar zone. The protruding chain ends may fold over in the interlamellar region. This requires that a minimum of four carbon number units should extend past the crystalline thickness boundary. The penultimate CC bond will assume a *gauche* conformation. For chain folding to occur, the chain length difference in a solid solution should be greater than six carbon number units. [88] The interlamellar region grows in size as chains melt, indicating the onset of a higher degree of *gauche* conformational disorder. [72] Therefore, disordering on melting is confined to chain ends. [98]

The longer chains in binary mixtures are generally more disordered than the shorter chains. As the average chain length increases, so the concentration of disorder for the long and short components equalise. [88, 98] The overall crystallinity of a polymer with a high level of chain defects is lower than one without such defects. Chain defects contribute to the amorphous content of a polymer. [65]

A number of regions in the Raman spectrum may be used to study conformational disorder. The Raman spectrum of an extended chain with all-*trans* structures will show bands at ca. 1064 cm^{-1}, ca. 1130 cm^{-1} and 1075-1100 cm^{-1}. The collapse of the first two bands during melting into a central maximum at ca. 1090 cm^{-1} indicates the onset of a kinked conformation as a result of the appearance of *gauche* conformers. [90, 96] Accoustical vibrations associated with the occurrence of random *gauche* isomers give rise to a broad band at ca. 230 cm^{-1}. Another way to estimate disorder is to compare the intensities of the bands at ca. 2850 cm^{-1} and ca. 2880 cm^{-1}. The latter is usually more intense than the former in an ordered system, but their relative intensities equalize or even reverse as system disorder increases. [96] Furthermore, *gauche* rotations which develop as a result of melting will give rise to new bands at ca. 108 cm^{-1} and ca. 235 cm^{-1}. [96] A Raman band at ca. 844 cm^{-1} is characteristic of a *gauche* structure at

chain end positions three or four which is called a *gt*-isomer. A Raman band at ca. 866 cm^{-1} is indicative of a *tg*-isomer in positions two or three. [90]

The total conformational disorder may also be estimated from the tailing of the low-frequency side of the ca. 890 cm^{-1} Raman peak. The intense 890 cm^{-1} band is a measure of chain ends that terminate in a sequence of six or more *trans*-bonds, i.e. highly ordered ends. [88, 90] The tailing of this band on the low-frequency side at ca. 800 cm^{-1} originates from chains with conformationally disordered ends. The ratio of the intensity of the band shoulder to that of the sum of the intensities of these two bands may therefore be used as a measure of the degree of disorder. Solid solutions will show greater disorder than eutectics due to the minimization of chain-end mismatch in a completely demixed system. [88]

Table 4.4 summarises the assignment of bands in Raman spectra that may be used to assess chain conformation.

Table 4.4: Raman bands that may be used to assess chain conformation [90, 96]

Raman feature, cm^{-1}	**Assignment**
1064, 1075-1100, 1130	All-*trans* structure
1090 at expense of 1064 and 1130	Appearance of *gauche* structure on melting
230 (broad band)	Random *gauche* isomers
I_{2880}/ I_{2850}	>1 indicates high system order (*trans* structure)
108, 235	*Gauche* conformers
844	*Gauche* at chain-end positions 3-4
866	*Gauche* at chain-end positions 2-3
891	*Trans* structure
890 band tailing	Total conformational disorder

Figures 4.7 and 4.8 show the Raman spectra of the Sasol waxes C80, H1 and C105 in the 700-1800 cm^{-1} and 1800-3000 cm^{-1} regions respectively.

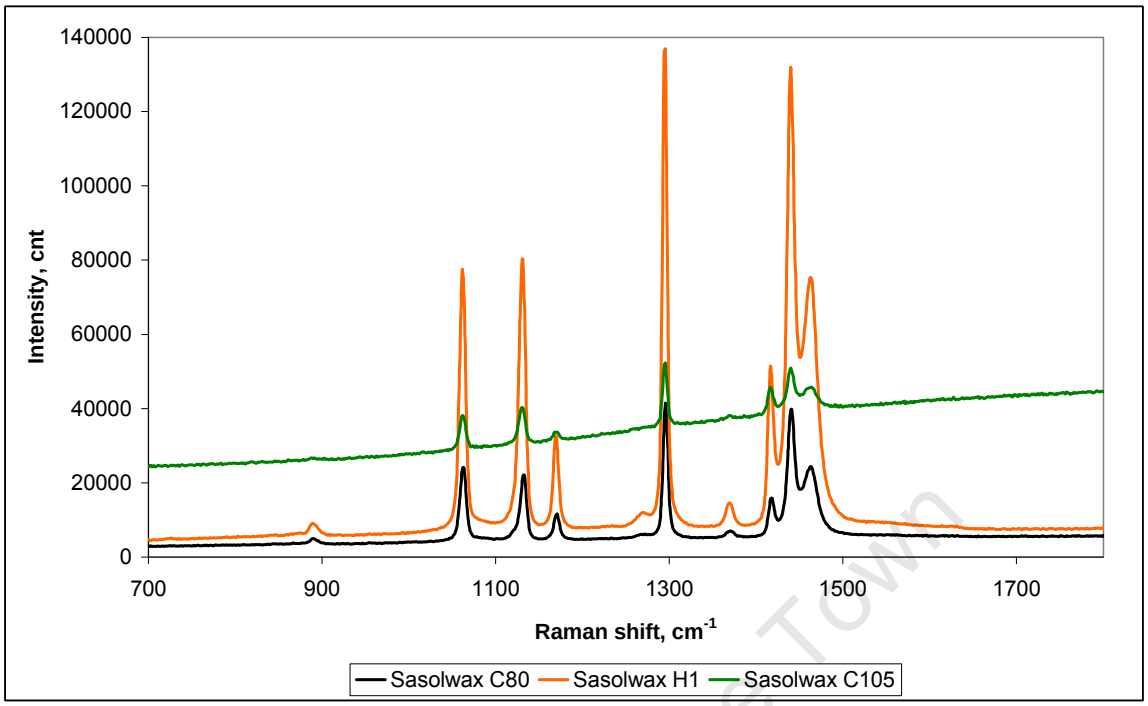

Figure 4.7: Raman spectra of Sasol waxes C80, H1 and C105 (700-1800 cm^{-1})

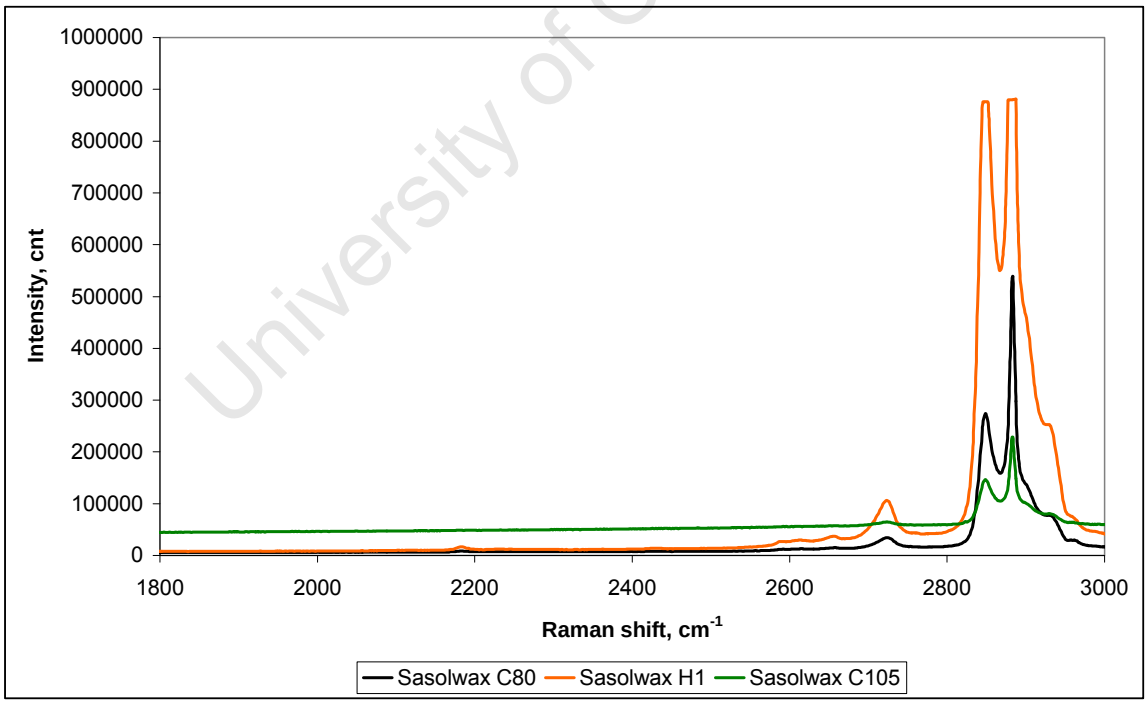

Figure 4.8: Raman spectra of Sasol waxes C80, H1 and C105 (1800-3000 cm^{-1})

Figure 4.7 shows strong bands at ca. 1063 cm^{-1} and ca. 1130 cm^{-1} that are indicative of a *trans* conformation, with a very weak band at ca. 1090 cm^{-1}, indicating that the *gauche* conformation is indeed present. The ratio of the intensities of the bands at ca. 2880 cm^{-1} and ca. 2850 cm^{-1} is >1, indicating a high degree of conformational order in these waxes. The low-frequency Raman spectra which will b shown later in this Chapter indicate that the conformational disorder band at ca. 230 cm^{-1} is absent. It therefore appears that only low levels of conformational disorder are incorporated into the crystalline morphology of the FT waxes.

4.1.6 Low-frequency Raman measurements of wax samples to investigate chain folding effects

The low-frequency Raman spectra were obtained as described in Chapter 2. The instrument was tested by analysing a sample of dotriacontane ($C_{32}H_{48}$) to ensure that the expected LAM modes were detected. This spectrum is shown in Figure 4.9.

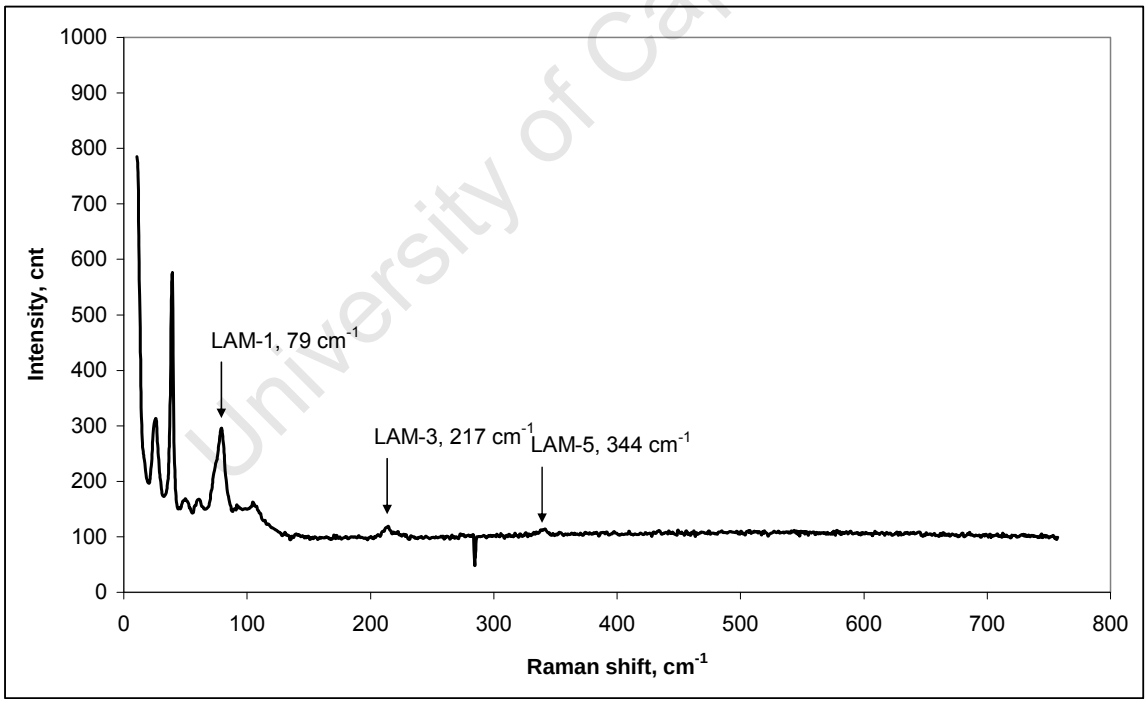

Figure 4.9: Low-frequency Raman spectrum for C_{32} n-alkane

This spectrum shows a first-order LAM at ca. 79 cm^{-1}. The equivalent chain length of the crystalline core thickness represented by this LAM is calculated by substituting ν_1 = 79 cm^{-1} into the equation $n_{LAM} = 2489.4/\nu_1$. The extended chain length within the sample's

lamellar core thickness may therefore be calculated as equivalent to carbon number 31.5 and correlates well with the n-C_{32} equivalent chain length (n_{LAM}). The spectrum also shows a progression of LAMs with a numerical relationship (factors 3 and 5 respectively) with that of the LAM-1 frequency (ca. 217 cm^{-1} and 344 cm^{-1}). This indicates that their origin is similar. The intensities of the third-order LAM-3 and fifth-order LAM-5 bands are lower than that of the associated LAM-1 band, as expected. [27, 32, 73, 82, 86, 92, 99] The additional low-frequency peak at ca. 26 cm^{-1} is possibly due to a TAM vibration. The peak at ca. 39 cm^{-1} is a silicon plasma line. The LAMs observed for C_{32} are in excellent agreement with those that are recorded in the literature. [37]

Figures 4.10 and 4.13 show the low-frequency Raman spectra of Polywax 1000 and Polywax 2000. The two curves displayed in Figure 4.13 are repeat analyses showing the analytical reproducibility. Figures 4.11 and 4.14 show the Boltzmann-corrected data. The spectra show an appreciable amount of noise, which is also apparent in those shown in the literature. [13, 29, 32, 37-38, 65, 79, 84, 95-96] They were therefore smoothed using a moving-average technique with a period of 10 in order to introduce a level of confidence into the assignment of the LAM vibrations. [38] These data are shown for the two waxes in Figures 4.11 and 4.14 respectively. The smoothing may be done in Excel using the "Data Analysis" function. Figures 4.12 and 4.15 show the smoothed data on expanded scales in order to demonstrate the assignment of peaks. All obvious bands are indicated, but the main interest here is the identification of LAM-1 peaks. The existence of LAM-3 peaks is used where possible to confirm the LAM-1 identification, but assignments are not extended to higher order modes. Note that the Boltzmann-corrected data are plotted on a secondary x-axis when compared with the raw data, but that the numerical units are not shown. Baseline correction has also not been performed due to its exact nature being unknown.

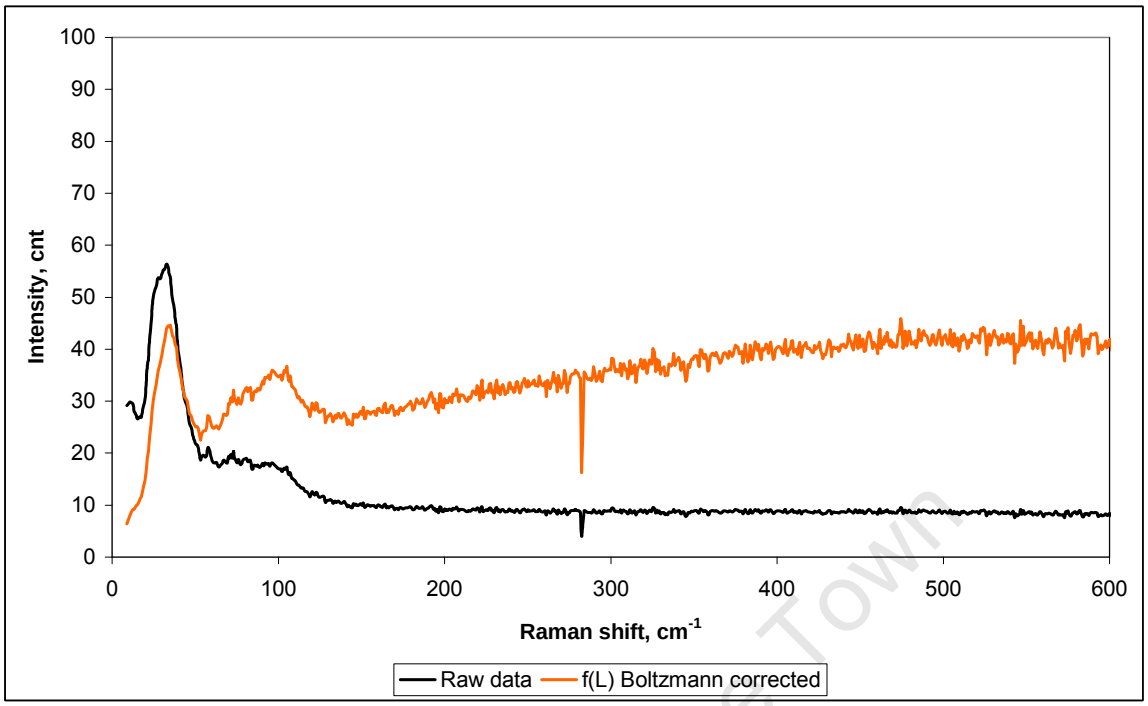

Figure 4.10: Low-frequency Raman spectrum for Polywax 1000 showing Boltzmann correction

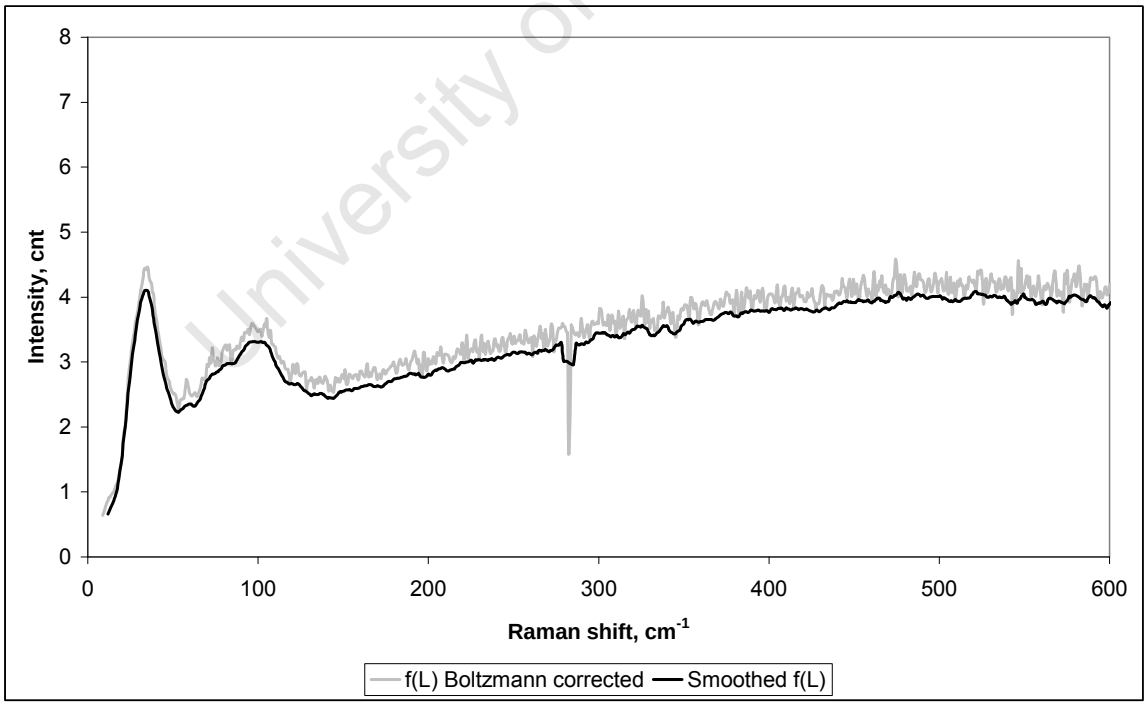

Figure 4.11: Smoothed Polywax 1000 Boltzmann-corrected Raman spectrum

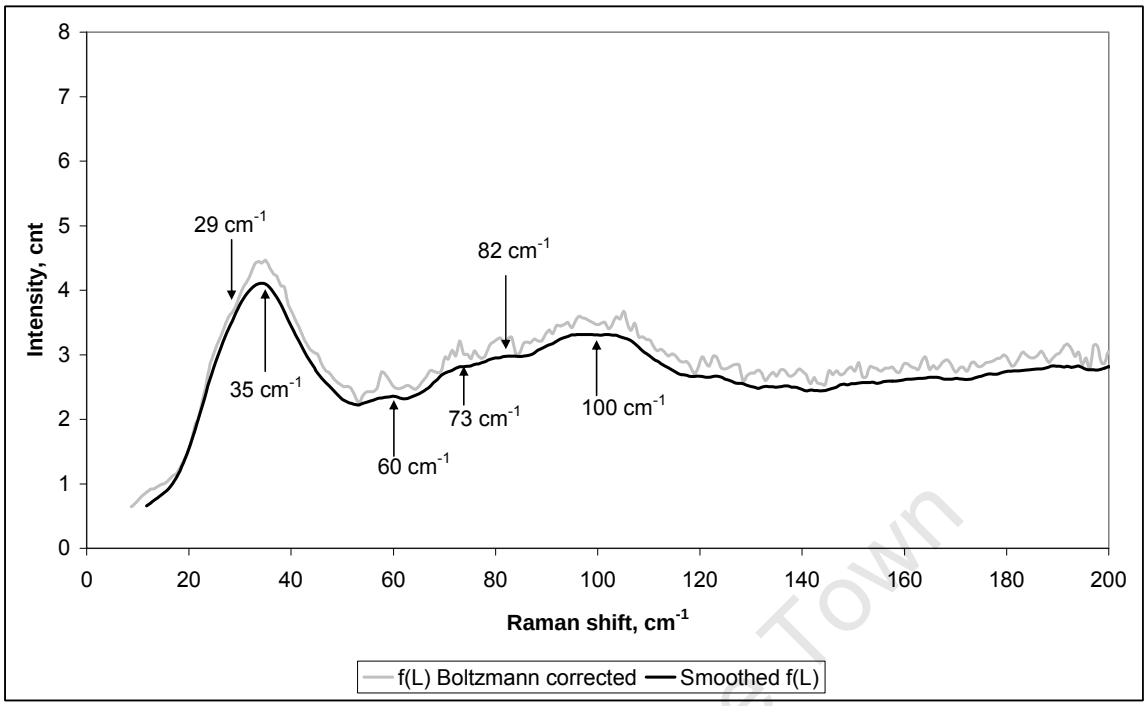

Figure 4.12: Smoothed Polywax 1000 Boltzmann-corrected Raman spectrum – expanded scale

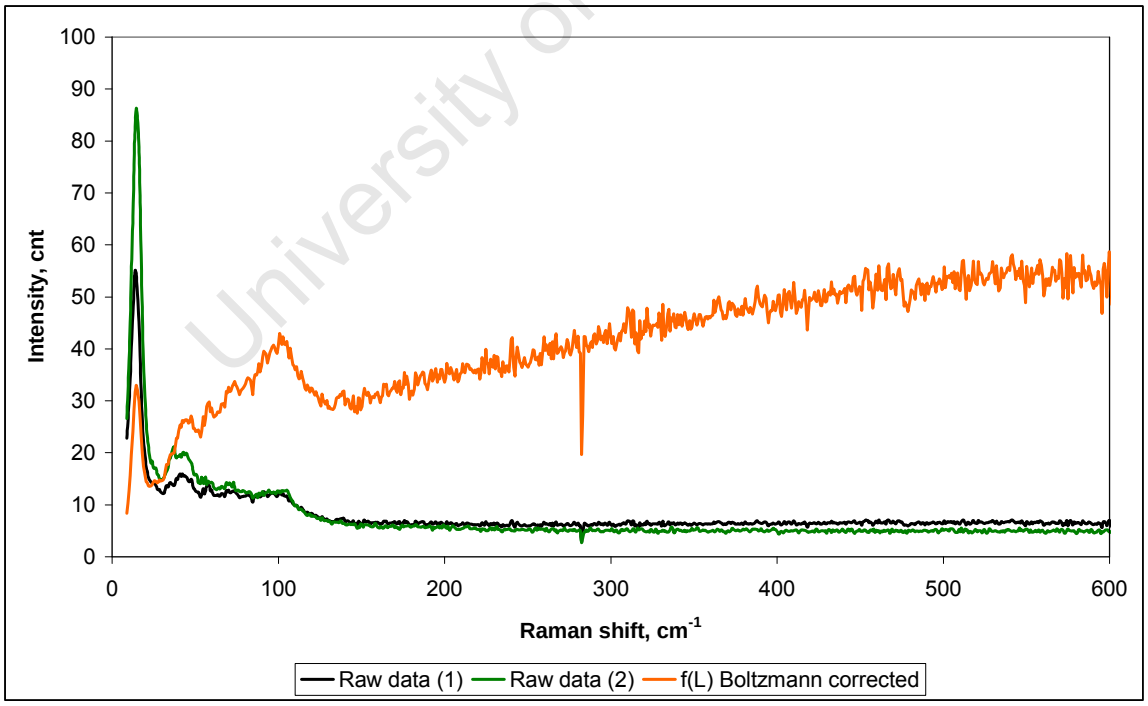

Figure 4.13: Low-frequency Raman spectra for Polywax 2000 showing Boltzmann correction

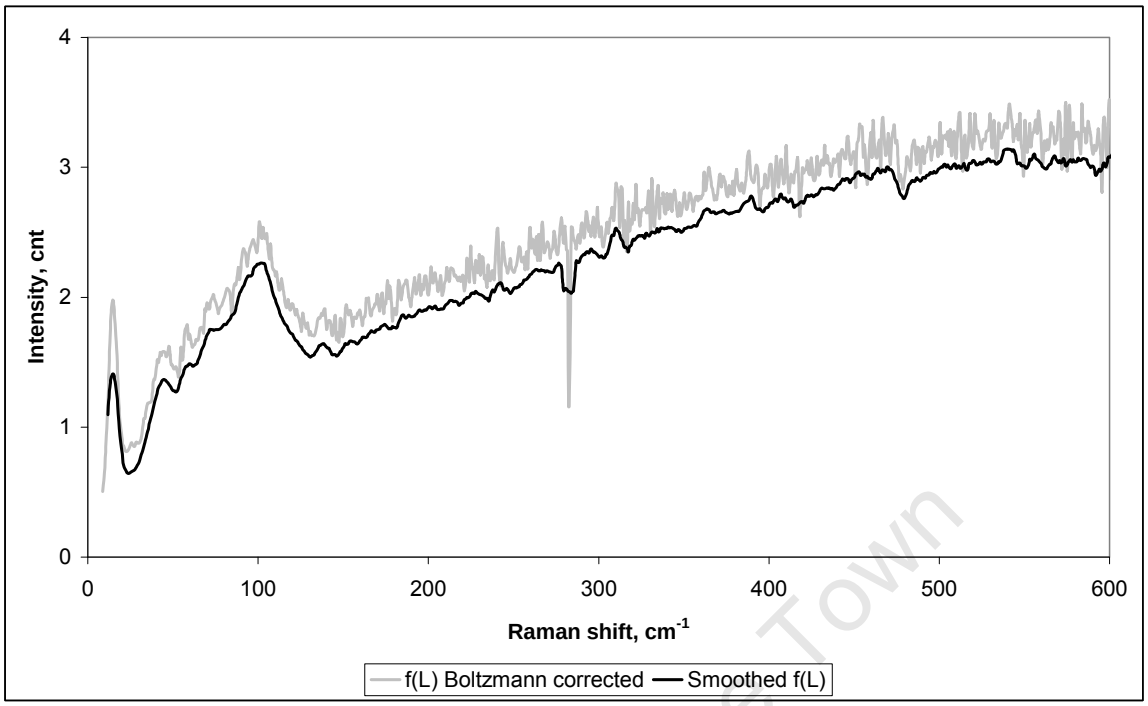

Figure 4.14: Smoothed Polywax 2000 Boltzmann-corrected Raman spectrum

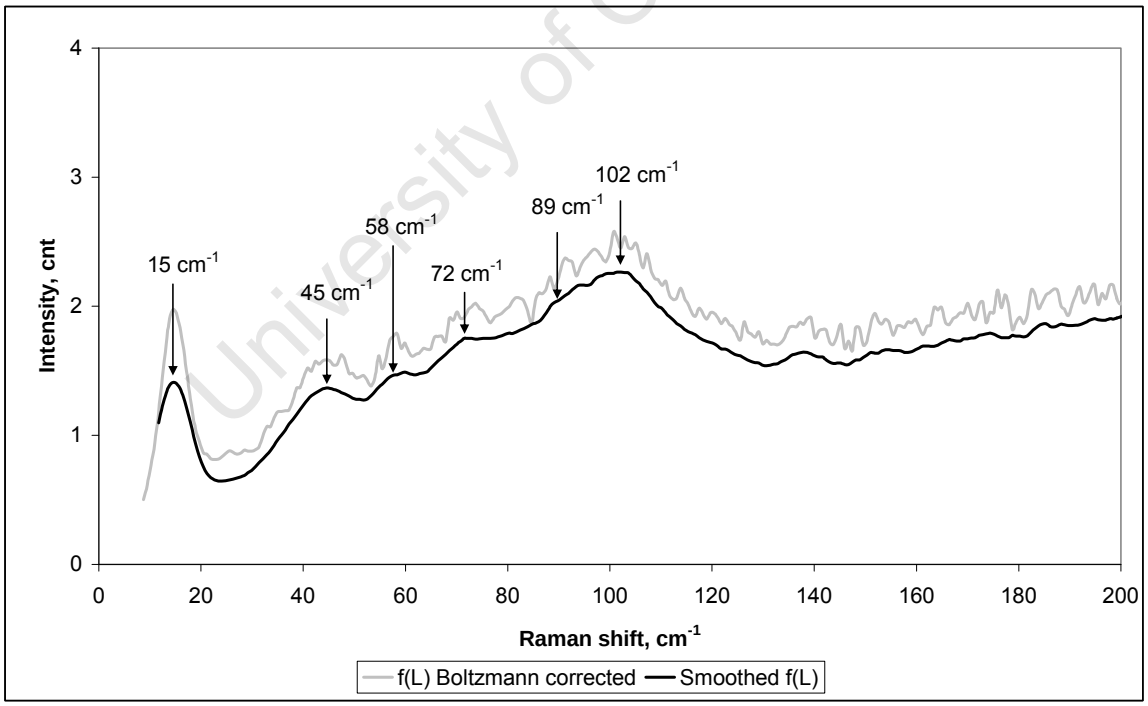

Figure 4.15: Smoothed Polywax 2000 Boltzmann-corrected Raman spectrum – expanded scale

The wax spectra are congested, indicating that the samples are complex. In general, there appear to be dominant peaks on a broad background, which would be indicative of an inhomogeneous sample.

The Boltzmann-corrected spectrum of Polywax 1000 shows an intense asymmetric peak at ca. 35 cm^{-1} and additional low-intensity peaks at ca. 60 cm^{-1} and 73 cm^{-1}. The occurrence of the ca. 35 cm^{-1} vibration in this wax has been documented in the literature. [94] The asymmetry of this intense peak indicates that it is probably composed of overlapping bands representing crystalline core thicknesses of different dimensions. There appears to be a discontinuity in the peak at ca. 29 cm^{-1} which could support this. The band at ca. 82 cm^{-1} could be the LAM-3 of a band under the ca. 35 cm^{-1} vibration. There is further activity at the expected LAM-3 positions for the ca. 29 cm^{-1} band but it has not been assigned due to spectral congestion and the very low intensity. The band related to the orthorhombic subcell structure occurs at ca. 100 cm^{-1}.

The Polywax 2000 corrected spectrum shows peaks at ca. 15 cm^{-1}, 45 cm^{-1}, 58 cm^{-1}, 72 cm^{-1}, 89 cm^{-1} and 102 cm^{-1}. The band at ca. 15 cm^{-1} is truncated as the exciting laser line has been filtered out experimentally. It is a definite band and is documented in the literature. [93] The bands at 45 cm^{-1} and 71 cm^{-1} are most likely higher order vibrations of the LAM-1 represented by the 15 cm^{-1} band. The band at ca. 102 cm^{-1} is also observed in the Polywax 1000 spectrum. The remaining bands at ca. 58 cm^{-1} and 89 cm^{-1} are also common with peaks seen on the Polywax 1000 spectrum.

The obvious spectral complexities observed in the low-frequency Raman spectra could be problematic for the accurate identification of LAMs. The correlation of the Raman data with information from other analytical techniques could therefore be helpful for its interpretation.

Table 4.5 shows the measured LAM-1 frequencies and corresponding derived carbon number chain lengths, n_{LAM}, for the Polywax samples. The wax molecular weight data are also included. Peaks are assigned as LAM-1 only where there is certainty in doing so.

Table 4.5: LAM-1 frequencies and n_{LAM} data for the Polywax samples

Sample	ν 1, cm^{-1}	n_{LAM} 1	ν 2, cm^{-1}	n_{LAM} 2	C# from M_n	C# from M_w	C# from M_z
Polywax 1000	29	C86	35*	C71	74	85	98
Polywax 2000	15*	C166	-	-	159	185	219

* most intense bands

The Polywax 1000 data indicate that this wax contains lamellae which are equivalent in size to chain lengths of C_{71} and C_{86}, calculated from the equation $n_{LAM} = 2489.4/\nu_1$. The MW data for this wax are comparable with the n_{LAM} values.

The Polywax 2000 data shows one n_{LAM} equivalent to C_{165} that is comparable with the MW data, indicating that EC material is present in the crystalline structure of this wax. This therefore indicates that the structures of both Polywax 1000 and Polywax 2000 may be comprised of extended-chain material only. A LAM-1 band originating from chain-folded material could be superimposed on one of the common bands, but the evidence for this in inconclusive.

The literature assigns the Raman shifts apparent at ca. 100 cm^{-1} in the spectra of polyethylene and n-alkane samples to the motion of the rigid chain in the orthorhombic crystal habit. [40, 47, 82, 90] It is assumed that this is the reason for this band, as polyethylene is often used as a model for n-alkane systems; as this shift is also apparent in the spectrum of the C_{32} sample (Figure 4.9); and as it is known that these waxes assume an orthorhombic crystal habit.

A similar exercise was performed for the Sasol FT waxes. Figures 4.16 to 4.24 show their low-frequency Raman spectra and Table 4.6 summarises their n_{LAM} data. The data have also been Boltzmann-corrected and smoothed by averaging over a period of 10 data points. The multiple curves in Figure 4.16 are again an indication of analytical repeatability.

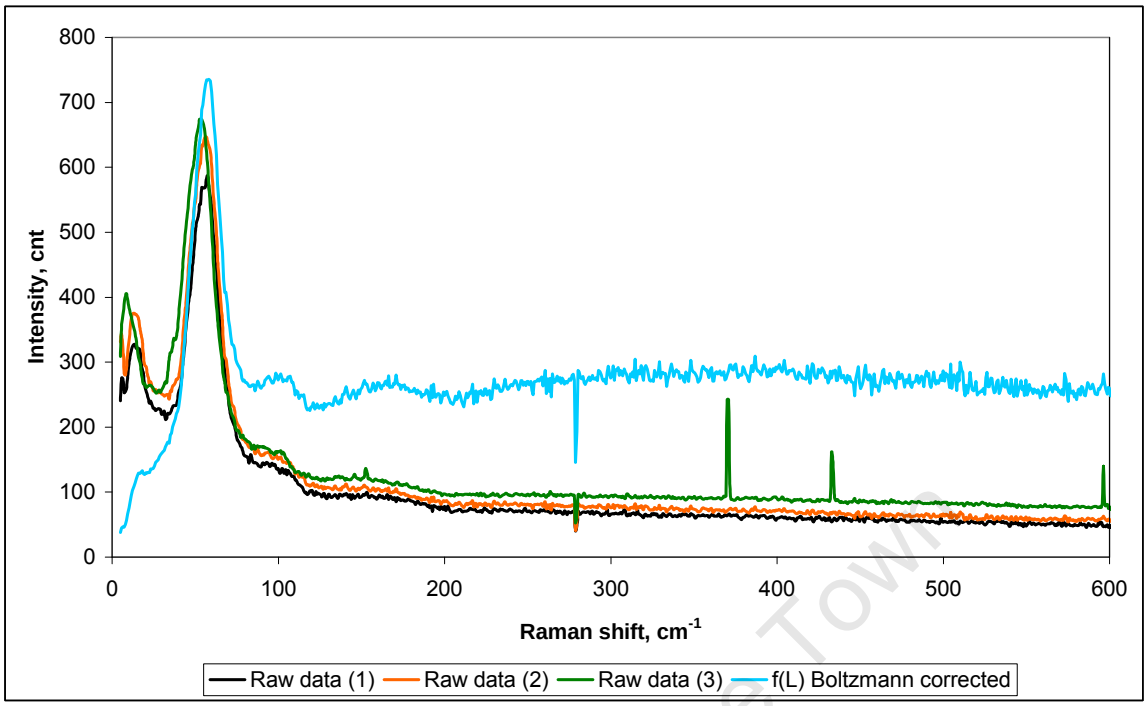

Figure 4.16: Low-frequency Raman spectra for Sasolwax C80 showing Boltzmann correction

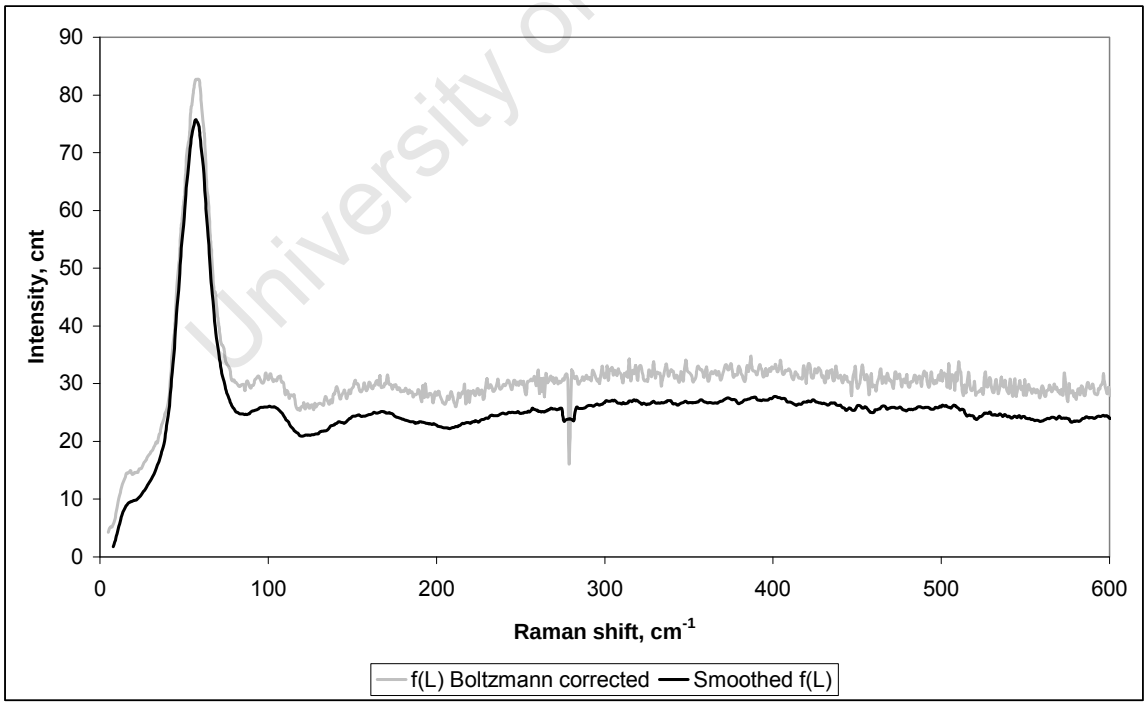

Figure 4.17: Smoothed Sasolwax C80 Boltzmann-corrected Raman spectrum

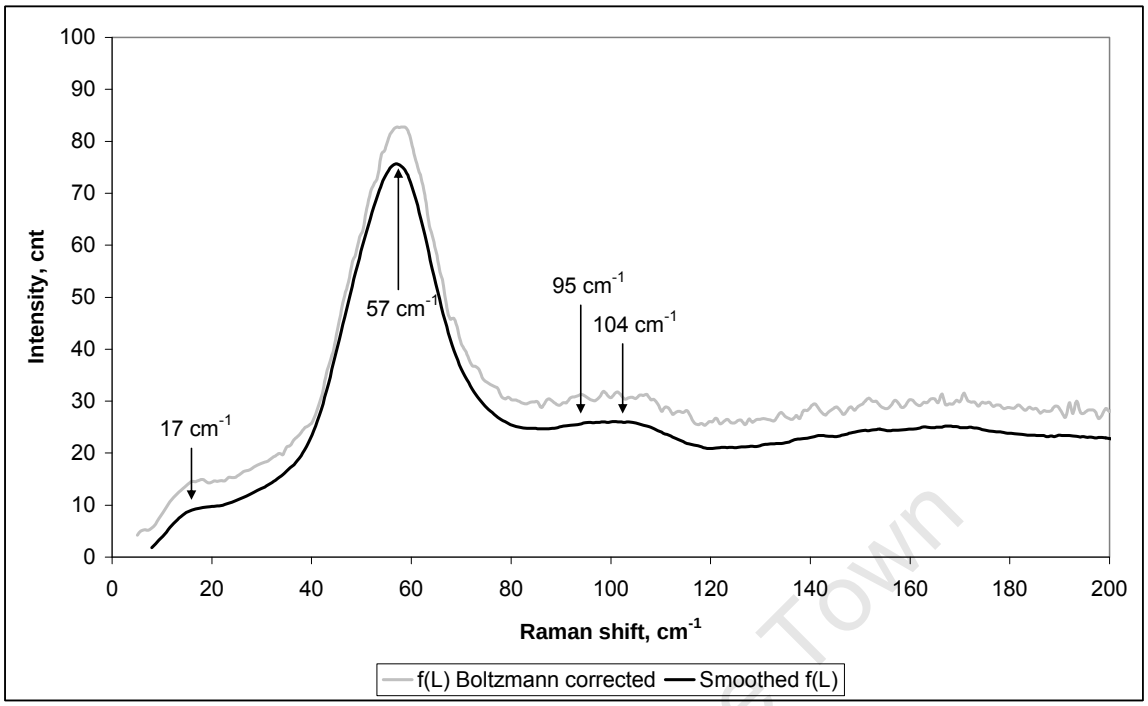

Figure 4.18: Smoothed Sasolwax C80 Boltzmann-corrected Raman spectrum – expanded scale

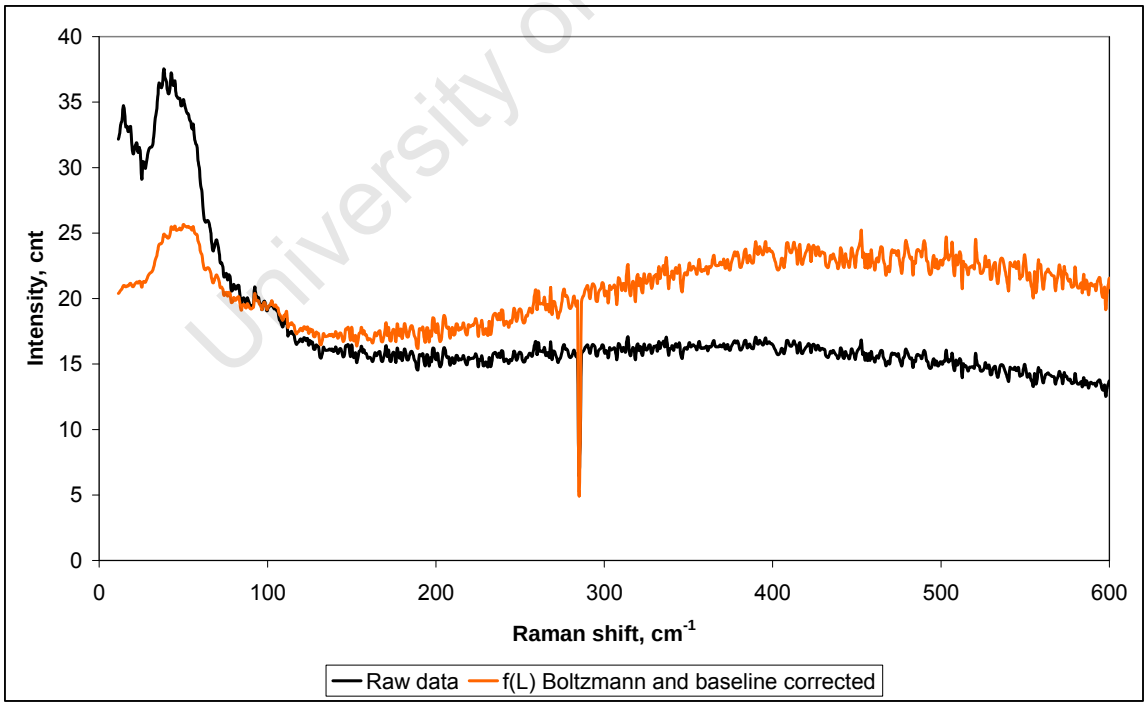

Figure 4.19: Low-frequency Raman spectrum for Sasolwax H1 showing Boltzmann and baseline correction

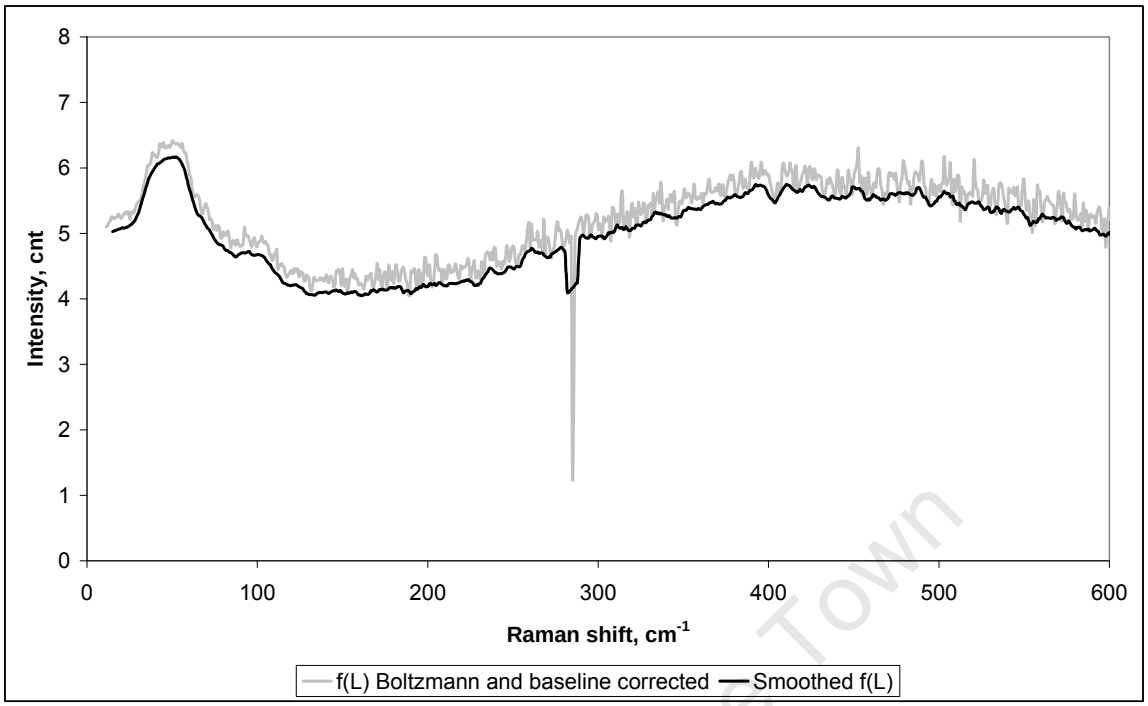

Figure 4.20: Smoothed Sasolwax H1 Boltzmann-corrected Raman spectrum

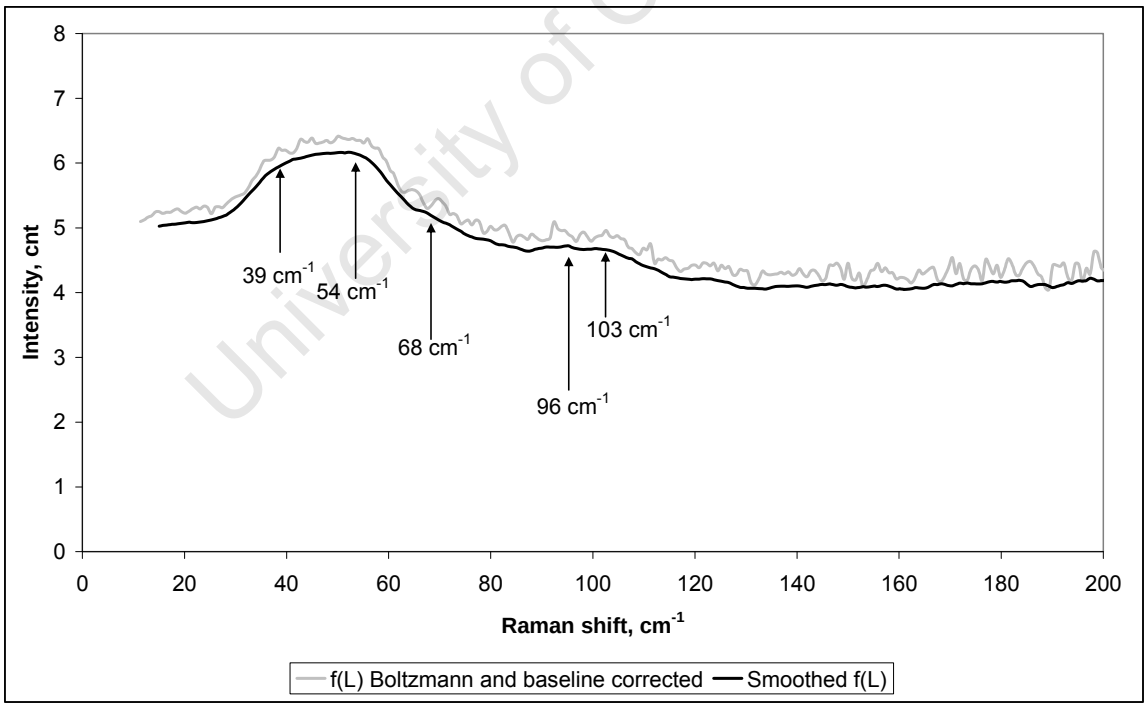

Figure 4.21: Smoothed Sasolwax H1 Boltzmann-corrected Raman spectrum – expanded scale

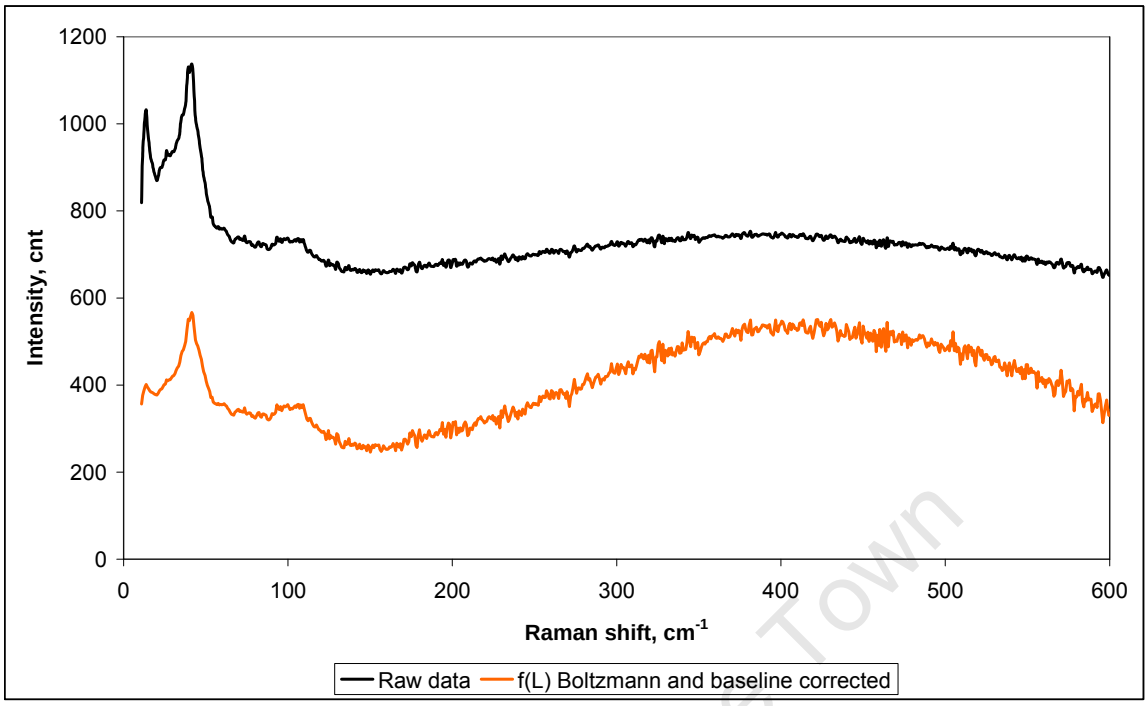

Figure 4.22: Low-frequency Raman spectrum for Sasolwax C105 showing Boltzmann and baseline correction

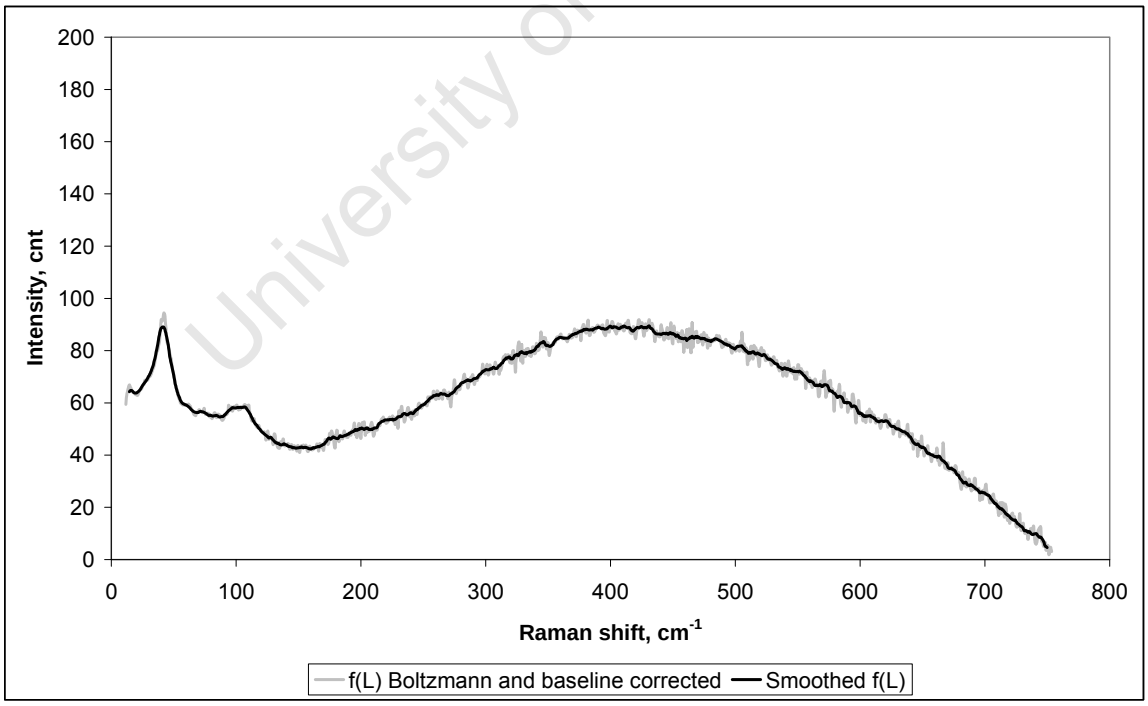

Figure 4.23: Smoothed Sasolwax C105 Boltzmann-corrected Raman spectrum

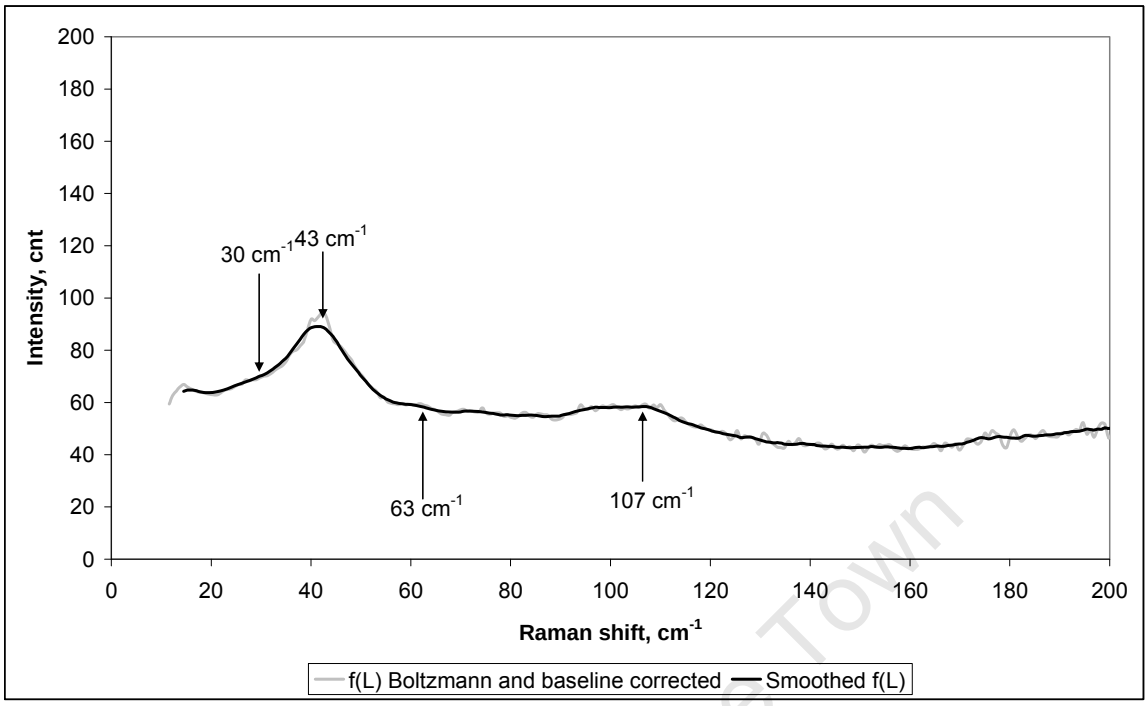

Figure 4.24: Smoothed Sasolwax C105 Boltzmann-corrected Raman spectrum – expanded scale

Excessive baseline slopes were observed in the spectra of Sasol waxes H1 and C105 and are due to Raman scattering from the samples. This has been corrected by mathematically adjusting the baseline slope. This procedure does not approximate the true Raman scattering from the sample but only makes the LAM peaks more evident. [99]

The Sasolwax C80 data show a single, broad intense band at ca. 57 cm^{-1}. A low-intensity band is apparent at ca. 17 cm^{-1}. The Sasolwax H1 data indicate a broad asymmetric band with a discontinuity occurring on the low-frequency side of the peak between 35 cm^{-1} and 42 cm^{-1}. As this asymmetric peak almost certainly is a result of overlapping bands, the average of these two wavenumbers (ca. 39 cm^{-1}) was assigned to the occurrence of a LAM-1 band. The bulk of the peak occurs at ca. 54 cm^{-1}. An additional low-intensity peak occurs at ca. 68 cm^{-1}. This appears to be a common band that may display overlap with a LAM-1 band due to the manner in which it overlaps the intense peak at ca. 54 cm^{-1}. It will for now be interpreted as a LAM-1 band. The Raman spectrum of Sasolwax C105 shows a broad, intense peak at ca. 43 cm^{-1}. There is a discontinuity in the slope of the peak on the low-frequency side at ca. 30 cm^{-1}. This is again likely to be indicative of overlapping bands of multiple crystalline core thicknesses.

A lower intensity band also occurs at ca. 63 cm^{-1}. The common band at ca. 100 cm^{-1} originating from the orthorhombic structure is again apparent for all three waxes. A further peak common to all spectra occurs at ca. 95 cm^{-1}. There is no mathematical progression of the LAMs and all peaks, excluding those that are common to all samples, could therefore be interpreted as first-order. The LAM-1 frequencies are summarized in Table 4.6.

Table 4.6: LAM-1 frequencies and n_{LAM} data for the Sasolwax samples

Sample	ν 1, cm^{-1}	n_{LAM} 1	ν 2, cm^{-1}	n_{LAM} 2	ν 3, cm^{-1}	n_{LAM} 3	C# from M_n	C# from M_w	C# from M_z
Sasolwax C80	57*	C44	-	-	-	-	43	44	45
Sasolwax H1	39*	C64	54*	C46	68	C37	53	61	72
Sasolwax C105	30	C83	43*	C58	-	-	70	77	87

* most intense bands

All three Sasol waxes show n_{LAM} data that are comparable with their MW parameters. The n_{LAM} quantifies the extended all-*trans* portion of the crystalline chains. The correlation between n_{LAM} and the MW parameters indicates that very little conformational disorder (appearance of *gauche* conformers) occurs within the crystalline lamellae as *gauche* bonds will decouple the crystalline all-*trans* stem length. [88-89] The band at ca. 17 cm^{-1} on the Sasolwax C80 spectrum does not relate to the wax MW parameters and the origin of this band is perhaps not a LAM vibration. The TAM bands are known to occur below the LAM-1 band frequency and it is possible that a different type of vibration, such as a TAM, is the origin of this band. The band could also be an artifact due to its proximity to the filtered Rayleigh line. Furthermore, the bands at ca. 65 cm^{-1} (Sasolwax H1 and Sasolwax C105) and ca. 95 cm^{-1} appear to be common bands. These bands are also evident in the spectra of the two Polywax samples. The band at ca. 63 cm^{-1} in the Sasolwax H1 spectrum may be superimposed on a LAM-1 band.

It may therefore be concluded that the multiple melt peaks observed for the Sasol hard waxes H1 and C105 are not as a result of a FC and EC mixed morphology. The data in Tables 4.2 and 4.3, however, indicate that there is a percentage of material $>C_{100}$ in the waxes studied here that would be expected to chain fold. Chain-folded lamellae are not identified in any of the waxes from their low-frequency Raman spectra. This therefore implies that the carbon number onset is greater than C_{100} for polydisperse materials and is possibly also concentration and/ or MWD dependent.

This was investigated further by preparing four fractions (F1-F4) of the highest molecular weight FT hard wax, Sasolwax C105, using the temperature rising elution fractionation (TREF) technique which is described in Chapter 2.

Figure 4.25 shows the DSC analyses of the fractionated samples. These are second melt analyses. Fraction F1 melts with a slight shoulder on the high temperature side of the main melting peak. Fractions F2-F4 all show clear melting bimodality.

Table 4.7 shows the DSC and GPC parameters of each of the fractions. Figure 4.26 shows their carbon number distribution analyses derived from GPC profiles.

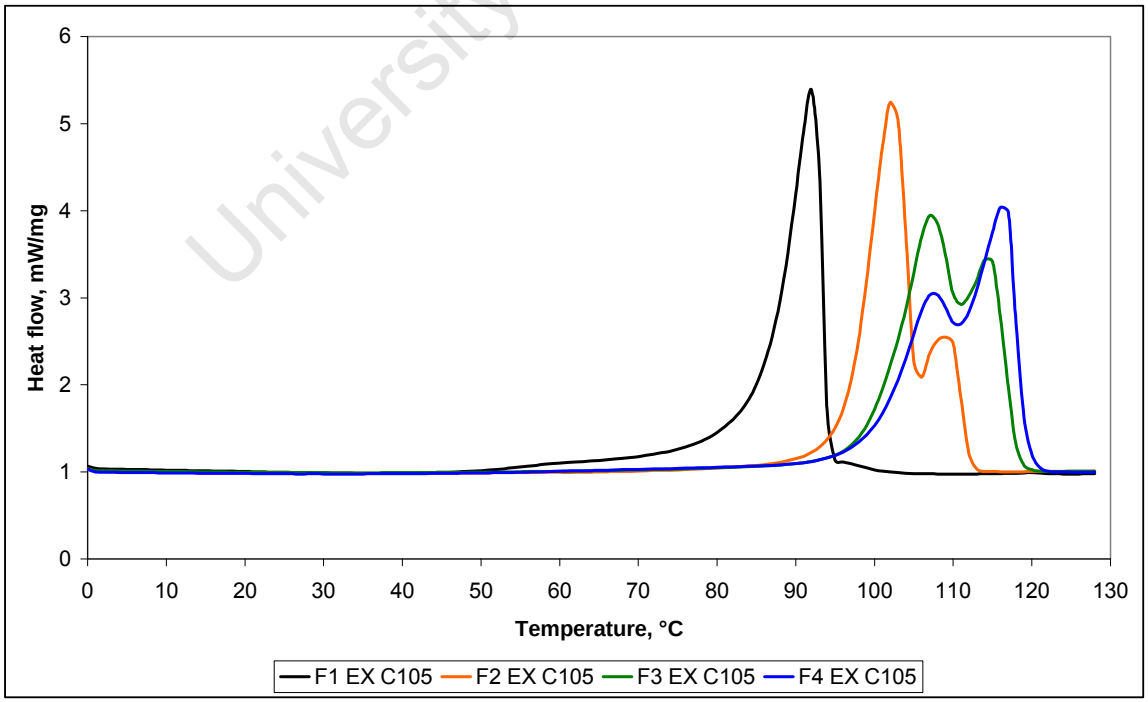

Figure 4.25: DSC analysis for Sasolwax C105 fractions

Table 4.7: DSC and GPC data for four fractions from Sasolwax C105

GPC/ DSC parameter	F1	F2	F3	F4
M_n, dalton	823	1075	1309	1403
Carbon # from M_n	59	77	94	100
M_w, dalton	872	1156	1454	1557
Carbon # from M_w	62	83	104	111
M_z, dalton	943	1263	1648	1755
Carbon # from M_z	67	90	118	125
% material due to 1st DSC melt peak	99	78	66	49
% material due to 2nd DSC melt peak	1	22	34	51
% material >C_{80} (GPC)	10	41	71	79
% material >C_{100} (GPC)	4	18	41	53
% material >C_{120} (GPC)	2	9	24	32
% material >C_{150} (GPC)	1	2	12	14

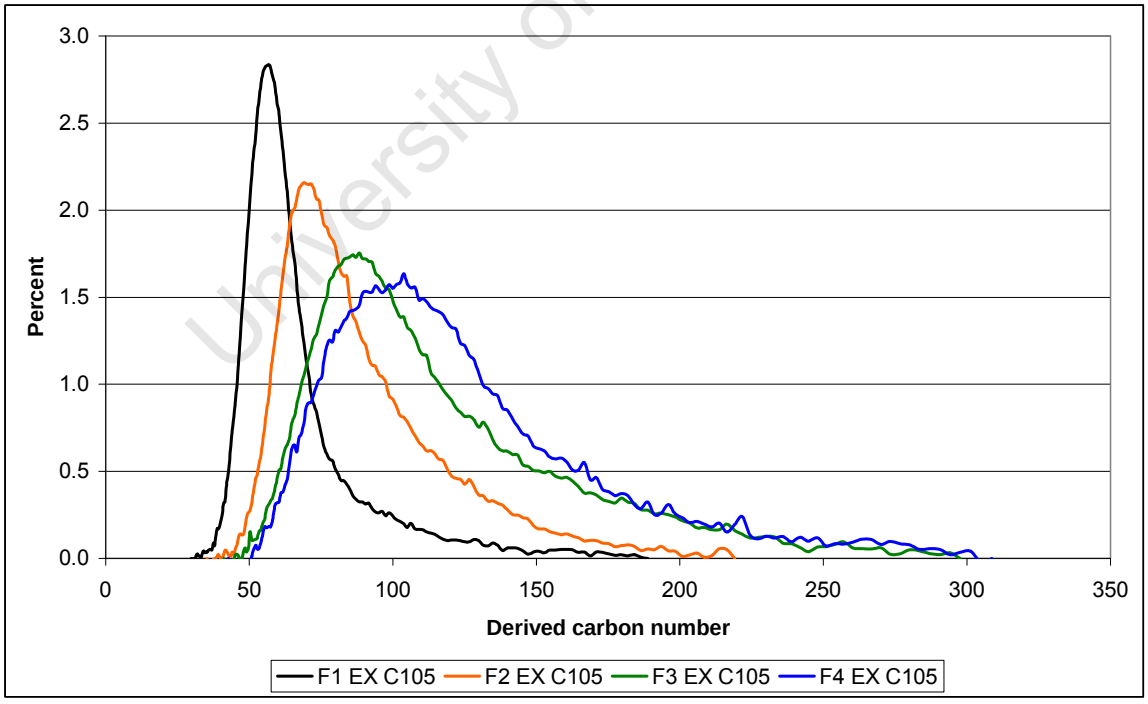

Figure 4.26: Carbon number distributions derived from GPC data for Sasolwax C105 fractions

The above data show the expected progression in the properties of the consecutive fractions with regard to increasing melting temperatures and molecular weight or carbon number distributions. The correlation between the percentage material in the samples greater than any of the given carbon numbers with the areas under either the first or second DSC melt peaks is unclear.

Low-frequency Raman analysis was performed on the samples, following the methodology for the wax samples studied previously in this chapter. Figures 4.27 to 4.38 show the spectra and Table 4.8 summarises the LAM-1 data for the four fractions.

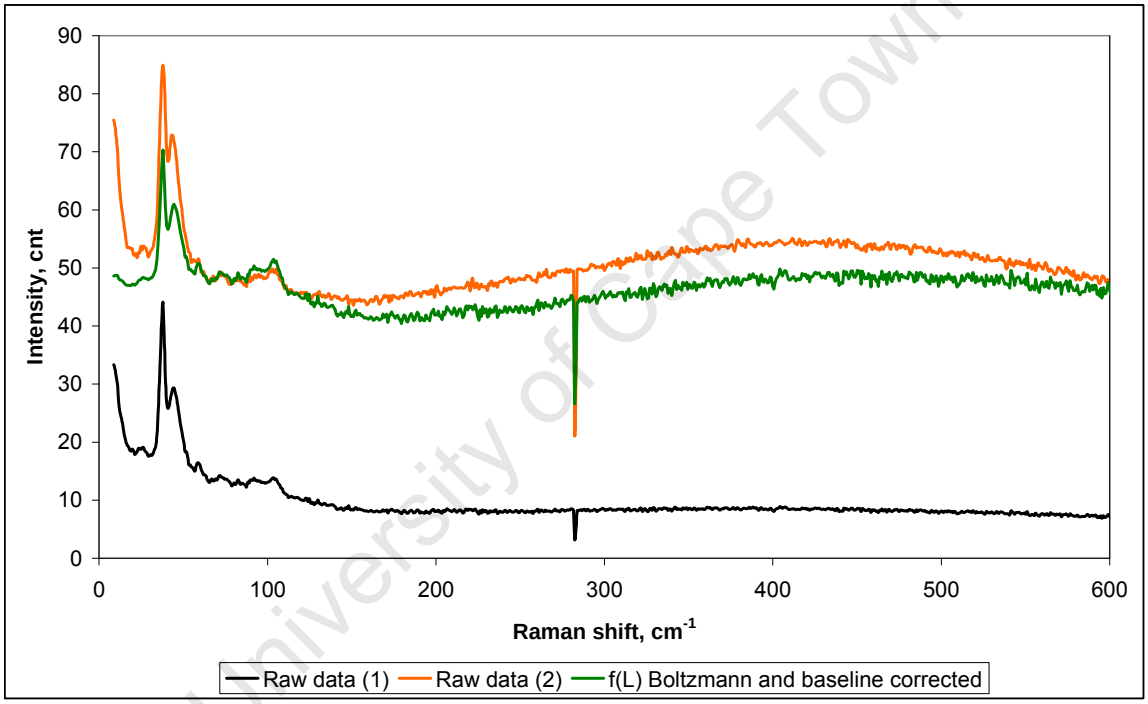

Figure 4.27: Low-frequency Raman spectra for Sasolwax C105 fraction F1 showing Boltzmann and baseline correction

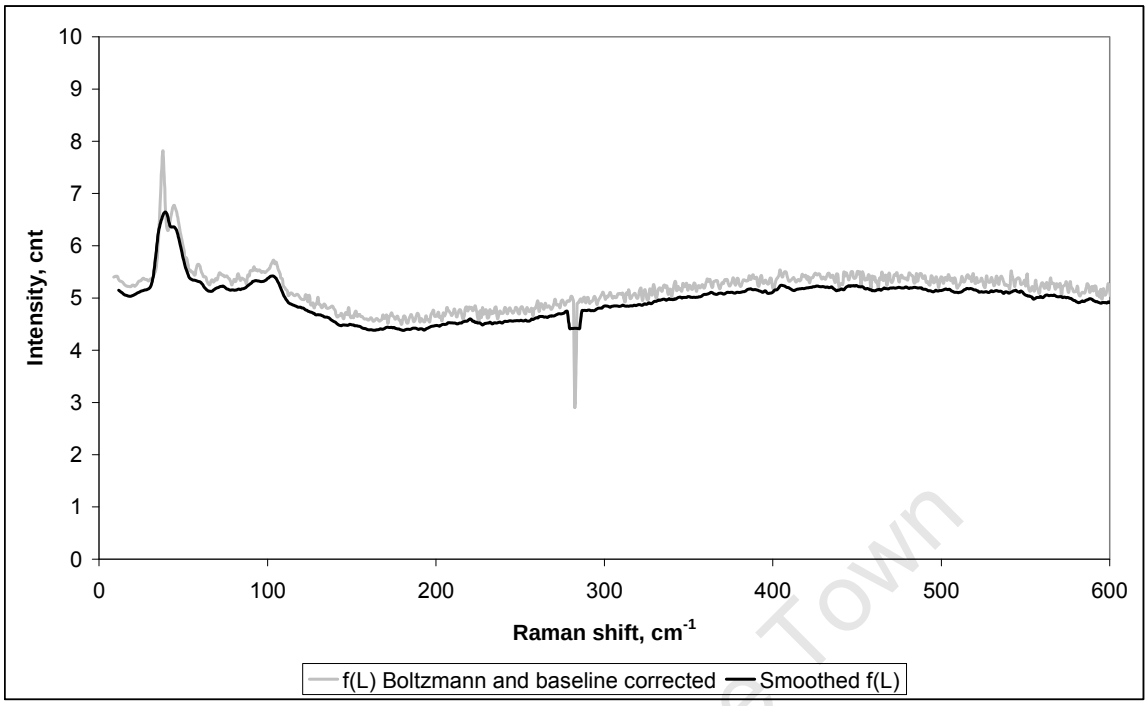

Figure 4.28: Smoothed Sasolwax C105 fraction F1 Boltzmann-corrected Raman spectrum

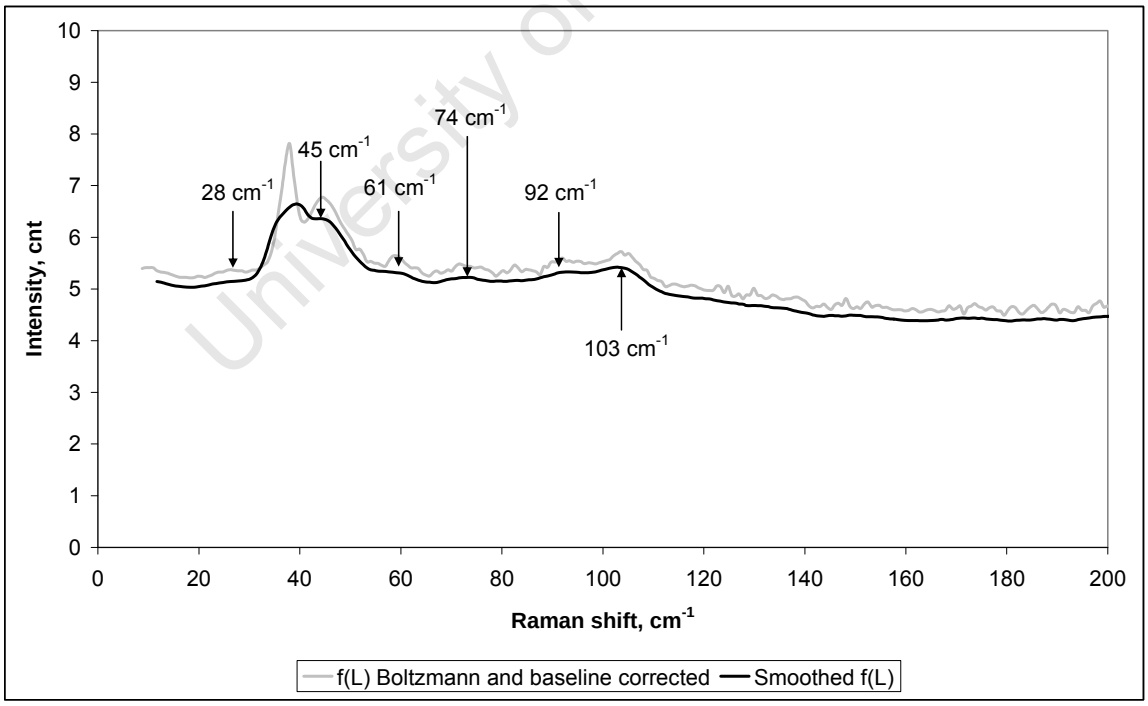

Figure 4.29: Smoothed Sasolwax C105 fraction F1 Boltzmann-corrected Raman spectrum – expanded scale

The spectrum for fraction F1 shows an intense, narrow peak at ca. 38 cm^{-1} which is characteristic of a Si plasma line. This assignment is highly probable due to the position of the peak as well as its narrow bandwidth, and this contamination may interfere with the interpretation of the spectrum. It was not possible to subtract this peak from the spectrum due to baseline uncertainty. An intense peak due to the sample is observed at ca. 45 cm^{-1}. Low-intensity peaks are apparent at ca. 28 cm^{-1}, 61 cm^{-1}, 74 cm^{-1} and 92 cm^{-1}. The characteristic orthorhombic band is apparent at ca. 103 cm^{-1}. The baseline slope was again adjusted mathematically.

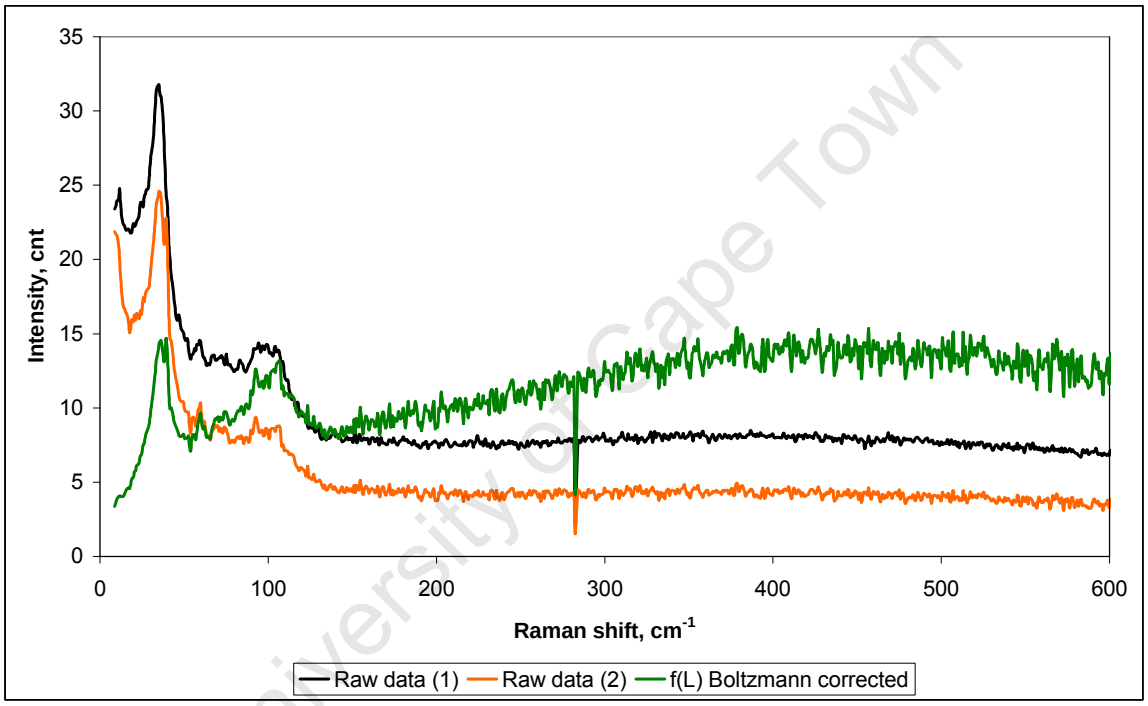

Figure 4.30: Low-frequency Raman spectra for Sasolwax C105 fraction F2 showing Boltzmann correction

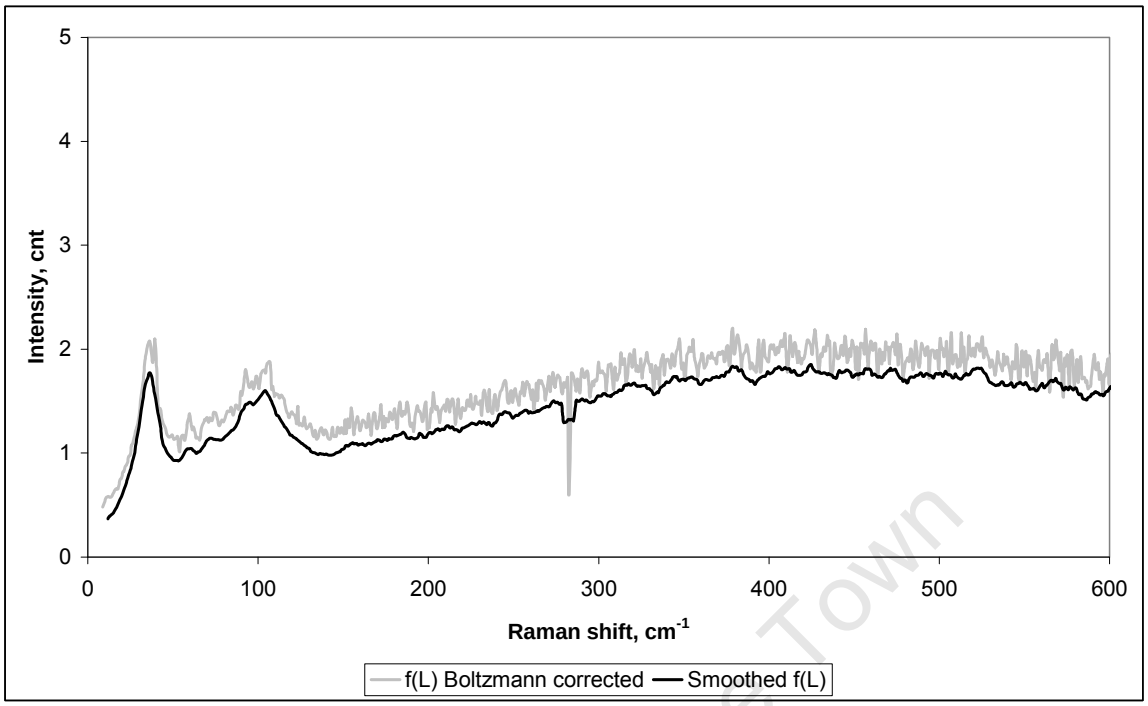

Figure 4.31: Smoothed Sasolwax C105 fraction F2 Boltzmann-corrected Raman spectrum

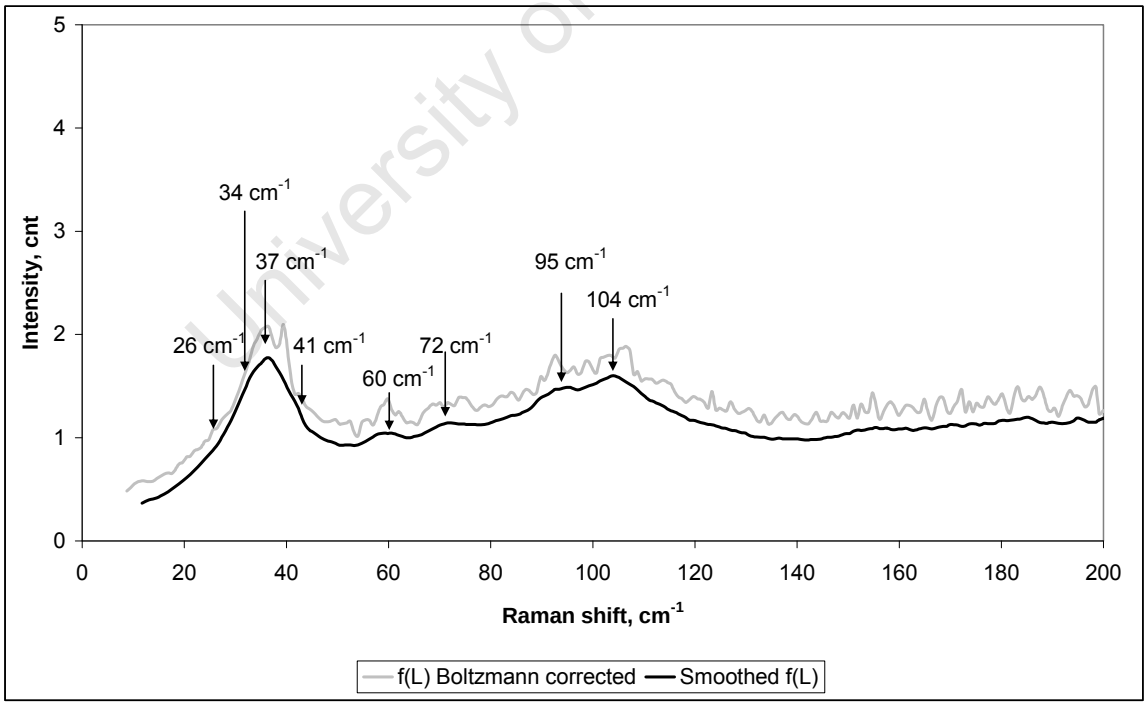

Figure 4.32: Smoothed Sasolwax C105 fraction F2 Boltzmann-corrected Raman spectrum – expanded scale

The spectrum of fraction F2 shows an intense asymmetric peak at ca. 37 cm^{-1} which is superimposed on a Si plasma line at ca. 39 cm^{-1}. The peak asymmetry is apparent at ca. 34 cm^{-1}. A discontinuity on the high-frequency band-edge is seen at ca. 41 cm^{-1}. Additional low-intensity peaks are apparent at ca. 60 cm^{-1} and ca. 72 cm^{-1}. Another peak is apparent at ca. 95 cm^{-1}, as well as the orthorhombic band at ca. 104 cm^{-1}.

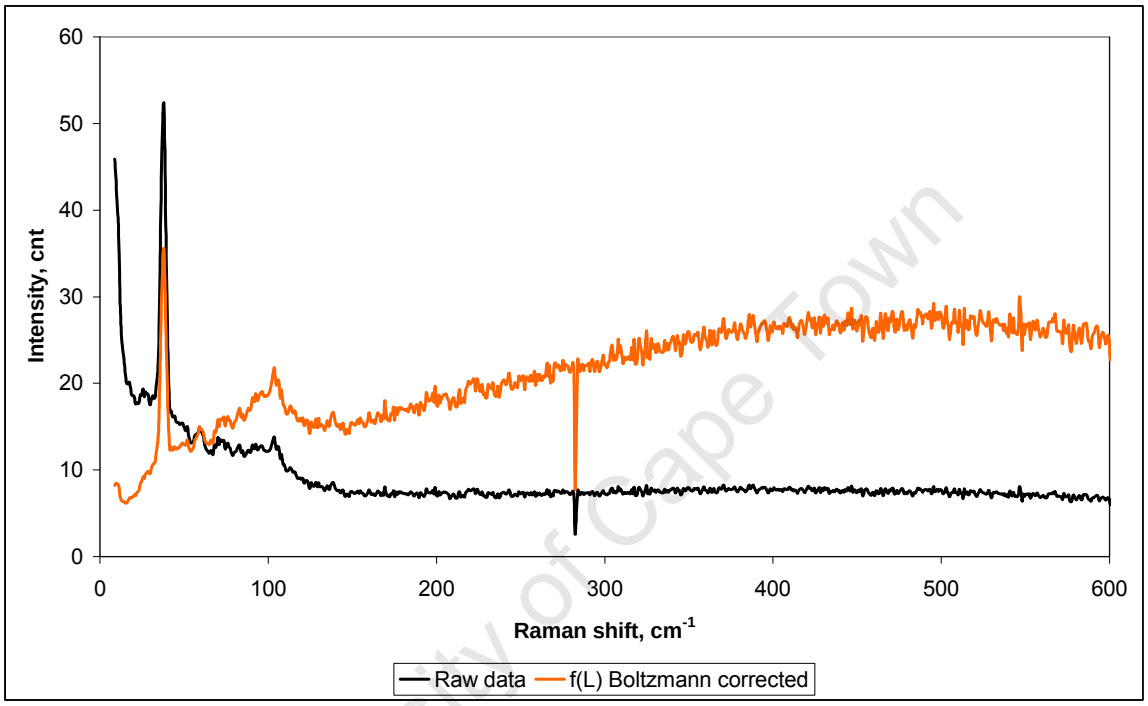

Figure 4.33: Low-frequency Raman spectrum for Sasolwax C105 fraction F3 showing Boltzmann correction

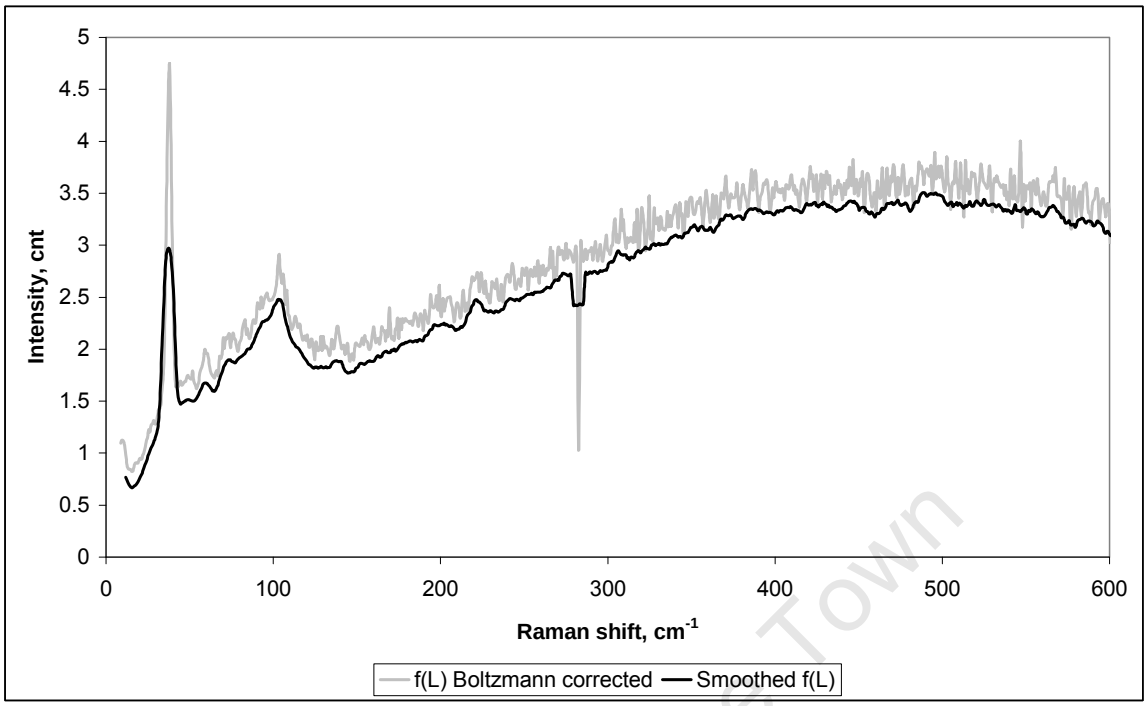

Figure 4.34: Smoothed Sasolwax C105 fraction F3 Boltzmann-corrected Raman spectrum

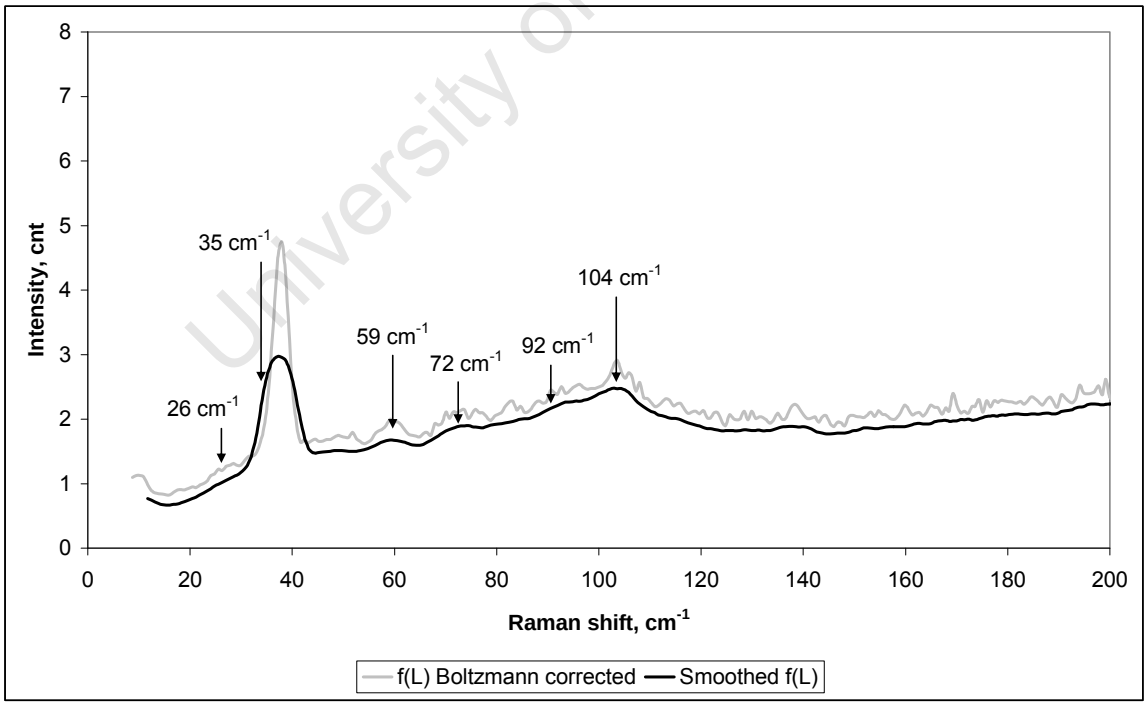

Figure 4.35: Smoothed Sasolwax C105 fraction F3 Boltzmann-corrected Raman spectrum – expanded scale

The sample F3 spectrum is difficult to interpret, due to the apparent absence of an intense vibration. A Si plasma line is again apparent at ca. 37 cm^{-1}. The band appears to be slightly broader than observed in the spectra of fractions F1 and F2 and n-C_{32} (Figure 4.9). It could therefore be superimposed on a LAM vibration at ca. 35 cm^{-1}. Low-intensity sample bands are apparent at ca. 26 cm^{-1}, ca. 59 cm^{-1} and ca. 72 cm^{-1}. The band at ca. 26 cm^{-1} is common with bands in the spectra of fractions F1 and F2. Its peak form on the Boltzmann-corrected spectrum may be indicative of overlap with a LAM band. An additional peak is apparent at ca. 92 cm^{-1}, with the ever-present orthorhombic band at ca. 104 cm^{-1}. The latter is more pronounced than in other spectra and may therefore be superimposed on a LAM-3 vibration.

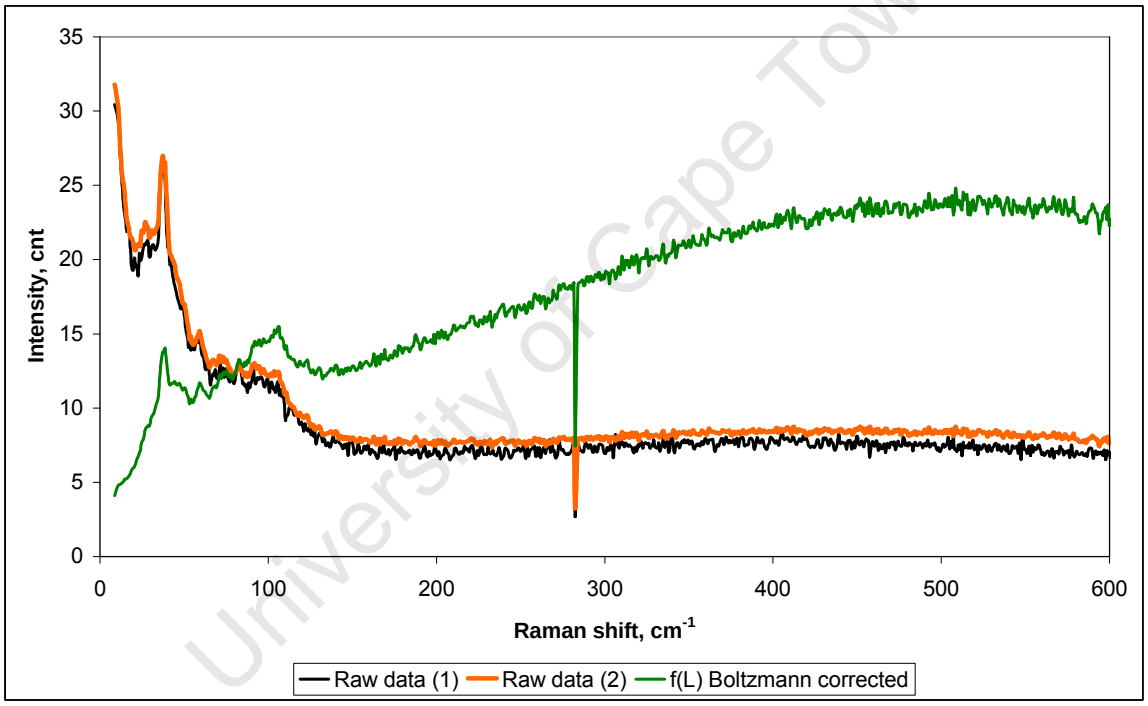

Figure 4.36: Low-frequency Raman spectra for Sasolwax C105 fraction F4 showing Boltzmann correction

Figure 4.37: Smoothed Sasolwax C105 fraction F4 Boltzmann-corrected Raman spectrum

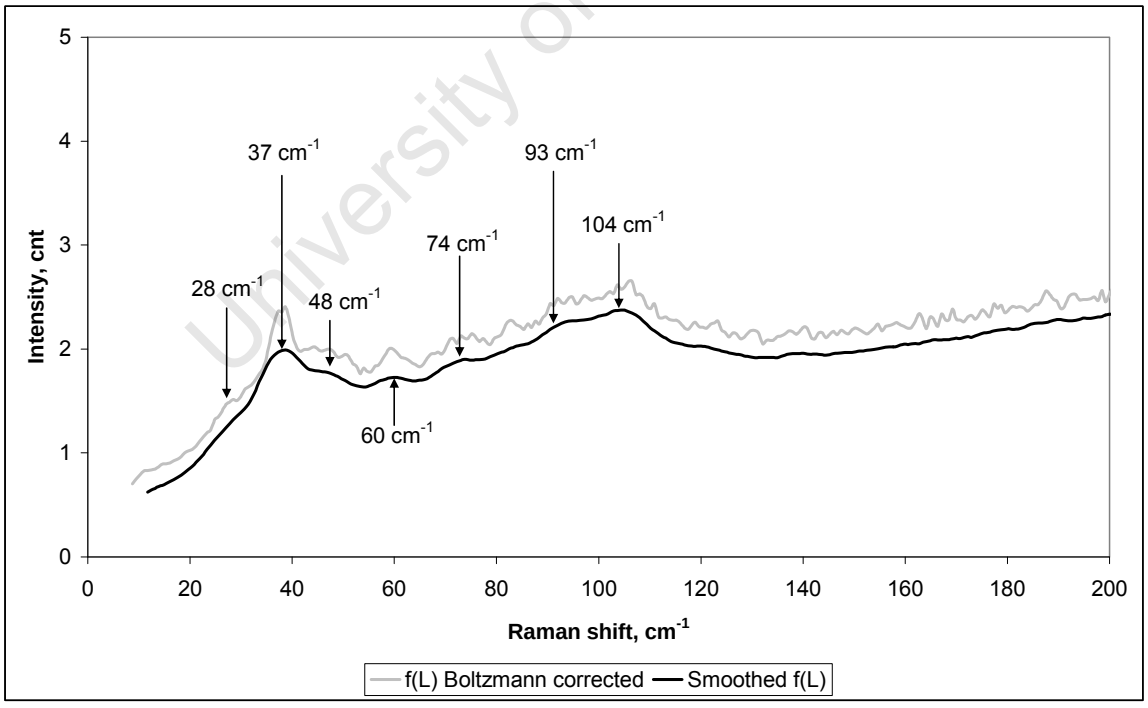

Figure 4.38: Smoothed Sasolwax C105 fraction F4 Boltzmann-corrected Raman spectrum – expanded scale

The spectrum of fraction F4 also shows contamination with the Si plasma line at ca. 38 cm^{-1}. An intense band is apparent at ca. 37 cm^{-1} with discontinuity due to asymmetry at ca. 28 cm^{-1}. The latter band appears as a definite discontinuity on both the smoothed and unsmoothed data and may therefore well originate from a LAM, despite its commonality with the spectra of the other C105 fractions. Further low-intensity bands are apparent at ca. 48 cm^{-1} and ca. 60 cm^{-1}. The band at ca. 74 cm^{-1} is most probably the LAM-3 band of the vibration at ca. 28 cm^{-1}. A band is also apparent at ca. 93 cm^{-1} and the orthorhombic band is again apparent at ca. 104 cm^{-1}. The latter again appears to be superimposed on a LAM-3 vibration.

A slight shift is observed in the positions of the Si plasma lines in the spectra of the wax fraction samples. The average of the plasma line peak positions from the spectra where it is observed is 37.3 ± 0.7 cm^{-1}. This degree of shift is not considered significant for these measurements. [97] The fact that the spectra of all four fractions show the Si plasma line seems to indicate impurities in the C105 starting material or contamination during sample preparation. The characteristic orthorhombic structure-related band is seen for all four wax fractions at ca. 100 cm^{-1}. Further common bands are observed for all four samples at ca. 60 cm^{-1}, ca. 74 cm^{-1} and ca. 93 cm^{-1}. These bands were also seen in all previously shown spectra.

Table 4.8: LAM-1 frequencies and n_{LAM} data for the Sasolwax C105 fractions

Sample	ν 1, cm^{-1}	n_{LAM} 1	ν 2, cm^{-1}	n_{LAM} 2	ν 3, cm^{-1}	n_{LAM} 3	C# from M_n	C# from M_w	C# from M_z
F1	45*	C55	-	-	-	-	59	62	67
F2	34	C73	37*	C67	-	-	77	83	90
F3	35	C71	-	-	-	-	94	104	118
F4	28	C89	37*	C67	48	C52	100	111	125

* most intense bands

All fractions show the n_{LAM} at ca. 100 cm^{-1}, which is indicative of the orthorhombic crystal habit. Common bands are also apparent at ca. 48 cm^{-1}, 60 cm^{-1}, ca. 74 cm^{-1} and ca. 93 cm^{-1} on all four spectra. Their assignment is uncertain, but they could be associated

with other non-LAM vibrations. The fact that they are common to all wax samples regardless of MW implies that they are not associated with a LAM. It is, however, not possible to discount that any of these bands are superimposed on LAM vibrations. There also appears to be a common band at ca. 27 cm^{-1}. The n_{LAM} derived from this vibration does not correlate or agree with the MW-derived carbon-number parameters for any of the samples with the exception of fraction F4. Its assignment as a LAM band therefore seems unlikely for the other three fractions. Figure 4.39 shows a comparison of the Boltzmann-corrected spectra of the four wax fractions. Although Raman spectroscopy is not a directly qualitative technique, visual inspection of the relative intensities of the ca. 27 cm^{-1} bands with respect to those of the common ca. 100 cm^{-1} bands indicates that this band on the F4 spectrum could be a LAM band which is superimposed on a common band. [38] Likewise, the 48 cm^{-1} band appears to be common, but is certainly superimposed on LAM bands in the spectra of fractions F1 and F4.

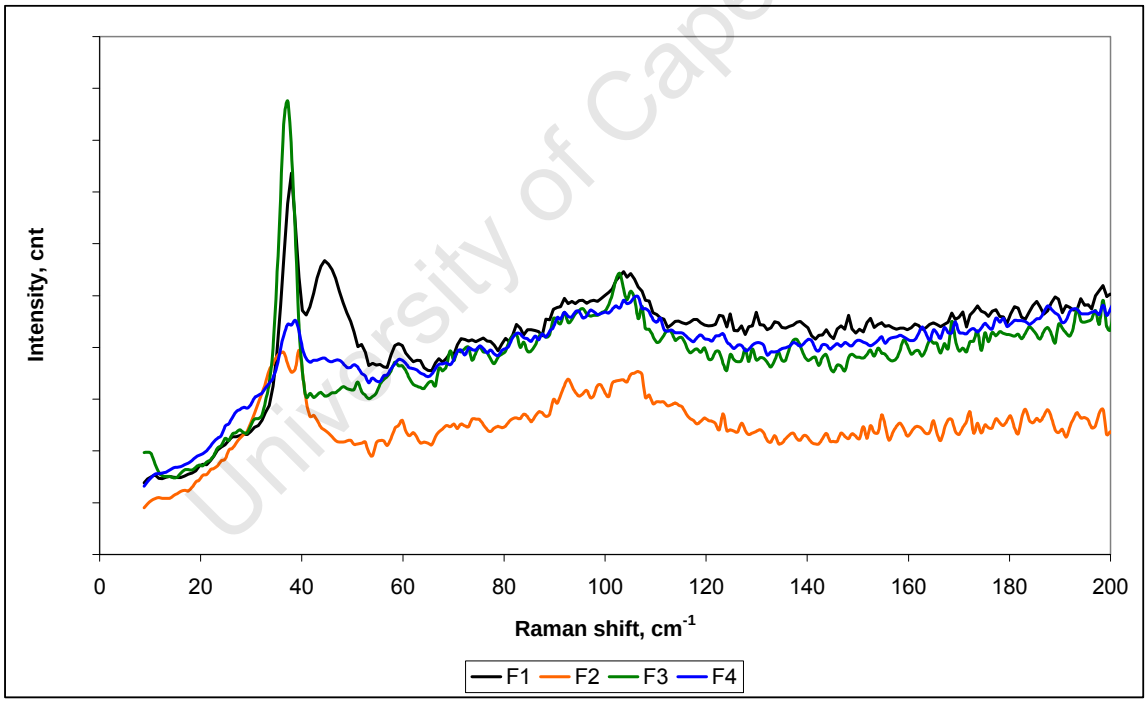

Figure 4.39: Comparison of the Boltzmann-corrected spectra of the C105 fractions F1, F2, F3 and F4

All spectra also show contamination by a plasma line at ca. 37 cm^{-1}. This is a plasma line which scatters from the sample and appears as a peak. [99]

The n_{LAM} parameters of all fractions indicate that the chain lengths present in the crystalline core thicknesses are similar to those derived from the MW data, except possibly fraction F4. There is evidence of an n_{LAM} which could be an integral reciprocal of the MW parameters. The DSC data shown in Table 4.7 does not, however, provide a conclusive means of confirming the existence of a FC morphology in this sample. There is therefore no convincing indication of chain-folded material in the fractions F1 to F3, but there could be slight evidence of this in fraction F4.

The bands at ca. 60 cm^{-1}, ca. 73 cm^{-1}, ca. 84 cm^{-1} and ca. 93 cm^{-1} again appear to be common bands for all samples. Where they have not been mentioned for a specific sample, a review of its spectrum always indicates possible spectral activity. These bands may therefore not have their origin in a LAM vibration, but it may also not be discounted that a LAM vibration is not superimposed on any of these common bands.

This indicates that chain folding could potentially be induced by fractionation of Sasolwax C105, either by concentrating the higher MW portion of the sample or reducing sample polydispersity. The evidence for this is, however, by no means conclusive.

A summary of the spectral bands that may be identified as originating from LAM-1 vibrations for all samples is given in Table 4.9. This data provides a reason for the poor correlation between the areas under the first or second DSC melt peaks of these samples with the amounts of material greater than the fold onset carbon numbers given in the literature. The Raman data provides little evidence of chain-folding in these samples. Therefore none of the DSC melt peaks represent the melting of FC material. The sample F4 may be an exception, but the evidence for chain folding is slight.

The polydispersity data of these waxes and wax fractions and their carbon number equivalent MW parameters are summarised in Table 4.10 in order to demonstrate the range over which chain folding would not be expected to occur.

Table 4.9: Proposed LAM-1 frequencies and n_{LAM} data for all wax samples

Sample	ν 1, cm^{-1}	n_{LAM} 1	ν 2, cm^{-1}	n_{LAM} 2	ν 3, cm^{-1}	n_{LAM} 3	C# from M_n	C# from M_w	C# from M_z
Polywax 1000	29	C86	35	C71	-	-	74	85	98
Polywax 2000	15	C166	-	-	-	-	159	185	219
Sasolwax C80	57	C44	-	-	-	-	43	44	45
Sasolwax H1	39	C64	54	C46	68	C37	53	61	72
Sasolwax C105	30	C83	43	C58	-	-	70	77	87
C105 fraction F1	45	C55	-	-	-	-	59	62	67
C105 fraction F2	34	C73	37	C67	-	-	77	83	90
C105 fraction F3	35	C71	-	-	-	-	94	104	118
C105 fraction F4	28	C89	37	C67	48	C52	100	111	125

Table 4.10: Polydispersity of waxes and wax fractions

Sample	Carbon number from M_n	Carbon number from M_w	Carbon number from M_z	P_d
Polywax 1000	74	85	98	1.15
Polywax 2000	159	185	219	1.16
Sasolwax C80	43	44	45	1.03
Sasolwax H1	53	61	72	1.14
Sasolwax C105	70	77	87	1.11
Sasolwax C105 fraction F1	59	62	67	1.06
Sasolwax C105 fraction F2	77	83	90	1.08
Sasolwax C105 fraction F3	94	104	118	1.11
Sasolwax C105 fraction F4	100	111	125	1.11

The data in Table 4.10 indicate that the onset of chain folding in polydisperse waxes would be above a weight-average derived carbon number of C_{185} and possibly even C_{111}.

4.2 MWD BIMODALITY

It is almost stating the obvious that a bimodal wax MWD would result in a bimodal melting distribution. Figure 4.40 shows the carbon number distribution data for Sasolwax H1 and Sasolwax C105. These data are derived from the GPC analyses of the waxes. HTGC analysis was not used due to the inability of the technique to properly quantify material above C_{40} or measure material above C_{100}. [42] The GPC y-axis parameter has not been corrected for an actual mass-percent correlation. [25]

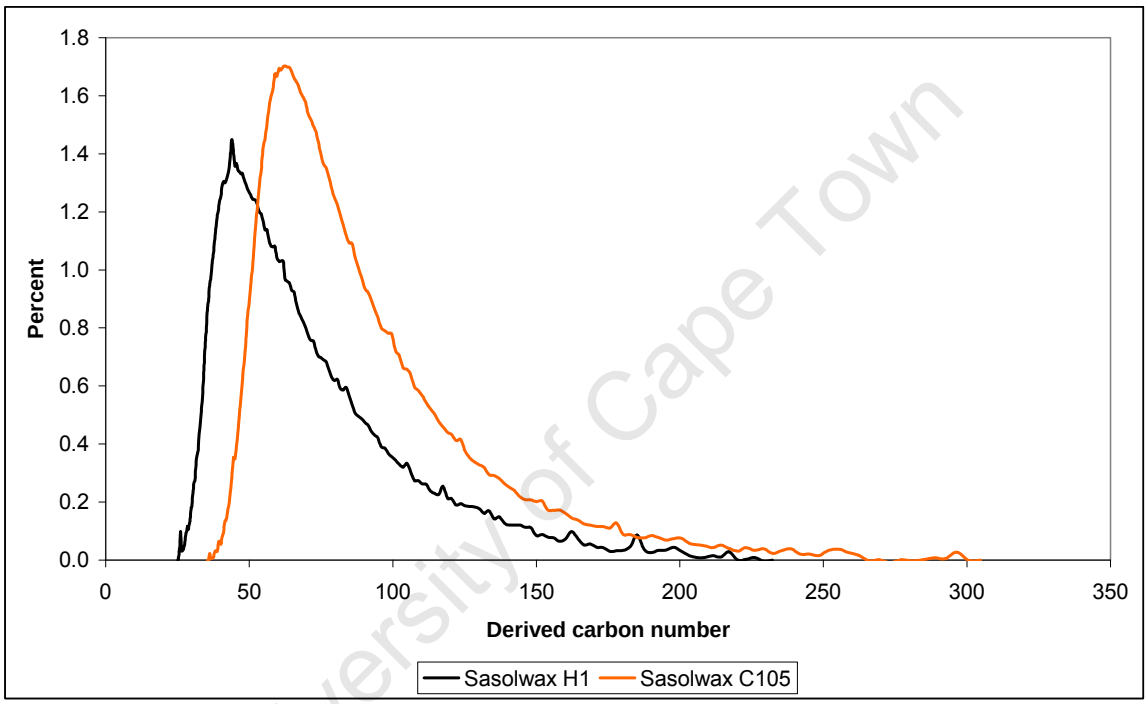

Figure 4.40: Derived carbon number distribution analyses of Sasolwax H1 and Sasolwax C105

Neither of the derived carbon distributions of these two waxes show multiple modes. The non-Gaussian distributions are due to the fact that both of these waxes are residue fractions from distillation. This explains the tailing at high carbon numbers, as the low molecular mass material of the original waxes have been removed.

It has been documented that the GPC analysis of Sasolwax H1 has a bimodal MW distribution. It was concluded that this is the cause of the observed DSC melting behaviour. The pore size distribution of the columns used for the GPC analysis, however, did not cover the entire MW range of the sample on the low MW side of the

distribution. This would result in a fully-resolved GPC peak appearing beyond the permeation limit of the column set, which appears to have been incorrectly interpreted as representing a portion of the sample MWD. The chromatogram presented for Sasolwax H1 was raw data, hence the occurrence of the permeation limit peak. This peak would not be apparent should these data be represented as a molecular weight plot. [16]

It may therefore be concluded that the multiple melt peaks observed for the FT hard waxes are not due to molecular weight bimodality.

4.3 CONCLUSION

This chapter has shown that the FT hard wax multiple DSC melt peaks are not due to molecular weight effects, viz. chain folding due to material $>C_{100}$ or a bimodal MWD. Fractionation of the highest MW FT hard wax, Sasolwax C105, shows that chain folding may possibly be induced by effectively increasing the concentration of the amount of long-chain material or decreasing the wax polydispersity. Low-frequency Raman analyses of many of the waxes measured more than one first-order LAM peak. This is indicative of the presence of crystalline lamellae of different thicknesses within the samples.

CHAPTER 5

CRYSTALLINE CORE THICKNESSES IN FT HARD WAXES

5.1 THEORY OF LOW-FREQUENCY RAMAN MEASUREMENT OF WAXES

The low-frequency Raman data presented in Chapter 4 for the FT hard waxes show evidence of multiple LAM peaks. LAM peaks may be correlated to crystalline core thicknesses of specific sizes. There is a possibility that a Raman peak appearing at a higher wavenumber is a higher order vibration of the first Raman peak. The second-order vibration is not Raman active, but the third-order vibration may be measured. A numerical relationship between Raman peaks could indicate that their origin is similar. [27] It may be assumed that the multiple peaks observed in the work presented in Chapter 4 represent multiple crystalline core thicknesses of different sizes in the wax samples. Where more than one peak is present, the lowest wavenumber peak is referred to as peak 1 and the numbering increases according to the increase in the vibrational frequency. [27] n-Alkanes, their mixtures, waxes and crystalline polymeric materials are known to crystallise in a lamellar structure with their molecules generally arranged perpendicular to the crystal surface. [12, 25-26, 28, 54, 58, 69-70] It should therefore be possible to measure crystalline core thicknesses that are related to these lamellae using low-frequency Raman analysis. By implication, multiple core thicknesses inferred from LAMs would be indicative of different lamellar thickness populations.

The frequency of the LAM vibration arises from the all-*trans* chain lengths that are present in the lamellae. As indicated in the previous Chapter, this chain length may be calculated using the relationship $\nu_m = (m/2L_{LAM})(E/\rho)^{1/2}$, where ν_m is the vibrational frequency of the LAM mode; m is the order of the vibration; L_{LAM} is the length of the vibrating chain; E is the Young's modulus; and ρ is the density of the material. This relationship has been developed for n-alkanes and PE. [27-40, 73, 80-82, 89] The carbon number chain length equivalent of the crystalline core thickness, n_{LAM}, may then be calculated using the first-order LAM (L_{LAM}) and the equation may be rewritten as $n_{LAM} = 2489.4/\nu_1$ by substituting the parameters obtained from the literature. [13]

Low-frequency Raman provides an only semi-quantitative means of measuring lamellar thickness as it is documented that the technique may underestimate the lamellar core thickness. The LAM-derived thickness may be smaller than the actual crystal thickness as the Raman measurement considers only the crystalline portion of the crystal and not the amorphous contribution in the interlamellar regions. A departure from an exact integer relationship of actual chain length to measured lamellar thickness may be attributed to the interference of amorphous material. [70] There may also be an error in this correlation due to the chains not being perpendicular to the lamellar plane. [25, 27] The quantitative uncertainties in using the LAM to determine the chain length, however, may be overshadowed by the other benefits of the technique, such as its ability to detect multiple lamellar thicknesses independently from the lamellar stacking arrangement. [25]

A relationship has been established between the Raman and DSC data of ultra-long n-alkanes in one of the very few articles correlating DSC melting phenomena to crystalline behaviour other than polymorphism in a material. [13] These data showed that melting bimodality is due to the manifestation of chain folding behaviour, which is not helpful for solving the FT hard wax multiple melt peak problem. The onset of chain folding was given to be C_{150} in these materials. Various other onset fold lengths are also given in the literature for other types of materials, such as single or binary mixtures of n-alkanes and polymers. [12, 18, 40, 71] The lowest fold length identified by Raman analysis in these samples was found to be C_{65}. [13]

DSC melt bimodality has been observed in a relatively narrow MW polybutadiene sample. The reference claims that the bimodality is due to the presence of two crystallite-size distributions, but this is not supported with LAM data. The article does, however, use low-frequency Raman analysis to investigate the lamellar structure of a high molecular weight polyethylene sample (M_w = 166,000). [30]

Once it has been established that the peaks in the low-frequency Raman spectra are all due to first-order LAM modes, it may be inferred that multiple LAMs are indicative of fractionation in the sample. This fractionation results from rejection of the lower MW portion of the sample. [27] The different species in polydisperse polymers crystallise at different stages (related to a specific crystallisation temperature or time). The high molecular weight (HMW) material crystallises first, rejecting the low molecular weight

(LMW) material. The HMW material therefore forms separate crystalline lamellae, resulting in molecular weight segregation. [65]

In general, the crystalline length or lamellar thickness determines the material melting point. [65, 70] This correlates to the fold length in the FC conformation or the chain length in the EC conformation.

5.2 CORRELATING DSC MELT PEAKS WITH A CHAIN LENGTH

The question is: can the average material chain lengths represented by the DSC melting peak temperatures be correlated with the lamellar sizes derived from the LAM peaks of the sample? In order to do this, the DSC melt peak temperature would need to be correlated to a representative carbon chain length. If it is assumed that the DSC melting peaks of the waxes studied are representative of an average melting point of a distribution of n-alkanes, then it could be possible to correlate the melting temperature to the equivalent average carbon number of this distribution.

According to the literature, the Won and Broadhurst models may be used to calculate the fusion temperatures of petroleum waxes. [100] Won has suggested the following relationships for determining the melting points of n-alkanes: M≤ 450: T_f = 374.5+ 0.0261M - (20172/M) and M>450: T_f = 411.44 – (32326/M), where M is the molecular weight of the component and T_f is the fusion temperature in Kelvin. [100]

The Broadhurst equation is as follows: $T_f = a + bC_n + cC_n^2 + d/C_n + e/C_n^2 + f \ln(C_n)$, where C_n is the carbon number and coefficients *a*, *b*, *c*, *d*, *e* and *f* are listed in Table 5.1. The equation is valid for calculating the melting points of odd and even numbered n-alkanes from C_9 and C_4, respectively. Coefficient *e* is used to calculate melting points of iso-alkanes and naphthenes and is therefore not relevant to the n-alkanes. [100]

.

Table 5.1: Coefficients for the Broadhurst equation [100]

Carbon number	*a*	*b*	*c*	*d*	*e*	*f*
Even	-426.659	-16.560	0.1238	690.670	-	326.469
Odd	156.871	-2.086	0.01223	-775.598	-	76.219

The application of the Won and Broadhurst equations to calculate the melting points of the n-alkanes over a range that would be present in the waxes studied yielded the results shown in Table 5.2 on the next page.

The data in Table 5.2 show good correlation between the fusion temperatures predicted by the two models for the even-numbered n-alkanes up to ca. C_{62}. The Broadhurst data for the even-numbered chains start to deviate from this point, obviously not accurately accounting for the expected flattening of the melting point as the chain length of the molecule increases. There is good correlation between the Broadhurst data for the odd-numbered chain lengths and the Won model in general, while the data for the even-numbered chain lengths > C_{62} seem to be overestimated by Broadhurst. At higher carbon numbers, the Broadhurst data do not make sense! This was tested by comparing the modeled data with actual n-alkane melting points. [101] These are plotted along with data derived from the Won and Broadhurst models in Figure 5.1 and are also shown in Table 5.3.

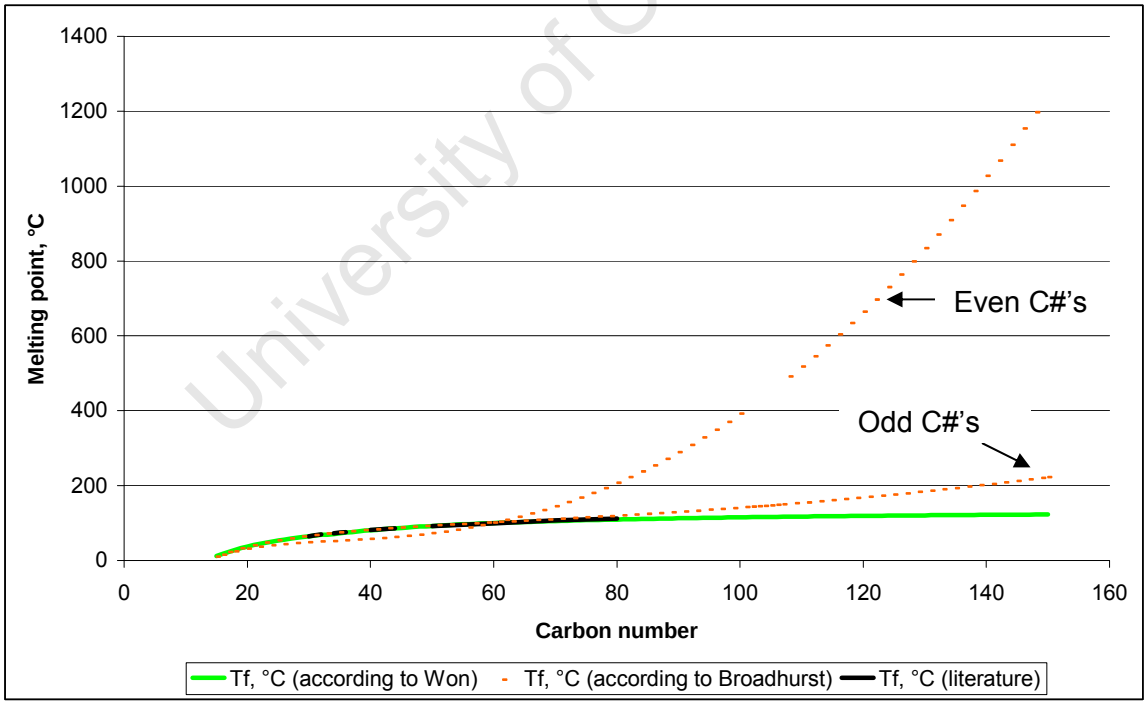

Figure 5.1: Comparison of actual n-alkane melting points with data derived from the Won and Broadhurst equations

Table 5.2: Melting points of a range of n-alkanes calculated using the Won and Broadhurst equations

C#	Mol. Mass	T_f, °C (according to Won)	T_f, °C (according to Broadhurst)	C#	Mol. Mass	T_f, °C (according to Won)	T_f, °C (according to Broadhurst)	C#	Mol. Mass	T_f, °C (according to Won)	T_f, °C (according to Broadhurst)
15	212	11.9	10.0	61	856	100.7	102.7	107	1500	116.9	149.6
16	226	18.1	15.4	62	870	101.3	108.0	108	1514	117.1	490.8
17	240	23.7	22.3	63	884	101.9	104.5	109	1528	117.3	152.3
18	254	28.7	24.4	64	898	102.4	116.1	110	1542	117.5	517.6
19	268	33.2	32.3	65	912	103.0	106.2	111	1556	117.7	155.0
20	282	37.3	31.2	66	926	103.5	124.9	112	1570	117.9	545.2
21	296	41.1	40.6	67	940	104.1	107.9	113	1584	118.0	157.8
22	310	44.5	36.5	68	954	104.6	134.4	114	1598	118.2	573.7
23	324	47.7	47.6	69	968	105.0	109.6	115	1612	118.4	160.6
24	338	50.6	40.5	70	982	105.5	144.6	116	1626	118.6	603.1
25	352	53.4	53.7	71	996	106.0	111.4	117	1640	118.7	163.6
26	366	55.9	43.7	72	1010	106.4	155.6	118	1654	118.9	633.4
27	380	58.3	58.9	73	1024	106.9	113.2	119	1668	119.1	166.6
28	394	60.6	46.2	74	1038	107.3	167.3	120	1682	119.2	664.6
29	408	62.7	63.6	75	1052	107.7	114.9	121	1696	119.4	169.6
30	422	64.7	48.4	76	1066	108.1	179.8	122	1710	119.5	696.7
31	436	66.6	67.7	77	1080	108.5	116.8	123	1724	119.7	172.8
32	450	68.4	50.2	78	1094	108.9	193.0	124	1738	119.8	729.7
33	464	68.8	71.3	79	1108	109.3	118.6	125	1752	120.0	176.0
34	478	70.8	52.0	80	1122	109.6	207.1	126	1766	120.1	763.6
35	492	72.7	74.7	81	1136	110.0	120.5	127	1780	120.3	179.3
36	506	74.6	53.7	82	1150	110.3	221.9	128	1794	120.4	798.4
37	520	76.3	77.7	83	1164	110.7	122.4	129	1808	120.6	182.7
38	534	77.9	55.6	84	1178	111.0	237.6	130	1822	120.7	834.2
39	548	79.5	80.5	85	1192	111.3	124.4	131	1836	120.8	186.1
40	562	80.9	57.6	86	1206	111.6	254.0	132	1850	121.0	870.8
41	576	82.3	83.0	87	1220	111.9	126.4	133	1864	121.1	189.7
42	590	83.7	59.9	88	1234	112.2	271.3	134	1878	121.2	908.4
43	604	84.9	85.4	89	1248	112.5	128.5	135	1892	121.4	193.3
44	618	86.1	62.5	90	1262	112.8	289.4	136	1906	121.5	946.9
45	632	87.3	87.7	91	1276	113.1	130.6	137	1920	121.6	197.0
46	646	88.4	65.5	92	1290	113.4	308.4	138	1934	121.7	986.3
47	660	89.5	89.8	93	1304	113.7	132.8	139	1948	121.8	200.7
48	674	90.5	68.9	94	1318	113.9	328.2	140	1962	122.0	1026.6
49	688	91.5	91.8	95	1332	114.2	135.0	141	1976	122.1	204.6
50	702	92.4	72.8	96	1346	114.4	348.8	142	1990	122.2	1067.9
51	716	93.3	93.8	97	1360	114.7	137.3	143	2004	122.3	208.5
52	730	94.2	77.2	98	1374	114.9	370.3	144	2018	122.4	1110.1
53	744	95.0	95.6	99	1388	115.2	139.6	145	2032	122.5	212.5
54	758	95.8	82.2	100	1402	115.4	392.7	146	2046	122.6	1153.2
55	772	96.6	97.5	101	1416	115.6	142.0	147	2060	122.7	216.6
56	786	97.3	87.7	102	1430	115.8	143.2	148	2074	122.9	1197.3
57	800	98.0	99.3	103	1444	116.1	144.5	149	2088	123.0	220.8
58	814	98.7	93.8	104	1458	116.3	145.7	150	2102	123.1	1242.3
59	828	99.4	101.0	105	1472	116.5	147.0				
60	842	100.0	100.6	106	1486	116.7	148.3				

Table 5.3: Comparison of the melting points of some n-alkanes calculated using the Won and Broadhurst equations with literature data [101]

Carbon number	Molecular weight	T_f, °C (according to Won)	T_f, °C (according to Broadhurst)	T_f, °C (literature)
30	422	64.7	48.4	65.1
31	436	66.6	67.7	67.9
32	450	68.4	50.2	69.4
34	478	70.8	52.0	72.5
35	492	72.7	74.7	74.6
36	506	74.6	53.7	75.8
40	562	80.9	57.6	81.5
44	618	86.1	62.5	85.6
50	702	92.4	72.8	92.1
60	842	100.0	100.6	99.3
70	982	105.5	144.6	107.0
80	1122	109.6	207.1	112.0

This shows that the actual data lies along the Won prediction up to C_{80}. The odd-even influence on the physical properties of the n-alkanes is well known, but obviously not adequately modelled with the Broadhurst equation. [45] For this reason, further discussion will consider the Won model only.

The Won model was used to predict the average carbon number represented by the DSC melt peak temperatures of the wax samples studied. These data are shown for a C_{32} n-alkane, selected FT waxes, their blends and fractions and some PE waxes in Table 5.4. The DSC first-melt data were used unless indicated otherwise in order to ensure that the thermal histories of the samples were equivalent to those used for the low-frequency Raman measurements. Table 5.4 therefore shows a Won-model derived carbon number for each of the DSC melt peaks that were measured for a specific sample.

Shell Sarawax SX-105 is a product of Shell MDS. The origin of the other waxes is summarised in Chapter 2.

Table 5.4: Wax DSC melting peak data with corresponding carbon chain lengths derived from the Won model

Sample name	Wax type	DSC melt peak 1	Calc C#1 (Won)	DSC melt peak 2	Calc C#2 (Won)	DSC melt peak 3	Calc C#3 (Won)	DSC melt peak 4	Calc C#4 (Won)
n-C_{32}	n-alkane	69	33	-	-	-	-	-	-
C80	FT	60	28	83	42	85	43	-	-
H1	FT	83	42	100	60	107	73	-	-
C105	FT	98	57	108	76	110	81	-	-
90-C80/ 10-C105	FT	83	42	95	53	100	60	-	-
50-C80/ 50-C105	FT	84	42	104	67	107	73	-	-
C105 fraction F1*	FT	92	50	97	56	-	-	-	-
C105 fraction F2*	FT	102	63	109	78	90	47	-	-
C105 fraction F3*	FT	107	73	114	94	-	-	-	-
C105 fraction F4*	FT	107	73	116	103	-	-	-	-
SX-105	FT	66	31	86	44	104	67	113	91
Polywax 1000	PE	72	35	103	65	108	76	111	84
Polywax 2000	PE	99	58	124	160	-	-	-	-

***** second melt analyses

It was shown in Chapter 4 that low-frequency Raman analysis may be used to determine the lamellar thickness populations present in the samples studied and the average chain lengths that these LAM modes represent. [25, 27-40, 73, 80-82, 89] A summary of the calculated n_{LAM} values from their low-frequency Raman data for the samples shown in Table 5.4 is given in Table 5.5.

Table 5.5: Wax LAM-1 frequencies with corresponding derived carbon chain lengths (n_{LAM})

Sample name	ν 1	n_{LAM} 1	ν 2	n_{LAM} 2	ν 3	n_{LAM} 3
n-C_{32}	79	C32	-	-	-	-
C80	57	C44	-	-	-	-
H1	39	C64	54	C46	68	C37
C105	39	C83	43	C58		
90-C80/ 10-C105	36	C69	48	C52	57	C44
50-C80/ 50-C105	28	C89	40	C62	56	C44
C105 fraction F1	45	C55	-	-	-	-
C105 fraction F2	34	C73	37	C67	40	C61
C105 fraction F3	35	C71	-	-	-	-
C105 fraction F4	28	C89	37	C67	48	C52
SX-105	27	C92	40	C62	51	C49
Polywax 1000	29	C86	35	C71	-	-
Polywax 2000	15	C166	-	-	-	-

5.3 CORRELATING CRYSTALLINE CORE THICKNESS WITH DSC DATA

Figures 5.2 to 5.27 compare the low-frequency Raman and DSC analyses for n-C_{32}, and all the wax samples. The equivalent carbon numbers represented by the LAM modes and DSC melt peaks are indicated on each plot. The low-frequency Raman data for the wax samples show both raw and Boltzmann-corrected spectra.

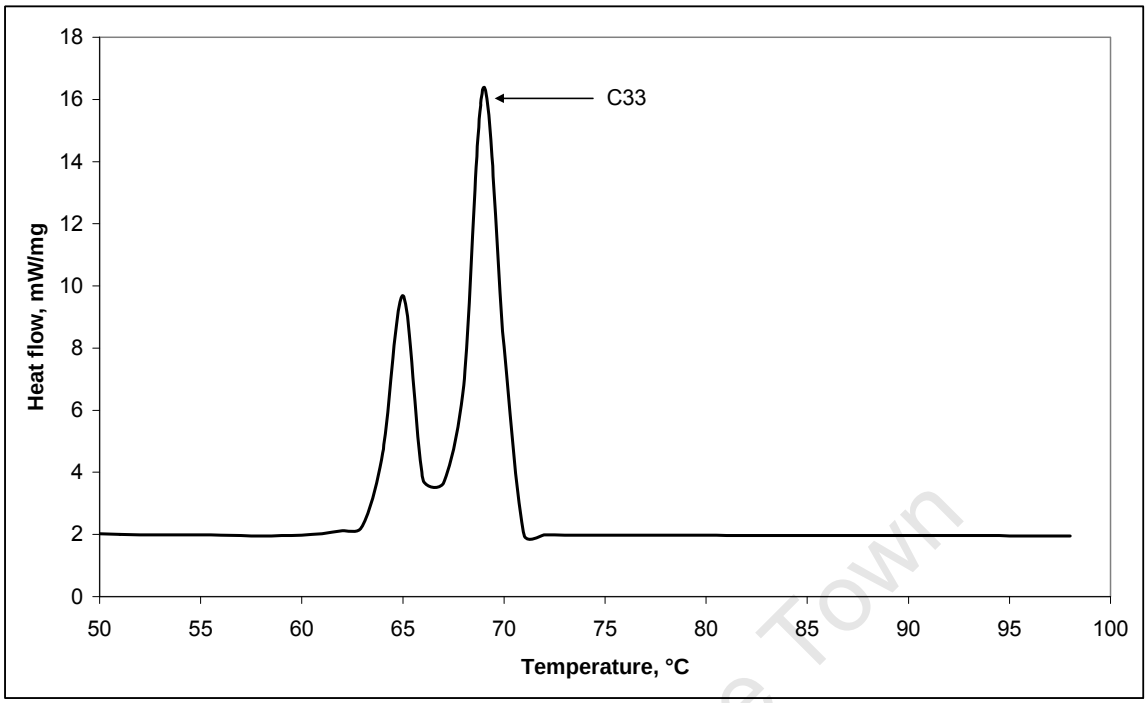

Figure 5.2: DSC analysis of n-C_{32}

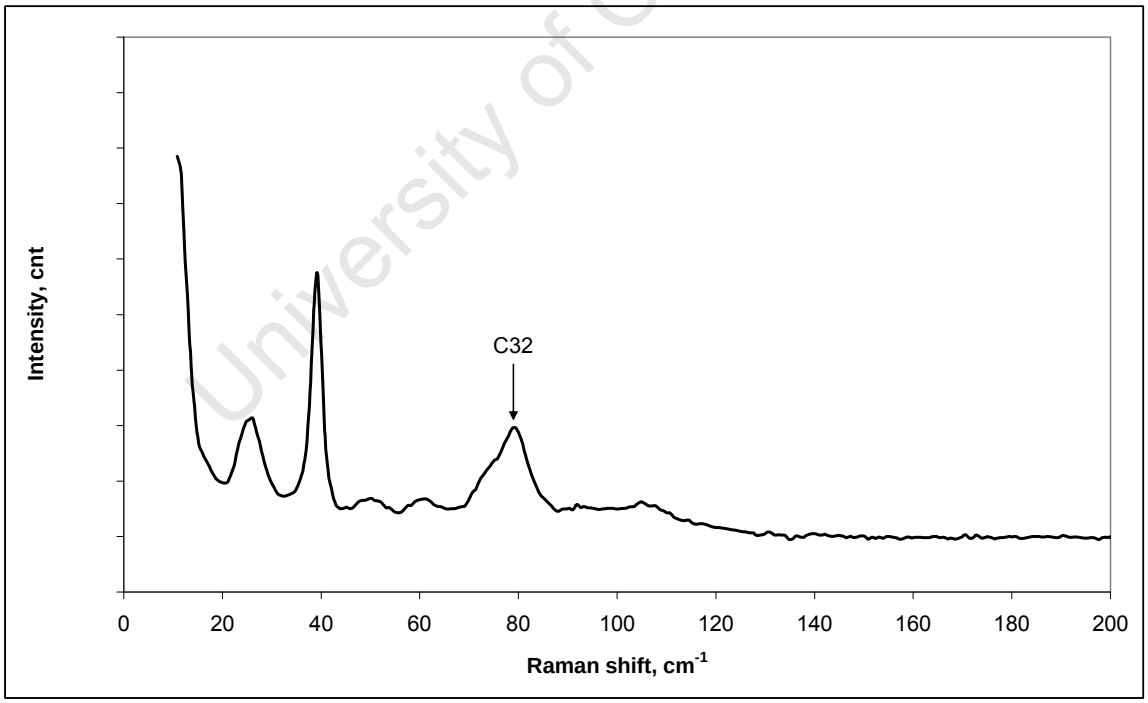

Figure 5.3: Low-frequency Raman spectrum of n-C_{32}

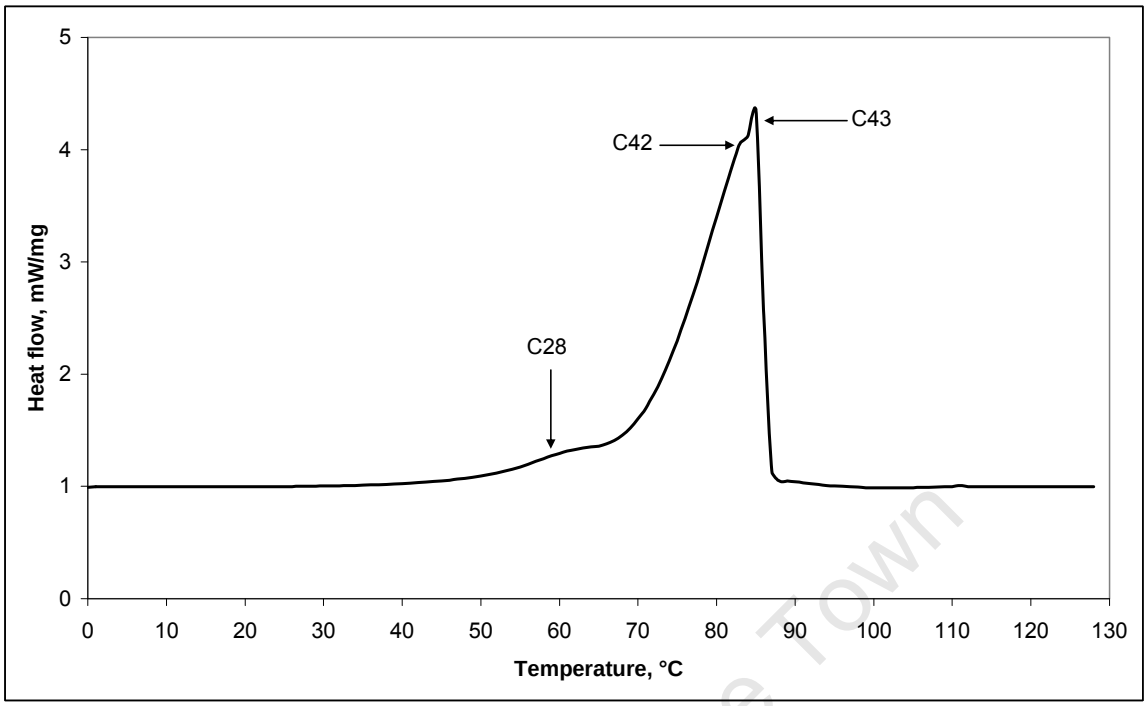

Figure 5.4: DSC analysis of Sasolwax C80

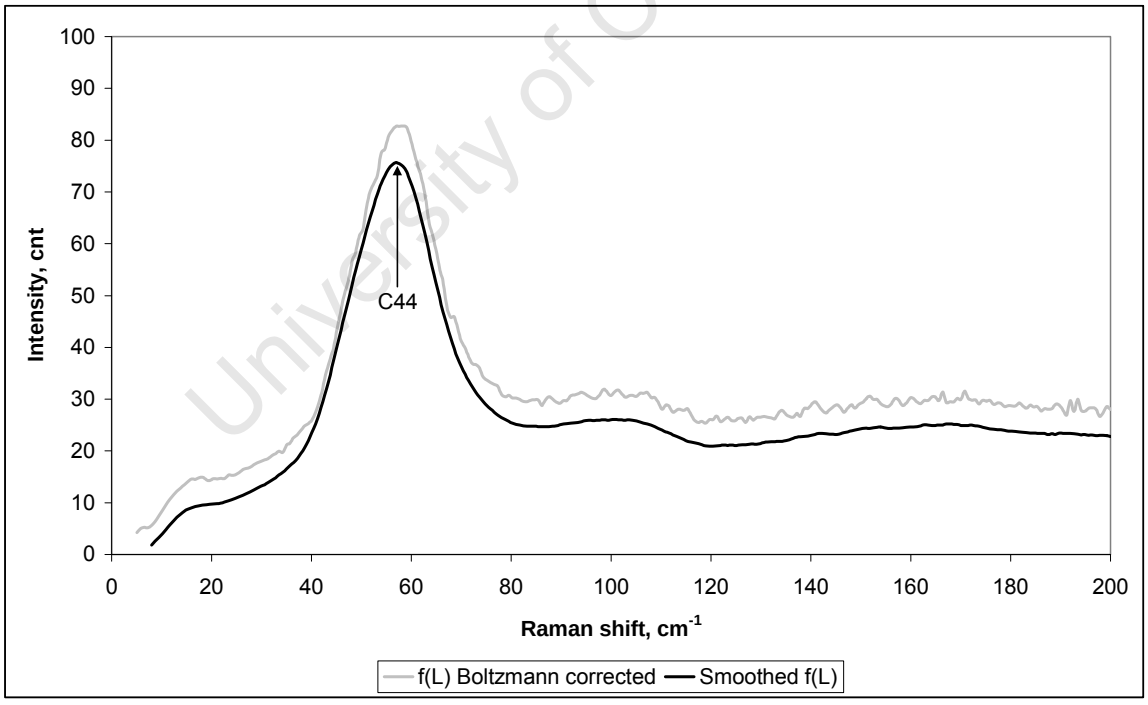

Figure 5.5: Boltzmann-corrected low-frequency Raman spectrum for Sasolwax C80

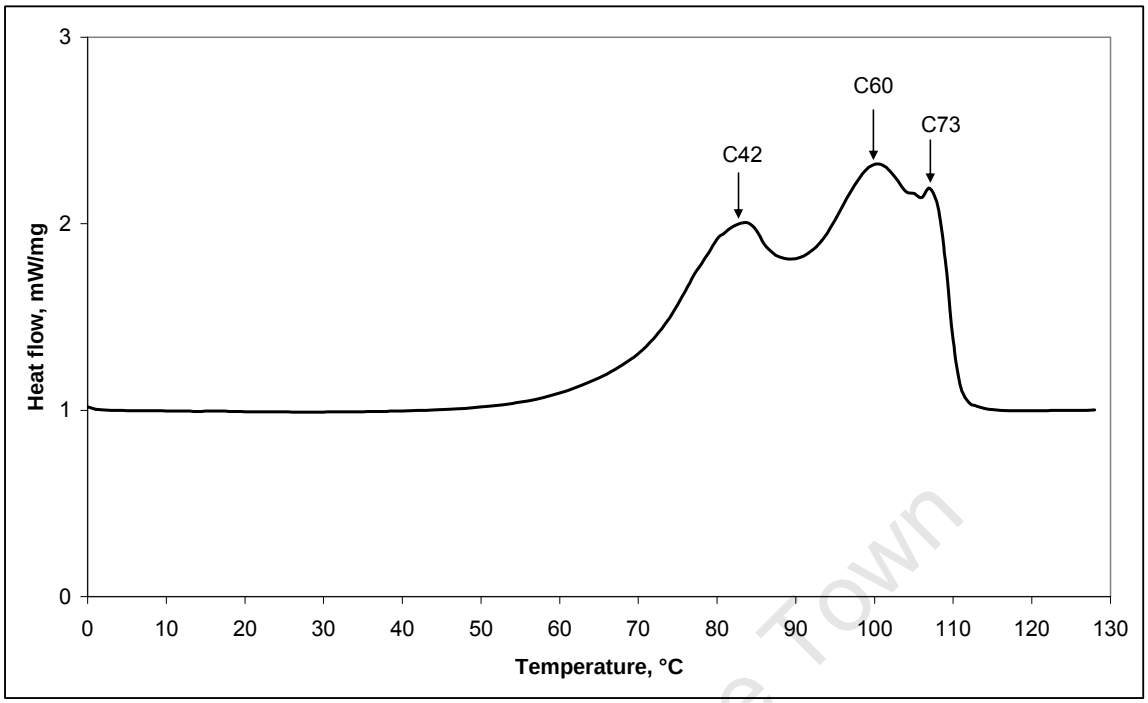

Figure 5.6: DSC analysis of Sasolwax H1

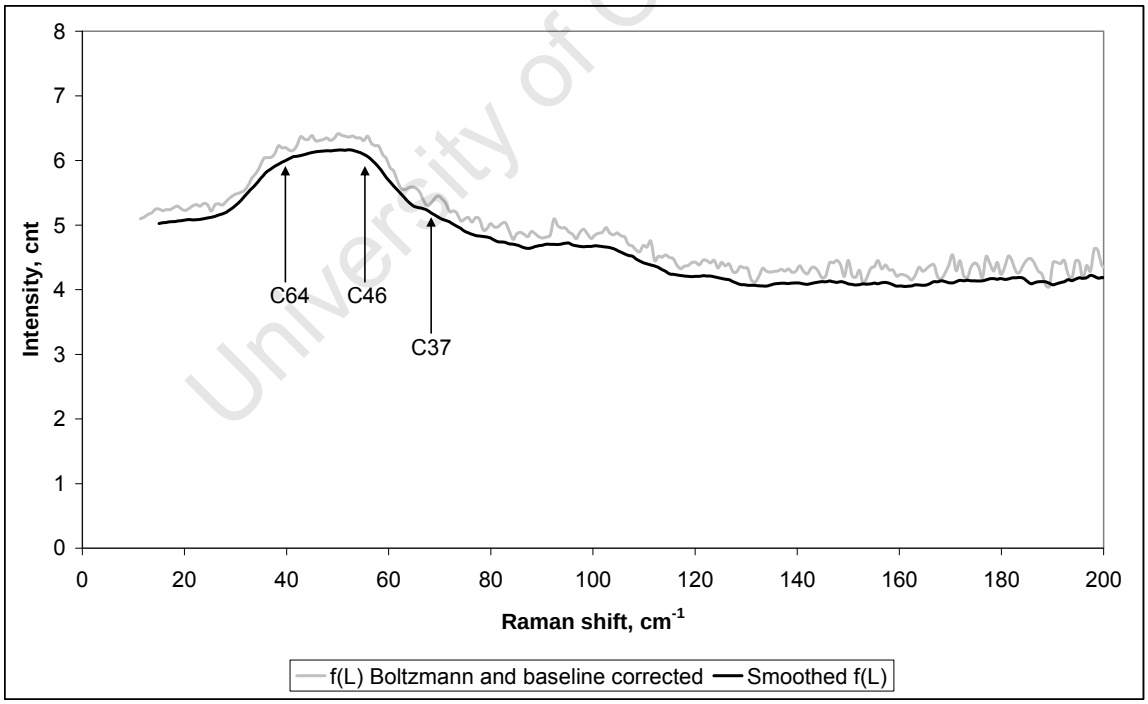

Figure 5.7: Boltzmann-corrected low-frequency Raman spectrum for Sasolwax H1

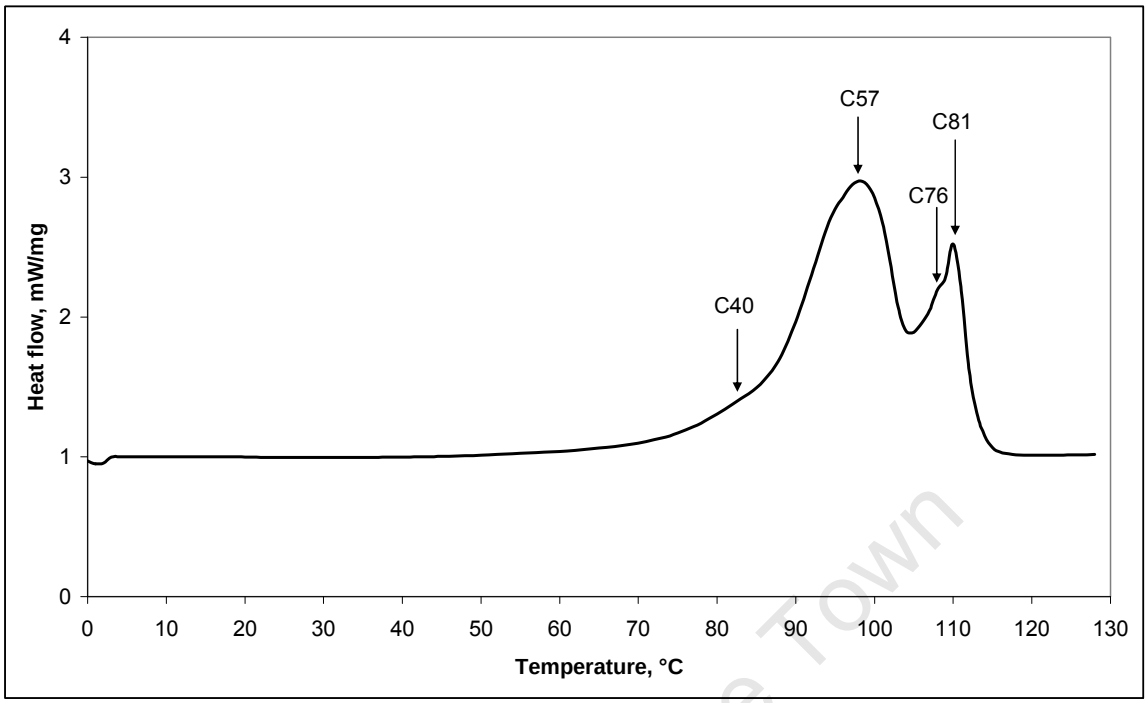

Figure 5.8: DSC analysis of Sasolwax C105

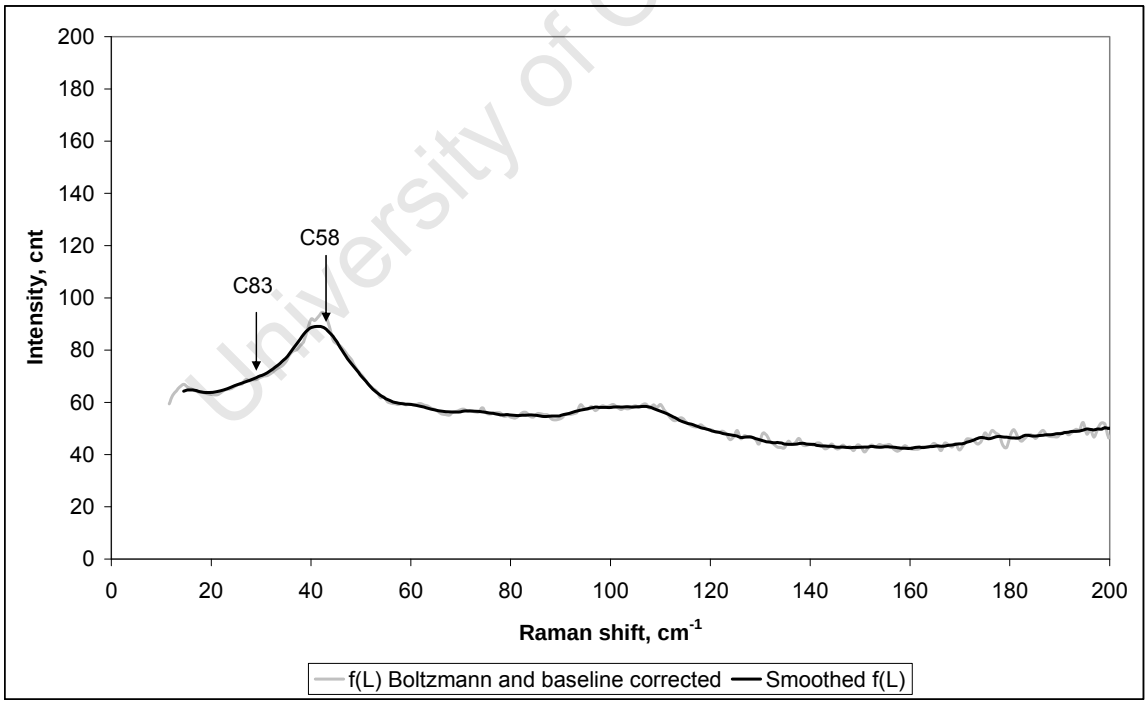

Figure 5.9: Boltzmann-corrected low-frequency Raman spectrum for Sasolwax C105

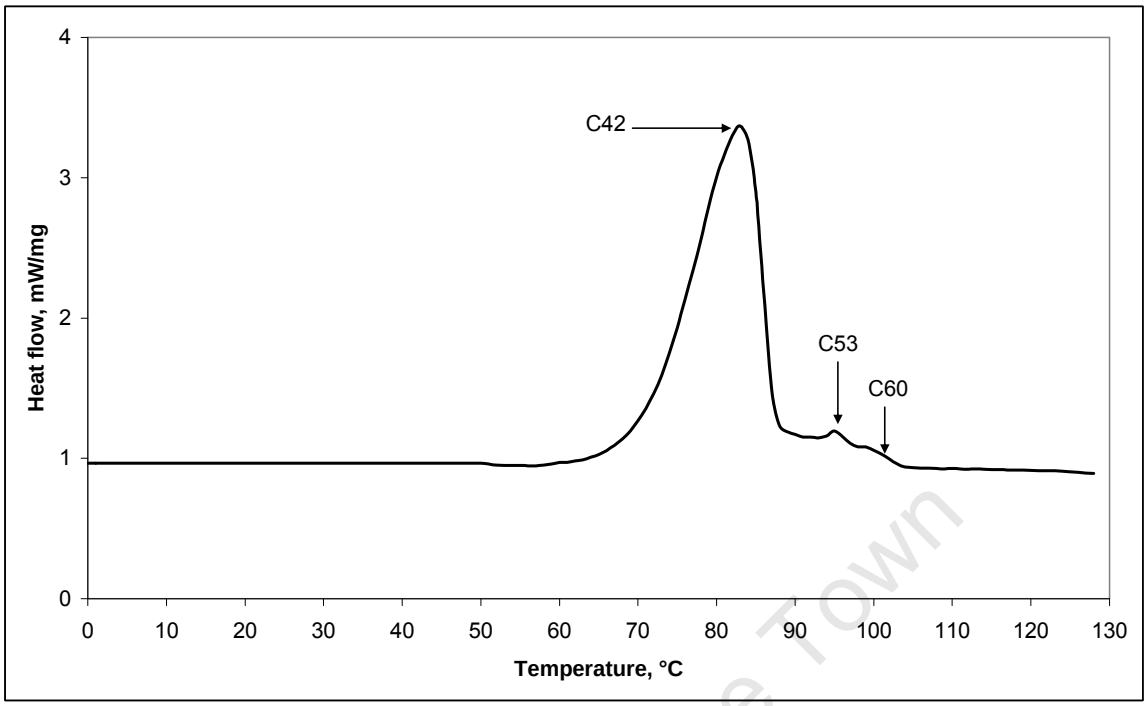

Figure 5.10: DSC analysis of 90-C80/ 10-C105

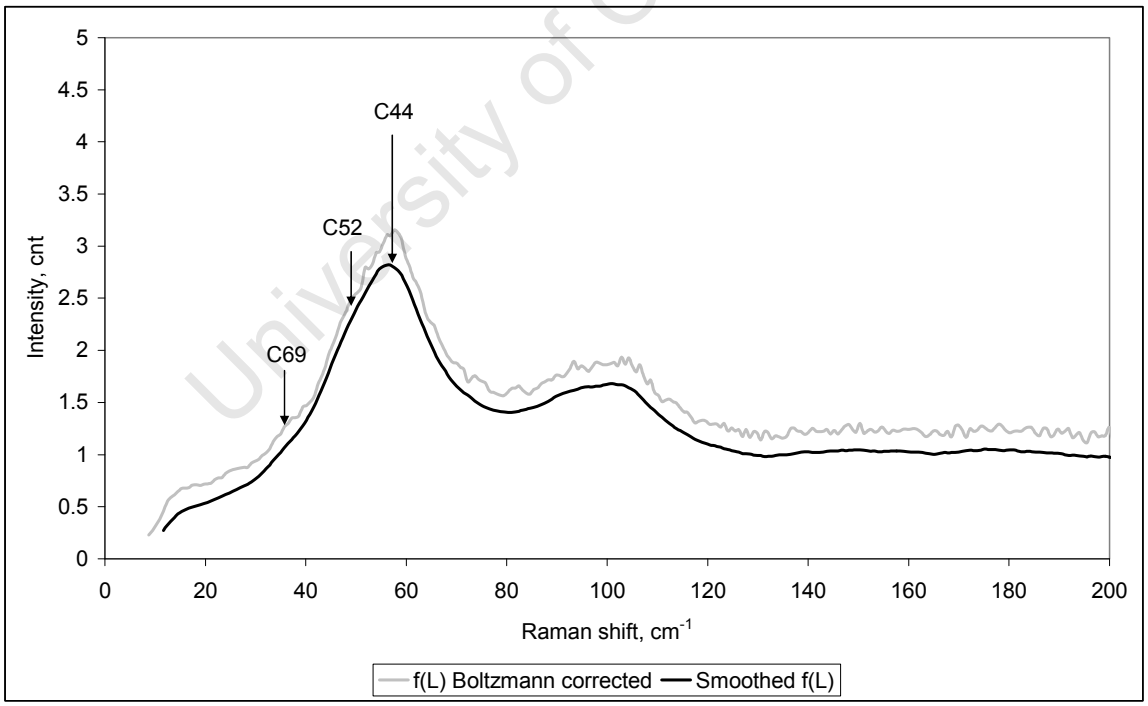

Figure 5.11: Boltzmann-corrected low-frequency Raman spectrum for 90-C80/ 10-C105

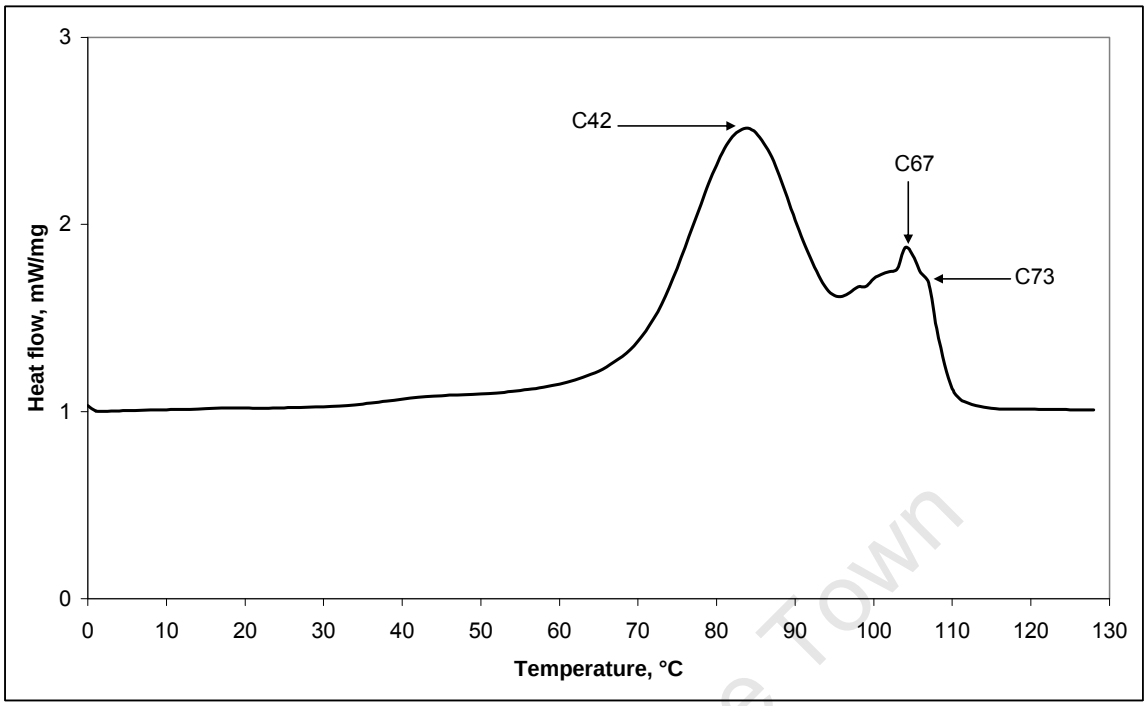

Figure 5.12: DSC analysis of 50-C80/ 50-C105

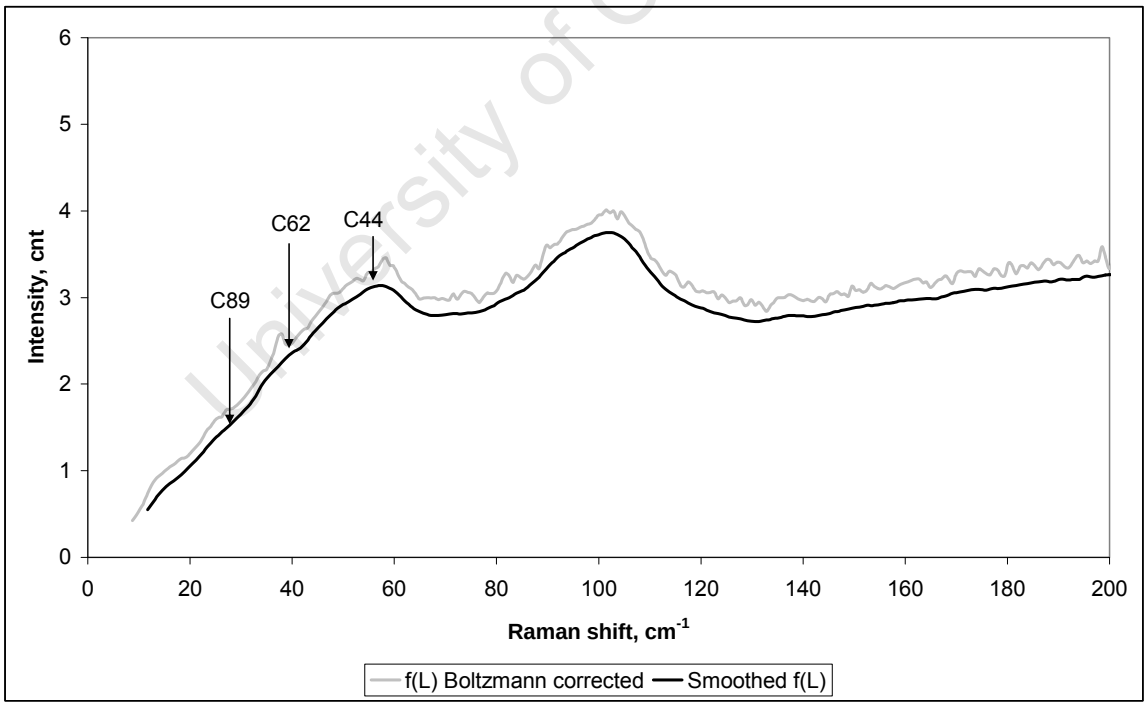

Figure 5.13: Boltzmann-corrected low-frequency Raman spectra for 50-C80/ 50-C105

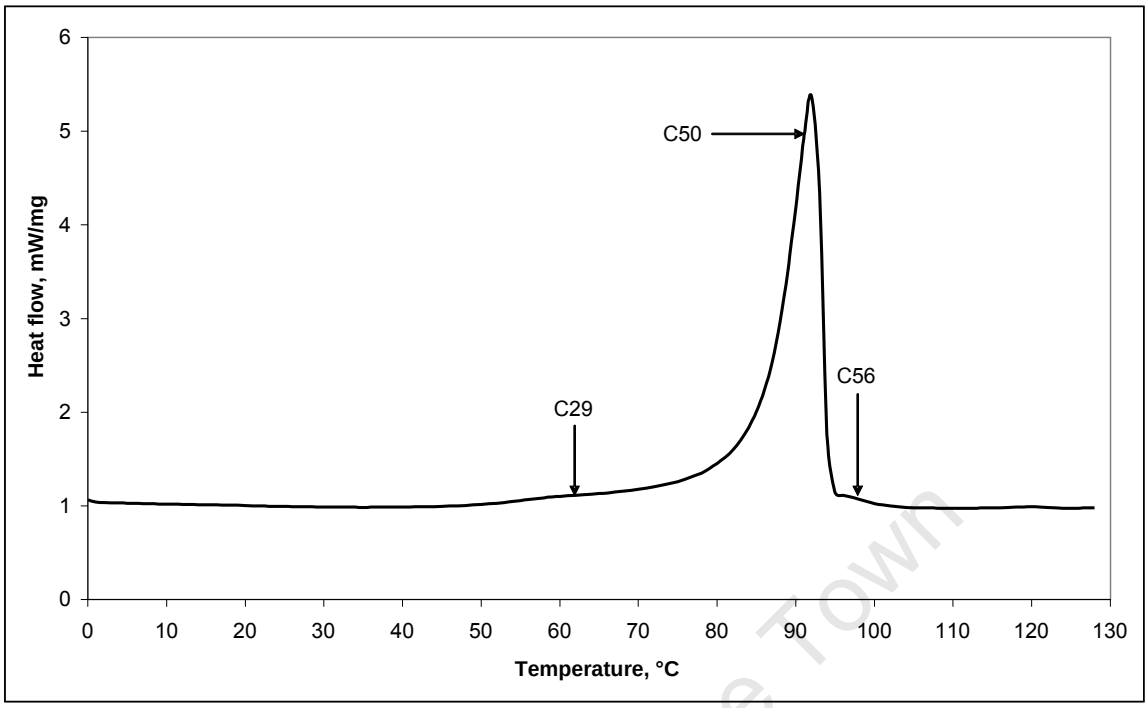

Figure 5.14: DSC analysis of Sasolwax C105 fraction F1

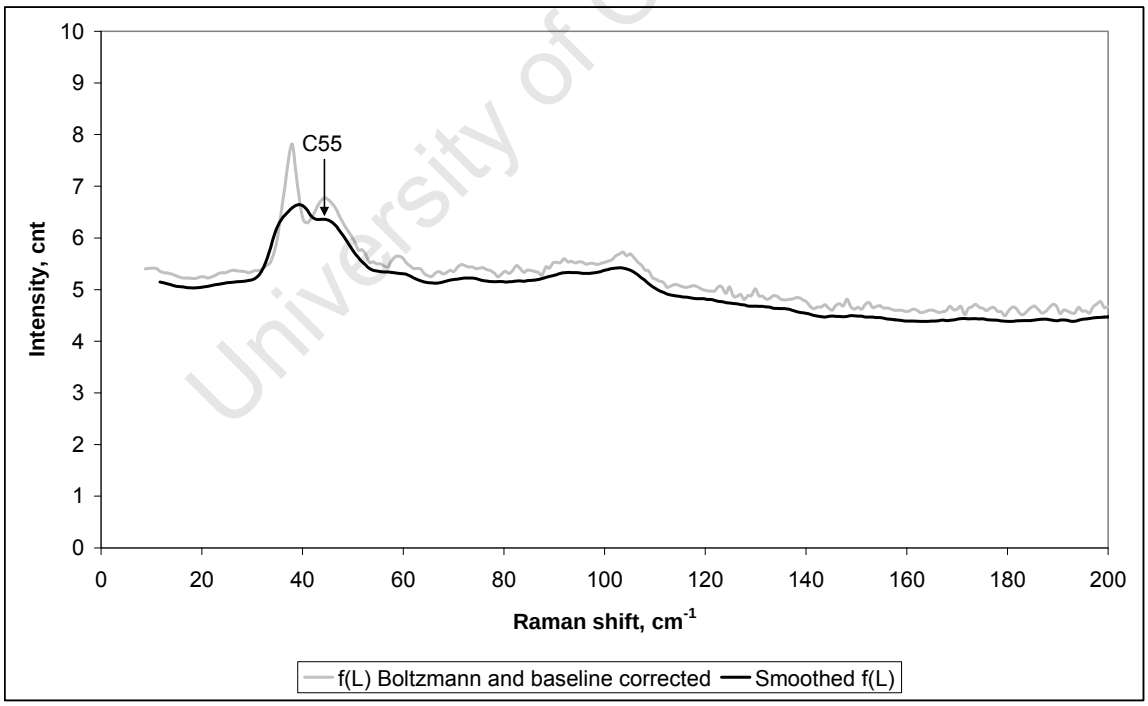

Figure 5.15: Boltzmann-corrected low-frequency Raman spectrum for Sasolwax C105 fraction F1

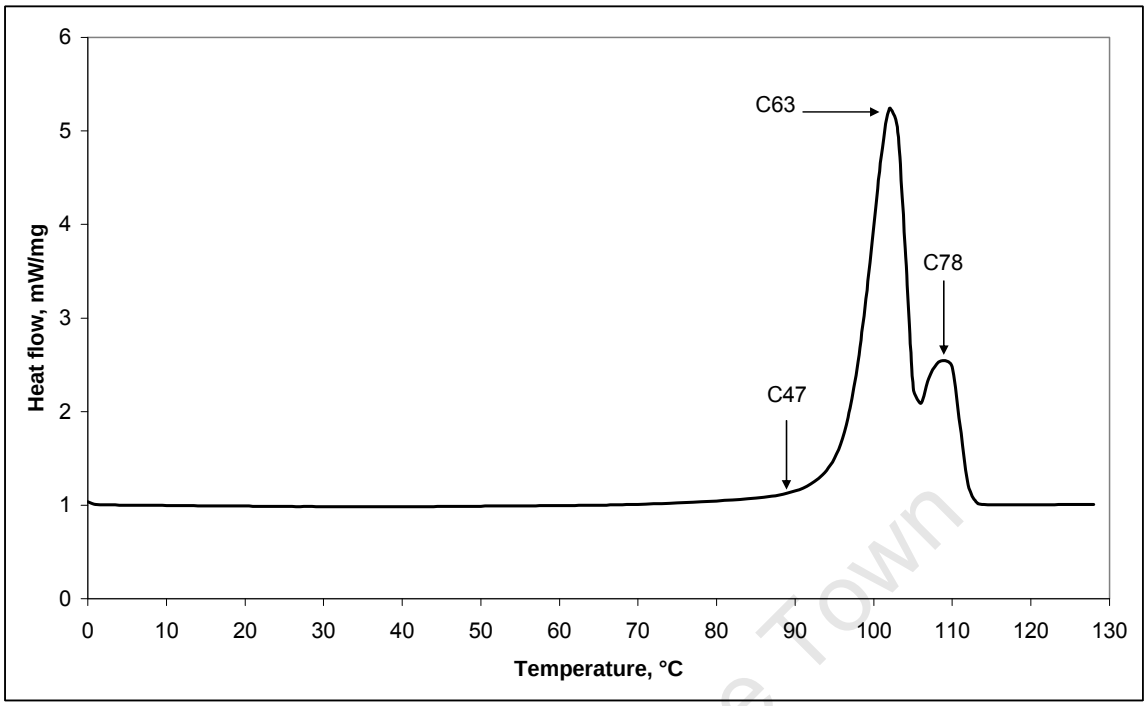

Figure 5.16: DSC analysis of Sasolwax C105 fraction F2

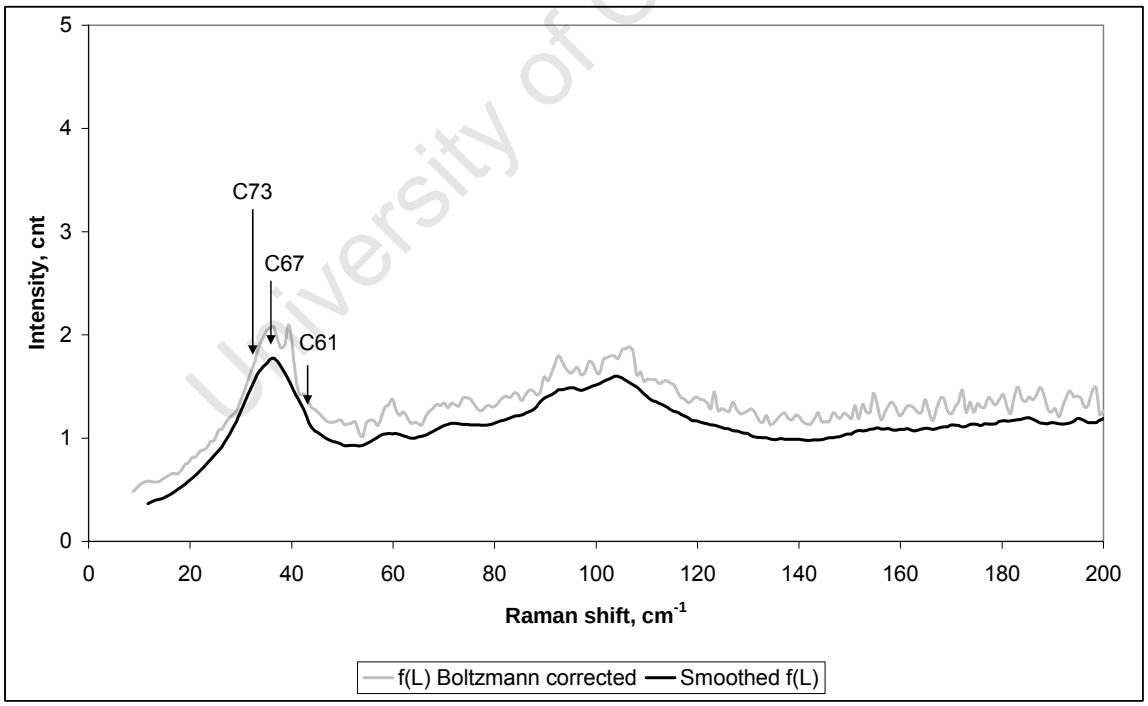

Figure 5.17: Boltzmann-corrected low-frequency Raman spectrum for Sasolwax C105 fraction F2

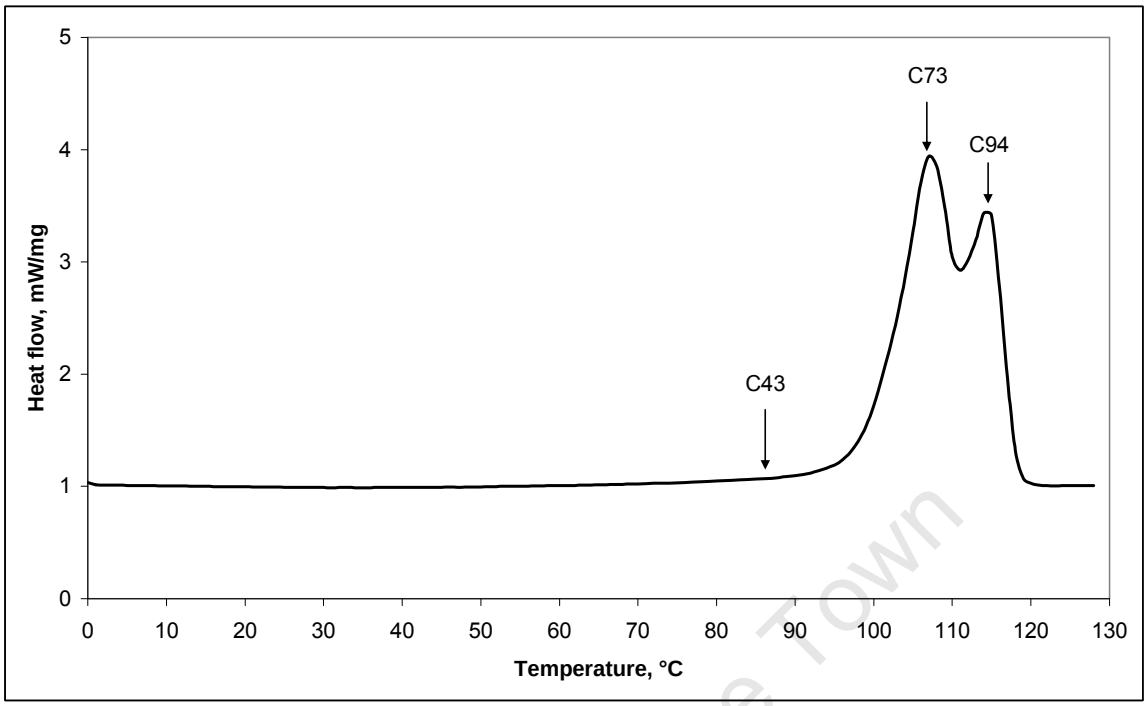

Figure 5.18: DSC analysis of Sasolwax C105 fraction F3

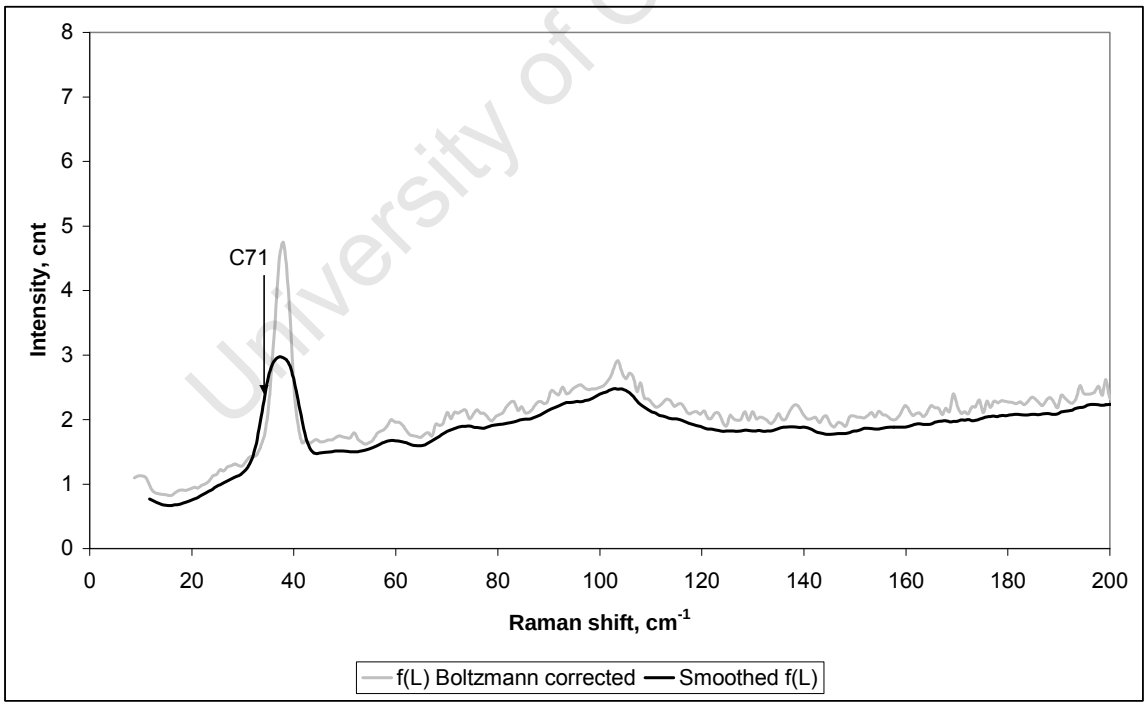

Figure 5.19: Boltzmann-corrected low-frequency Raman spectrum for Sasolwax C105 fraction F3

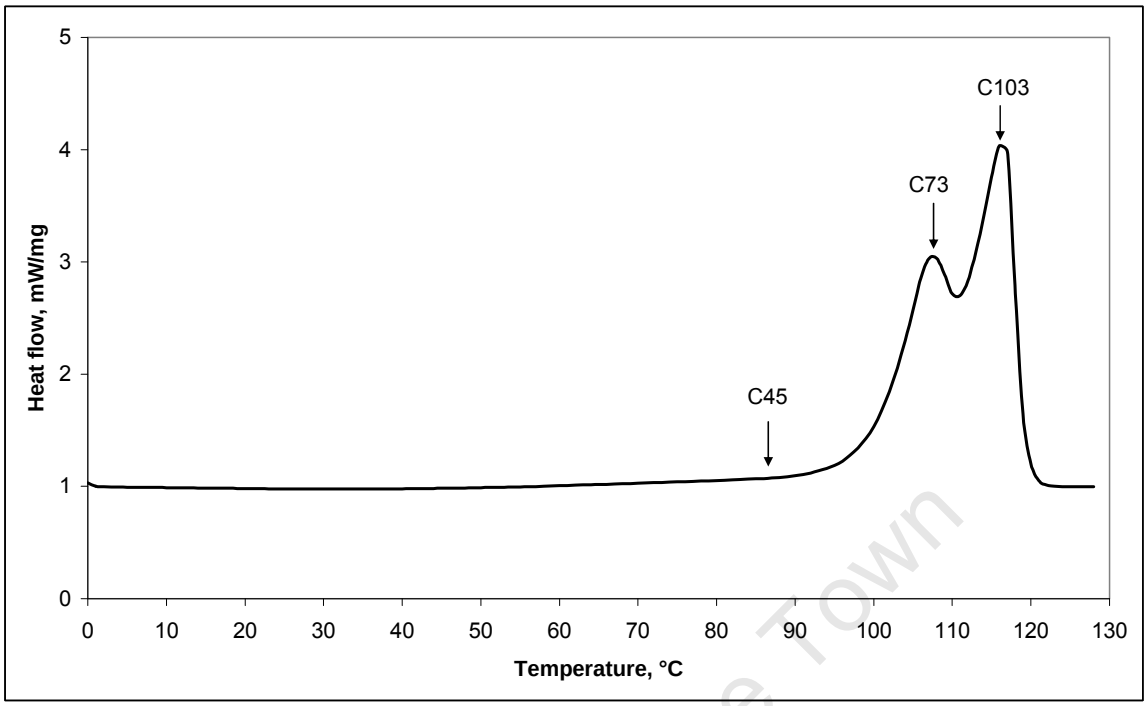

Figure 5.20: DSC analysis of Sasolwax C105 fraction F4

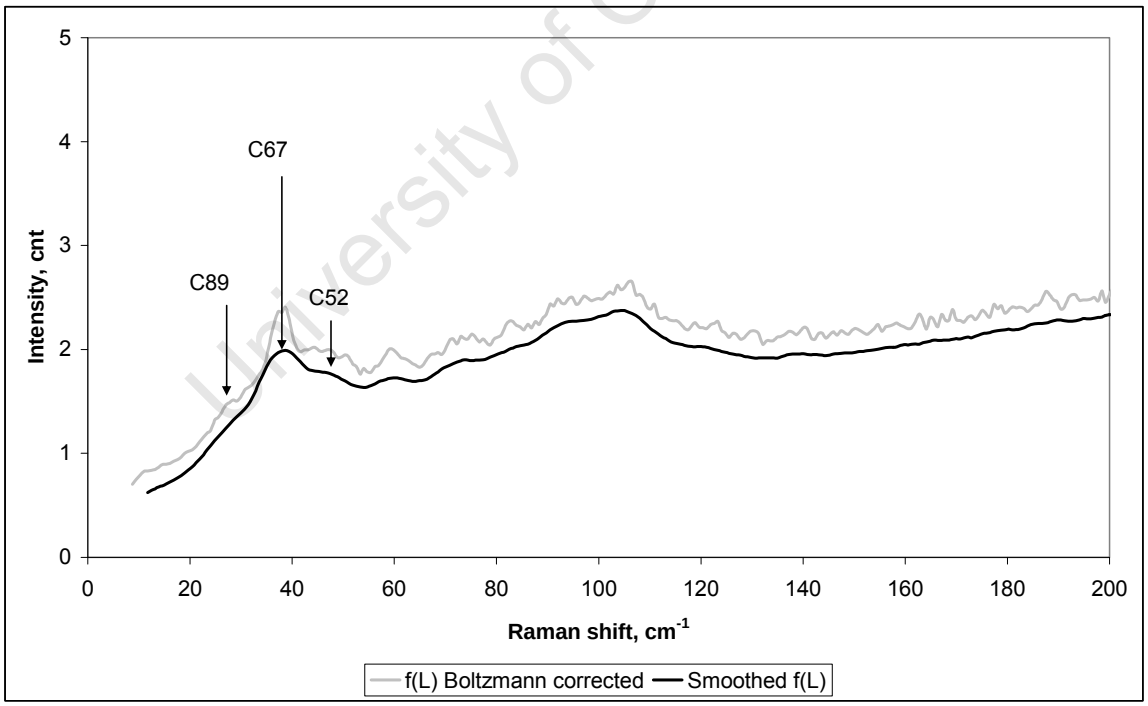

Figure 5.21: Boltzmann-corrected low-frequency Raman spectrum for Sasolwax C105 fraction F4

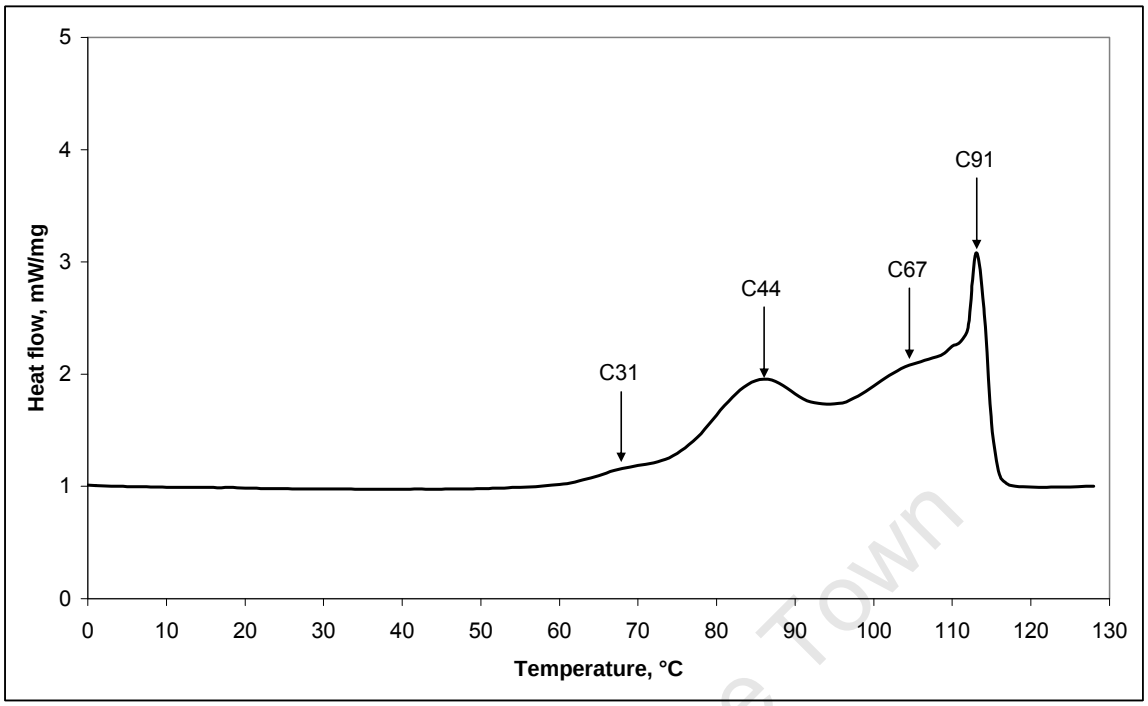

Figure 5.22: DSC analysis of SX-105

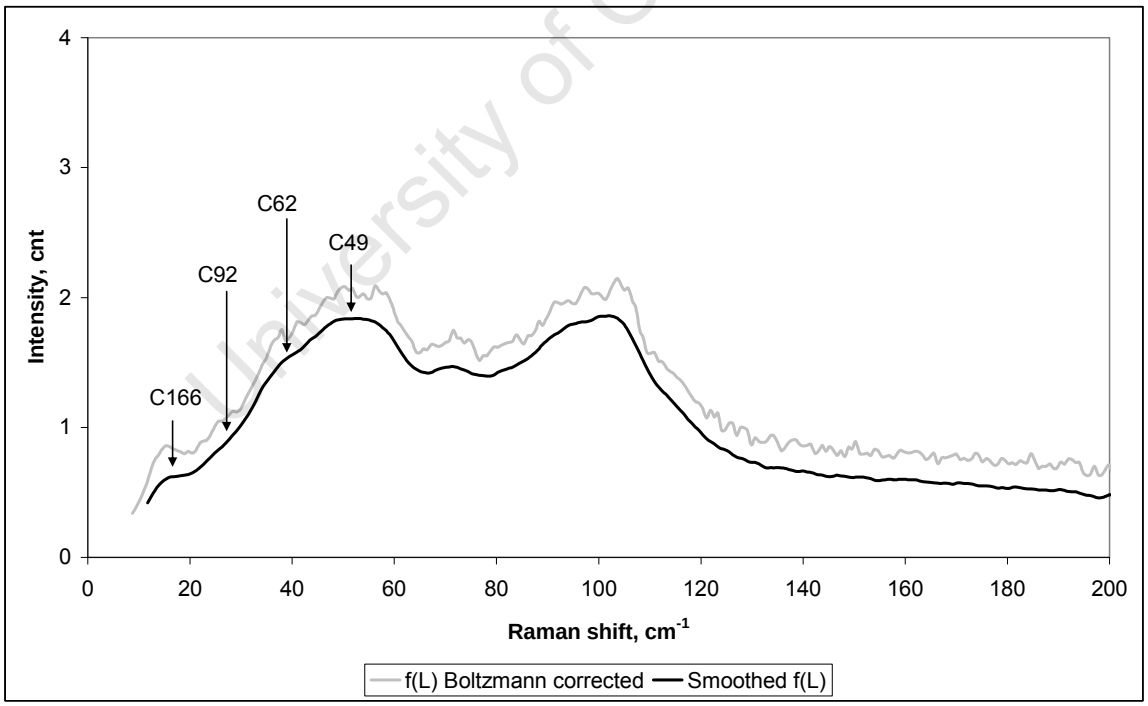

Figure 5.23: Boltzmann-corrected low-frequency Raman spectrum for SX-105

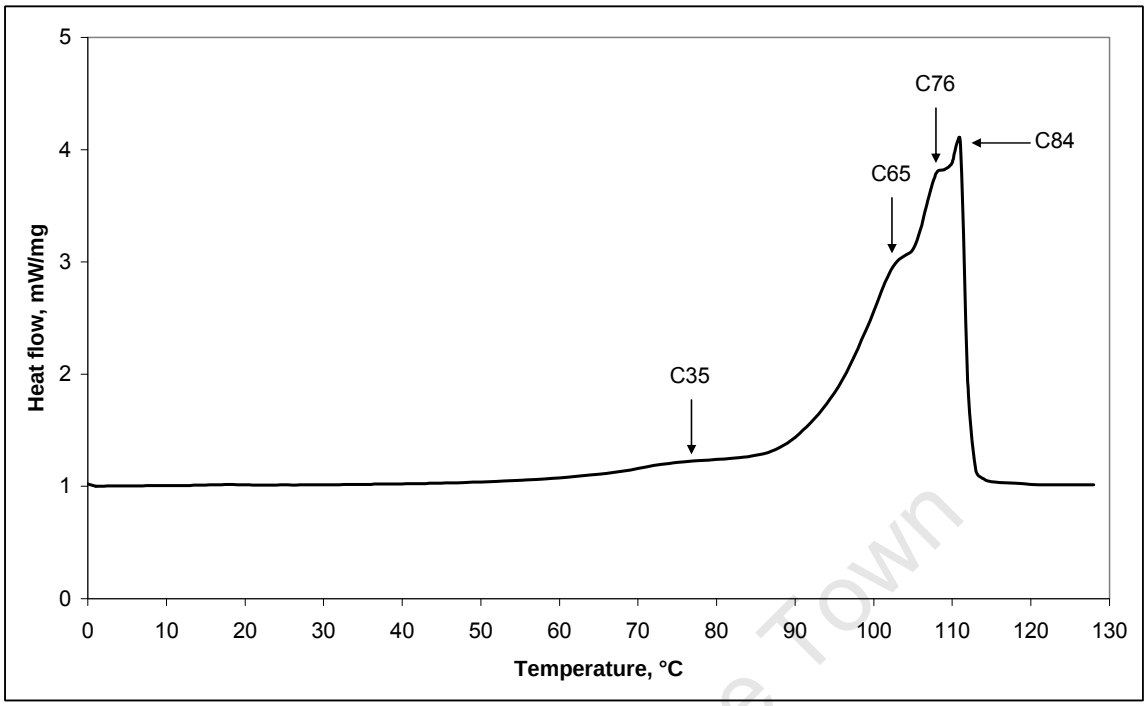

Figure 5.24: DSC analysis of Polywax 1000

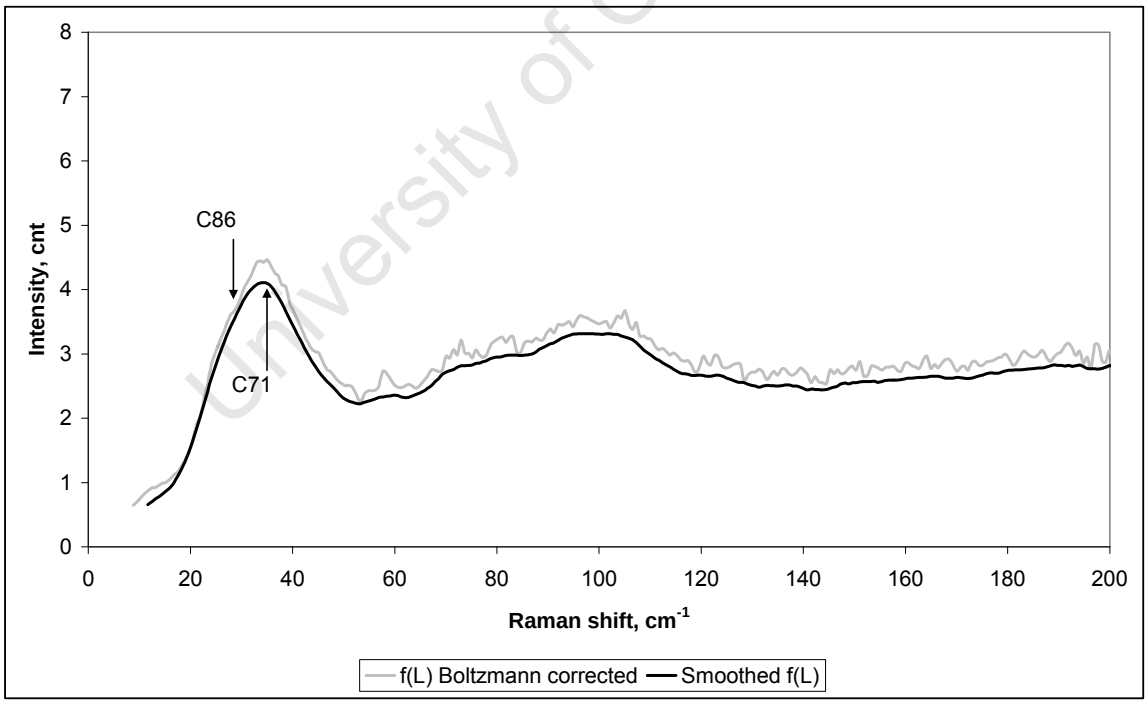

Figure 5.25: Boltzmann-corrected low-frequency Raman spectrum for Polywax 1000

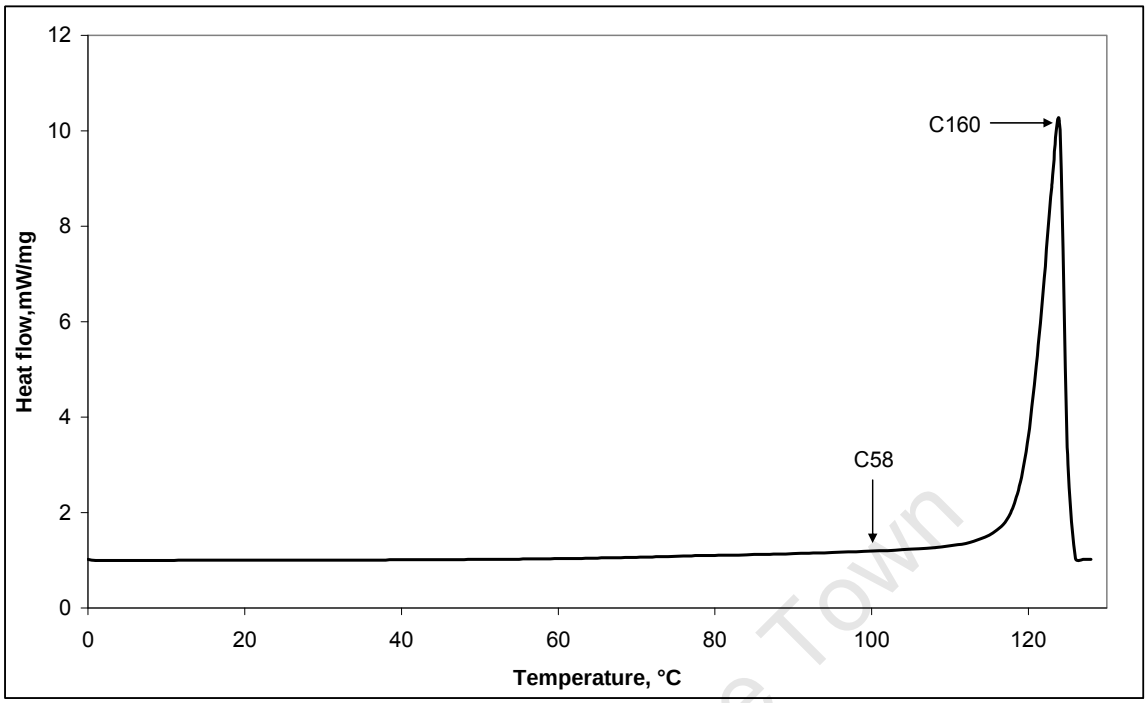

Figure 5.26: DSC analysis of Polywax 2000

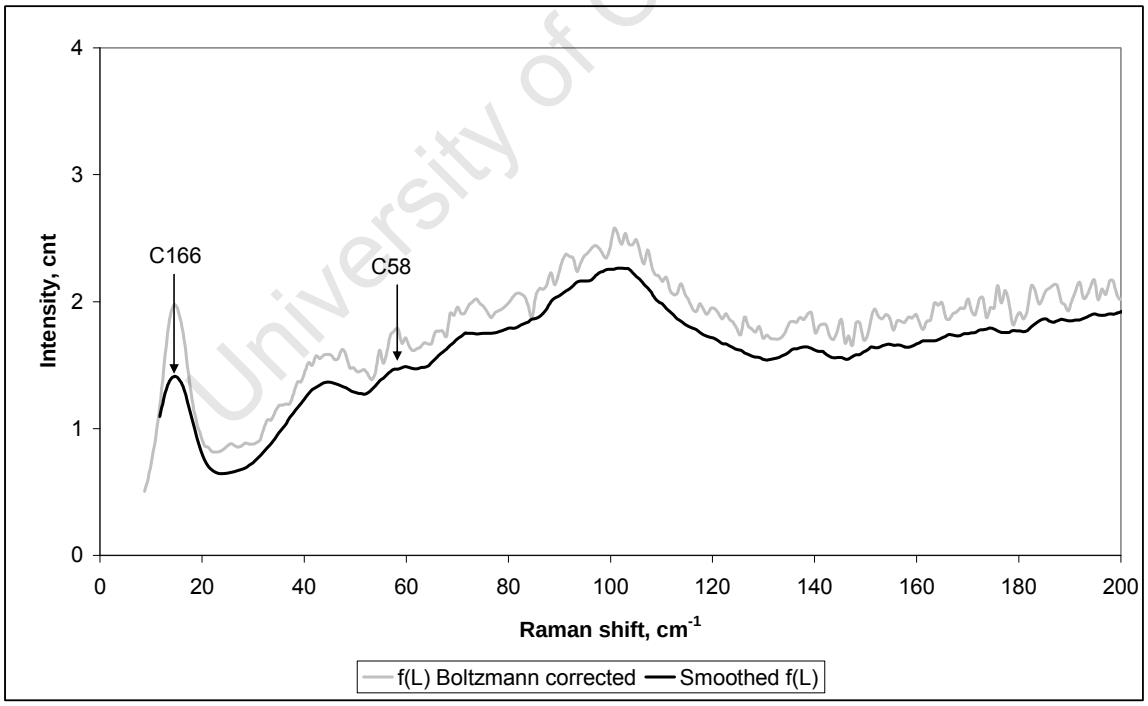

Figure 5.27: Boltzmann-corrected low-frequency Raman spectrum for Polywax 2000

Table 5.6 summarises the equivalent carbon numbers derived from both DSC and low-frequency Raman analyses shown in Figures 5.2 to 5.27 for all the samples studied. The GPC data of the wax samples are also included to illustrate how the derived data compare with the actual MW parameters of the samples.

Table 5.6: Comparison of carbon chain lengths derived from DSC, low-frequency Raman and GPC analyses

Sample name	DSC derived C#	n_{LAM}	GPC derived C#			P_d
			From M_n	From M_w	From M_z	
n-C_{32}	33	32	-	-	-	-
C80	28/ 42/ 43	44	43	44	45	1.02
H1	42/ 60/ 73	37/ 46/ 64	53	61	72	1.15
C105	58/ 83	58/ 83	70	77	87	1.10
90-C80/ 10-C105	42/ 53/ 60	44/ 52/ 69	44	46	48	1.05
50-C80/ 50-C105	42/ 67/ 73	44/ 62/ 89	51	58	68	1.14
C105 fraction F1	50/ 56	55	59	62	67	1.05
C105 fraction F2	63/ 78	40/ 67/ 73	77	83	90	1.08
C105 fraction F3	73/ 94	71	94	104	118	1.11
C105 fraction F4	45/ 73/ 103	52/ 67/ 89	100	111	125	1.11
SX-105	31/ 44/ 67/ 91	49/ 62/ 92	56	67	86	1.20
Polywax 1000	35/ 65/ 76/ 84	71/ 86	77	85	98	1.10
Polywax 2000	160	166	159	185	219	1.16

As the low-frequency LAM-1 vibrations originate from the all-*trans* portion of the chain lengths, the n_{LAM} is therefore a measure of the crystalline lamellar size only if the arrangement of chains is perpendicular. The crystalline chain length determines the material melting point. [65, 70] These two measurements, therefore, determine the same aspect of the crystalline structure and the two derived chain lengths may therefore be correlated directly without the need to consider the possibility of chain tilt. A consideration of chain tilt is therefore not required to solve the multiple melting peak problem. It may be relevant to wax structure, but may be evaluated only by direct measurement of the crystalline core thickness.

There is good correlation between the LAM-derived (n_{LAM}) and actual carbon numbers of the C_{32} sample. The spectra of the wax samples are all congested, indicating that the samples have complex lamellar structures. The spectra show dominant peaks on broad backgrounds, which may be interpreted as lamellar inhomogeneity. The implication of this is that there may be some overlap in the LAM modes which would make it difficult to accurately identify or assign them. Where asymmetric peaks are apparent, it is almost certain that their origin is a result of overlapping LAM modes. [96] In general, there is little evidence of LAM progressions for the wax samples, which allows most peaks to be interpreted as first-order modes, therefore indicating discretely different lamellar sizes. [27] All of the samples, including C_{32}, show a band at ca. 100 cm^{-1}. In some of the samples, this manifests as a broad band edge rather than a discrete peak. This behaviour indicates a spacing or crystalline core thickness associated with a size comparable to that of a C_{25} chain. This is interpreted in the literature as being indicative of an orthorhombic crystal system. [29] Additional peaks at ca. 60 cm^{-1}, ca. 73 cm^{-1}, ca. 84 cm^{-1} and ca. 93 cm^{-1} are observed which are common to all samples. A plasma line at ca. 37 cm^{-1} is observed with some samples, which is problematic as it appears that these samples show LAM activity around this wavenumber, making interpretation difficult.

The comparison in Table 5.6 shows correlation between the represented carbon numbers derived from the DSC and low-frequency Raman results. Although not exact, the correlation is remarkable considering the difficulties in interpreting the complex Raman spectra. The existence of a degree of correlation with the DSC results may be considered sufficient evidence to uphold the interpretation of the low-frequency Raman spectra. This technique was chosen above XRD, SAXS and ED for this work as a review of the literature indicated that it would allow multiple crystalline core thicknesses to be measured, which the alternative measurements are incapable of doing. Considering the sample complexities, the conclusion that may be made from the low-frequency Raman work is that there is indeed evidence of the occurrence of multiple core thicknesses having different sizes. Furthermore, a correlation was additionally seen with the GPC derived carbon number parameters. Some expected LAM peaks seem to be missing, but this could be due to overlap in bands corresponding to different crystalline core thicknesses.

5.4 CONCLUSION

The n_{LAM} values of a number of wax samples were correlated with a DSC-derived chain length associated with each melt peak. Although not exact, this correlation may be regarded as remarkable considering the difficulties associated with interpreting the complex Raman spectra of the waxes. It is certain that a LAM is associated with a crystalline core thickness of specific size, or the length of the all-*trans* portion of the chains in these lamellae. It may therefore be concluded that the multiple DSC melt peaks observed for some of these waxes are due to different crystalline core thicknesses of discrete average chain lengths forming during the crystallisation of these waxes.

CHAPTER 6

QUALITATIVE MODEL FOR THE STRUCTURE OF FT HARD WAX

6.1 STRUCTURE OF SOLIDS

The lamellar nature of the crystalline habit of n-alkanes, their mixtures, waxes and polymers has been described in Chapter 4. An understanding of how molecules in a mixed system co-exist in the crystalline phase is of relevance here. Models for the crystal structure of polymers, specifically PE, are often used to predict the behaviour of n-alkane mixtures. [51, 75, 77, 101]

The lamellar structure of n-alkanes, their mixtures, waxes and polymers is separated by a disordered interlamellar layer. [51, 53, 72, 88, 102] The thickness of the interlamellar gap is of a defined size. [53] Chain defects are concentrated at the chain ends or in the interlamellar region. [26, 53, 65, 71-72, 88, 103] The packing in an n-alkane mixture may be less than ideal due to the incorporation of different chain lengths in the structure. [53] The amorphous contribution or interlamellar disorder of the chain ends in polydisperse systems is greater than in single n-alkanes due to the disruption caused by the molecular weight distribution component. [13, 25-26, 43, 102, 104] This interlamellar region is consequently larger in n-alkane mixtures, low MW waxes and polydisperse systems. [42, 53-54, 101, 104] The size distribution of crystallites or lamellae in a multi-component system is related to the chain length distribution of the material that crystallises. [12, 26, 45, 74] Electron diffraction, low-frequency Raman and X-ray analyses allow crystalline core thickness to be measured. [26, 42-43, 53, 75] This correlates with the expected mathematical average chain length of a polydisperse system. [105-106] ED measures an *average* lamellar thickness in a localised region. [42]

The existence of the interlamellar region has important implications for the properties of a material. The degree to which the interlamellar region is able to accommodate deformation determines the tensile strength of the sample. Chain entanglements located at the interphase help to manage the extent of the deformation. [29] The Van der Waals forces between lamellae are small. Bridging of layers by longer chain molecules will

cause the material to become hard and brittle. [26] The wax-like properties of n-alkane mixtures is said to originate from the occurrence of the disordered interlamellar region. [88] There are two components to the development of a structural model in these systems, viz. the packing of molecules in layers and the packing of layers. [51]

The central postulate of polymer crystallinity is that crystallisation occurs into the lowest possible energy conformation. [92] The lowest energy state is an extended chain, all-*trans* conformation. [65]

The literature describes three types of mixed solid systems in n-alkane mixtures, viz. solid solutions, superlattices and eutectics. The progression from solid solution to fractionated solid solution (superlattice) to eutectic is a function of the relative molecular volume or chain length difference in the system. This progression may be concentration dependent. [26, 44, 49, 51, 53, 75, 107-109] Electron diffraction patterns allow the three solid-state forms to be distinguished from each other. [26] Electron diffraction may not be able to measure a distribution of crystalline core thicknesses and orientations when the stacking is irregular. [16, 28] X-ray and DSC data have also been used to distinguish solid solution and eutectic behaviour in binary mixtures of n-alkanes and perfluorinated n-alkanes. [109]

A solid solution is a stable mixture that remains randomly co-mixed over time. [105] A superlattice is a combination of both solid solution and eutectic structures. [109] A eutectic is a system in which demixing of the components occur. Demixing is fractionation which results in the lamellae consisting primarily of one component. [105] Figure 6.1 shows a schematic representation of the three types of solid state systems in polydisperse materials.

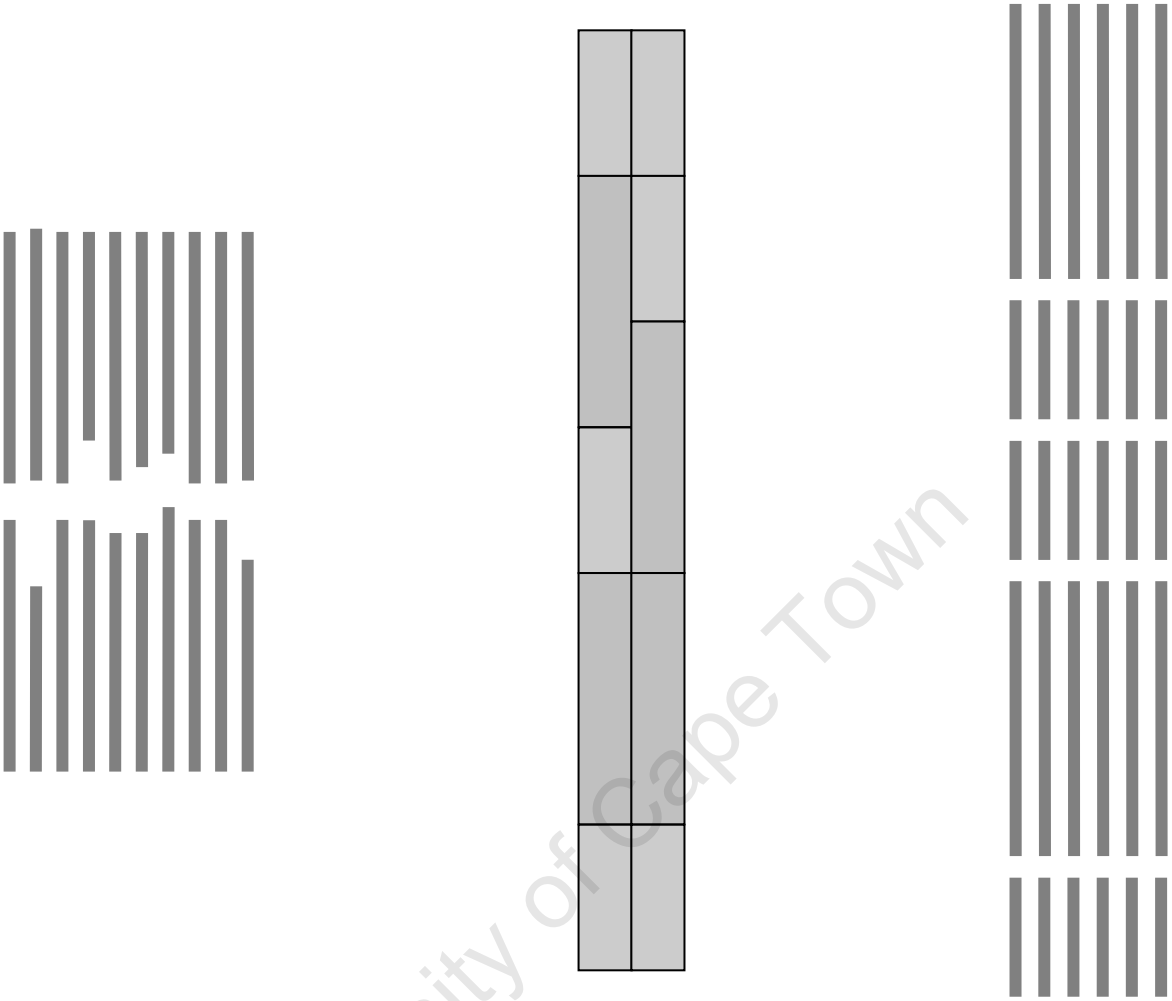

(a) **(b)** **(c)**

Figure 6.1: Schematic of the habit of the three solid-state systems in polydisperse materials: (a) solid solution, showing the coexistence of different chain lengths (note disordered lamellar surface); (b) superlattice, where lamellae of different sizes co-exist; (c) eutectic, showing complete separation of different sized lamellae. [26]

6.1.1 Solid solutions

Heterogeneous solid solution formation implies the random co-packing of chain lengths in an averaged structure. [106] The formation of a solid solution in a binary mixed n-alkane system is dependent on the chain length difference of the components. [26, 44, 50, 52, 75, 77, 88, 107, 109-110] The lamellae in a lamellar crystalline system are comprised of the straight-chain portion of the chains in the material. The average lamellar spacing for any binary n-alkane system is therefore equivalent to that of the

average carbon number of the system. It was also shown that a commercial paraffin wax displays an ED pattern similar to that of a binary n-alkane solid solution having an average chain length equivalent to the average chain length of the wax. [108]

Various quantitative criteria are given for solid solution formation. $C_t \leq 1.22\ C_s$ is an empirical rule for solid solution approximation in binary systems of n-alkanes, where C_t is the longer n-alkane component and C_s the shorter component. [26] This condition was derived from the Bragg-Williams approximation for a solid-solution lattice. Crystalline similarity as a condition for solid solution formation is not considered to be a determining factor, but molecular size and shape are. The formation of a solid solution is additionally dependent on the relative composition of the components. The lattice dimension of the solid solution will increase linearly with an increase in the mole fraction of the larger species in a binary n-alkane mixture. Chains which are longer than C_{44} all melt from the orthorhombic form, which also negates the influence of crystal habit on solid solution formation. [40] When the longer n-alkane in a binary mixture exceeds the "lattice length" of the shorter n-alkane, solid solution formation cannot occur as ideal mixing becomes improbable. The < 22% chain length difference criterion for solid solution formation is also valid for polyethylene systems. [26, 109]

Another reference states that for n-alkane pairs having a chain length ratio of 1.3-1.7, or a chain length difference of ten carbon number units, a superlattice structure forms. [55, 59, 71] The carbon number difference that may be accommodated in a solid solution is three or four. [71, 88] The shorter molecule dominates the effective lamellar spacing in longer chain n-alkane binary systems ($>C_{100}$), with the excess length of the longer molecule being accommodated in the amorphous interlamellar region. [101, 103] It has also been proposed that binary long-chain n-alkane systems with a chain length difference of up to 100 carbon number units may be tolerated in a solid solution. [68, 78, 111] The shorter chain length n-alkanes will dissolve in the longer chains with preservation of the structure of the solvent (longer chains) to a greater extent than the reverse case, which contradicts the information given in the previous references. [51, 101, 103] This is dependent on the concentration of the longer component being predominant. [53, 77, 106] This means that as the concentration of the longer chain component increases, so the lamellar spacing takes on its characteristics. [77] When the longer component is dilute, its chain ends are highly disordered. [106] The average lamellar spacing of a polydisperse

solid solution is therefore concentration dependent. [106, 108] This is probably the best conclusion that may be drawn from the conflicting literature references.

A third quantitative condition found in the literature is that when the chain length difference between components in a binary n-alkane mixture is six units or more, a solid solution forms on crystallisation from the melt, which slowly fractionates into a superlattice. The boundary condition for continuous solid solution formation is $C_N^{max} = 1.244C_N^{min} – 0.411$, where C_N^{max} and C_N^{min} are the respective maximum and minimum chain lengths in the binary mixture. Below this condition, solid solution behaviour occurs at all concentrations of components. [44]

Another model quantifies the boundary between stable and metastable solid solutions in binary n-alkane mixtures to be $C_N^{max} = 1.20C_N^{min} – 1.60$. This work also states that the maximum chain length difference that would be tolerated for solid solution formation is less than ten. [75]

In a stable solid solution, there is a higher concentration of non-planar conformers at the chain ends (interlamellar region) and void sites due to the necessity to incorporate different chain lengths into the crystalline lamellae. This will influence the interlamellar thickness. The values of the interlamellar thickness were found to be the lowest for n-alkanes, then binary n-alkane systems and highest for multi-component waxes. [42] If the chain-length mismatch in a mixture is relatively small, then solid solution stability is attained by filling of the void space in the interlamellar region by means of chain end rearrangement. The consequence of this would be a planar lamellar interface, which was observed for binary n-alkane solid solutions, multi-component paraffin waxes and low MW PE. [51, 105] Chain kinks could be introduced into the longer chain in the binary system to allow optimal packing. This could shorten the average crystal structure. Kinks and chain translation are two means to accommodate two different chain lengths in a single average crystal structure. [106] End conformational twisting could help to fill the voids left at the chain ends of shorter components. [106] Kinks and twisting occur as a result of bond rotation to assume a *gauche* conformation. These *gauche* bonds contribute to overall stability by allowing denser chain packing. [88] A PE-type structure is distinguished by XRD which involves structural disorder along the *c*-axis and chain-end bending or folding. [53]

Conformational disorder in the *c*-axis direction (length) arises due to the presence of chains of mixed length in the structure. This could result in differences being observed in the lamellar thickness determination depending on the analysis used. The *c*-axis parameter increases as the amount of the longer molecule in the sample increases. Chain length mismatches will influence the packing density, especially at the interlamellar region where disorder is accommodated. As the polydispersity of a system increases, so does the lattice strain as a result of increasing chain-length mismatch. The disorder in the interlamellar region will affect the solid solution stability of the wax.

Different packing arrangements may be realized at the interlamellar region as the size of the chain length mismatch increases. These possibilities are as follows and are illustrated in Figure 6.2 on the following page:

(1) a single n-alkane structure with little or no disorder in the interlamellar region;
(2) chain-length mismatch of three or four carbon atoms resulting in protrusion of chain ends into the interlamellar region;
(3) twisting and folding back of chain ends, resulting in an increased interlamellar spacing; or
(4) bridging of lamellae combined with chain end twisting and/ or folding. [26]

The projection of longer molecules across lamellae is said to be energetically less suitable than the accommodation of voids in solid solutions. [51]

Separation of the phases would occur in a binary mixture with a carbon chain-length difference of eight. However, the introduction of a third component into this mixture with an intermediate carbon chain length will prevent this separation. [88] In binary mixtures the longest chain is the most disordered. In a ternary mixture, the middle chain is the most disordered. [88]

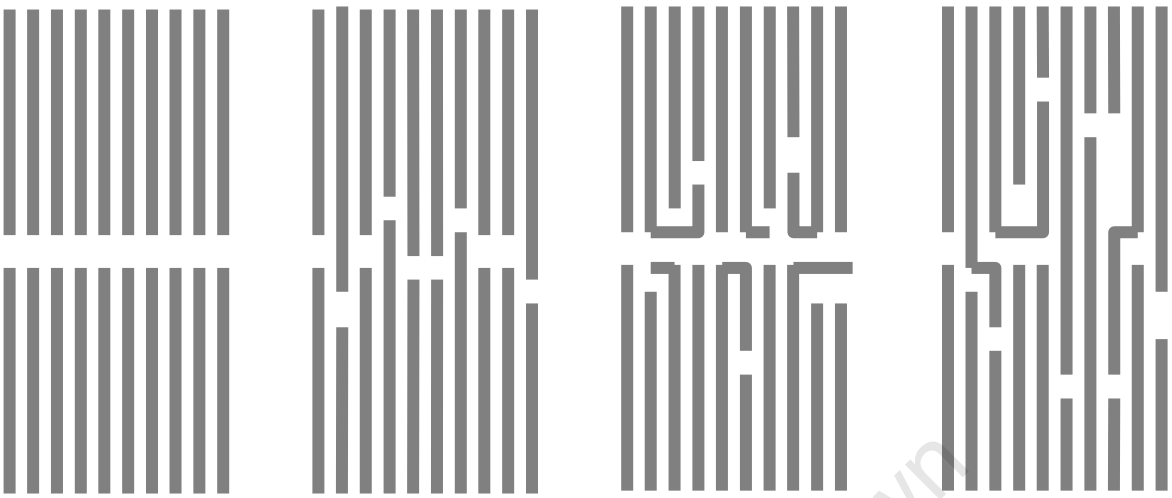

Fig 6.2: Solid solution packing options showing interlamellar packing with increasing chain-length mismatch due to the MWD. (1) Single n-alkane structure with well-ordered interlamellar region. (2) Inter-chain mixing due to low chain mismatch in the distribution. (3) Chain-end twisting and folding disorder due to higher chain mismatch in a broader MWD sample. (4) Combined inter-chain mixing and folding/ bending due to high chain mismatch. [53]

6.1.2 Bridged systems as a class of solid solutions

Where low-angle lamellar spacings are absent in an electron diffraction measurement, it has been proposed that a bridged or nematic structure is assumed by the material, without the lamellar layers observed for n-alkanes, blends of higher chain length n-alkanes (C_{60} to C_{80}), waxes and other materials. [15-16, 104] Longitudinal alignment of chains will form periodic clusters of average chain length distribution, but no true lamellae, resulting in a bridged lamellar structure. [60] Such a structure prevents complete separation of adjacent lamellae. [16, 112] Bridging molecules always orientate in the longitudinal direction of the crystal. [60]

Figure 6.2 proposes two types of bridged systems, viz. (2) and (4). A second, slightly different model has been proposed for this type of solid solution behaviour elsewhere and is shown in Figure 6.3 (a) and (b). [104]

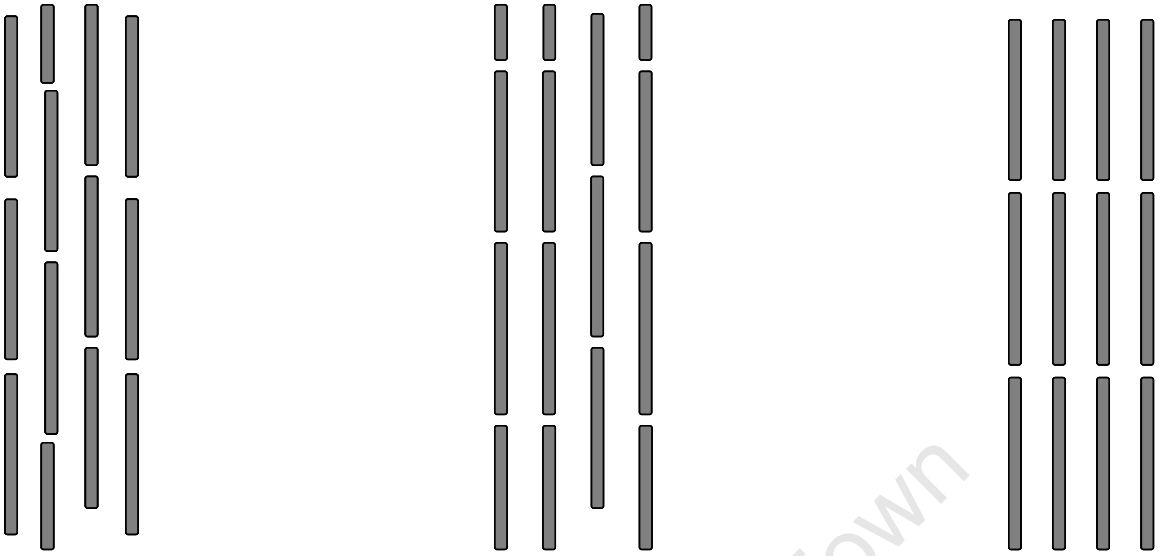

(a) **(b)** **(c)**

Figure 6.3: Schematic of possible chain packing arrays for linear chains in solid solutions. (a) Nematic order (nematocrystalline) with no average lamellae. (b) Bridged lamellar structure. (c) True lamellar structure. [104]

Annealing of a binary system of n-alkane mixtures may lead to a transition from a nematocrystalline to a separated lamellar structure. [15, 76] Broader chain length distributions will lead to a bridged structure. [15] Only a certain fraction of molecules are able to bridge lamellae. [112] They are by necessity the longer chain length molecules. If sufficient bridging molecules are present in the material to prevent the formation of a well-developed lamellar structure, the ED pattern will resemble that of high molecular weight polyethylene and oriented chain-folded PE. [60, 112]

It has been reported that true lamellae do not form in Shell Callista FT wax (melting point 72°C; carbon range C_{17} to $C_{63;}$ peak carbon number C_{33}) or in Sasolwax C105 due to a nematocrystalline arrangement of the very long chain components. This results in a continuous chain direction through adjacent lamellae. [15, 42, 60]

A nematocrystalline structure influences the material hardness as it reinforces the packing arrangement. The average contact at the interface in a true lamellar structure allows deformation here and results in material softness. [60] The amorphous phase

contributes significantly to the properties of semi-crystalline polymers. Thus the strength and ductility of a polymer are determined by the amorphous interlamellar region due to high molecular mass components that crystallise as tie chains across the interlamellar gap, resulting in the nematocrystalline structure. [65] The nematocrystalline structure therefore influences wax hardness, ductility and tensile strength.

6.1.3 Superlattice structure

A just large enough volume difference between components in a binary mixture of n-alkanes will result in the formation of a metastable solid solution that will fractionate over time due to lateral phase separation of the components. [45, 110] When the chain length difference of the two components becomes too large, the accommodation of strain in the crystal lattice increases and a superlattice or inter-block array forms. The boundary for the solid solution stability in terms of C_n^{min} vs. C_n^{max} is very sharp. As the chain length mismatch increases, a point is reached at which greater stability is attained through demixing than through interlamellar chain-end rearrangement. [88, 105] The chain-length mismatch boundary is six carbon number units. This corresponds to the maximum conformational disorder that may be tolerated in a metastable structure. [88] When this boundary is crossed, a metastable solid solution forms. This results in the formation of a superlattice, which is again concentration dependent. [44, 71, 111] A superlattice consists of a triple layer of crystalline domains sandwiching two internal amorphous regions. A schematic diagram of a superlattice is shown in Figure 6.4. The outer crystalline domains consist of the extended chains of the shorter chain component and a matching length of the longer chain component. The latter components traverse the internal amorphous zones and their excess lengths crystallise in the inner crystalline domain. The crystallinity of this internal crystalline domain is known to be poor. Extending the chain length of the longer chain component causes the crystalline core thickness of the internal crystalline layer to increase without affecting the sizes of the sandwiched amorphous layers. [71-73, 111] The triple-layer periodicity and stacking order may be determined by constructing electron density profiles (EDPs) from SAXS measurements. [71, 75, 111] The periodicity may be related to the length of the extended chain n-alkanes with a correction for an expected chain tilt of 35°. [71-73, 111] A greater degree of tilt occurs if the molar fraction of the longer component is less than 0.5 in order to compensate for the material deficiency. [111] The occurrence of superlattice reflections indicates metastable crystalline domains. [88] Raman analysis of a superlattice structure measures

LAM-1 bands occurring at frequencies that represent the crystalline length of the inner and outer domains. The implication of this is that the LAM vibration of the longer chain n-alkane is decoupled as a result of it traversing the internal amorphous phases in the superlattice structure. [71-72, 111]

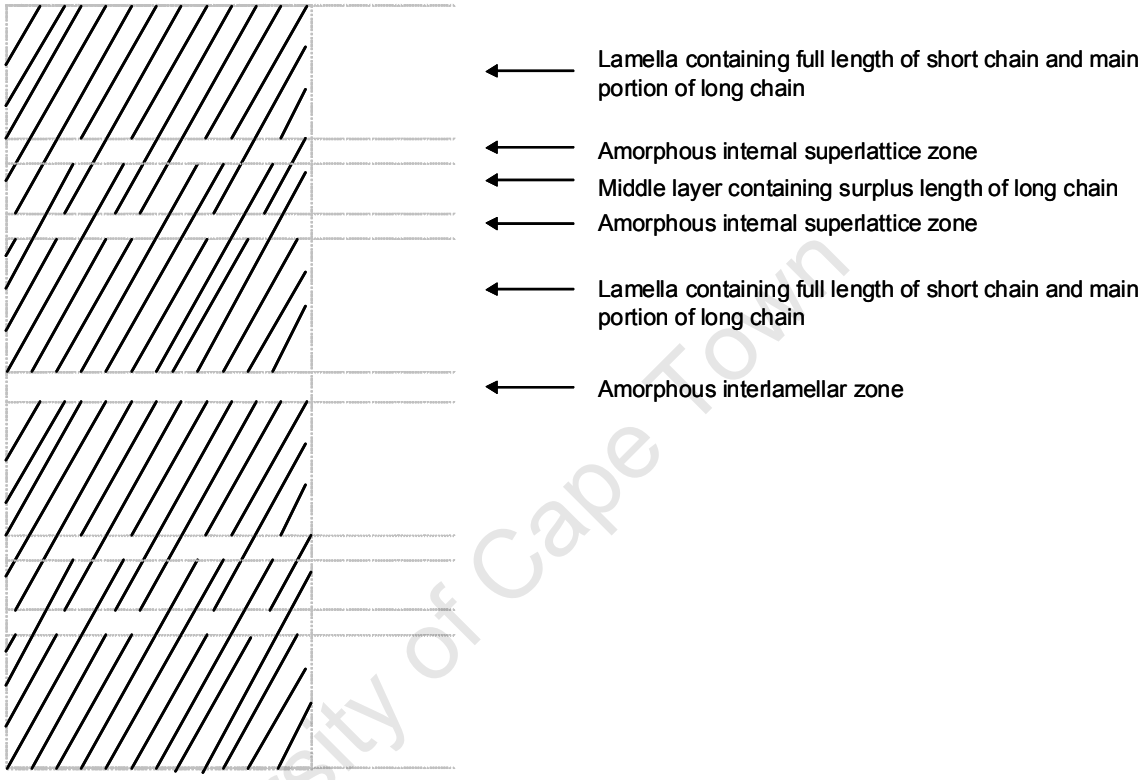

Figure 6.4: Schematic structure of a triple-layer superlattice [71]

DSC melting peaks which disappear when a sample is cooled and reheated have been attributed to metastable behaviour, which is when a solid solution forms at first and then fractionates over time. [44] ED measurements have shown only one lamellar spacing, even when DSC indicates that fractionation of a solid solution occurs. [107] This would be due to the limitations of ED analysis. [44, 113]

A superlattice is reported to occur in binary n-alkane pairs with a chain length ratio between 1.2 and 2, but some work shows that a chain length difference of up to 100 carbon atoms may be accommodated in very long n-alkane mixtures. [71, 103, 111]

6.1.4 Eutectic

The boundary between superlattice and eutectic behaviour is also very sharp. [40] Eutectics form when the chain-length difference becomes too large to accommodate the resulting lattice strain. [53, 109-110] ED measurements for a eutectic show only lamellar spacings associated with the two pure components with no evidence of a superlattice intermediate form. The eutectic in a binary n-alkane system is usually a mixture of two completely separated components. [107]

Stable eutectic behaviour is not influenced by ageing or reheating. The components of this system are totally immiscible. The ED measurement of a superlattice shows the pure component and an intermediate spacing, the latter being constant over all compositions. Domain ordering in the superlattice is random. In a eutectic, however, a pure phase domain for a single component could exist over several lamellae. [44] Eutectic behaviour is also concentration dependent. [26]

Microphase separation (eutectic formation, demixing) has been observed in binary n-alkane systems where one of the species is deuterated. This magnifies the effective chain length difference of the components. The eutectic behaviour was observed with IR, ED and DSC. Quench cooling of a mixed sample will serve to accelerate demixing. [110]

6.2 SOLID STRUCTURE AND POLYDISPERSE SYSTEMS

Two different models for multi-component wax systems have been proposed - a true lamellar packing model and a nematocrystalline system with bridging molecules linking adjacent layers. [26, 42, 60, 112] Both systems are stable multi-component solid solutions of n-alkane type material. [26] The former structure was proposed for narrow-cut petroleum distillates, petroleum waxes and binary and ternary n-alkane solid solutions. The latter structure was proposed for long-chain n-alkanes, carnauba, beeswax, Sasolwax C105, Shell Callista FT wax and low molecular weight linear PE. [42, 60] Broader chain length distributions encourage the formation of a nematocrystalline structure. [60] When chains are too short to fold but are too long to fit into a mean chain length structure, bridging occurs. [26] ED analysis of the true lamellar waxes has measured discrete lamellar spacings. As with the n-alkane binary systems, disorder as a result of chain-length mismatch is compensated for at the lamellar interface. [109] It was postulated that in low

MW waxes a broader MWD would better accommodate inter-chain mixing than narrow MWD waxes (see Figure 6.2). [54] The wax lamellar thickness for Carnauba wax as determined by ED is similar to the equivalent average n-alkane represented by the wax carbon distribution. [112] Three dimensional ED analysis shows evidence of bridged chain segments in some waxes and polymers. If there are enough bridging molecules to keep the interlamellar gap dimension, then the underlying lamellar structure may still be measured. [26]

6.2.1 Low molecular weight waxes

Petroleum distillate wax, paraffin wax and a multi-component n-alkane mixture (a pseudo-wax) all showed ED patterns which are characteristic of a lamellar solid solution. There is a significant concentration of defects in the interlamellar region, but the wax crystalline region is highly ordered. There is no difference in the crystalline structure of petroleum and narrow-cut FT waxes in terms of the ED data. FT waxes show a chain structure which is nematocrystalline and characteristic of chain folded PE. Annealing of an intermediate FT wax gives an ED pattern characteristic of a stable solid solution, as for paraffin wax. Broad distributions of molecules assume a nematocrystalline structure to allow the incorporation of the longer extended-chain molecules into the crystalline structure. [26]

XRD measurements on petroleum waxes showed that the *c*-axis length and molecular volume increased with increasing average carbon number. The wax crystallinity decreases as the number of components in the system increases. Evidence was found of a structure with chain-end disorder (folding and twisting) and inter-chain mixing. The amorphous peaks on the XRD analysis may be used to measure the size of the interlamellar gap region. [53]

The lamellar packing of narrow distillate cuts allows for the incorporation of the oil fraction into the interlamellar region. The nematocrystalline structure does not make provision for this oil fraction in the structure. [60]

6.2.2 Fischer-Tropsch hard waxes

ED analysis has shown evidence of Sasolwax C105 having a nematic structure with definite bridging having been identified. [15, 53, 114] The structure was likened to that of

unfolded low MW PE. The PE ED structure referred to is one in which polymethylene chain order is observed, but no distinct lamellar structure occurs. [112] The DSC melt bimodality was attributed to "fractionation", but no attempt was made to correlate this bimodality with the polymer structure. [15] The average chain length of Sasolwax C105 was measured by ED to be C_{63} or C_{68}. [26] The crystallite size of Sasolwax C105 was also described as a distribution of structures in the range C_{60} to C_{68}. [15] This correlates with one of the n_{LAM} values determined for this wax and shown in Chapter 5 (Table 5.5 and Figures 5.8 and 5.9). It should be kept in mind that a nematic structure is considered a special class of solid solution behaviour. It was postulated that the hardness of FT hard wax is related to the bridged crystal structure, despite the broad chain length distribution of the wax. [60] No evidence was found of the incorporation of methyl branching into the lattice. [15] The bridged structure would account for the manner in which material greater than the M_z parameter, which generally does not correlate with an n_{LAM} or DSC-derived carbon chain length, is incorporated into the crystalline lattice.

The same structure was also used to characterise the lower melting FT wax Shell Callista (melting point 72°C; carbon chain distribution C_{17} to C_{63}; carbon number peak maximum C_{33}). [60, 77] The DSC analysis of this wax does not show melting bimodality. [15] It was also found that the space group symmetry for this wax correlated with that of higher molecular weight polyethylene and not a shorter chain orthorhombic n-alkane. [60]

The solid-state structure of a broad MWD wax may change if it is fractionated, as evidenced in FT wax cuts. A nematocrystalline structure that manifests with a broad MWD material may change to a true solid solution structure in its fractions. [26]

6.2.3 Polymers

A PE type structure is distinguished by XRD which involves chain-end bending or folding. [53] The lamellar structure does not appear to be completely separated due to residual bridging molecules that span adjacent lamellae. The ED data of paraffin waxes were very similar to those of the LMWPE sample, particularly as the former contains extended chains. A distribution of chain lengths in a single lamellar was also indicated. The LMWPE sample additionally shows an ED feature not seen in the patterns of binary n-alkanes and paraffin wax. This characteristic is attributable to chain folding which disappears when the sample is annealed and is similar to that obtained for a nematic

array. In this structure, the interlamellar gap spacing is constrained. The population of bridging material was found to be small. The ED for LMWPE is therefore distinct from that of n-alkanes and paraffin wax. The DSC melting peak position of this sample was shown to be cooling-rate dependent. [102]

Multiple peaks were observed in the melting profiles of co-polymers and were assigned to the melting of branched and unbranched material. The DSC melting bimodality was shown to be cooling-rate dependent. The lower melting DSC peak was related to the melting of branched material. The higher melt peak was assigned to the melting of unbranched material. The unbranched material is therefore said to be unable to crystallise out separately at higher cooling rates and this material therefore dominates the crystalline structure. [115]

6.2.4 General structural aspects in binary n-alkane systems

The average lamellar packing assumes the dimensions of the next longest paraffin structure as the concentration of the longer chain increases in a binary n-alkane system. [110] The longer chain core thicknesses grow at a faster rate than those of the shorter chains. A long chain is more soluble in short chain lamellae than the reverse. When a longer chain is a minority component, the end may bend over and lie along the lamellar surface (see Figure 6.5). If a short chain is the minority component, its inclusion in the lamellae results in the creation of voids within the lattice. The filling of these voids by the more predominant longer chains is energetically more expensive. Structure (a) in Figure 6.5 is therefore thermodynamically preferred. [75] The long chain phase admits fewer chains of the second component than the short chain phase and the former therefore maintains integrity over a greater compositional range. [75]

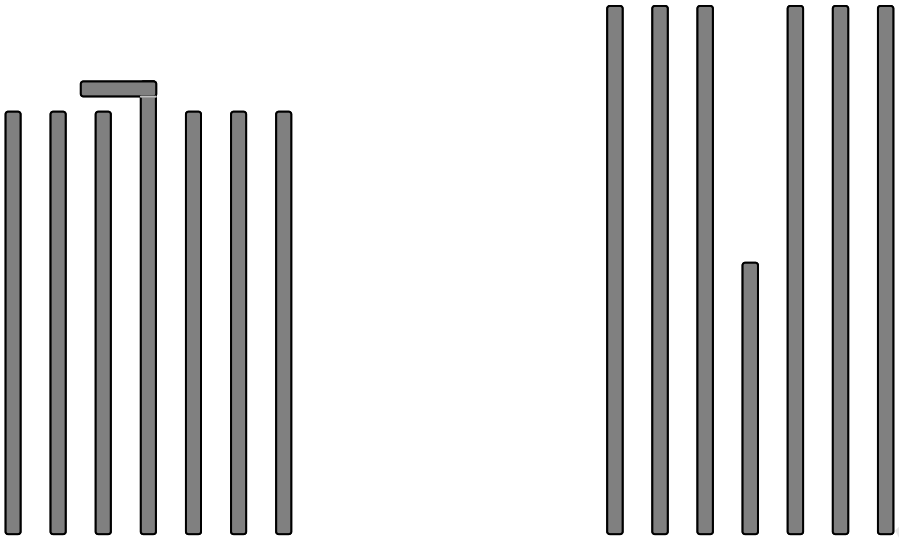

(a) **(b)**

Figure 6.5: Implications of the concentration dependence of chain-end mismatch in binary systems of n-alkanes. (a) A long chain isolated in a lamellar of short chains. (b) A short chain isolated in a lamellar of long chains. [75]

6.3 THE IMPLICATION OF BRANCHING FOR THE CRYSTALLINE STRUCTURE

Linear paraffin molecules stack more easily than branched material. Branching destroys the symmetry required for crystal formation. [98] High levels of chain defects and branching in polymers inhibit crystallisation. There are known exceptions in crystalline atactic polymers due to the small size of the branch group or the ability of the branch to crystallise itself. [65]

There is a debate on whether branches in PE are accommodated in the crystalline lattice or not. It is generally believed that a proportion of them are accommodated. [38] The inclusion of methyl- and ethyl-branching into the crystalline lattice of polyethylene will result in considerable expansion of the crystalline lattice in the *a*- and *b*-directions. [65] It has also been suggested that branching of small methyl- and possibly ethyl-groups would be located in the vicinity of structural kink defects. [65] Raman bands at ca. 927 cm^{-1} and ca. 773 cm^{-1} in PE are due to the occurrence of methyl- and ethyl-branching, respectively. [38] These bands are not apparent in the spectra of the FT wax samples (Figure 4.7).

The general opinion is that if the chain length is short, the branch is accommodated in the crystalline region. Branching is therefore said to induce a superlattice structure in long-chain n-alkanes. This contradicts other work which shows that the methyl branch will be rejected to the lamellar interface. This was determined from measuring the lamellar thickness to be equivalent to the length of the segments either side of the branch in symmetrically branched long-chain n-alkanes. [63]

Decoupling may also occur at a conformational disorder site, such as a *gauche* or kink defect. Disordered chains have an effectively shorter length than ordered chains as the LAM measures the length of the all-*trans* portion of the chain. [88-89] This type of disorder results in effectively two shorter chain segments which are able to vibrate independently of each other. [39-40, 83]

Short-chain, terminally methyl-branched n-alkanes were found to crystallise with the branch inside the crystalline region, which was clearly evident from expansion of the subcell parameters. [40, 94] Regular branching is not tolerated within the crystalline lattice as the sites would accumulate within a single atomic plane. Random branching may be accommodated in a distorted crystal lattice. A sizeable number of branches may therefore be included in the crystalline lattice in this way. It was found that for ethylene-propylene copolymers, seven methyl-branches per 100 carbon atoms could be incorporated into the crystal lattice due to its expansion. [94] In the long-chain n-alkanes, the branches are not tolerated in the crystalline lattice and the chains crystallise in a superlattice structure with the branches rejected to the amorphous region. [94] In asymmetrically branched long-chain n-alkanes, the shorter side of the chain may be either fully crystalline or fully amorphous. The long arm may traverse the crystalline region only once and its surplus is therefore found in the amorphous region. [93] If the branch is of sufficient size, it may crystallise itself, contributing to the overall crystallinity of the material. [40, 63] A LAM vibration in branched n-alkanes that gives the length of the branch segment, or a corresponding XRD diffraction pattern, is indicative that the branches form their own discrete crystalline domains. Branched n-alkanes do not chain fold. [40] Microcrystalline waxes showed that methyl branching is accommodated at the lamellar interface. [116]

In organic acids, a methyl branch may also be accommodated in the crystalline structure even if there is an appreciable level of branching. Chain tilt may occur in order to allow the methyl branches to be accommodated into the crystalline structure by expanding the crystal lattice to allow more room for the branch site. [117]

Cyclic branches impede crystallisation. The size of the branch determines the degree to which crystallisation is impeded. [40] Large branches will inhibit crystallisation and promote amorphous content. [63]

6.4 CHAIN TILT AND CRYSTALLINE STRUCTURE

Chain tilt is known to occur with FC materials, polymer crystals and long chain n-alkanes. [39, 65, 74-75, 82, 85] It develops as a result of crystallisation or annealing at high temperatures. [85] Tilt may also develop from initially perpendicularly arranged chains below the melting point as the temperature is increased. [85] Melt crystallisation at higher temperatures (>60-70°C) usually results in lamellae comprised of tilted chains. [85, 93] A perpendicular arrangement results below this crystallisation temperature. [85] It has also been reported that melt-crystallised long-chain n-alkanes and PE may initially crystallise below 80-100°C and 127°C, respectively, in perpendicular fashions with chain tilting occurring on heating or at a later stage. [85] The tilt angle increases gradually with heating until it reaches an angle of 35°. [85] A slow rate of crystallisation also favours the growth of tilted chains in lamellae. [63]

The most observed tilt angle is 35°. [85, 94] Larger angles have been observed in PE in exceptional cases and smaller angles may be observed during heating of a crystalline material with perpendicular chains, with the tilt angle approaching 35°. [85, 94]

Solution-crystallised n-alkanes crystallise with their molecules oriented perpendicular to the plane of the lamellae. As they are heated above 80-90 °C, the chains start to tilt, as in short-chain n-alkane systems. [85]

A perpendicular arrangement is therefore generally favoured by conditions of low crystallisation temperature and molecular weight, while chain tilt occurs with high crystallisation temperature and molecular weight. [85] Chain tilt is also favoured when the rate of crystallisation is low. [63]

Thermally induced end-group disorder is responsible for tilt. A tilt angle of 35° allows a longitudinal shift in the chains by one repeat unit, thereby preserving the crystallographic subcell, but allowing a greater surface area in which to accommodate the chain end disorder. [72, 85] Chain tilting therefore serves to alleviate the overcrowding problem of end-groups in the interlamellar region which is most problematic with a smooth lamellar surface. [85, 94] Melt crystallisation of long chain n-alkanes ($<C_{390}$) occurs at temperatures where tilted chains are stable and chain tilt therefore always occurs. [72, 88] This translates to a high interlamellar gap size and surface disorder in EC material. [72]

In FC materials, tilt is induced by the occurrence of a certain type of chain fold which induces a small vertical displacement of chains in order to optimise the crystal packing arrangement by lowering the energy. [65] Chain tilt gives a lower amount of amorphous entries per unit of fold surface and therefore contributes to lowering the energy state of the crystallised polymer. [65] Steric overcrowding may also be exacerbated by the inclusion of methyl branching in the interlamellar region. [94]

The tilt angle may be calculated from $\beta = \cos^{-1}(L/L_0)$, where β is the tilt angle, L is the crystalline core thickness and L_0 is the extended chain length. [72, 82, 85] SAXS and XRD measurements may be used to study chain tilt. [85] The onset of chain tilt is inferred by SAXS measurements by a shift in the diffraction peaks which represent the chain-stem length to wider angles. [85]

The low-frequency Raman measurement determines the length of the all-*trans* segment of a chain. This is equivalent to the lamellar thickness only when the chains are arranged in a perpendicular fashion within the lamellae. It is known that it is difficult to accurately determine the lamellar sizes of waxes due to their polydisperse natures. The existence of multiple lamellae of different sizes exacerbates this problem. XRD, SAXS and ED measurements are able to measure an average crystalline core thickness only, which would not allow the accurate evaluation of chain tilt in waxes displaying multiple crystalline core thicknesses. [42, 65, 111]

The phenomenon of chain tilt and its relevance to the structure of FT hard wax has therefore not been evaluated in this work. Although the literature does not refer directly to whether FT waxes display chain tilt, the previous work on wax crystallography,

including that of FT wax, implies a perpendicular arrangement of chains in the lamellae. [113] There is also evidence that the perpendicular orthorhombic crystal structure is favored in longer chain n-alkanes containing homologous impurities. [58]

6.5 LITERATURE EVIDENCE FOR FT HARD WAX STRUCTURE

The structure of Sasolwax C105 is described as a bridged solid solution with a crystalline core thickness equivalent to that of a C_{63} or C_{68} chain length. [15, 60] There is, however, no evidence given to explain the multiple melt peaks of FT hard wax, probably due to the fact that the ED measurements are able to measure an average crystalline core thickness only. The low-frequency Raman work discussed in Chapter 5 indicates that multiple crystalline core thicknesses of discrete sizes are apparent in the solid structure of FT hard wax. The crystalline core thicknesses correlate fairly well with average chain-length populations derived from the positions of the DSC melt peaks.

The question is why this crystalline core thickness segregation would occur. A number of facts could be pertinent to this issue. Firstly, solid solution formation in binary systems is dependent on the magnitude of the chain length mismatch. [26, 44, 50, 52, 77, 101, 106, 108-109, 118] Short-chain n-alkanes form solid solutions only when the chain-length difference is less than three or four carbon atoms. [72] Longer chain binary n-alkane systems are said to be capable of tolerating a chain length difference of up to 100 carbon number units. [41, 75] It is also known that the long-chain phase is less tolerant to the inclusion of shorter chains than the reverse, which might imply a molecular weight dependence of the segregation. [101]

In general, the factors affecting segregation in mixed systems are the chain length, chain length difference, concentration ratio, temperature and pressure. [118]

An example of molecular segregation in PE is practically related to the fact that the sample crystallises over a broad temperature range due to its composition. Only a certain portion of the material crystallises at higher temperatures. The higher molecular weight material crystallises first into dominant crystalline lamellae. The low molecular weight species crystallise subsequently at lower temperatures in separate lamellae. This is termed molar mass segregation. [65]

Table 6.1 evaluates the relevant average crystalline core thicknesses in each of the waxes studied in Chapter 5 against the literature criteria for segregation in binary n-alkanes. From this data there are some qualitative evidence that the segregation seen in the FT hard waxes could be due to chain length mismatch as a result of material polydispersity. The influence of chain length mismatch on the solid-state behaviour of n-alkane systems is so well documented that it is certain that the origin of crystalline core thickness segregation in FT hard wax is similar. [26, 44, 50, 52, 77, 101, 106, 108-109]

The samples Sasolwax C80, the blend consisting of 90-C80/ 10-C105 and C105 fraction F1 do not meet the criteria for segregation. The DSC analyses of the latter two samples, which are shown in Figures 5.10 and 5.14 in Chapter 5, indicate that the peaks associated with the higher temperature phases are very small, which could explain this. The DSC analysis of Sasolwax C80 shown in Figure 5.4 shows only a single melt peak.

Table 6.1 shows that the sample 90-C80/ 10-C105 (Figure 5.10) meets only one of the evaluated segregation criteria. The same is true of Polywax 1000 (Figure 5.24).Sasolwax C80 does not meet any of the criteria. It also appears that Criterion 2 shows full correlation with the empirical assessment of fractionation derived using DSC analysis. It should be kept in mind that these criteria were developed for binary n-alkane systems and that a different measurement is probably required for polydisperse systems. The wax polydispersities may therefore play a role in determining the onset of crystalline core thickness segregation, although this parameter considers only a portion of the distribution. The alternative term M_z/M_n will take into account a greater portion of the distribution. These data are given in Table 6.1. If the relative concentration of material in a specific crystalline core thickness is much smaller than in the others, the associated MW parameter may be significantly affected and this would reduce the sensitivity of either P_d or M_z/M_n. The evaluation of segregation in materials such as 90-C80/ 10-C105 and C105 Fraction F1 will therefore be problematic. The parameters P_d and M_z/M_n indicate that above 1.10 and 1.20, respectively, crystalline core thickness segregation will occur.

Table 6.1: An evaluation of the chain-length mismatch criteria for solid solution formation applied to the wax samples in this study

Sample name	DSC-derived C#	GPC derived C#			P_d	M_z/M_n	Would seg-regation occur based on Criterion 1? *(a)*	Would seg-regation occur based on Criterion 2? *(b)*	Would seg-regation occur based on Criterion 3? *(c)*
		From M_n	From M_w	From M_z					
C80	42	43	44	45	1.02	1.05	N	N	N
H1	43/ 53/ 71	53	61	72	1.15	1.36	Y	Y	Y
C105	57/ 78	70	77	87	1.10	1.24	Y	Y	Y
90-C80/ 10-C105	42/ 54	44	46	48	1.05	1.09	Y	N	N
50-C80/ 50-C105	42/ 65	51	58	68	1.14	1.33	Y	Y	Y
C105 fraction F1	50/ 56	59	62	67	1.05	1.14	N	N	N
C105 fraction F2	63/ 78	77	83	90	1.08	1.17	Y	Y	Y
C105 fraction F3	73/ 94	94	104	118	1.11	1.25	Y	Y	Y
C105 fraction F4	73/ 103	100	111	125	1.11	1.25	Y	Y	Y
SX-105	44/ 52/ 71/ 99	56	67	86	1.20	1.50	Y	Y	Y
Polywax 1000	69/ 78	77	85	98	1.10	1.27	N	Y	N
Polywax 2000	58/160	159	185	219	1.16	1.40	Y	Y	Y

(a) % chain length difference derived from M_n and M_z, >22% [26, 107]

(b) C_n^{max} that would be tolerated by C_n^{min} equivalent to DSC max 1 C#, from $C_n^{max} = 1.244C_n^{min}-0.411$ [44]

(c) difference between DSC max 1 C# and DSC max 2 C#, >10 [75, 98]

6.6 PHENOMENA ASSOCIATED WITH THE MELTING OF FT HARD WAX

Some other phenomena regarding the melting of FT hard wax have been observed. These are related to the relative DSC melt peak intensities as a function of either sample thermal history or sample concentration.

6.6.1 Thermal history dependence of segregation in FT hard wax

The thermal history dependence of the FT hard wax DSC melting peak temperatures was investigated. Figures 6.6 and 6.7 show for Sasol waxes C105 and H1 how the DSC melting peaks and their intensities vary as a function of the thermal history in terms of the cooling rate used prior to the melt analysis.

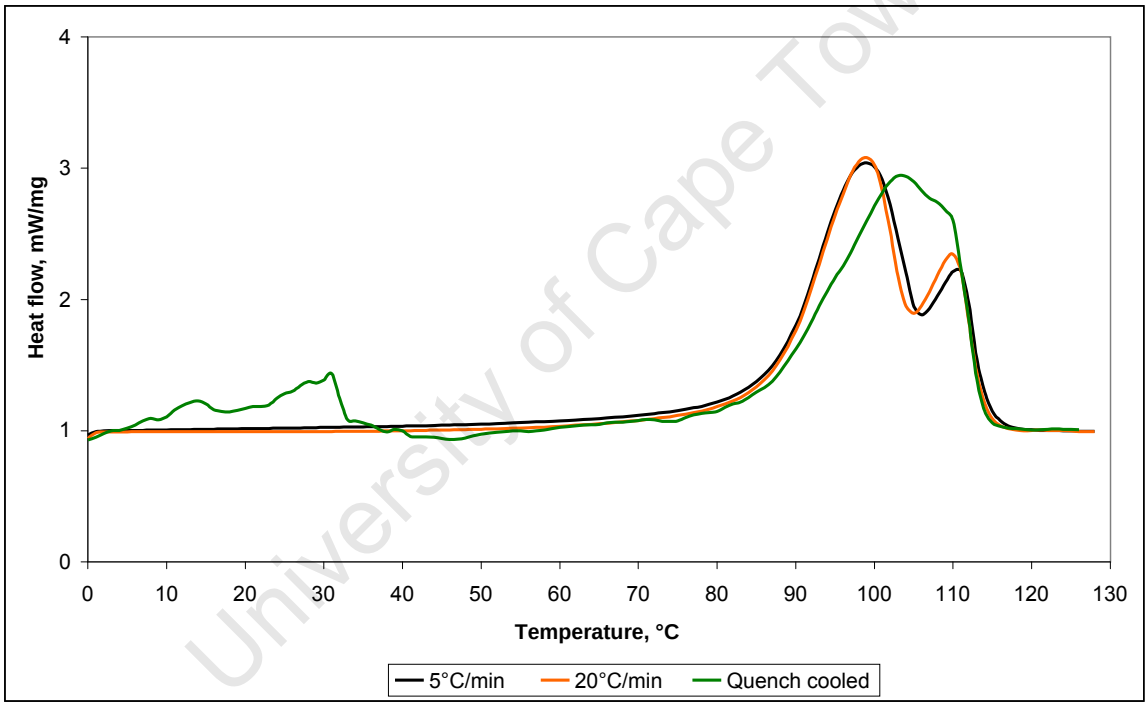

Figure 6.6: Thermal history dependence of Sasolwax C105 DSC melting profiles

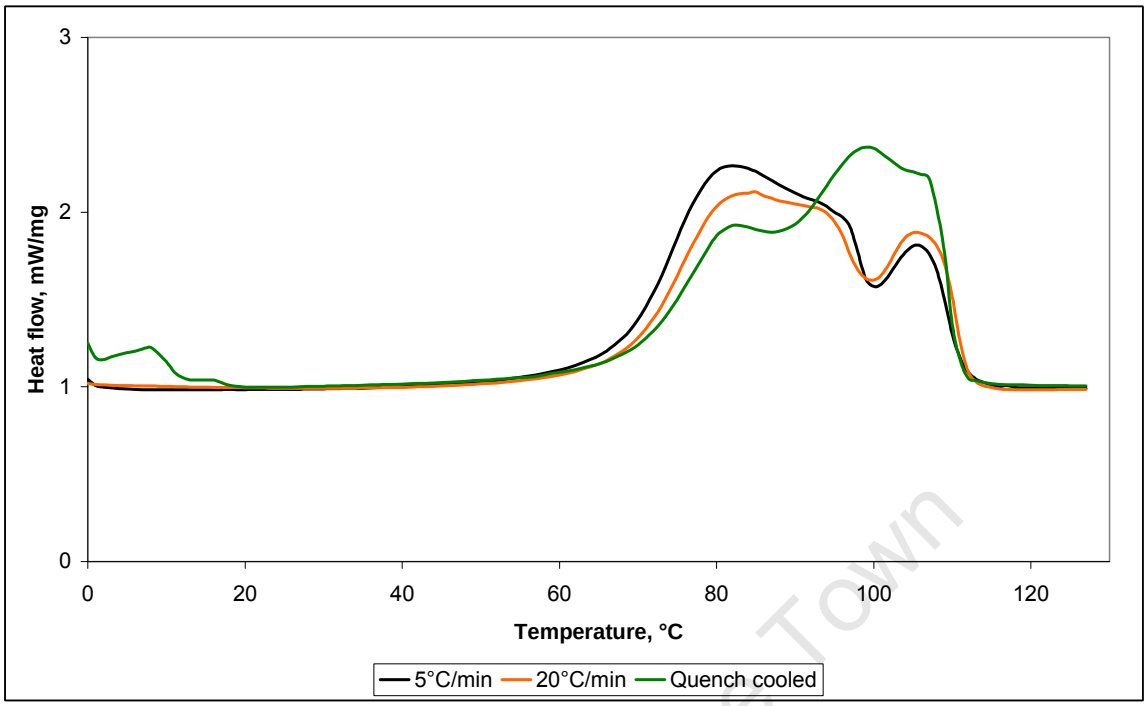

Figure 6.7: Thermal history dependence of Sasolwax H1 DSC melting profiles

Figure 6.6 shows that at relatively low cooling rates (5°C and 20°C), the relative intensities of the second DSC melting peaks are lower than that of the sample that was quench cooled. This would indicate a time-dependent component of FT hard wax crystallisation. The longer crystallisation time at lower cooling rates allows only the highest MW material, which is associated with the larger crystalline core thickness, to undergo preferential segregation. At a higher cooling rate (quenching), more low-melting material becomes entrapped in the longer chain core thicknesses due to less time being available to allow for complete segregation of the higher MW material. As a result, the relative intensity of the first peak is lower in the quench-cooled samples than in the samples cooled at lower rates. The same effect is seen in Figure 6.7 for Sasolwax H1 at the very high cooling rate. Figure 6.6 shows that the resolution between the two crystalline core thicknesses is poor when the sample is quench-cooled. This is once again a time-related effect due to the faster rate not allowing sufficient time for optimal crystalline core thickness segregation to occur. The shift in peak intensities on fast cooling is related to a change in the relative amounts of material that are present in each of the lamellae sizes. Note that the thermal activity apparent below 50°C for the quench-cooled samples is due to sample temperature equilibration and is not a characteristic of sample melting.

The fact that the DSC peak positions of the quench-cooled samples are entirely different to those of the samples that were cooled more slowly is indicative that the melting behaviour of FT hard wax is not a direct function of the MWD. This illustrates the crystallisation rate or thermal history dependence of the crystalline core thicknesses in FT hard wax.

6.6.2 Concentration dependence of segregation in FT hard wax

DSC analyses were performed on blends of Sasol waxes H1 and C80 and Sasol waxes H1 and C105. These results appear in Figures 6.8 and 6.9.

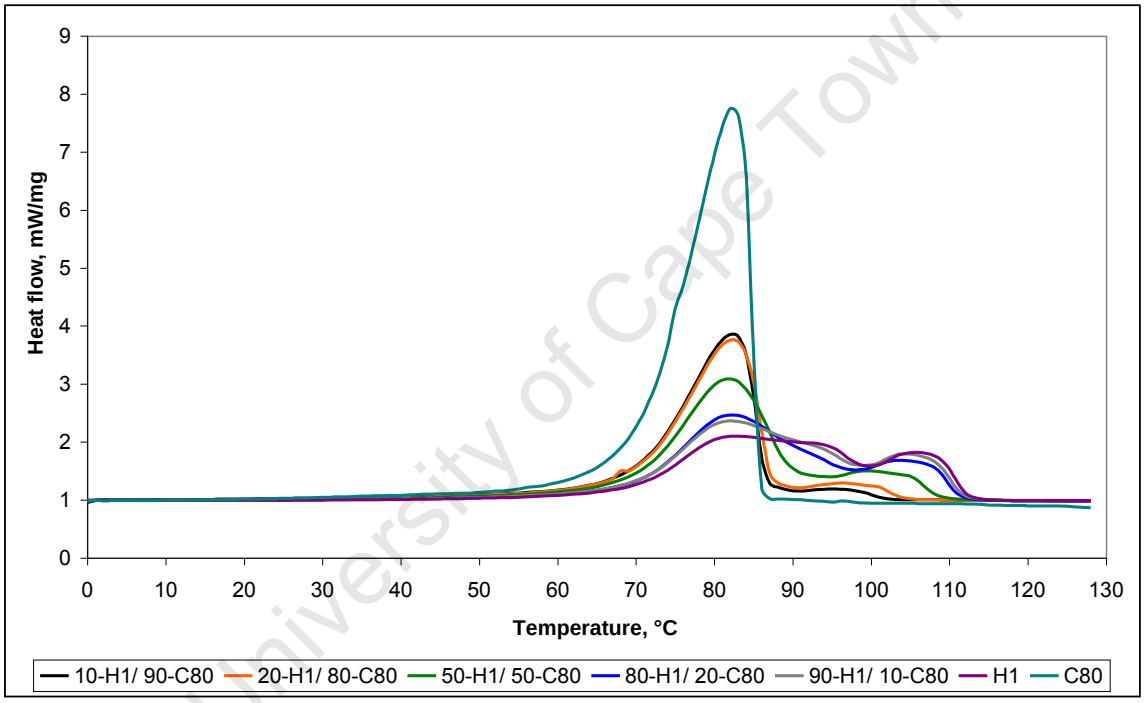

Figure 6.8: DSC analysis of blends of Sasol waxes H1 and C80

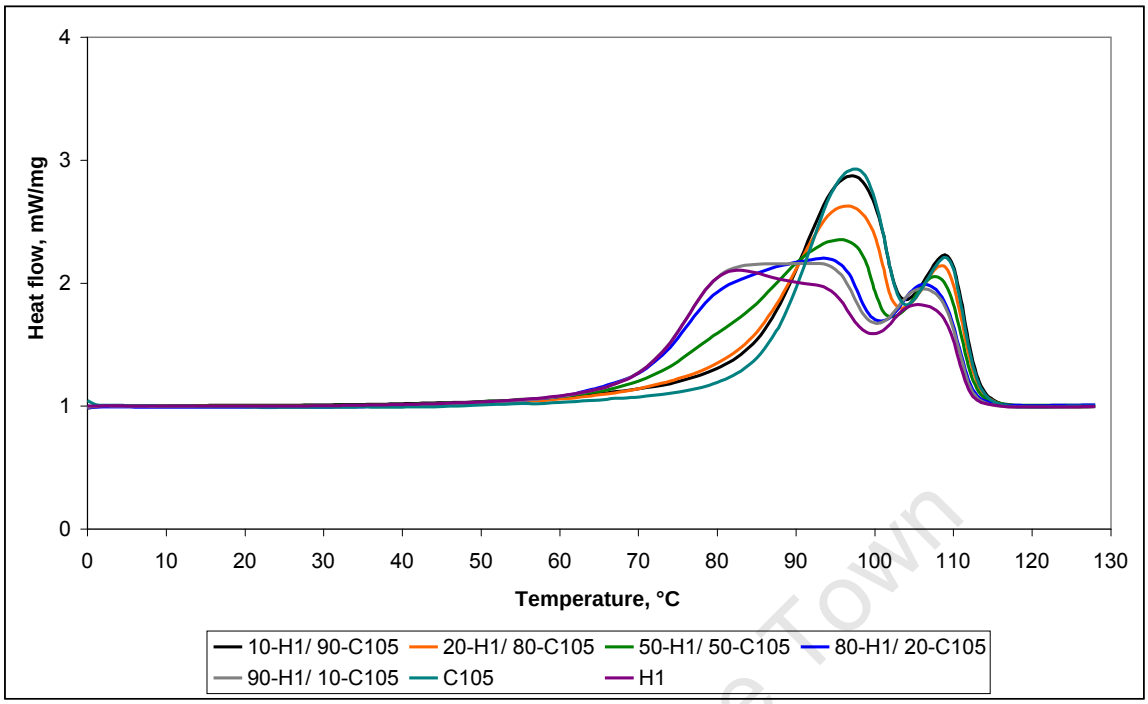

Figure 6.9: DSC analysis of blends of Sasol waxes H1 and C105

Figure 6.8 shows that the average crystalline core thickness of the smaller population remains constant for all concentrations in the H1/ C80 blends. This is inferred from the unchanging position of the first melting peak. This peak gradually broadens with a reduction in intensity as the amount of H1 in the blend increases, eventually leading to the development of a third, intermediate crystalline core thickness above a blend composition of ca. 20% C80. A progressively greater concentration of the higher molecular weight H1 component causes the average crystalline core thickness of the larger population to increase gradually, as implied by the increase in the temperature of the higher melt peak. This illustrates that the longer chain material is less tolerant to the inclusion of shorter chain material as the melting temperatures of the highest MW material progressively increases as a function of the concentration of H1. The implication of this is that the longer-chain material excludes the shorter-chain material during crystallisation, causing the latter to crystallise in a separate core thickness.

Figure 6.9 shows a similar trend in that the average crystalline core thickness associated with the longer chain material component increases with an increase in its concentration in the blends. The average core thickness represented by the first DSC melting peak of Sasolwax H1 eventually disappears at a composition of between 20% and 50% of this

component. This implies that the longer chain material will tolerate the inclusion of shorter chain material if the concentration of the latter is low enough. When apparent, the DSC melting peak position of the lower melting population in Sasolwax C105 again remains relatively constant for all compositions of the blend, while that of the higher melting population increases with a progressively greater composition between 50% and 100% C105.

These results show that the crystalline core thickness of longer chain material in FT hard waxes is determined by its concentration. It also shows that the longer chain material becomes less inclined to co-crystallisation with shorter chain material as the concentration of the latter increases.

6.7 A QUALITATIVE EMPIRICAL MODEL FOR FT HARD WAX STRUCTURE

A lamellar packing model for FT hard wax has been proposed which comprises four distinct structural zones.[120-121] These zones are described as:

- an amorphous zone containing the chain ends (interlamellar region)
- a rigid amorphous defect zone caused by the inclusion of methyl branches into the crystalline lattice
- a mobile amorphous phase, or oil fraction
- the crystalline phase. [120-121]

A schematic representation of this structure is shown in Figure 6.10.

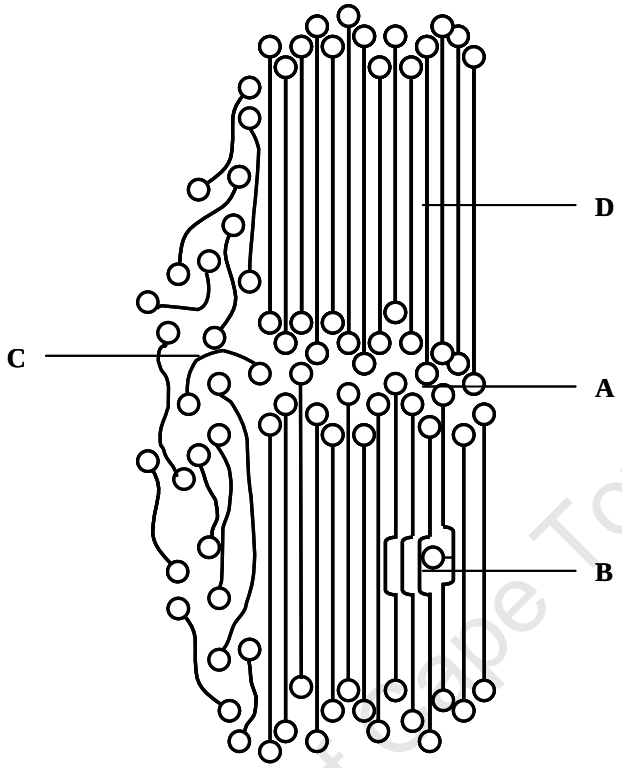

Figure 6.10: Schematic representation of the structure of a paraffinic or Fischer-Tropsch wax. A: Chain-end defect zone; B: branch defect zone; C: mobile amorphous zone; D: crystalline zone. [120-121]

The chain-end defect zone, or interlamellar gap, and the crystalline zone have been discussed extensively and there is sufficient evidence to support their existence and nature. The model in Figure 6.10 does not, however, represent the nature of the multiple lamellar sizes in FT hard wax. It also does not account for the bridged structure that has been demonstrated in previous work.

It is well known that only methyl branching occurs in FT wax. [122] The occurrence of branching is 0.41 per 100 carbon atoms. [120-121] This translates to approximately one branch for every third carbon chain, assuming an average chain length of 80 carbon atoms and only one branch per chain. Table 3.3 shows that the *b*- and *c*-axis parameters for the crystal lattice of the FT hard waxes are 4.966 Å and 2.589 Å respectively. The C-

C and C-H bond lengths are 1.20-1.54 Å and 1.06-1.12 Å, respectively. [123] It is also known that the lattice strain caused by a too large chain-length difference in a sample cannot be accommodated in a solid solution and therefore gives rise to superlattice or eutectic behaviour. It is therefore intuitively unlikely that the degree of lattice strain that would be propagated by the inclusion of a methyl branch site in the crystalline portion of the lattice structure could be tolerated in the lattice *b*- and *c*-axis directions without rotation or lengthening of the *c*-axis parameter. It is also unlikely that methyl branching could be accommodated within the crystal lattice dimensions of the crystalline structure measured in this work (see Chapter 3) for FT hard wax. The probability of branching in FT wax decreases as the MW of the chain increases and is predominantly terminal. [124-125] It is therefore highly likely that branching could be accommodated in the disordered interlamellar region. Branching at these positions in the chain and in the structure would also afford a greater degree of mobility to allow an energetically favourable conformation. The result of this would be to reduce the crystalline core thickness by the effective length of the branched segment that would be incorporated into the disordered region. It is known that in polymer systems chain defects, such as branching, are excluded from the crystalline phase. In the case of exclusion, the branched molecules are relegated to the amorphous portion of the material. [65]

Chapter 2 shows that the FT waxes also contain low levels of oxygenates and olefins. Oxygenates would be tolerated by the crystalline structure in the same way as branched material would. Their inclusion in the crystalline domain would result in an expansion of the subcell parameters. The oxygenate functionality could also be excluded to the interlamellar zone or the entire oxygenated molecule could present itself in the mobile amorphous zone. Olefins could be tolerated in the crystalline region or in the mobile amorphous zone.

The extent of the mobile amorphous zone has not been quantified. It would be sensible to expect that the structural nature of this material is the reason for it being totally excluded from the crystalline lattice. It is most likely that the material in this region would be preferentially extracted as oil in a wax oil-content determination due to its greater solubility in the solvents used [methyl-ethyl ketone (MEK) or methyl-isobutyl ketone (MIBK)] at the specific temperature (-34.5°C) of the test. [126] There is some evidence that the MEK extractables of a lower MW FT wax contain very short chain material with

multiple branches. [124] It could also contain any other material that cannot be tolerated by the crystalline domain, such as oxygenates.

In qualitative terms, a new model for FT hard wax may, therefore, be proposed which expands on those that have been published previously. The model incorporates the aspects of FT hard wax crystalline structure that have been discussed in this section, some elements of which have been determined by this work and others inferred from previous work. These aspects include a crystalline lamellar zone; a disordered interlamellar zone which accommodates disorder arising from chain-length mismatch, chain-end folding and terminal branch sites; an amorphous zone accommodating non-crystallisable material; and the occurrence of lamellar bridging by longer chain material. The model also accounts for the co-existence of crystalline lamellae of differing crystalline core thicknesses. It may not be entirely valid for waxes that display an appreciable level of branched molecules, but will describe the structure of other highly linear waxes, e.g. the intermediate FT wax, Sasolwax C80, and some petroleum waxes, with the exclusion of only the multiple crystalline core thicknesses. The model is shown schematically in Figure 6.11 on the following page.

6.8 CONCLUSION

This model captures all the structural elements described in the previous paragraphs to describe an empirical structure for FT hard wax. It would also be valid for any other wax with a predominantly linear structure. The model would apply with only one crystalline core thickness if only one is apparent in a wax, such as Sasolwax C80. It would also account for multiple crystalline core thicknesses that have been found to be responsible for the multiple melting peaks of the FT hard waxes.

The significance of this structure to wax properties and performance is that its overall crystallinity is optimised. The multiple lamellae structure effectively reduces the sizes of the amorphous interlamellar gaps. The incorporation of methyl branches into the interlamellar gaps would also increase the overall crystallinity by allowing a more optimal crystal packing arrangement. The occurrence of bridging molecules would also serve to optimise wax crystallinity by helping to fill voids that result from chain-end mismatches. Bridging molecules would also reduce the ease of crystal fracture at the interlamellar region, resulting in a harder and tougher wax.

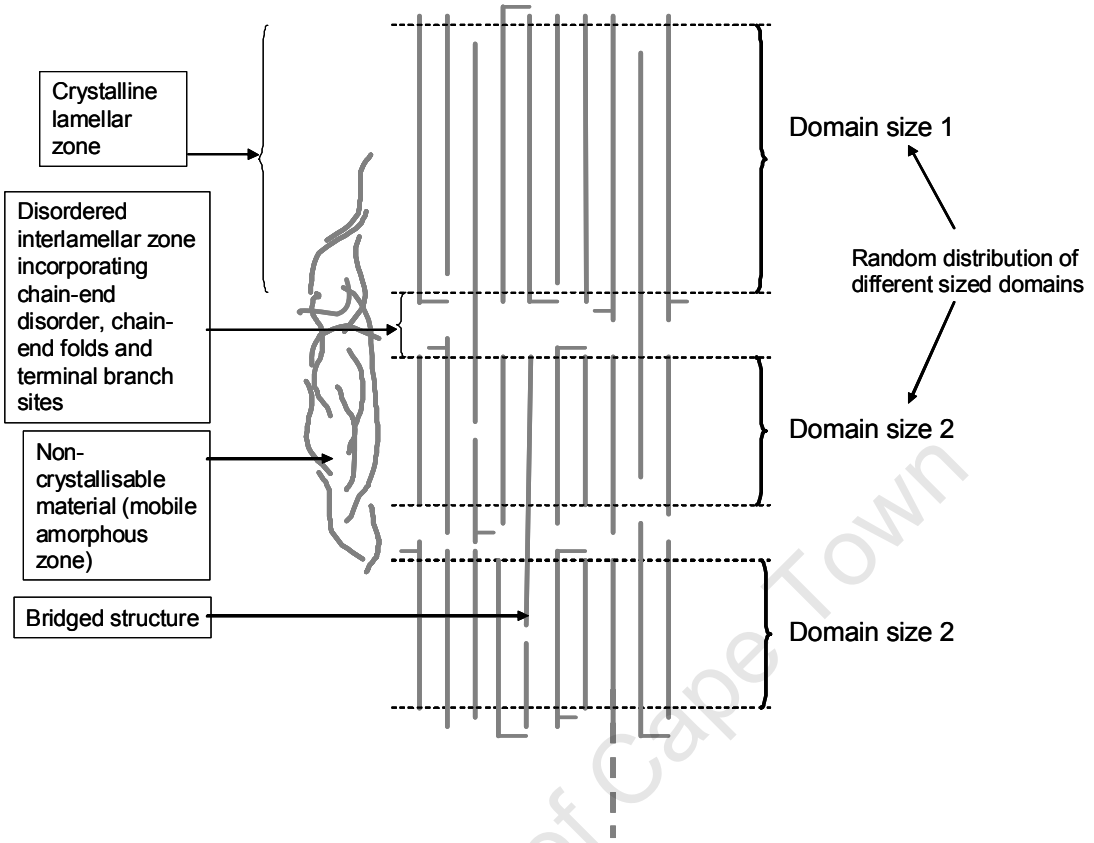

Figure 6.11: Proposed model for the structure of FT hard wax

The oil binding and solvent retention properties of Sasolwax C80 are well-known to polish formulators. The transition observed here from a single to multiple DSC melting peaks for Sasolwax C80 and Sasolwax H1, respectively, and the MW and MWD dependence of this transition, indicates that the size of the interlamellar region would likely approach a maximum for the former wax. The interlamellar gap size would then decrease abruptly with the onset of fractionation into different crystalline core thicknesses. A larger interlamellar gap, with the associated greater free volume, might allow small solvent or oil molecules in a formulation to become entrapped in the interlamellar region during crystallisation, thereby embedding them into the structure. Further work would be required to prove this theory.

CHAPTER 7

CONCLUDING REMARKS

The purpose of this work was to investigate the nature of the multiple melt peaks observed in the DSC melting profiles of the Fischer-Tropsch (FT) hard waxes Sasolwax H1 and Sasolwax C105. The Sasol waxes C80, H1 and C105 were the main focus of this study. The melt distribution of the former wax shows only one peak, while those of the latter two display multiple modes (see Figure 7.1). There is no documented explanation for the cause of this melting behaviour.

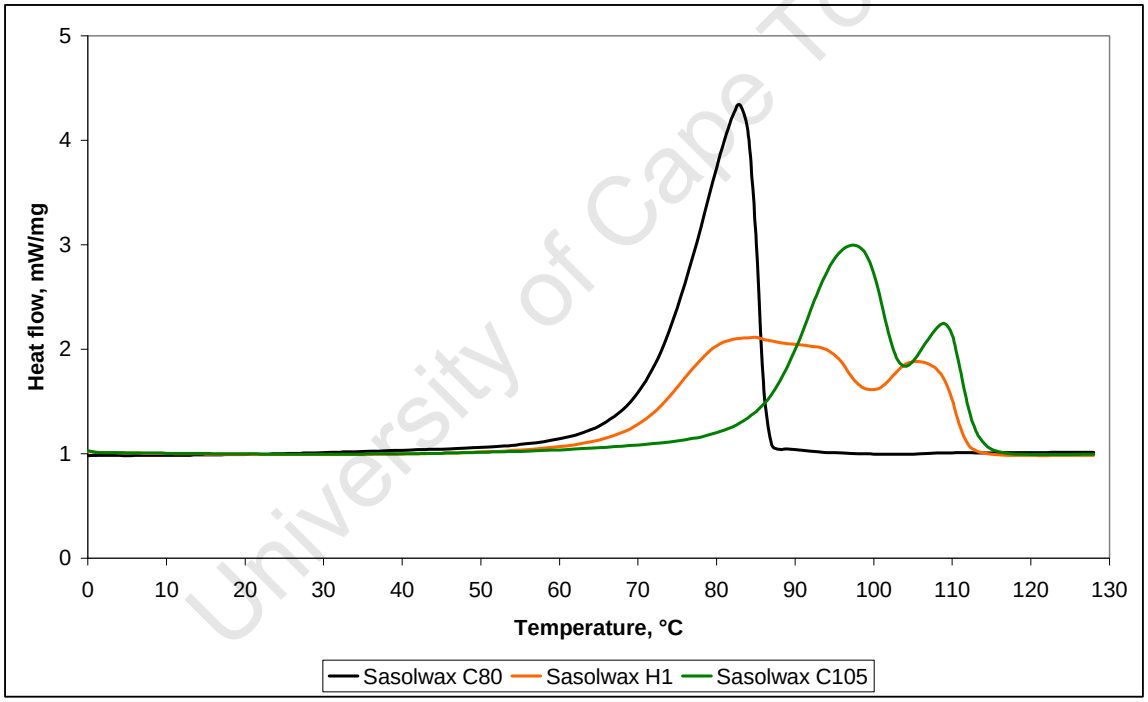

Figure 7.1: DSC analysis of the Sasol FT waxes

This work investigated the following aspects.

7.1 KNOWN CAUSES OF MELTING BIMODALITY AND ITS RELEVANCE TO FT HARD WAXES

There are three causes of melting bimodality in waxes or similar materials that are documented. These are polymorphism (crystal lattice transition); the co-existence of

extended (EC) and folded (FC) chain material in the crystalline structure; and a bimodal molecular weight distribution (MWD).

Polymorphism is known to exist in low melting n-alkanes, their binary mixtures and low melting paraffin waxes. [7, 11] This transition from the orthorhombic to the hexagonal form a few degrees below the melting point of the wax occurs in waxes only when the melting point is <75°C or the average carbon number is $<C_{39}$. [11, 47] All three of the FT hard waxes studied do not meet the criteria for polymorphism. XRD analysis at a series of temperatures up to the wax melting points confirmed that the orthorhombic phase is the only crystalline form present in these three waxes. The FT hard wax multiple melting peaks are therefore not due to polymorphism.

The onset of chain folding in polyethylene polymer occurs at C_{100}. [12, 45] If the MWD is broad and the sample spans the onset carbon number, then EC and FC material may co-exist in the crystal lattice. [12, 70] The resulting lamellae of different thicknesses pack together randomly to form clusters of finite sizes. [12] GPC analysis shows that FT hard waxes do contain some material $>C_{100}$. Low-frequency Raman analysis was used to determine if longitudinal acoustic modes (LAMs) could be measured in the FT hard waxes which represent a carbon chain length that is an integral reciprocal of their MW parameter-derived carbon numbers. This was not the case and it was therefore concluded that a heterogeneous EC/ FC structure is not the cause of FT hard wax melting bimodality.

It was shown that the MWDs of the FT hard waxes are not multi-modal and this can therefore not be a reason for their multiple DSC melting peaks.

7.2 AN EXPLANATION FOR THE CAUSE OF MULTIPLE MELT PEAKS IN FT HARD WAX

The low-frequency Raman work showed that multiple LAMs are present in the Sasol waxes H1 and C105. Only one LAM was measured for Sasolwax C80. A degree of correlation between the carbon chain lengths calculated from these LAMs and a mathematical derivation of an average chain length represented by the DSC melt peaks was demonstrated. The degree of correlation is considered adequate to establish that multiple crystalline core thicknesses are present in Sasol waxes H1 and C105. The

effective chain length and therefore lamellar thickness of a material determines its melting point. The multiple lamellar thicknesses that were identified in these waxes are therefore a feasible explanation for the melting bimodality in these waxes.

7.3 PHENOMENA ASSOCIATED WITH THE MELTING OF FT HARD WAX

It was shown that the nature of the bimodal melting peaks in FT hard waxes is determined by the thermal history of the sample. The crystalline core thicknesses are dependent on the crystallisation rate of the wax sample. It was also shown that the segregation that occurs in these waxes is concentration dependent in blends of the FT hard waxes. The longer chain material in FT hard waxes dominates the average lamellar thickness distributions of the higher melting lamellae.

7.4 A QUALITATIVE EMPIRICAL MODEL FOR THE CRYSTALLINE NATURE OF FT HARD WAX

A model has been proposed that describes four aspects of the crystalline nature of FT hard wax (Figure 7.2). The elements of this model were derived from this work and an overview of various previous studies. The four aspects are a crystalline lamellar zone; a disordered interlamellar zone which accommodates disorder arising from chain-length mismatch, chain-end folding and terminal branch sites; an amorphous zone accommodating non-crystallisable material; and the occurrence of lamellar bridging by longer chain material. The model also accounts for the co-existence of crystalline lamellae of differing sizes.

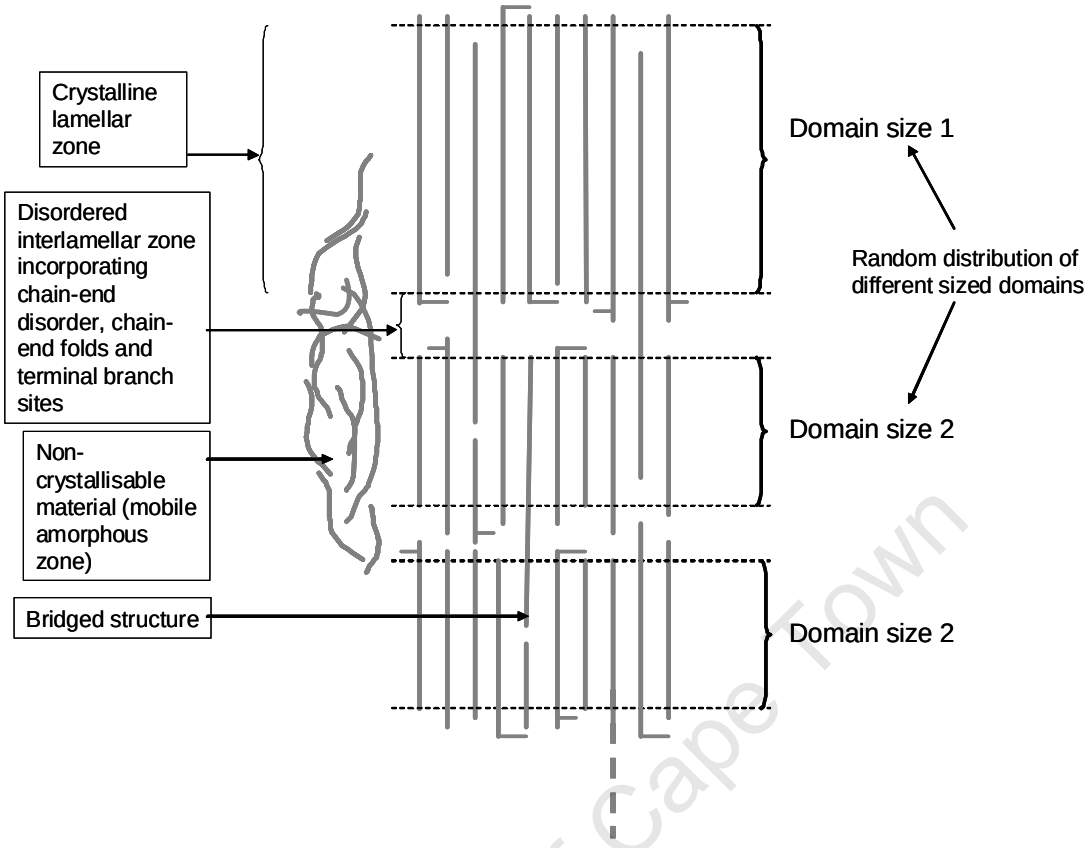

Figure 7.2: Proposed model for the structure of FT hard wax

7.5 FURTHER WORK

Further work should focus on quantifying some of the empirical aspects of this model. This could include:

- Measuring the relationship between interlamellar gap size and accommodation of chain-end mismatch in the crystalline regions. The gap size should grow as the mismatch increases and then decrease again as a function of segregation. This could be done by making use of SAXS measurements. (EDPs from SAXS measurements might be used to evaluate the periodicity of lamellar stacks.)
- A quantitative evaluation of the end-group conformation across, and chain folding in, the interphase region (boundary between crystalline and amorphous zones) using spectroscopic methods.
- Quantifying and qualifying the structure of the oil component of FT and other wax as a function of the wax MW. Sasolwax C80 is renowned for its ability to bind oil and solvents in wax blends and polish preparations. This may imply that it has the ability to entrap the oil in the interlamellar zone, rather than excluding it into

the mobile amorphous zone. It could be expected that the interlamellar zone size of this specific wax has approached a maximum limiting value due to its ability to crystallise in a single crystalline core thickness, whereas the next wax in the MW series of the FT wax family (Sasolwax H1) tends to segregate. It would be useful to correlate the results of such a study with the sample crystallinity.

- Determining a structural model for waxes with a greater degree of branching than the FT wax. Some evidence has been proposed in the literature for structural segregation on the basis of branching.
- Establishing a quantitative means of predicting the onset of chain folding in waxes.
- Establishing a viable means to evaluate chain tilt in broad MWD waxes, such as the FT hard waxes.

REFERENCES

(1) Ullmann's Encyclopedia of Industrial Chemistry, Chapter "Waxes", 6th Ed., Electronic release, 2000.

(2) G. V. Webber, Wax Characterisation by Instrumental Analysis, M.Sc. Thesis, University of Stellenbosch, 2000.

(3) ASTM D4419, American Society for Testing and Materials Standard, 1990, WorldWide Standards Service Plus, Issue 00-06 v4.0, Electronic Version.

(4) ASTM D341, American Society for Testing and Materials Standard, 1993, WorldWide Standards Service Plus, Issue 00-06 v4.0, Electronic Version.

(5) ASTM D3418, American Society for Testing and Materials Standard, 1999, WorldWide Standards Service Plus, Issue 00-06 v4.0, Electronic Version.

(6) Differential Scanning Calorimetry of a Wax using a Perkin-Elmer Pyris 1, Internal Sasol Wax method, HP 100, rev. March 2008.

(7) S. P. Srivastava, J. Handoo, K. M. Agrawal and G. C. Joshi, *J. Phys. Chem. Solids*, 1993, **54** (6), 639-670.

(8) R. Miller and G. Dawson, *Thermochim. Acta*, 1980, **41**, 93-105.

(9) B. Flaherty, *J. Appl. Chem. Biotechnol.*, 1971, **21**, 144-148.

(10) H. R. Faust, *Thermochim. Acta*, 1978, **26**, 383-398.

(11) D. S. Barmby, L. G. Bostwick and J. A. Huston, Jr., *Proceedings 6th World Petroleum Congress*, **VI** (21), 1-17, Verien Welt-Kongr, Frankfurt, 1963.

(12) M. Sawodny, G. Asbach and H. Kilian, *Makromol. Chem.*, *Macromol. Symp.*, 1990, **39**, 229-247.

(13) G. Ungar, J. Stejny, A. Keller, I. Bidd and M. C. Whiting, *Science*, 1985, **229**, 386-389.

(14) L. Mandelkern and G. A. Rufina, Raman Spectroscopy and Crystalline Polymers: the Polyethylenes, ACS Polym. Mater. Sci. Eng. Conf. Proc., **75**, Orlando, 1996.

(15) D. L. Dorset, *Z. Kristallogr.*, 2000, **215**, 190-198.

(16) A. S. Luyt and I. Krupa, *Thermochim. Acta*, 2008, **467**, 117-120.

(17) P. W. Atkins, Physical Chemistry, 3rd edition, Oxford University Press, Oxford, 1987.

(18) H. H. Bauer, G. D. Christian and J. E. O'Reilly (Ed.), Instrumental Analysis, Allyn and Bacon, Inc., Massachusetts, 1978.

(19) Dr. A. Baran, Sasol Technology R&D, personal communication, January 2009.

(20) Determination of the Carbon Number Distribution and Simulated Distillation of Waxes using High Temperature Gas Chromatography (HTGC), Internal Sasol Method, HP 030, rev. March 2008.

(21) W. W. Yau, J. J. Kirkland, and D. D. Bly, Modern Size-Exclusion Liquid Chromatography: Practice of Gel Permeation and Gel Filtration Chromatography, John Wiley and Sons, New York, 1979.

(22) S. R. Holding and E. Meehan, Molecular Weight Characterisation of Synthetic Polymers, RAPRA review report 83, **7** (11), RAPRA Technology Ltd., Shropshire, 1995.

(23) Determination of Molecular Weight and Molecular Weight Distribution by Gel Permeation Chromatography Analysis, Internal Sasol Wax method, HP 101, rev. March 2008.

(24) G. V. Webber, H. Boikanyo and M. Bekker, to be published, "Verification of the quantitative aspect of the GPC analysis of hard wax. Part 2 – y-axis calibration".

(25) G. V. Fraser, *Ind. J. Pure & Appl. Phys.*, 1978, **16**, 344-353.

(26) D. L. Dorset, *Structur. Chem.*, 2002, **13** (3-4), 329-337.

(27) J. Dlugosz, G. V. Fraser, D. Grubb, A. Keller, J. A. Odell and P. L. Goggin, *Polymer*, 1976, **17**, 471-480.

(28) J. Martinez-Salazar, P. J. Barham and A. Keller, *J. Mater. Sci.*, 1985, **20**, 1616-1624.

(29) L. H. Wang, R. S. Porter, H. D. Stidham and S. H. Hsu, *Macromol.*, 1991, **24**, 5535-5538.

(30) R. Alamo and L. Mandelkern, *J. Polym. Sci.: Part B: Polym. Phys.*, 1986, **24**, 2087-2105.

(31) L. H. Wang, S. Ottani and R. S. Porter, *J. Polym. Sci.: Polym. Phys*., 1991, **29**, 1189-1192.

(32) R. G. Snyder and J. R. Scherer, *J. Polym. Sci.: Polym. Phys. Ed*., 1980, **18**, 421-428.

(33) S.-I. Mizushima and T. Simanouti, *J. Amer. Chem. Soc*., 1949, **71**, 1320-1324.

(34) D. A. Cates, H. L. Strauss and R. G. Snyder, *J. Phys. Chem*., 1994, **98**, 4482-4488.

(35) T. Shimanouchi, Xth Symp. Macromol., Conformational Structure of Polymers, Prague, 1972.

(36) G Minoni and G Zerbi, *J. Phys. Chem*., 1982, **86**, 4791-4798.

(37) R. F. Schaufele and T. Shimanouchi, *J. Chem. Phys*., 1967, **47** (9), 3605-3610.

(38) D. L. Gerrard, W. F. Maddams, *Appl. Spectros. Rev.*, 1986, **22** (2&3), 251-334.

(39) R. G. Snyder, J. R. Scherer and A. Peterlin, *Macromol.*, 1981, **14**, 77-82.

(40) K. Ikedou, H. Yamamoto, H. Nagashima, N, Nemoto and K. Tashiro, *J. Phys. Chem. B.,* 2005, **109**, 10668-10675.

(41) G. V. Webber, H. Boikanyo and M. Bekker, to be published, "Verification of the quantitative aspect of the GPC analysis of hard wax. Part 1 – x-axis calibration".

(42) D. L. Dorset, H. Hu and J. Jäger, *Acta Cryst.*, 1991, **A47**, 543-549.

(43) D. L. Dorset, R. G. Alamo and L. Mandelkern, *Macromol.*, 1992, **25**, 6284-6288.

(44) D. L. Dorset, *Macromol.*, 1986, **19**, 2965-2973.

(45) S. R. Craig, G. P. Hastie, K. J. Roberts and J. N. Sherwood, *J. Mater. Chem.*, 1994, **4** (6), 977-981.

(46) R. R. Matheson Jr. and P. Smith, *Polymer*, 1985, **26**, 288-292.

(47) R. Miller and G. Dawson, *Thermochim. Acta*, 1980, **41**, 93-105.

(48) R. J. Howes, *Proc. 2nd European Symp. Thermal Analysis*, Aberdeen, UK, 1981.

(49) G. Ungar and A. Keller, *Colloid Polym. Sci.*, 1979, **257** (1), 90-94.

(50) W. M. Mazee, *Symp. Recent Advances Chem., Thermodynamics Hydrocarbons Rel. Substances*, 1958, **B**, 35-47.

(51) Y. V. Mnyukh, *Zh. Strukt. Khim*, 1960, **1**, 370-388.

(52) J. A. P. Coutinho and E. H. Stenby, *Ind. Eng. Chem. Res.*, 1996, **35** (3), 918-925.

(53) S. R. Craig, G. P. Hastie, K. J. Roberts, A. R. Gerson, J. N. Sherwood and R. D. Tack, *J. Mater. Chem.*, 1998, **8** (4), 859-869.

(54) G. P. Hastie and K. J. Roberts, *J. Mater. Sci.*, 1994, **29**, 1915-1919.

(55) L. Mandelkern, Crystallization of Polymers, Volume 1, Equilibrium Concepts, 2nd Ed., Cambridge University Press, Cambridge, 2002.

(56) H. G. Olf and B. Fanconi, *J. Chem. Phys*., 1973, **59** (1), 534-544.

(57) A. E. Smith, J. Chem. Phys., 1953, 21, 2229-2231.

(58) M. G. Broadhurst, *J. Res. Nat. Bureau Stand. – A. Phys. Chem.*, 1962, **66A** (3), 241-249.

(59) H. Hu and D. L. Dorset, *Acta Cryst.*, 1989, **B45**, 283-290.

(60) D. L. Dorset, *Z. Kristallogr.*, 2001, **216**, 234-239.

(61) J. W. Mullin, Crystallisation, 2nd Ed., Butterworths, London, 1972.

(62) W. R. Turner, *Ind. Eng. Chem. Prod. Res. Develop.*, 1971, **10** (3), 238-258.

(63) R. A. Pethrick, Polymer Structure, Characterization: from Nano to Macro Organization, RSC, Cambridge, 2007.

(64) A. Keller, *Pure & Appl. Chem*., 1992, **64** (2), 193-204.

(65) U. W. Gedde, Polymer Physics, Springer, New York, 1995.

(66) www.eng.uc.edu/~gbeaucag/Classes/MorphologyofComplexMaterials/Chapter%2061%20Swedish.pdf (accessed September 2008 and January 2009).

(66a) J-P. Gorce, S. J. Spells, X. Zeng and G. Ungar, *J. Phys. Chem. B*, 2004, **108**, 3130-3139.

(67) W. Billmeyer, Textbook of Polymer Science, 2nd Ed., John Wiley and Sons Inc., New York, 1971.

(68) R. J. Young and P. A. Lovell, Introduction to Polymers, 2nd Ed., Chapman & Hall, London, 1983.

(69) J. I. Lauritzen Jr. and E. Passaglia, *J. Res. Nat. Bureau Stand. – A. Phys. Chem.*, 1967, **71A**, 261-275.

(70) A. Keller and Y. Udagawa, *J. Polym. Sci.: Part A-2*, 1972, **10**, 221-238.

(71) X. Zeng and G. Ungar, *Phys. Rev. Lett*., 2001, **86** (21), 4875-4878.

(72) X. Zeng and G. Ungar, *Polymer*, 1998, **39** (19), 4523-4533.

(73) G. V. Fraser, P. J. Hendra, M. E. Cudby and H. A. Willis, *J. Mater. Sci.*, 1974, **9**, 1270-1274.

(74) W. Glenz, H. G. Kilian, D. Klattenhoff and F. R. Stracke, *Polymer*, 1977, **18**, 685-696.

(75) X. Zeng and G. Ungar, *Polymer*, 2002, **43** (2), 1657-1666.

(76) S. F. Parker, J. Tomkinson, D. A. Braden and B. S. Hudson, *Chem. Comm*., 2000, 165-166.

(77) W. P. Zhang and D. L. Dorset, *J. Polym. Sci.: Part B: Polym. Phys.*, 1990, **28**, 1223-123.

(78) M. Soutzidou, A. J. Masters, K. Viras and C. Booth, *Phys. Chem. Chem. Phys*., 1999, **1**, 415-419.

(79) K. Khoury, B. Fanconi, J. D. Barnes and L. H. Bolz, *J. Chem. Phys*., 1973, **59** (11), 5849-5857.

(80) S. L. Hsu, G. W. Ford and S. Krimm, *J. Polym. Sci.: Polym. Phys. Ed*., 1977, **15**, 1769-1778.

(81) J. Runt, I. R. Harrison, W. D. Varnell and J.-I. Wang, *J. Macromol. Sci.-Phys.*, 1983, **B22** (2), 197-212.

(82) G. V. Fraser, *Polym*., 1978, **19**, 857-858.

(83) D. L. Dorset, *Acta Cryst.*, 1996, **B52**, 753-769.

(84) W. L. Peticolas, G. W. Hibler, J. L. Lippert, A. Peterlin and H. Olf, *Appl. Phys. Lett*., 1971, **18**, 87-89.

(85) D. Sujeewa, M. da Silva, X. Zeng, G. Ungar and S. J. Spells, *Macromol*., 2002, **35**, 7730-7741.

(86) D. A. Braden, S. F. Parker, J. Tomkinson and B. S. Hudson, *J. Chem. Phys.*, 1999, **111** (1), 429-437.

(87) S. F. Parker, D. A. Braden, J. Tomkinson and B. S. Hudson, *J. Phys. Chem. B*., 1998, **102**, 5955-5956.

(88) D. Clavell-Grunbaum, H. L. Strauss and R. G. Snyder, *J. Phys. Chem. B*., 1997, **101**, 335-343.

(89) D. H. Reneker and B. Fanconi, *J. Appl. Phys*., 1975, **46**, 4144-4148.

(90) G. Zerbi, R. Magni, M. Gussoni, K. H. Moritz, A. Bigotto and S. Dirlikov, *J. Chem. Phys.*,1981, **75** (7), 3175-3194.

(91) B. Fanconi and J. Crissman, *J. Polym. Sci.: Polym. Lett. Ed.,* 1975, **13**, 421-426.

(92) H. G. M. Edwards, V. Fawcett and M. T. Lung, *J. Incl. Phen. Mol. Recog. Chem*., 1991, **11**, 267-279.

(93) M. Glotin and L. Mandelkern, *J. Polym. Sci., Polym. Lett. Ed*., 1983, **21**, 807-811.

(94) X. Zeng, F. Xie and G. Ungar, *Macromol*., 2007, **40**, 5750-5758.

(95) P. C. H. Mitchell, S. F. Parker, A. J. Ramirez-Cuesta, J. Tomkinson, Vibrational Spectroscopy with Neutrons: with Applications in Chemistry, Biology, Materials Science and Catalysis, Imperial College Press, London, 2005.

(96) K. Kalyanasundaram and J. K. Thomas, *J. Phys. Chem*., 1976, **80** (13), 1462-1473.

(97) R. G. Snyder, G. Conti, H. L. Strauss and D. L. Dorset, *J. Phys. Chem*., 1993, **97**, 7342-7350.

(98) R. Krishna and B. Smit, *Chem. Innov*., 2001, 27-33.

(99) Prof. S. Asher, Asher and Day Consulting, personal communications, October 2008 to November 2009.

(100) www.ripi.ir/congress11/wax%20definition.pdf (accessed September 2008 and January 2009).

(101) D. R. Lide (Ed.), Handbook of Chemistry and Physics, Web Version, 89th edition, 2008-2009.

(102) R. G. Snyder, V. J. P. Srivatsavoy, D. A. Cates, H. L. Strauss. J. W . White and D. L. Dorset, *J. Phys. Chem.*, 1994, **98**, 674-684.

(103) D. L. Dorset, *Z. Kristallogr.*, 1999, **214**, 229-236.

(104) X. B. Zeng, G. Ungar, S. J. Spells and S. M. King, *Macromol.*, 2005, 38, **17**, 7201-7204.

(105) D. L. Dorset, *Macromol.*, 1999, **32**, 162-166.

(106) D. L. Dorset and R. G. Snyder, *Macromol.*, 1995, **28**, 8412-8418.

(107) D. L. Dorset, *Z. Kristallogr.*, 1999, **214**, 223-228.

(108) D. L. Dorset, *Macromol.*, 1990, **23**, 623-633.

(109) D. L. Dorset, *Macromol.*, 1987, **20**, 2782-2788.

(110) J. Visjager, T. A. Tervoort and P. Smith, *Polymer*, 1999, **40**, 4533-4542.

(111) D. L. Dorset, *J. Phys. Chem. B*, 1997, **101**, 4870-4874.

(112) X. Zeng and G. Ungar, *Macromol*., 2003, **36**, 4686-4688.

(113) D. L. Dorset, *J. Appl. Phys.*, 1999, **32**, 1276-1280.

(114) C. Wutz, E. T. Samulski, M. Tanner and M. Brookhart, *Polym. Preprints*, 2001, **42** (1), 51-52.

(115) D. L. Dorset and R. G. Snyder, *Macromol.*, 1995, **28**, 8412-8419.

(116) D. L. Dorset. *Energy & Fuels*, 2000, **14**, 685-691.

(117) S. Abrahamsson, *Ark. Kemi*., 1959, **14**, 65-83.

(118) R. W. Ford and R. A. Scott, *J. Appl. Polym. Sci.*, 1967, **11**, 2325-2330.

(119) M. Maroncelli, H. Strauss and R. Snyder, *J. Phys. Chem*., 1985, 89, 4390-4395.

(120) J. H. le Roux and S. Pretorius, *Int. Symp. Anal. Chem in Exploration, Mining and Processing of Materials*, Johannesburg, 1976.

(121) E. C. Reynhardt, *J. Phys. D. Appl. Phys.*, 1985, **18**, 1185-1197.

(122) J. H. le Roux, *J. Appl. Chem., Lond.*, 1969, **19**, 230-234.

(123) http://en.wikipedia.org/wiki/Bond_length (accessed November 2008 and January 2009).

(124) A. Steynberg and M. Dry (Ed.), Fischer-Tropsch Technology (Studies in Surface Science and Catalysis), Elsevier, Amsterdam, 2004.

(125) www.fischer-tropsch.org/DOE/DOE_reports/88014638/wax-sct4.pdf (accessed November 2008 and January 2009).

(126) Oil Content Determination of Waxes, Internal Sasol Wax method, HP 009, rev. March 2008.